Implications of permeability uncertainty within engineered geologic fluid systems

Richard Scott Jayne Jr.

Dissertation submitted to the Faculty of the
Virginia Polytechnic Institute and State University
in partial fulfillment of the requirements for the degree of

Doctor of Philosophy
in
Geosciences

Ryan M. Pollyea, Chair
Robert J. Bodnar
Madeleine Schreiber
Richard Law
Yingqi Zhang

September 4, 2019
Blacksburg, Virginia

Keywords: Permeability, CO_2 Sequestration, Numerical Modeling, Heterogeneity

Implications of permeability uncertainty within engineered geologic fluid systems

Richard Scott Jayne Jr.

(ABSTRACT)

Carbon-capture and sequestration (CCS) in geologic reservoirs is one strategy for reducing anthropogenic CO_2 emissions from large-scale point source emitters. Recent developments have shown that basalt reservoirs are highly effective for permanent mineral trapping on the basis of CO_2-water-rock interactions, which result in the formation of carbonate minerals. However, the injection of super-critical CO_2 into the subsurface causes a disturbance in the pressure, temperature, and chemical systems within the target reservoir. How the ambient conditions change in response to a CO_2 injection ultimately affects the transport and fate of the injected CO_2. Understanding the behavior and transport of CO_2 within a geologic reservoir is a difficult problem that is only exacerbated by heterogeneities within the reservoir; for example, permeability can be highly heterogeneous and exhibits significant control on the movement of CO_2. This work is focused on constraining the permeability uncertainty within a flood basalt reservoir, specifically the Columbia River Basalt Group (CRBG). In order to do so, this dissertation is a culmination of four projects: (1) a geostatistical analysis resulting in a spatial correlation model of regional scale permeability within the CRBG, (2) a Monte Carlo-type modeling studying investigating the effects that permeability uncertainty has on the injectivity and storativity of the CRBG as a storage reservoir, (3) a modeling study utilizing 1-, 2-, and 3-D numerical models to investigate how the thermal signature of the CO_2-water system evolves during a CO_2 injection, and (4) a Monte Carlo-type modeling study focused on the integrity of the CRBG as a CO_2 storage reservoir through a probabilistic assessment of static threshold criteria.

Implications of permeability uncertainty within engineered geologic fluid systems

Richard Scott Jayne Jr.

(GENERAL AUDIENCE ABSTRACT)

The process of capturing CO_2 from point-source emitters, such as power plants and injecting that CO_2 into a geologic formation is one way to reduce anthropogenic CO_2 emissions. Recent field studies have shown that basalt reservoirs may be very effective at permanently storing the injected CO_2 making them a secure geologic formation to store the CO_2. However, basalt reservoirs can be highly fractured, which causes the properties of the reservoir (e.g. permeability, porosity, etc.) to be nonuniform. Having nonuniform reservoir properties creates uncertainty when planning a large-scale CO_2 injection. This research is focused on understanding and constraining the uncertainty of nonuniform reservoir properties associated with a large-scale CO_2 injection. The work presented utilizes a geostatistical analysis of permeability to inform a variety of numerical models to study how nonuniform reservoir properties affect CO_2 injection rate, how much CO_2 can be stored, how the pressure and temperature of the reservoir changes, and how secure the storage reservoir is during a CO_2 injection.

Dedication

I could not have done this without the support of my wonderful wife, Elsbeth. Her encouragement and support over the last 3.5 years have been unparalleled, she has heard and given feedback on enough practice talks about geology/numerical modeling that she could give her own seminar talk. The company of our animals Juniper, Mittens, and Splat always helped to relieve stresses from submitting manuscripts and applying for jobs.

I've really enjoyed my time here at Virginia Tech working towards my Ph.D. and it is all because of the people (and animals) that have helped and supported me. The best way I can sum up this Ph.D. is this, its been real, its been fun, its been real fun.

Acknowledgments

First, I would like to thank my advisor Ryan Pollyea for his guidance, encouragement, and support from the very beginning. It is because of his advising and mentorship during my graduate career that made all of this possible. Thank you to my committee members Bob Bodnar, Madeline Schrieber, Rick Law, and Yingqi Zhang for giving your time and expertise. Over the last 3.5 years I have made a number of friends here at Virginia Tech that have helped make this an enjoyable and successful experience. I'd also like to thank the Virginia Tech Geosciences Department for graduate student support through teaching and research assistantships throughout my Ph.D.

This work received financial support from the U.S. Department of Energy National Energy Technology Laboratory through cooperative agreement DE-FE0023381. Additional funding sources include Virginia Tech Geosciences Department and the Graduate Student Assembly at Virgnia Tech. This work also received support from the Advanced Research Computing at Virginia Tech, thank you for providing computational resources and technical support that have contributed to this research.

Contents

List of Figures

List of Tables

Chapter 1

Introduction

One of the main challenges of this century is the stabilization of the climate by making a dramatic reduction in anthropogenic CO_2 emissions [Wigley et al., 1996, Lackner, 2003, Pacala and Socolow, 2004, McGrail et al., 2006, Hegerl et al., 2007, Matter and Kelemen, 2009]. The reduction of CO_2 emissions may be achieved through two different approaches, each with challenges. CO_2 emissions can be cut by reducing our reliance on fossil fuels and hydrocarbon products or through new energy-efficient technologies. One of the most promising technological solutions is carbon capture and sequestration (CCS), which involves the storage of anthropogenic CO_2 in deep geological (>800m) formations [Pacala and Socolow, 2004, Bachu, 2008, Matter and Kelemen, 2009]. The efficacy of this method is dependent on the target reservoir, which in the context of CCS, is measured by (1) the capacity (mass of CO_2), (2) injectivity (ability to take in CO_2 at the rate that it is supplied), and (3) confinement (storage duration and the risk for leakage within the reservoir) [Hawkins, 2004, Rochelle et al., 2004, Bachu, 2008]. The primary targets for CCS are deep geologic reservoirs because they have the potential to store tens of millions of metric tons of CO_2 [Orr, 2009]. Deep geologic reservoirs (>800 m) are also favorable for CCS because at these depths CO_2 exists as a supercritical phase fluid, which maximizes CO_2 density and increases storage efficiency [Bachu, 2000, Orr, 2009]. Sedimentary formations have been extensively studied due to their ubiquity, large storage capacity, and relatively high permeability, which are all required for large-scale CO_2 injections [Bachu, 2003, Metz et al., 2005, McGrail et al., 2006]. Other op-

tions for CCS include depleted oil/gas reservoirs and deep, un-mineable coal seams [Brennan and Burruss, 2003]. However, continental large igneous provinces are gaining recognition as suitable reservoirs for commercial-scale CCS [McGrail et al., 2006, Matter et al., 2016]. Unlike sedimentary aquifers that keep the CO_2 trapped via capillary and solubility trapping mechanisms, igneous rocks have a higher potential for permanent mineral trapping of CO_2 [McGrail et al., 2006, Matter et al., 2007, Matter and Kelemen, 2009, Zakharova et al., 2012]. In basalt reservoirs, CO_2 trapping occurs primarily through two mechanisms: (1) physical trapping, which involves injection the CO_2 below an impermeable caprock, and (2) geochemical trapping, which involves a series of chemical reactions between the CO_2, aquifer water, and reservoir rock resulting in the precipitation of a thermodynamically stable carbonate minerals. However, the injection of super-critical CO_2 into the subsurface causes a disturbance in the pressure, temperature, and chemical systems within the target reservoir. How the ambient conditions change in response to a CO_2 injection ultimately affects the transport and fate of the injected CO_2. Understanding the behavior and transport of CO_2 within a geologic reservoir is a difficult problem that is only exacerbated by heterogeneities within the reservoir; for example, permeability can be highly heterogeneous and exhibits significant control on the movement of CO_2. Additionally, spatial heterogeneities are present at all geologic scales, from pore [Chang et al., 2016] to reservoir scales [Doughty and Pruess, 2004]. Understanding how spatial heterogeneity affects fluid flow is critical for engineered CCS reservoirs in terms of monitoring, management, and verification. T

This dissertation focuses on constraining and understanding how permeability uncertainty affects industrial-scale CO_2 injections within a flood basalt reservoir, specifically the Columbia River Basalt Group (CRBG). The methods utilized here to understand the effects of permeability uncertainty within the CRBG consist of a geostatistical analysis coupled with numerical modeling studies to answer the following questions: (1) Can the permeability

distribution within the CRBG be described by a mathematical model? (2) How do equally-probable permeability distributions within the CRBG affect injectivity and storativty of CO_2 injected into the CRBG? (3) How does the thermal signature of a CO_2 plume vary between homogeneous and heterogeneous formations, and can temperature be used as a way to monitor CO_2? (4) How do industrial-scale CO_2 injections affect reservoir integrity (storage security) in heterogeneous flood basalt formations? Answering these questions is critical for determining the efficacy of basalt reservoirs as a suitable storage site for industrial-scale CO_2 sequestration operations.

The first question is addressed in Chapter 2, does permeability within the CRBG exhibit any spatial correlation? This work has resulted in several notable findings, including a geostatistical analysis of CRBG permeability which suggests that the rapid loading and subsequent subsidence caused by the emplacement of the CRBGs results in bending moment stresses that cause a reversal in the depth-decaying permeability trend. This study further implies that increasing permeability at depth may be a characteristic feature of continental large igneous provinces (LIPs). Additionally, the geostatistical analysis reveals that CRBG permeability is spatially correlated with a 5:1 anisotropy ratio, and the direction of maximum horizontal correlation is at N40°E. This direction of maximum spatial correlation has implications for both natural and engineered geologic fluid systems within the CRBG.

These geostatistical correlation models developed in Chapter 2 are used in Chapter 3 to create an ensemble of stochastically generated and equally-probable reservoir domains. The ensemble of equally-probable reservoir domains are then used to create an ensemble of equally-probable CO_2 injection models, the results of which bound the uncertainty associated with spatially variable reservoir properties. This Monte Carlo simulation strategy is used to investigate the feasibility of industrial-scale CO_2 injections in the CRBG. Results from this study provide (1) a link between permeability heterogeneity and CO_2 storage efficiency; (2)

a first-order approximation of the level of sensitivity associated with CO_2 storage and heterogeneous petrophysical properties; and (3) ensemble results that show average CO_2 saturation over the ensemble results in circular-shaped plume, however the ensemble variance shows an ellipse of uncertainty around the injection well trending in the direction of maximum spatial correlation. The results of this study show the thermal effects accompanying CO_2 injections into a highly heterogeneous formation may be a precursor to leakage.

As a result, Chapter 4 focuses on the thermodynamic effects of a CO_2 injection, which leads to significant changes in temperature in both the reservoir water and rock, which can affect the injectivity, movement, and reactivity of CO_2 within a basalt reservoir. During a CO_2 injection there are two competing thermal processes, the heat of dissolution and Joule-Thomson cooling. To investigate these thermal effects, 1-, 2-, and 3-D numerical modeling studies are utilized to analyze the temperature variability associated with a CO_2 injection over a range of porosities and permeabilities. Understanding these non-isothermal effects has implications for engineered CCS reservoirs in terms of monitoring, management, and verification. Results from this study show that within a homogeneous reservoir temperature migrates contemporaneously with the CO_2 plume, but within heterogeneous formations temperature migrates ahead of the CO_2 plume suggesting that temperature monitoring is an effective predictor of CO_2 break-through over a range of reservoir parameters.

Finally, Chapter 5 describes a second Monte Carlo modeling study that utilizes ensemble statistics to investigate geomechanical reservoir integrity of the CRBG on the basis of Mohr-Coulomb failure, borehole breakdown pressure, joint-initiation pressure, and fracture dilation criteria associated with carbon capture and storage (CCS) operations. Results show that for a constant mass CO_2 injection scenario into 35 equally-probable model domains within the CRBG can cause the injection pressures to vary over a range of 25 MPa, which results in borehole breakout in 50% of the simulations. Additionally, mean ensemble pressure shows

that (1) after 1 year of injecting CO_2 results in a region that has a >1% probability of the CRBG undergoing shear failure, which extends 7 times greater distances from the injection well than the CO_2 migrates and (2) joint initiaion pressures are localized within the volume comprising the CO_2 plume.

Flood basalts have been gaining recognition as potential reservoirs for carbon capture and sequestration. The success of recent field experiments in Washington State, USA, and Iceland show that injected CO_2 will interact with the basalt to form carbonate minerals at the field-scale and very short timescales. However, upscaling these field-scale experiments to industrial-scale CO_2 injections is required if CCS is going to be an effective strategy to aid in mitigating climate change. Transitioning basalt CCS from the pilot-scale to industrial scales introduces a number of uncertainties, including feedbacks between multi-phase flow processes and fracture-controlled reservoir properties, incomplete knowledge of reservoir characteristics, and coupled dynamics between hydraulic, thermal, mechanical, and geochemical processes. Reservoirs that are targeted for CCS require extensive site characterization to ensure that the reservoir meets the requirements for capacity, injectivity, and confinement for a given CCS project. Reservoir integrity within highly heterogeneous reservoirs is one of the main concerns surrounding the idea of industrial-scale CCS projects because leakage from CO_2 storage sites may have negative health, safety, and environmental impacts at the surface. Quantifying, understanding, and minimizing these risks effectively is necessary if industrial-scale CO_2 injections are to become a viable option to mitigate climate change. The studies presented here are an important first step towards understanding the relationships between multi-phase fluid flow processes, spatial reservoir uncertainty, and reservoir geomechanics.

Chapter 2

Permeability Correlation Structure of the Columbia River Plateau

The well-known observation that permeability tends to decrease with depth has been invoked to explain and/or model the effects of fluid and heat flow within numerous societally relevant geological processes. However, this study finds that continental large igneous provinces may deviate from the classical permeability decay trend. We compile a new permeability database for the Columbia River Basalt Group (CRBG), USA, and show that average CRBG permeability (1) exhibits little depth dependence between 0 and 500 m; (2) systematically decays between ∼500 and 950 m depth; and (3) increases by 1.5 orders of magnitude between 950 and 1,450 m depth. Further analysis indicates that CRBG permeability is spatially correlated with a 5:1 horizontal anisotropy ratio, and the direction of maximum horizontal spatial correlation is parallel to the longitudinal axis of the bedrock depression underlying the CRBG. To explain these observations, we hypothesize that rapid CRBG emplacement and subsequent lithospheric subsidence induces bending moment stresses within the CRBG that result in spatially correlated permeability at regional scales and increasing permeability at depth. Because continental large igneous provinces (LIPs) are characterized by rapid emplacement and subsequent subsidence, this study implies that that bending moment stresses may be a characteristic feature affecting the permeability structure of continental LIPs.

2.1 Introduction

Permeability within the Earth's brittle crust governs heat and mass transport from microscopic to continental scales. At the macro-scale, crustal permeability is known to regulate Earth's natural CO_2 emissions, thermal output, and pore-fluid pressure within the lithosphere [Ingebritsen and Manning, 1999]. Consequently, permeability plays a fundamental role in earthquake occurrence and crustal strength [Townend and Zoback, 2000], metamorphic CO_2 degassing [Kerrick and Caldeira, 1998], global geothermal resource distributions [Saar, 2011], and ore deposits [Weis, 2015]. While the importance of crustal permeability is well known, mapping the spatial variability of permeability remains a fundamental challenge in the geosciences, particularly at depths greater than several hundred meters [Gleeson et al., 2011]. To overcome this barrier, the geoscience community has a rich history developing permeability scaling relationships. In one classic example, Neuman [1990] found that while hydraulic conductivity (a proxy for permeability) is scale-dependent, the superposition of homogeneous hydraulic conductivity fields into successively larger scales exhibits self-similar scaling dynamics that can be adequately characterized by a random fractal model. Perhaps the most well-known and widely implemented permeability scaling law is the permeability-depth ($k - z$, where k is permeability (m^2) and z is depth (m)) relation discovered by Manning and Ingebritsen [1999], which shows that crustal-scale permeability in metamorphic terrain decreases with depth as a power law, $k \approx 10^{-14}$ m^2 $\times (z/1000\text{m})^{-3.2}$. The Manning and Ingebritsen [1999] k-z scaling relation has been invoked to explain numerous geologic phenomena. For example, Townend and Zoback [2000] invoke k-z scaling to support the observations that permeability is $\sim 10^{-17}$ to 10^{-16} m^2 at 1 – 10 km depth, which permits hydraulic communication between the atmosphere and seismogenic zone and prevents long term overpressure on critically stressed faults. To extend this k-z model to shallow depths, Saar and Manga [2004] combined heat flow and hydroseismicity observations

from the Oregon Cascades with numerical modeling to propose a piecewise k-z scaling relation in which vertical permeability undergoes exponential decay until ∼800 m depth, beyond which the power law k-z relation holds. The combined k-z relation is often implemented in numerical modeling studies of deep geological processes where permeability data are either sparse or not available. The k-z scaling relation has been used to refine our understanding of classical basin-scale fluid flow [Jiang et al., 2009], and to constrain numerical modeling studies of ore formation [Weis, 2015], hydrothermal fluid circulation within mid-ocean ridges [Barreyre et al., 2018], heat flow estimates within continental large igneous provinces [Burns et al., 2015], meteoric water infiltration within orogenic belts [Pollyea et al., 2015], and permeability on Mars [Clifford and Parker, 2001].

This study considers the applicability of k-z scaling in large igneous provinces by developing a new permeability database (874 records) for the Columbia River Basalt Group (CRBG), USA, (Figure 2.1) and calculating the permeability-depth profile. Our analysis indicates that bulk permeability within the CRBG does not follow the expected depth-dependent trend between 950 and 1,450 m, and we hypothesize that this deviation from classical k-z scaling laws results from rapid emplacement, subsequent lithospheric subsidence, and the development of bending moment stresses.

2.2 Methods

A database of spatially referenced permeability values is compiled from previously published aquifer test data within the CRBG. This database shows that CRBG permeability spans 13 orders of magnitude (10^{-21} m^2 to 10^{-8} m^2). After filtering the data to exclude measurements from the low permeability flow interiors, the resulting database used for analysis comprises 800 bulk permeability measurements from 577 wells. The complete description of database

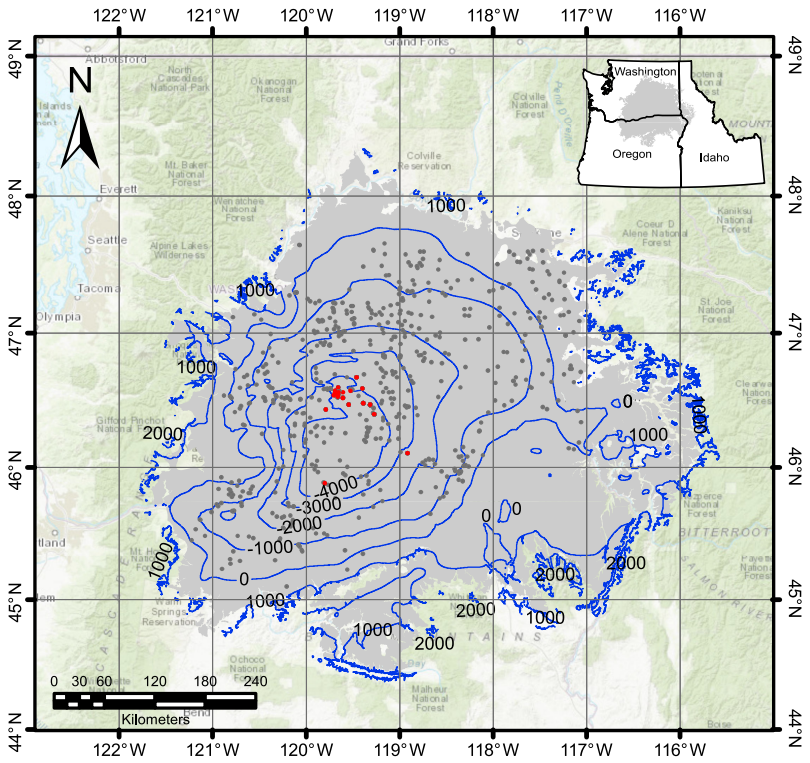

Figure 2.1: Map of the Columbia River Basalt Group. Study area map of the Columbia River Plateau, USA, with Columbia River Basalt Group in gray shading. Dark gray circles denote well locations with hydrologic data used in this study, and red circles denote wells greater than 950 m depth (Table DR1). Blue contour lines show the bedrock elevation in meters above mean sea level (m amsl) [Burns et al., 2011]. Basemap from ESRI.

sources, quality control measures, and verification of internal consistency is described in the Supplemental Information in GSA Data Repository1.

The permeability-depth (k-z) profile is calculated on the basis of a 200 m moving average using the methods proposed by Burns et al. (2015), and 1σ dispersion about the mean is calculated to quantify uncertainty in the k-z profile (Figure 2.2). The spatial correlation of CRBG bulk permeability is quantified by first applying a $\log_{10}$ transform to the data and then calculating the experimental semivariogram as:

$$\gamma(h) = \frac{1}{2N(h)} \sum_{i=1}^{N(h)} (z_i - z_{1+h})^2 \tag{2.1}$$

where, $N(h)$ is the total number of data pairs separated by a spatial lag distance (h), and z_i and z_{i+h} are the head and tail values of each data pair, respectively (Deutsch and Journel, 1998). The 2-D semivariogram map reveals the presence of spatial anisotropy oriented N40°E and N130°E (Fig. DR1 in the Data Repository), and directional experimental semivariograms are modeled to quantify correlation range in the direction of maximum (N40°E) and minimum (N130°E) spatial continuity.

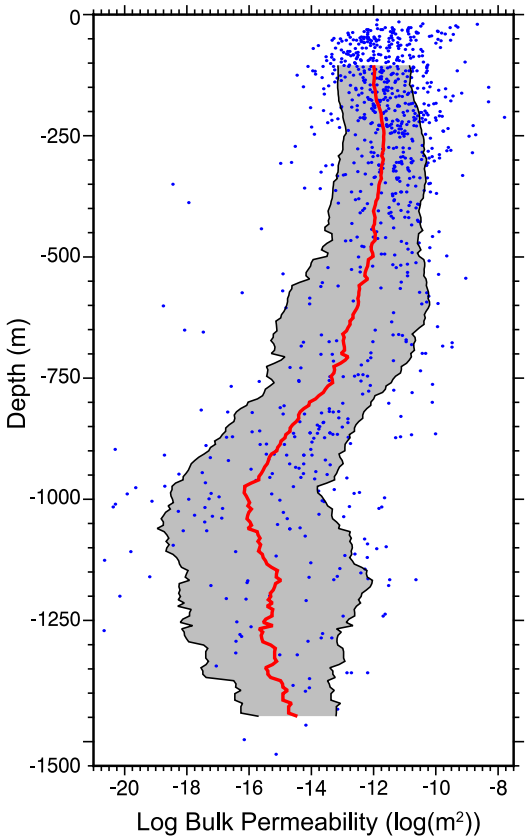

Figure 2.2: Permeability vs. depth profile. Permeability-depth profile calculated as a 200 m running average (red line) with 1σ dispersion (gray shading) and individual permeability values (blue dots).

2.3 Results

The permeability-depth calculations (Figure 2.2) show that average bulk CRBG permeability (1) exhibits no apparent depth dependence between 0 and 500 m; (2) systematically decays by four orders of magnitude between ∼500 and 950 m depth; and (3) increases by 1.5 orders of magnitude between 950 and 1,450 m depth. The k-z results between 0 and 950 m are generally consistent with Burns et al. [2015]; however, their study suggests that the CRBG k-z profile likely exhibits power law decay at depths beyond 950 m. In contrast, our results indicate that permeability increases by 1.5 orders of magnitude between 950 and 1,450 m depth. To support the results presented in Figure 2.2, we observe that 1σ dispersion about the moving average systematically decreases with increasing depth beyond 950 m despite fewer data within the 950 - 1,450 m depth interval. Moreover, there are 21 permeability data above the 1 threshold, while only 9 data points are below. The increasing k-z trend beyond 950 m is further supported by a single CRBG permeability measurement of 5.7×10^{-15} m^2 at 1,828 m depth, which is not included in the moving average calculations because the depth is more than 200 m beyond the deepest datum shown in Figure 2.2. These results suggest that the trend of increasing permeability within the 950 - 1,450 m depth interval may be robust on the basis of currently available data.

Semivariogram analysis reveals that: (1) CRBG permeability is spatially correlated with a 5:1 anisotropy ratio in the horizontal direction (Table 1); (2) the directions of maximum and minimum spatial correlation are oriented N40°E and N130°E, respectively; and (3) the vertical semivariogram is characterized by a power law model comprising a sill of 0.55 and exponent (ω) of 0.35 (Figure 2.3). In comparing the direction of maximum horizontal spatial correlation with the depth to bedrock below the CRBG [Burns et al., 2011], we find that the direction of maximum horizontal spatial correlation (N40°E) for CRBG permeability aligns remarkably well with the longitudinal axis of the bedrock underlying the Columbia River

Plateau, which is oriented N42°E (Figure 2.1).

Table 2.1: Directional variogram models. Three different variogram models are used with following parameters which describe the spatial variability of permeability within the Columbia River Plateau (A. Horizontal semivariogram at 40^o B. Horizontal semivariogram at 130^o).

Horizontal Variograms			
Model Type	Nugget	Sill	Range(km)
^{A}Exponential	0.45	0.55	35
^{B}Exponential	0.45	0.55	7.5
Vertical Variogram			
Model Type	Nugget	Slope	(ω)
Power	0.4	1.55	0.35

2.4 Discussion

Our results indicate that CRBG bulk permeability exhibits (1) an unexpected increasing trend within the 950 - 1,450 m depth interval (Figure 2.2) and (2) the direction of maximum spatial correlation is in alignment with the longitudinal axis of the underlying bedrock depression (Figure 2.1). We interpret these results in the context of CRBG emplacement. The CRBG is a continental large igneous province in the northwest United States (Figure 2.1). The CRBG comprises a layered assemblage of ~300 Miocene-age flood basalts with an areal extent of 200,000 km^2, aggregate thickness of 1 - 5 km, and total estimated volume of 224,000 km^3 [Reidel et al., 2002]. Long and Wood [1986] show that during emplacement, CRBG flows initially followed an east-to-west paleoslope, and then ponded within a north-south trending paleobasin that subsequently experienced local clockwise rotation [Hooper and Conrey, 1989]. This is evident in bedrock contours underlying the CRBG, which show that: (1) the CRBG occupies a bedrock depression trending N42°E (Figure 2.1), and (2) the thickness of individual CRBG members generally increases near the center of the bedrock depression [Burns et al., 2011]. At the time of initial CRBG eruptions (~17 Mya), the Columbia River

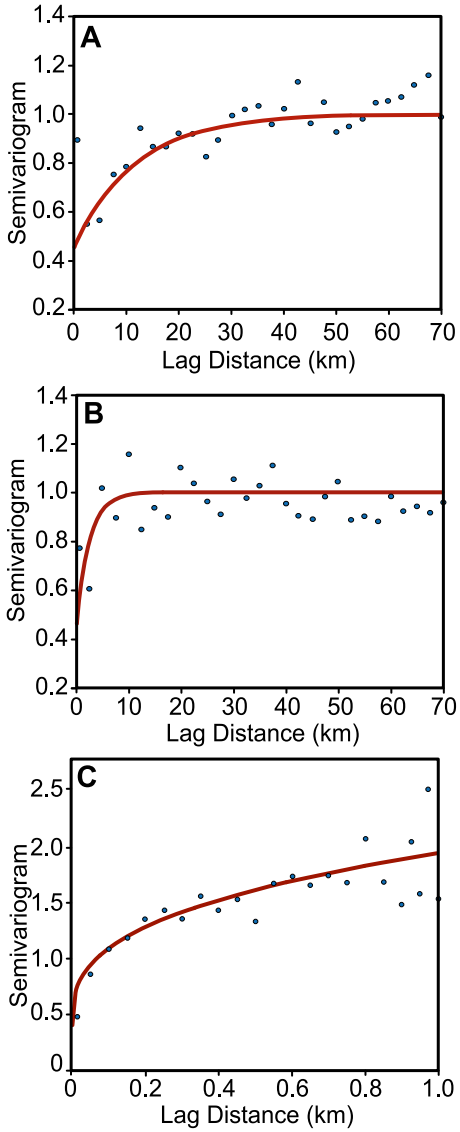

Figure 2.3: Spatial correlation model for the Columbia River Basalt Group. Spatial correlation model for Columbia River Basalt Group (CRBG) permeability. Horizontal experimental semivariograms for maximum (N40°E) and minimum (N130°E) spatial correlation directions are shown in A and B, respectively . Each semivariogram is normalized over the variance. Circles denote experimental semivariogram (Equation 2.1), and red line denotes model semivariogram with parameters shown in Table 2.1.

Plateau was undergoing uplift, and the Grande Ronde and Imnaha eruptions (17 - 15.5 Mya) produced 94% of the total CRBG volume over a period of 1.5 million years [Reidel et al., 1989]. This volume and emplacement rate rapidly loaded the underlying crust as high-density mafic rocks accumulated over comparatively lower density felsic rocks, which caused a down warp in the continental crust underlying the Columbia River Plateau [Hales et al., 2005]. Since this time, the Columbia River Plateau has been undergoing subsidence at a decreasing rate from 0.7 - 1 cm yr^{-1} (15.6 Mya) to the current rate of 0.003 cm yr^{-1} [Reidel et al., 1989].

The lithospheric response to loading is well documented in the case of continental ice sheet advance/retreat (e.g., Walcott [1970a]) and volcanism [Clague and Dalrymple, 1987, Jackson and Wright, 1970, Moore, 1970]. In the context of glacial advance and volcano construction, rapid lithostatic loading in both oceanic and continental crust induces rapid evolution in the principal stresses (e.g., Walcott [1970a], Bianco et al. [2005], Hieronymus and Bercovici [1999]). During continental glaciation, the lithostatic response to rapid loading has been linked to bending moment stresses at the base of an ice sheet that induce tensile fractures and increase the permeability of basal ice [Boulton and Caban, 1995]. Although there are fewer studies of the lithostatic response to continental large igneous provinces (LIPs), Walcott [1970b] showed that flexural rigidity of continental lithosphere decreases by two-orders of magnitude for long-term loading conditions ($>\sim 10^4$ yr), and that this flexural response is controlled by both elastic and viscous processes. In the presence of loading-induced subsidence, work by Johnston et al. [1998] suggests that a bending moment will increase lateral compressive stresses at shallow depths, while decreasing compressive stresses at greater depths.

Within the CRBG, Reidel et al. [1989] indicates that the Columbia River Plateau has been undergoing subsidence at a decreasing rate (0.1–0.003 cm yr^{-1}) since the Grande Ronde

eruptions. The occurrence of regional subsidence after CRBG emplacement suggests that the entire CRBG assemblage has been undergoing flexure, which would result in a bending moment about the longitudinal axis of the underlying bedrock depression (∼N42°E). The presence of a bending moment about this longitudinal axis is similar to the tangential longitudinal strain model of Ramsay [1967]. Within the CRBG, bending moment stresses acting orthogonal to the longitudinal axis of the underlying bedrock depression would preferentially dilate fracture apertures (and thus permeability) oriented parallel to longitudinal axis of the underlying depression (Figure 2.4). In the context of the CRBG k-z profile, most permeability data are from portions of the CRBG with thicknesses ranging from ∼1,000–4,000 m, which suggests a neutral surface between 500 and 2,000 m depth. Although this variability in CRBG thickness will dilute the signal of reversal in the k-z trend, the distinct permeability decay between 500 and 950 m combined with the modestly increasing permeability beyond 950 m depth suggests that the bending moment stress model reasonably explains the observed k-z trend even when taking into account the variable thickness of the CRBG.

Coffin and Eldholm [1994] compiled and analyzed all *in-situ* LIPs younger than 250 Ma and show that LIP emplacement is generally characterized by lithospheric uplift, rapid emplacement, and post-emplacement subsidence, which implies that bending moment stresses may be characteristic features of continental LIPs. Based on the present analysis of CRBG permeability architecture, the broader implication is that the k-z characteristics of continental LIPs may not follow classical decay trends. Because fracture permeability governs the rate of mass and heat flow through the mafic rocks (e.g., Garven [1995]), the bending moment hypothesis for the permeability architecture of continental LIPs may have important implications for groundwater resource management, geothermal heat flow, and the development of geo-engineered reservoirs. For example, Saar [2011] suggests that minimum permeability for thermal advection is 5×10^{-17} to 10^{-15} m^2, and, as a result, the thermal signature of

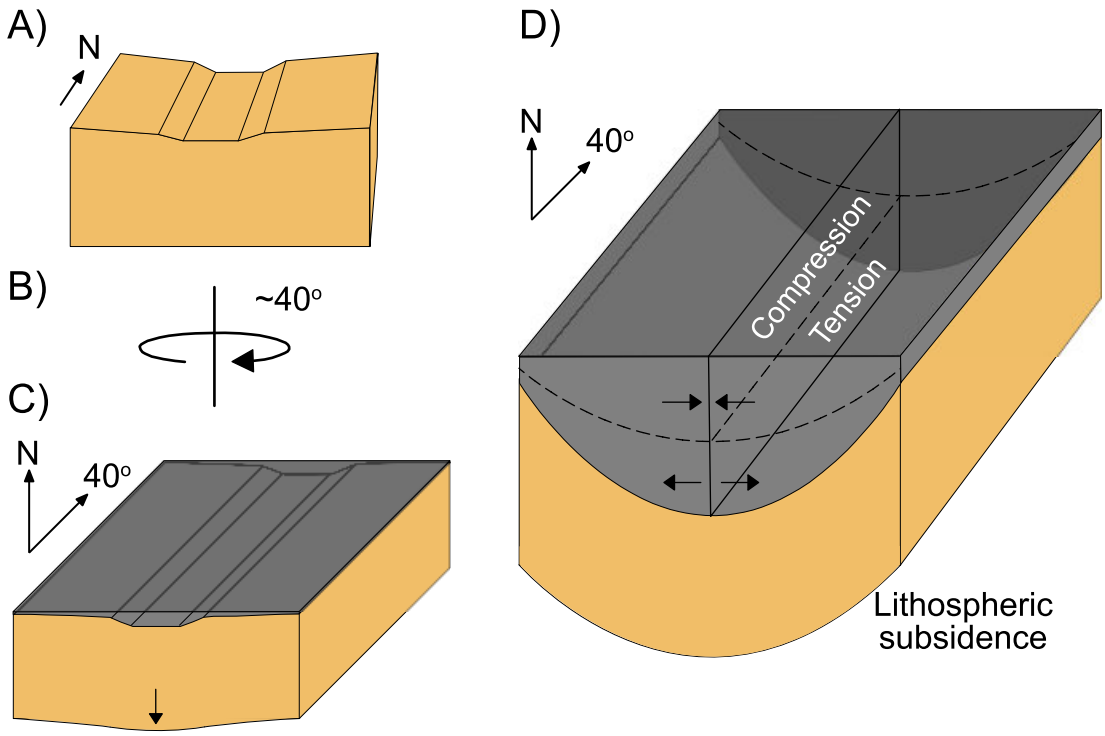

Figure 2.4: Schematic illustrating bending moment effects. Schematic illustrating the effects of a bending moment on Columbia River Basalt Group (CRBG) permeability: (A) Prior to Imnaha eruptions, the paleobasin is oriented north [Long and Wood, 1986]. (B) Columbia River Plateau experiences 40° rotation contemporaneously with initial CRBG emplacement 17 Mya. (C) ∼94% of total CRBG volume is emplaced between 17 and 15.5 Mya, which results in rapid loading and post-emplacement subsidence, and induces a bending moment about longitudinal axis of basin oriented N40°E; arrows denote compression and tension above and below the neutral axis (dashed line), respectively, and orthogonal to the longitudinal axis.

continental LIPs may exhibit unusual characteristics alternating between advection and conduction at depths below the neutral surface of the bending moment. Moreover, continental LIPs continue to be considered for a wide range of geological engineering applications, including long-term nuclear waste storage, natural gas storage, and geologic CO_2 sequestration ,the feasibility of which depend to a large extent on the hydraulic architecture of the host reservoir.

2.5 Conclusions

Permeability-depth (k-z) scaling is frequently invoked to explain and/or model the effects of fluid and heat flow on numerous societally relevant geological processes. In this study, we find that continental large igneous provinces may deviate from the classical permeability decay trend. Results show that CRBG permeability (1) exhibits little depth dependence between 0 and 500 m; (2) systematically decays between ∼500 and 950 m depth; and (3) increases by 1.5 orders of magnitude between 950 and 1,450 m depth. Further analysis indicates that CRBG permeability is spatially correlated with a 5:1 horizontal anisotropy ratio, and the direction of maximum horizontal spatial correlation is parallel to the longitudinal axis of the bedrock depression underlying the CRBG. To explain these observations, we hypothesize that rapid CRBG emplacement and subsequent lithospheric subsidence has induced bending moment stresses within the CRBG that affect the depth-dependence and spatial correlation of fracture-controlled permeability. Because uplift, rapid loading, and post-emplacement subsidence generally characterize continental LIP emplacement, we infer that the effects of bending moment stresses may be a characteristic feature of the LIP permeability structure.

1GSA Data Repository item 2018259, the Columbia River Basalt Group (CRBG) permeability database compiled for this study, is available online at http://www.geosociety.org/data repository/2018/ or on request from editing@geosociety.org.

Chapter 3

Geologic CO_2 Sequestration in a Highly Heterogeneous Reservoir

To understand the implications of permeability uncertainty in basalt-hosted CCS reservoirs, this study investigates the feasibility of industrial-scale CCS operations within the Columbia River Basalt Group (CRBG). It is generally accepted that plausible constraints on *in situ* fracture-controlled permeability distributions are unknowable at reservoir scale. In order to quantify the effects of this permeability uncertainty, stochastically generated and spatially correlated permeability distributions are used to create 50 synthetic reservoir domains to simulate constant pressure CO_2 injections. Results from this research illustrate that permeability uncertainty at the reservoir-scale significantly impacts both the accumulation and distribution of CO_2. After 20 years of injection the total volume of CO_2 injected in each simulation ranges from 2.4 MMT to 40.0 MMT. Interestingly, e-type calculations show that the mean CO_2 saturation over the ensemble of 50 simulations is concentric around the injection well, however, ensemble variance shows an ellipse of uncertainty that trends in the direction of maximum spatial correlation (N40°E). These results indicate that *a priori* knowledge of permeability correlation structure is an important operational parameter for the design of monitoring, measuring, and verification strategies in highly heterogeneous CCS reservoirs.

3.1 Introduction

Spatial heterogeneities are present at all geologic scales, from pore [Chang et al., 2016] to reservoir scales [Doughty and Pruess, 2004]. Understanding how spatial heterogeneity affects fluid flow is critical for engineered carbon capture and storage (CCS) reservoirs in terms of monitoring, management, and verification (MMV). Reservoirs that are targeted for CCS require extensive site characterization to ensure that the reservoir meets the requirements for capacity, injectivity, and confinement for a given CCS project. Numerical models are commonly used to predict what effects a large-scale CO_2 injection will have on the target reservoir and the behavior of the CO_2 plume. However, many numerical modeling studies employ a homogeneous representation of the geologic media [Van der Meer, 1995, Pruess and Garcia, 2002, Pruess et al., 2003]. For example, at the reservoir-scale it is common to implement a layered heterogeneity approach with internally homogeneous rock properties. Doughty [2010] simulates an injection of 1.1 million metric tons of CO_2 into a dipping sedimentary basin to investigate the spatial and temporal evolution of the CO_2 plume. While this approach may be reasonable for some geologic environments, it is also well established that uncertainty with the model parameters, such as, permeability will strongly affect the direction and extent of the CO_2 plume [Doughty, 2010]. Moreover, Doughty and Pruess [2004] investigate the physical processes associated with the sequestration of supercritical CO_2 and show that the highly heterogeneous nature of geologic media results in the formation of preferential flow paths which have a significant impact on the overall behavior of the injected CO_2.

Reservoir integrity within highly heterogeneous reservoirs is one of the main concerns surrounding the idea of industrial-scale CCS projects because leakage from CO_2 storage sites may have negative health, safety, and environmental (HSE) impacts at the surface. The difficulty in reducing HSE risks, is locating the source of the CO_2 leak from the reservoir or

any wells within the target formation. Previous works have investigated issues of CO_2 leakage from a CO_2 storage site into surface waters [Oldenburg and Lewicki, 2006], CO_2 leakage through fault or fracture pathways [Neufeld et al., 2009], and leakage through plugged and abandoned wells [Pawar et al., 2009]. The ability to monitor a CO_2 plume post-injection and subsequent leaks is the first step in mitigating these potential HSE risks. However, some monitoring efforts require *a priori* knowledge of the location of the CO_2 plume (i.e. well-based monitoring). This requires site-specific predictions from detailed characterization of the subsurface, which is a complicated and complex endeavor [Price and Oldenburg, 2009]. Quantifying, understanding, and minimizing these risks effectively is a necessity if industrial-scale CO_2 injections are to become a viable option to mitigate climate change [Navarre-Sitchler et al., 2013].

A number of geologic formations have been investigated over the years to study their potential for CCS. Sedimentary formations have been extensively studied due to their ubiquity, large storage capacity, and relatively high permeabilities, which are all required for large-scale CO_2 injections [Bachu, 2003, Metz et al., 2005]. Other options for CCS include depleted oil/gas reservoirs and deep, un-mineable coal seams [Brennan and Burruss, 2003]. In addition, flood basalt formations have been gaining recognition as suitable reservoirs for industrial-scale CCS. Unlike sedimentary aquifers that keep the CO_2 trapped via capillary and solubility trapping mechanisms, igneous rocks have a higher potential for permanent geomechanical trapping of CO_2 [McGrail et al., 2006, Matter et al., 2007, Matter and Kelemen, 2009, Zakharova et al., 2012, Pollyea and Rimstidt, 2017]. Geochemical trapping involves a series of chemical reactions between the CO_2, aquifer water, and reservoir rock resulting in the precipitation of thermodynamically stable and environmentally benign carbonate minerals. Recent developments at the CarbFix CCS pilot in Iceland [Matter et al., 2016] and the Wallula Basalt Pilot Project located in eastern Washington [McGrail et al., 2017] have shown

that basalt reservoirs are highly effective for permanent mineral trapping on the basis of CO_2-water-rock interactions. Specifically, pilot-scale basalt CCS at the CarbFix project showed 95% permanent CO_2 mineralization within two years of injection [Matter et al., 2016]. However, despite the effectiveness of trapping CO_2 via mineralization, the volumes injected in both pilot projects (270 tons CO_2 at CarbFix, 1,000 tons CO_2 at Wallula) are far from the scales required to mitigate climate change. Upscaling from a pilot project to an industrial-scale CO_2 injection requires a detailed characterization of the subsurface, which introduces a significant amount of uncertainty associated with reservoir parameters which affect the injectivity, capacity, and confinement of the target reservoir [Chadwick et al., 2008].

Chadwick et al. [2008] outlines the importance of reservoir characterization and how it is a necessary step to characterize both the hydrologic and structural properties of the target reservoir for a CCS project. For flood basalt reservoirs this can be challenging because it is generally accepted that plausible constraints on *in situ* permeability distributions are unknowable at reservoir scale. Previous studies have investigated this issue, for example, Pollyea et al. [2014] quantifies the effects of fracture-controlled heterogeneity by using stochastically generated model domains along with Monte Carlo CO_2 injection modeling to show the highly variable sealing behavior within the low-volume Snake River Plains basalts. Additionally, there remains significant uncertainty with respect to multiphase flow within heterogeneous media at all scales. For example,the effects of pore-scale heterogeneity on supercritical CO_2-water flow and relative permeability saturation curves have been investigated by Chang et al. [2016]. Gierzynski and Pollyea [2017] investigate outcrop-scale CO_2 flow within a basalt fracture network and show that CO_2 tends to accumulate at fracture intersection, which may yield self-sealing reservoir characteristics as mineralization focuses at the union of branching fractures. Bosshart et al. [2018] demonstrates how heterogeneities and

a range of petrophysical properties can significantly affect the CO_2 injection rate and storage capacity by modeling CO_2 injections into different depositional environments. Moreover, uncertainty in permeability distributions at any scale, especially site-scale or larger can have a substantial impact on the results of hydrogeologic models, as well as, numerical model-based risk assessment [NETL, 2011, Pollyea and Fairley, 2012, Pollyea et al., 2014]. To account for this uncertainty, stochastic methods have been increasingly deployed to understand how spatial permeability uncertainty affects feasibility assessments in fractured basalt reservoirs [Srivastava, 1994a, Li et al., 2005, Pollyea and Fairley, 2012, Pollyea et al., 2014, Popova et al., 2014, Gierzynski and Pollyea, 2017]. These methods constrain spatial permeability distributions on the basis of a known (or assumed) probability distributions and spatial correlation models (e.g., semivariogram). Byutilizing spatial correlation models and stochastic methods, this study is designed to assess the uncertainty of fracture-controlled permeability at the reservoir scale associated with a CO_2 injection scenario. As a result, this study provides a link between permeability heterogeneity and CO_2 storage efficiency, as well as providing a first-order approximation of the level of sensitivity associated with CO_2 storage and heterogeneous petrophysical properties.

3.1.1 Geologic Setting

Columbia River Basalt Group

The Columbia River Basalt Group (CRBG) is a continental large igneous province in the northwest United States (Figure 3.1), and comprises a layered assemblage of ∼300 Miocene-age flood basalts with an areal extent of 200,000 km^2, aggregate thickness of 1-5 km, and total estimated volume of 224,000 km^3 [Reidel et al., 2002, McGrail et al., 2009]. The CRBG has been extensively studied due to its wide range of resource potential, including

(1) groundwater production [Burns et al., 2011, Kahle et al., 2011], (2) nuclear waste storage (e.g., Gephart et al. [1983], (3) natural gas storage [Reidel et al., 2002], (4) geologic CO_2 sequestration [McGrail et al., 2017], and (5) geothermal resources [Burns et al., 2016]. Among the principal challenges in assessing the feasibility of engineered CRBG reservoirs is to understand how fracture-controlled reservoir properties (i.e., permeability and porosity) affect both local- and regional-scale fluid flow. These fracture-controlled reservoir properties are governed by individual basalt flow morphology, which is characterized by: (1) densely fractured, vesicular flow-tops, (2) a central entablature comprising narrow, fanning columnar joints, and (3) lower colonnades with vertical, column bounding joints (Figure 3.2) [Mangan et al., 1986]. Within CRBG flows, *in situ* pumping tests reveal that permeability ranges over thirteen orders of magnitude with the entablature zone generally inhibiting groundwater flow, while densely fractured flow tops and flow bottoms are highly productive [Kahle et al., 2011, Jayne and Pollyea, 2018] (Figure 3.3A). To further complicate CRBG reservoir characterization, individual basalt flows exhibit km-scale lateral dimensions and vertical dimensions from cm-scale to greater than 70m [Mangan et al., 1986].

Wallula Pilot Borehole

As part of the Big Sky Carbon Sequestration Partnership (BSCSP), the U.S. Department of Energy identified the Columbia River Basalt Group (CRBG) as a primary targetformation for CCS development in the Pacific Northwest. The CRBG was chosen on the basis of its' relatively high CO_2 storage estimates (10 - 50 Gt CO_2), potential for CO_2 isolation, and generally favorable reservoir characteristics [Litynski et al., 2006, McGrail et al., 2006, Rodosta et al., 2011, McGrail et al., 2017]. In order to locate a suitable site for a pilot injection, seismic surveys were conducted in Walla Walla County, WA, which identified areas where major geologic structures would not preclude a CO_2 injection [McGrail et al., 2011].

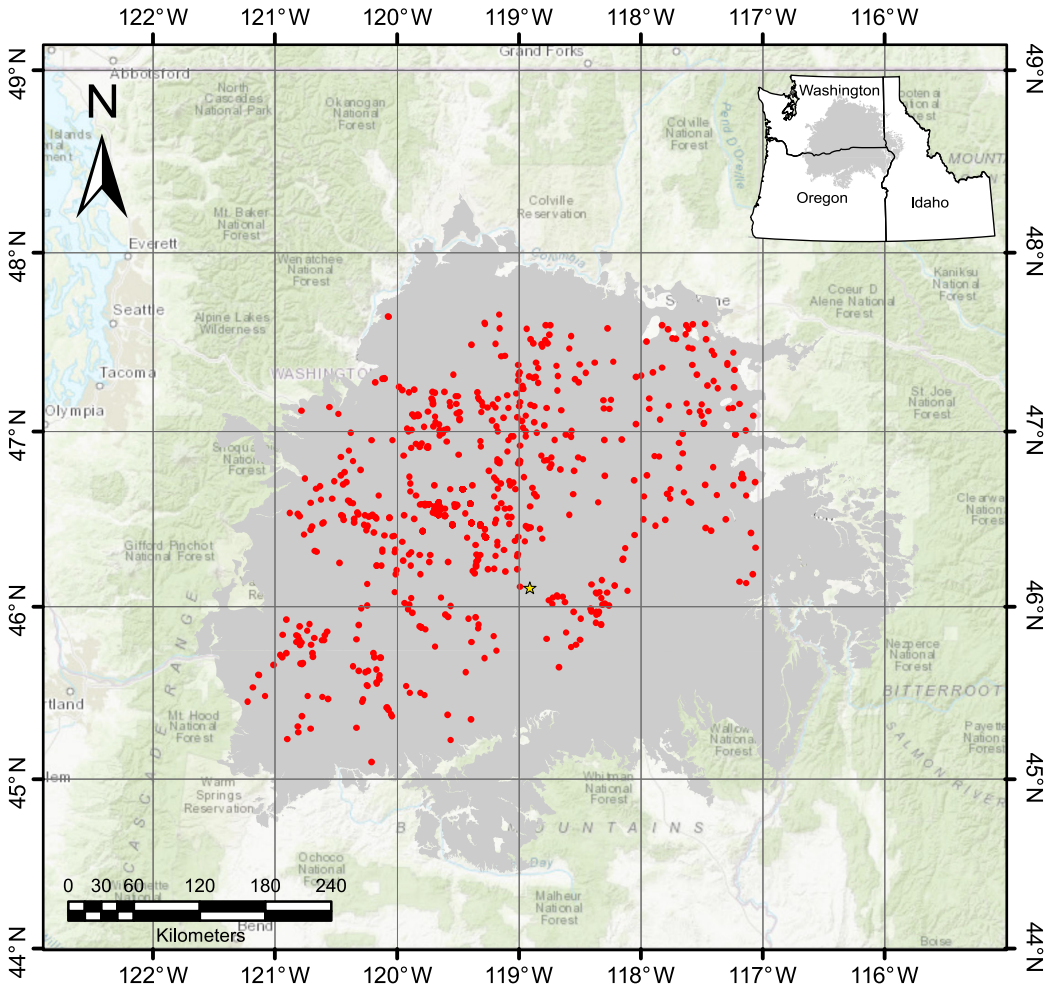

Figure 3.1: Map of the Columbia River Basalt Group. Map showing the areal extent of the Columbia River Basalts shaded in grey. Wells with permeability data compiled by Jayne and Pollyea [2018] within the CRBG are shown in red and the Wallula Pilot Borehole is denoted by the yellow star.

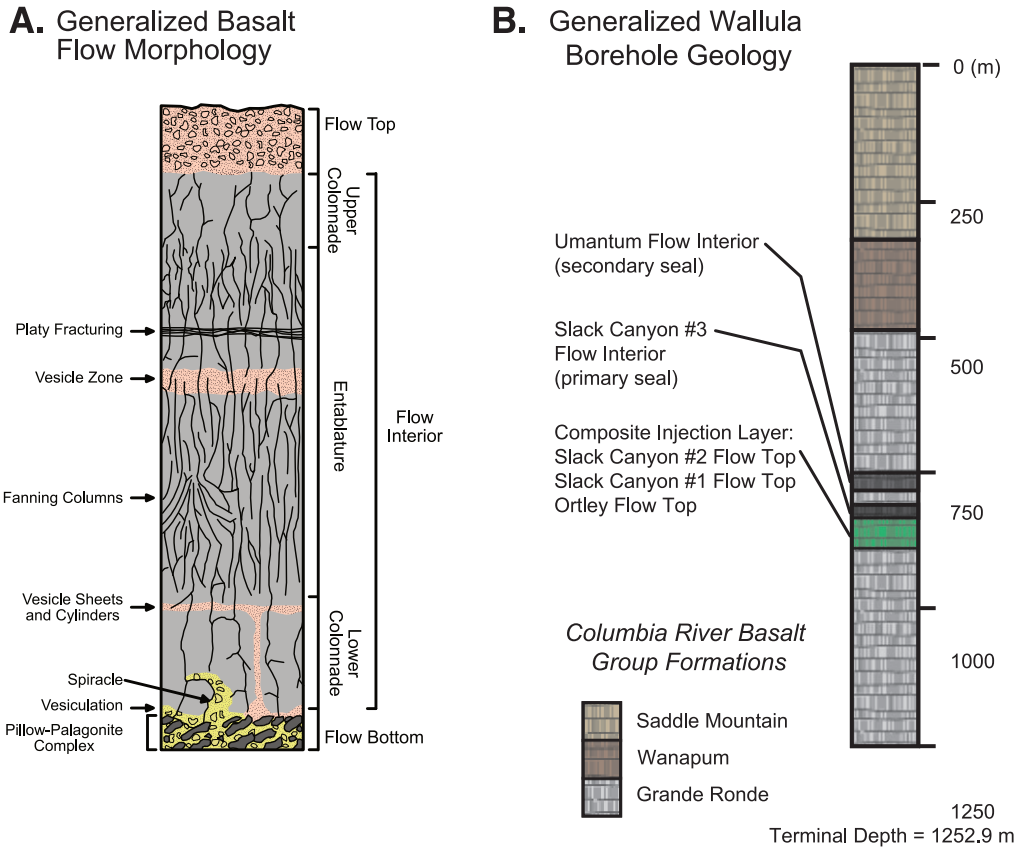

Figure 3.2: Individual CRBG flow morphology. A.Individual CRBG flow morphology (modified from Reidel et al. [2002]). B. Generalized geology within the Wallula Pilot Borehole.

In January 2009 drilling of the Wallula Pilot Borehole began and was completed in April 2009. The Wallula Pilot Borehole reaches a total depth of 1,253 m and intersects three CRBG formations: Saddle Mountain, Wanapum, and Grande Ronde [McGrail et al., 2009]. The target formation for injection is the Grande Ronde Basalt, of which the Wallula Pilot Borehole intersects 26 flows and 7 members. A candidate (composite) injection zone was identified at 828 - 887 m depth, spanning three brecciated interflow zones within the Grande Ronde Formation [McGrail et al., 2009]. Hydrologic characterization of these three zones show that they represent a single hydraulic unit with relatively high permeability and are bounded by thick low permeability flow interiors, which act as a natural caprock [McGrail et al., 2009]. In 2013, a nominal 1,000 metric tons (MT) of supercritical CO_2 was injected at the Wallula Pilot Borehole over the course of three weeks. Since the injection, results have been published validating the reactivity of supercritical CO_2 with basalts at the Wallula Pilot Borehole [McGrail et al., 2017]. Though these results are promising, transitioning to an industrial-scale CO_2 injection comes with a significant amount of uncertainty, and before an industrial-scale injection can be implemented a better understanding of these uncertainties is required. This study is designed to bound the uncertainty associated with incomplete knowledge of CRBG permeability during industrial-scale CO_2 injections. Specifically, we implement stochastic simulation strategy in combination with known geologic information from the Wallula borehole to quantify how permeability variability affects CO_2 storage capacity and leakage potential within a synthetic CCS reservoir comprising CRBG basalt.

3.2 Methods

This study combines geostatistical reservoir simulation with multiphase, multicomponent numerical modeling to investigate the influence that the spatial distribution of permeability

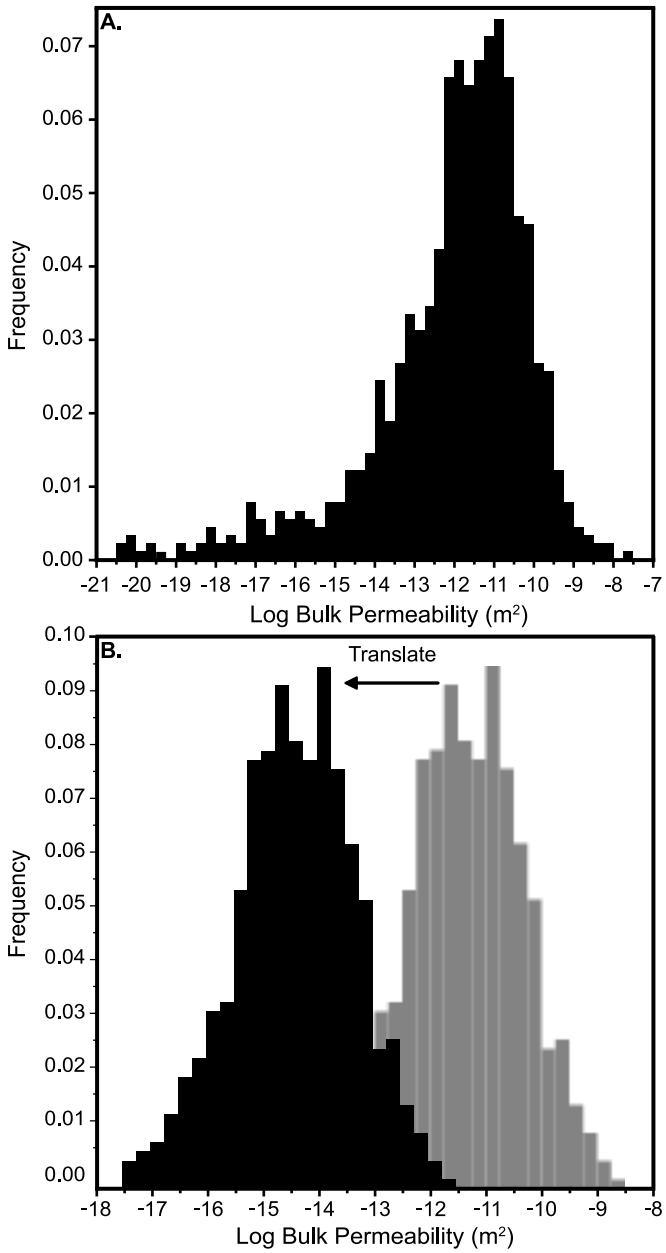

Figure 3.3: Histogram of permeability compiled from well data. A. Histogram of log permeability from well data compiled by Jayne and Pollyea [2018]. B. Histogram of the filtered permeability data to represent the high permeability flow tops. The mean of log permeability is -11.5 m^2 (grey), in order to make this range of permeabilities more representative at the depth of the injection zone the permeability distribution is translated downward so that the mean log permeability is -14.5 m^2, which is congruent with field test from the Wallula borehole.

has on the accumulation and distribution of the injected supercritical CO_2 within the Grande Ronde formation of the CRBG. The model scenario is designed to represent a large-scale constant pressure injection of supercritical CO_2 into the composite injection zone (775 m - 875 m) at the Wallula Pilot Borehole. While the hydrologic characterization within the Wallula Pilot Borehole has been extensive, the permeability distribution at intermediate- to long-range spatial scales is poorly constrained. As a result, this study uses a geostatistical analysis to constrain permeability at the reservoir-scale and provide a first-order approximation of the uncertainty associated with a large-scale CO_2 injection into a fracture-dominated, highly heterogeneous basalt reservoir.

3.2.1 Model Domain

The model domain for this study comprises an areal extent of 5,000 m $\times$ 5,000 m $\times$ 1,250 m, which represents ground surface to 1,250 m depth with the Wallula Pilot Borehole centrally located (Figure 3.4). This domain is discretized into 530,000 grid blocks with dimensions of 50 m $\times$ 50 m $\times$ 25 m. For this model, the CRBG is conceptualized on the basis of basalt flow morphology, which is a layered heterogeneous system consisting of highly fractured flow tops (high permeability) and flow interiors (low permeability). However, this layered heterogeneity does not take into account the wide range of permeability within individual basalt flow units, which are known to be internally heterogeneous due to the ubiquitous fracture networks within CRBG basalt. In order to account for the wide range of fracture-controlled permeability within the composite injection zone (775 - 875 m depth), sequential indicator simulation (sisim) is employed to generate stochastic permeability distributions for the injection zone [Deutsch and Journel, 1998]. In this approach, the sisim routine selects grid cells in random order and solves the ordinary kriging equations on the basis of (1) the cumulative distribution function for CRBG permeability, (2) known data points, which are

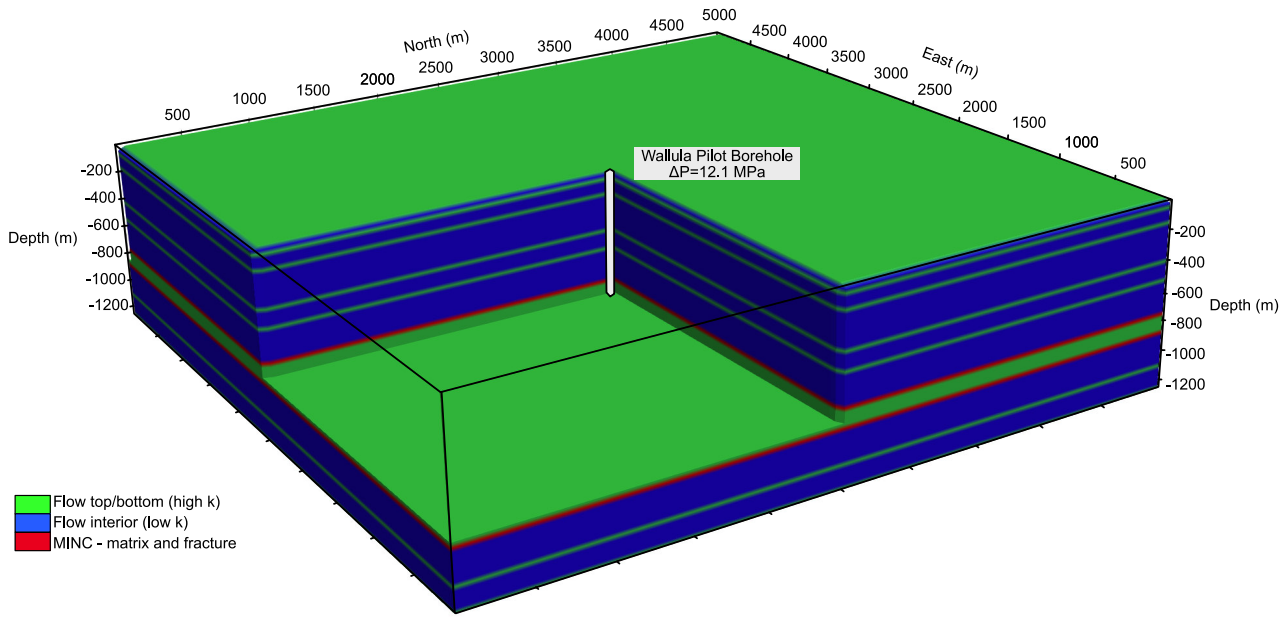

Figure 3.4: Model domain for CO_2 injection modeling study. The composite injection zone is bounded by the two red layers, the latter of which are specified as multiple interacting continua (MINC) to represent fracture-matrix flow within the bounding entablature units.

the borehole permeability tests from the Wallula borehole, (3) grid cells previously simulated by the sisim routine, and (4) the chosen spatial correlation model, which for this study is an anisotropic semivariogram model developed by Jayne and Pollyea [2018].

Jayne and Pollyea [2018] show that permeability within the Columbia River Plateau exhibits a direction of maximum and minimum spatial correlation oriented at N40°E and N130°E, respectively. In order to calculate these spatial correlation models Jayne and Pollyea [2018] compiled a regional database of CRBG permeability values from wells within the CRBG (Figure 3.1) to calculate semivariograms. To do this, permeability values were filtered on two standard deviations of the mean to ensure only the highly productive flow tops and bottoms were included in the calculations (Figure 3.3B). The present study adopts this convention to constrain the ranges of permeability within the high permeability zones that are representative of the composite injection zone. This results in a range of log permeabilities from -8.5 m^2 to -14.5 m^2 with a median permeability value of -11.5 m^2. However, the present

study is focused on permeability at depths greater than 750 m, where the log permeability in the Wallula Pilot Borehole is ∼-14.5 m^2. In order to account for this, the permeability distribution is translated so that the variability of permeability is maintained but the mean permeability is representative of the composite injection in the Wallula Pilot Borehole. This results in a new range of log permeabilities from -11 m^2 to -17 m^2. Using this approach, a total of 50 equally probable injection zones are simulated and inserted into the model domain between 775 and 875 m. It is important to note that sisim typically honors the original probability distributions of the original dataset with minor ergotic fluctuation. In this study, the resulting 50 equally-probable, spatially correlated permeability distributions vary slightly about the mean, with an average log permeability of -14.34 m^2 and a standard deviation of 0.27. While there is some variability in permeability distribution between the 50 synthetic reservoirs, each reproduces an equally-probable permeability distribution for the given dataset shown in Figure 3.3B. In order to model the effects of fracture-matrix flow within the entablature zones bounding the composite injection layer, the multiple-interacting-continua (MINC) method is utilized to produce a dual-permeability model that is representative of columnar jointing typical of basalt flow entablatures. The MINC method is a generalized dual-porosity concept, which allows for partitioning of the flow domain into different computational volumes within each element [Pruess, 1992]. In this approach, grid blocks are "nested" within one another allowing a single grid block to be defined by multiple finite elements (multiple rock properties can be used, such as, for fractured and unfractured rock matrix). A total of 50-equally probable synthetic reservoirs are simulated in which permeability within the injection zone is stochastically generated by sequential simulation and the entablature zones bounding the injection layer are modeled as a dual-continuum to represent columnar jointing.

For this modeling study, the relative permeability and capillary pressure models along with

Table 3.1: Model parameters - 20 year injection scenario.

	Matrix	Fracture	Flow Top	Basal Boundary
Density ($kg \cdot m^{-3}$)	2900.0	2300.0	2300.0	2900.0
Porosity	0.05	0.1	0.3	0.05
Permeability(m^2)	10^{-20}	10^{-16}	varies	10^{-20}
Thermal Conductivity ($W \cdot m^{\circ}C^{-1}$)	2.11	2.11	2.11	2.11
Heat Capacity ($J \cdot kg^{-1}{}^{\circ}C^{-1}$)	840	840	840	840
van Genuchten parameters				
Relative Permeability		Capillary Pressure		
λ	0.550	λ	0.457	
S_{lr}	0.30	S_{lr}	0.0	
S_{ls}	1.0	α (Pa^{-1})	5.e-5	
S_{gr}	0.25	P_{max} (Pa)	1e.7	
		S_{ls}	0.999	

the bulk fluid and rock properties are listed in Table 3.1. The bulk reservoir properties for the CRBG are consistent with those of Gierzynski and Pollyea [2017] and Zakharova et al. [2012]. Relative permeability and capillary pressure curves are used to simulate the effects of multiphase flow in a CO_2 and water system. Parameters for relative permeability and capillary pressure are described by the van Genuchten model, the van Genuchten parameters in Table 3.1 are based off of Pollyea [2016] where the influence of relative permeability on injection pressure is investigated within a mafic reservoir. Pollyea [2016] shows that for a constant mass CO_2 injection, maximum injection pressure can vary from 5 - 60 MPa over a range of van Genuchten parameters. Based off of these results, the phase interference (λ) and residual liquid saturation (S_{lr}) parameters corresponding to a maximum injection pressure of 25 MPa are chosen to keep CO_2 accumulation and distribution estimates modest for a constant pressure CO_2 injection.

3.2.2 Numerical CO_2 Flow Simulation

In order to investigate how the spatial distribution of permeability affects CCS reservoir performance in a flood basalt reservoir, CO_2 injection is simulated within each equally probable synthetic reservoir at constant pressure for 20 years. Constant pressure injections are simulated for this study within the composite injection zone at the Wallula Pilot Borehole to not only investigate the distribution of supercritical CO_2, but also compare the total mass of CO_2 injected over all 50 simulations. A constant overpressure of 12.1 MPa is used to simulate the CO_2 injection. This injection pressure represents 95% of the borehole breakout pressure as calculated by Pollyea [2016], borehole breakout pressure is used so that the maximum amount of CO_2 can be injected in each simulation without borehole failure. The code selection for this study is TOUGH3 [Jung et al., 2017] compiled with the ECO2M module [Pruess, 2011]. TOUGH3 solves energy and mass conservation equations for nonisothermal, multiphase flows in a porous geologic media. The ECO2M module simulates mixtures of H_2O - NaCl - CO_2, within the following ranges for temperature, pressure, and salinity conditions: 10°C $\leq$ Temperature $\leq$ 110°C, pressures $\leq$ 60 MPa, and salinity from zero up to full halite saturation. ECO2M can also simulate all possible phase conditions for CO_2 - brine mixtures, including transitions between super- and sub-critical CO_2 as well as phase transitions between liquid and vapor CO_2 [Pruess, 2011].

Initial conditions are specified with a hydrostatic pressure gradient ranging from 0.101 MPa (1 atm at ground surface) to 12.3 MPa at the bottom of the Wallula Pilot Borehole. Initial temperature is calculated by using the regional heat flux ~65 mW/m^2 [Pollack et al., 1993] as a thermal boundary at the base of the model and a constant temperature of 10°C at ground surface, resulting in a linear temperature gradient from 10°C at the surface to 50°C, and thermal effects are accounted for in the simulations. These initial conditions are consistent with the field measurements taken at the Wallula Pilot Borehole [McGrail et al., 2009].

Within the composite injection zone, initial temperature and pressure conditions range from 35 - 38°C and 7.7 - 8.4 MPa, which are within the supercritical field for CO_2. Dirichlet boundary conditions are specified at the upper boundary of the model domain to hold pressure and temperature constant at ground surface and at the lateral boundaries of the model domain to maintain temperature and pressure gradients in the far-field.

As with all modeling studies, a brief mention of the limitations of this model is warranted. This modeling study does not account for basalt dissolution or secondary mineral precipitation, and, as a result, this modeling study represents a conservative estimate of CO_2 storage capacity and leakage potential. Consequently, permeability alteration due to secondary mineral precipitation is neglected; however, we note that empirical permeability-porosity relationships have not yet been quantified in basalt reservoirs. Additionally, relative permeability hysteresis is not accounted for in the simulations, because only the injection phase of a CCS project is simulated so there is no imbibition for the wetting phase. Similarly, chemical diffusion is not accounted for because CO_2 is being continuously injected throughout the entire simulation resulting in a high Péclet number, which means the transport of mass and heat is dominated by advection.

3.2.3 Data Analysis

The ensemble of 50 simulations are analyzed using e-type estimates on a grid cell by grid cell basis to quantify the average overall behavior of CO_2 at the reservoir scale, as well as, the corresponding spatial uncertainty [Deutsch and Journel, 1998]. In this approach, the mean (N=50) CO_2 saturation ($\bar{S}_{(x,y,z)}$) within each grid cell is computed as:

$$\bar{S}_{(x,y,z)} = \frac{1}{50} \sum_{i=1}^{50} S_{i(x,y,z)} \tag{3.1}$$

where, $S_{i(x,y,z)}$ is the modeled CO_2 saturation for simulation i at location (x, y, z). Similarly, the variance $(s^2_{x,y,z})$ associated with Equation 3.1 for each grid cell is computed as:

$$s^2_{(x,y,z)} = \frac{1}{50}\sum_{i=1}^{50}(S_{i(x,y,z)} - \bar{S}_{i(x,y,z)})^2 \tag{3.2}$$

In the present study, the mean and variance are calculated for free-phase CO_2 saturation over all 50 simulations to investigate the uncertainty associated with a CO_2 injection into the Columbia River Basalt group.

3.3 Results and Discussion

3.3.1 Single Realization

Each numerical model accounts for 20 years of simulation time, in which supercritical CO_2 is injected within the Wallula Pilot Borehole at a constant pressure. For each analysis the simulations arereferred to by an integer index (1-50). In order to maintain consistency and facilitate comparison each analysis includes simulation 20 because the total mass of CO_2 injected for this simulation isclose to the ensemble mean. Simulation 20 also illustrates the effect of spatially correlated permeability within the CRBG, which is represented by Figure 3.5 and shows free-phase CO_2 saturation within each layer of the injection zone after 20 years. When comparing the accumulation and distribution of CO_2 within each layer in Figure 3.5, it is clear that top injection layer (Figure 3.5B) has the largest volume of CO_2 and this is due to buoyancy forces and the high permeability pathways that have formed due to the spatial heterogeneity. The combination of buoyancy-driven upward CO_2 flow and permeability heterogeneity results in CO_2 saturation patterns from the injection zone superimposed on the overlying entablature zone, which is the reservoir confining layer

(Figure 3.5A). As a result, permeability heterogeneity in the injection zone controls not only the accumulation and distribution of CO_2 within the reservoir, but also possible leakage pathways into the confining layers. High permeability pathways are apparent within the injection zone (Figure 3.5D, E) where there are small amounts of CO_2 that are completely disconnected from the main portion of the plume. This is due to the spatial distribution of permeability and the pressure gradient caused by the injection. As CO_2 is injected and migrates out into the formation, the CO_2 reaches areas of low permeability, which can inhibit flow. This causes injection pressure to accumulate, which causes the CO_2 to take the path that is most energetically favorable. In some instances, this effect forces vertical CO_2 flow as shown in Figure 3.5E. These results are congruent with those of Doughty and Pruess [2004] and show that there are high permeability pathways both horizontally and vertically. It is also important to note the control that the anisotropic permeability correlation structures exhibit on the accumulation and distribution of CO_2 in a single simulation. In simulation 20 (Figure 3.5) the injected free-phase CO_2 has migrated ~2,400 m away from the injection in the direction of maximum spatial correlation (N40°E) (Figure 3.5B), where as, CO_2 has only migrated ~1,100 m parallel to the direction of minimum spatial correlation (N130°E) (Figure 3.5C).

3.3.2 Ensemble Results

The complete ensemble simulation results (e-type estimates) for free-phase supercritical CO_2 saturation after 20 years of injection are shown in Figure 3.6. The ensemble mean CO_2 saturation in each injection layer, is a circular-shaped plume, which is similar to the individual model results from McGrail et al. [2009] and Bacon et al. [2014]. Interestingly, these latter studies implement radially symmetric model domains with layered heterogeneity and internally homogeneous injection zones to simulate an injection of 1,000 MT of CO_2 at the

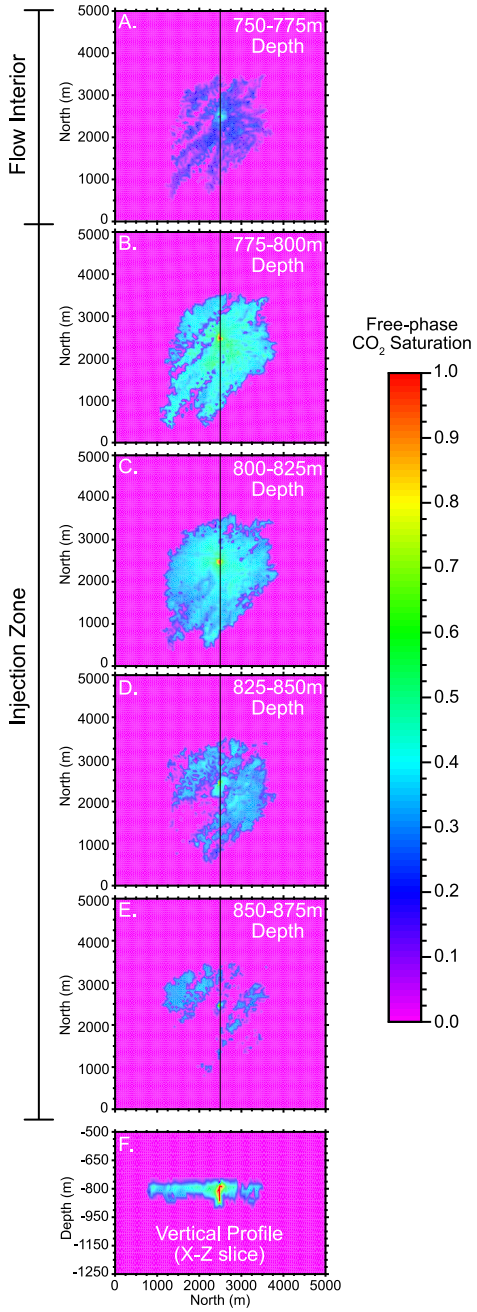

Figure 3.5: Single realization (20) of a 20-year constant pressure CO_2 injection. A. represents the layer above the injection zone and illustrates that free-phase CO_2 is present within the fractures. B-E. each represent an individual injection layer within the Wallula Pilot Borehole. F. A vertical north-south profile through the center (indicated by the black lines in A-E) of the model domain.

Wallula Pilot Borehole. However, the large scale CO_2 injection simulated by McGrail et al. [2012] is more comparable to this study where they use a radially-symmetric grid to simulate an annual injection of 0.8 MMT supercritical CO_2 into the Grande Ronde formation and sub-basalt sediment layers and show that after 10 years of injection the CO_2 migrates ∼500 m from the injection well and ∼1,000 m after 30 years. In comparison to the results from McGrail et al. [2012], Figure 3.6 illustrates after 20 years of a CO_2 injection that the plume migrates ∼900 m from the injection well. Which suggests that the permeability correlation structure does not strongly influence the mean ensemble behavior of CO_2.

While the ensemble mean behavior of CO_2 from this study is similar to the results from studies with internally homogeneous injection reservoirs, the variability in this study reveals dramatically different results. The variance of CO_2 saturation over all 50 simulations is shown in Figure 3.6, which illustrates an 'ellipse' of variability extending up to ∼1,800 m away from the injection well. The longitudinal axis of the ellipse trends N40°E, which is the direction of maximum spatial correlation. This result suggests that the uncertainty of CO_2 migration within CRBG basalt is strongly governed by the regional permeability correlation structure. This variability associated with the CO_2 plume is similar to the results of Pollyea and Fairley [2012], which implements a Monte Carlo simulation strategy to quantify the effects of spatial heterogeneity in low-volume basalt formations typical of the east Snake River Plains, Idaho. In this study, the ensemble variance exhibits a similar 'ring of uncertainty' with a very large range of variability within the basalt reservoir. While these results are similar, these studies differ with respect to geologic media being studied (low-volume basalts vs. flood basalts) and the correlation ranges use to create the permeability distributions. Pollyea and Fairley [2012] uses a geostatistical analysis of an outcrop scale low-volume basalt with a maximum correlation range of 38 m to simulate a reservoir-scale CO_2 injection, while this study uses a regional-scale geostatistical analysis with a correlation structure of 35 km presented by

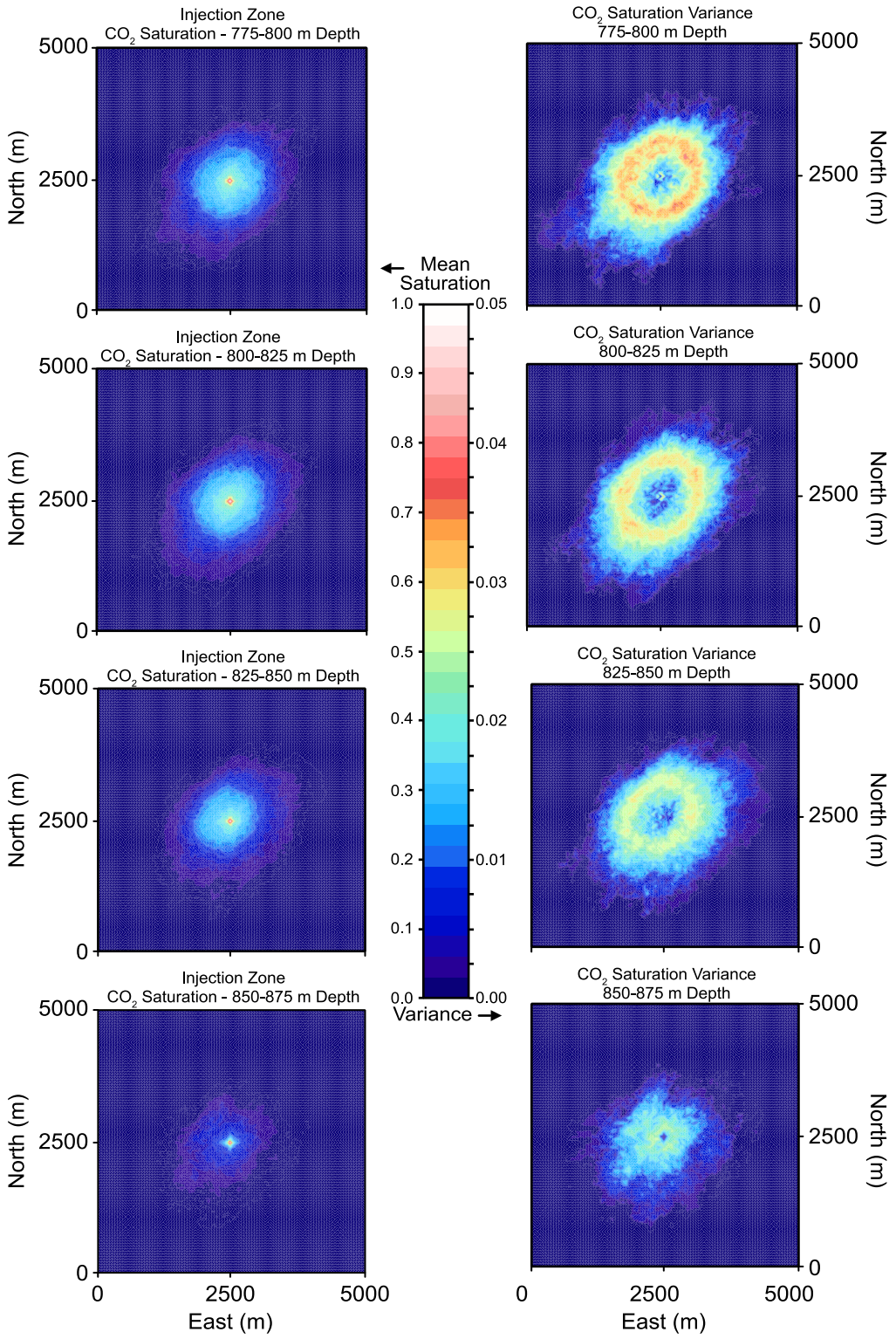

Figure 3.6: E-type estimates for (N=50) 20-year CO_2 injections. Average free-phase CO_2 saturation over all 50 simulations for the injection zones are shown on the left and the corresponding variance is shown on the right.

Jayne and Pollyea [2018]. Overall, the ensemble analysis indicates that the mean CO_2 plume geometry exhibits a circular shape around the injector, while the variance corresponding with this result is strongly affected by the direction of maximum spatial permeability correlation.

The variability over all 50 simulations is not only obvious in the shape of the individual plumes (Figure 3.5) and the ensemble variance (Figure 3.6), but also in the total volume injected in each simulation. The total volume of CO_2 injected into each of the 50 equally probable synthetic reservoirs ranges from a nominal 2.4 MMT (0.12 MMT year^{-1}) to 40 MMT (2 MMT year^{-1}), as shown in Figure 3.7. For reference, a small-scale 37 MW bio-mass fueled electric generator would emit ∼0.8 MMT year^{-1} [McGrail et al., 2012] and for a large-scale 1,000 MW gas-fired power plant would produce ∼ 1.36 MMT year^{-1} of CO_2. For equally-probable reservoirs, this is a significant amount of variability (Figure 3.7B). If the scenario presented by McGrail et al. [2012] were implemented at the Wallula Borehole, the results from this study show that a constant pressure injection at 95% of the borehole breakout pressure would result in 60% of the equally probable reservoirs successfully accepting enough CO_2 to meet the criteria for a 37 MW electric generator. Conversely, that would mean that 40% of the synthetic reservoirs would fail with the given scenario and if a larger volume of injected CO_2 were required the chances of success would quickly decrease. For example, only 20% of the reservoirs would have the injectivity for a modest increase in the injection rate to 1.15 MMT year^{-1}. While the average injection rate varies between each simulation, a similar trend in injection rate over time within each simulation is observed. The injection rate over all 50 simulations is highest at the beginning of the simulation and over the course of the injection; the injection rate steadily decreases as the CO_2 displaces larger volumes of water. This decrease in injectivity over time is similar to the results of Burton et al. [2009], which shows the effects of the relative permeability curve on injection rate within a sandstone reservoir.

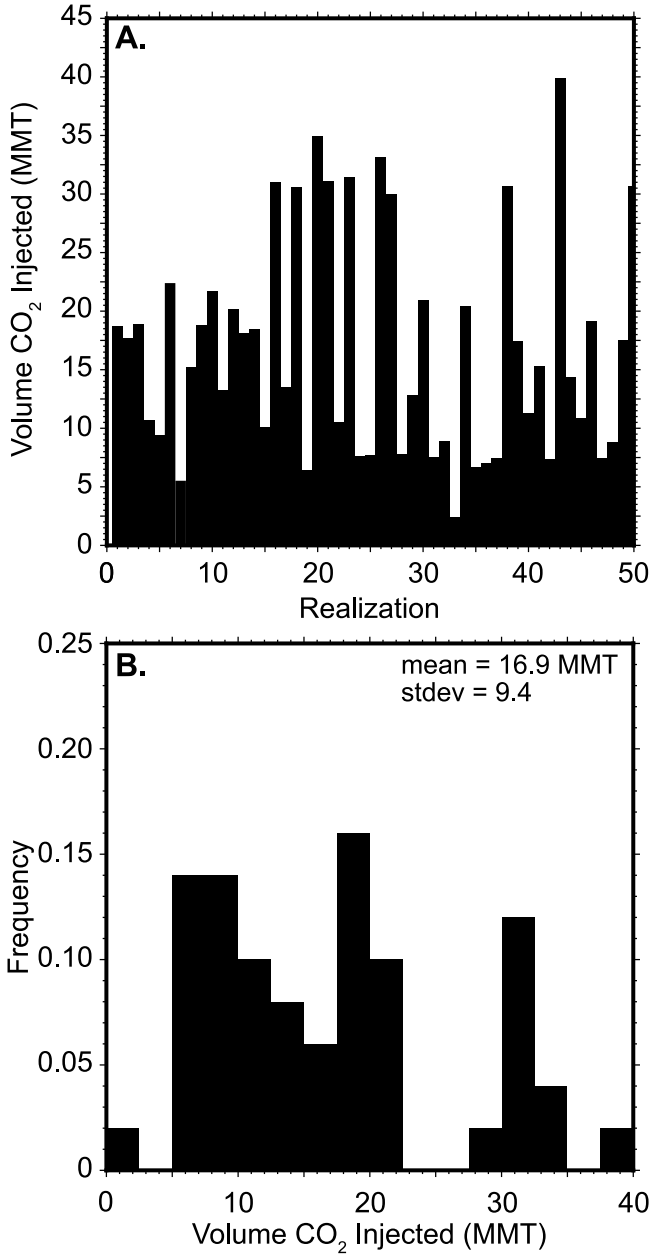

Figure 3.7: Total volume of CO_2 injected after 20 years. A. Total volume of CO_2 (in million metric tons, MMT) injected after 20 years of simulation for each of the 50 realizations. B. Histogram of the total volume injected of all 50 simulations along with the mean and standard deviation of the volume injected.

3.3.3 Individual Realizations

In order to visualize the variability in CO_2 injection volume for constant pressure injections, Figure 3.8 illustrates the isosurface at 1% gas saturation for four individual realizations, which represent the simulation closest to the mean CO_2 volume (Figure 3.8, realization 20), one standard deviation from the mean (Figure 3.8 realization 11), and the minimum and maximum CO_2 volumes (Figure 3.8, realizations 33 and 43, respectively). This variability in CO_2 plume shape and volume injected over the ensemble of simulations has important implications for MMV practices. There is a wide variety of methods available to monitor a CO_2 injection, such as, geophysical methods (e.g. seismic, electrical, gravity), pressure monitoring, well logging, fluid sampling, and soil gas monitoring. Each of these methods have their benefits but they also have drawbacks, e.g. detection occurs after potential impacts have occurred, significant effort for null result [Benson et al., 2006]. Mathieson et al. [2010] discusses the monitoring and verification methods carried out at a CO_2 sequestration site in Algeria and emphasizes that CO_2 plume development is far from homogeneous and that each storage site is unique. This requires a specific monitoring program tailored to the risks at each site. The results presented here show that the average CO_2 plume behavior may exhibit characteristics of an isotropic permeability distribution, but the variability over all 50 simulations is significant, and warrants a site specific monitoring program. In the case of the Wallula Site, leakage from the composite injection zone into the bounding entablature layers is a concern due to the highly-fractured nature of the CBRG. E-type estimates for the layers bounding the composite injection zone are presented in Figure 3.9. Owing to buoyancy forces, free-phase CO_2 migrates upward into the fractures within the flow interior and Figure 3.5A, B illustrate how spatial heterogeneity in the injection layer impacts the CO_2 plume shape within the flow interior. While the CO_2 saturation in Figure 3.9 is minimal compared to the injection zones, these results show that 0.1 - 1.05% of the total volume

injected has migrated outside of the composite injection zone. The USDOE [2013] requires that a successful CCS project keeps >99% of the injected CO_2 isolated within the reservoir for one-thousand years. However, in no simulation did the injected CO_2 migrate farther than the layers immediately bounding the composite injection zone, which is an area for possible mineralization of the CO_2. These results are also congruent with the high-resolution fracture modeling of Gierzynski and Pollyea [2017], which shows that CO_2 flow tends to converge on a single flow path within a fracture network and suggests that this flow path convergence leads to a physical trapping mechanism followed by possible mineralization.

3.3.4 Temperature Monitoring

Additionally, results from this study indicate that the thermal effects of a CO_2 injection may also be used for MMV practices. Specifically, the change in reservoir temperature from pre- to post-injection shows that temperature within the reservoir changes +/- 4°C as a result of the CO_2 injection (Figure 3.10). The areas that show the largest increase in temperature are near the edges of the plume, while areas that show the largest decrease in temperature are near the injection well. At the edges of the CO_2 plume, CO_2 dissolves into the reservoir water and releases heat, which is a process referred to as the heat of dissolution because CO_2 dissolution in water is an exothermic reaction [Pruess, 2005a]. In contrast, the cooling shown in this study is caused by Joule-Thomson expansion, which describes the temperature change associated with the expansion of a gas [Roebuck et al., 1942]. During injections, the CO_2 is injected at a high pressure and begins to expand and cool as it migrates away from the injection well [Oldenburg, 2007]. The competing effects of the heat of dissolution and Joule-Thomson expansion are shown in Figures 3.8 and 3.10. The isosurfaces in Figure 3.8 are contoured by temperature to illustrate the competing temperature effects of a large-scale CO_2 injection. As the CO_2 migrates away from the

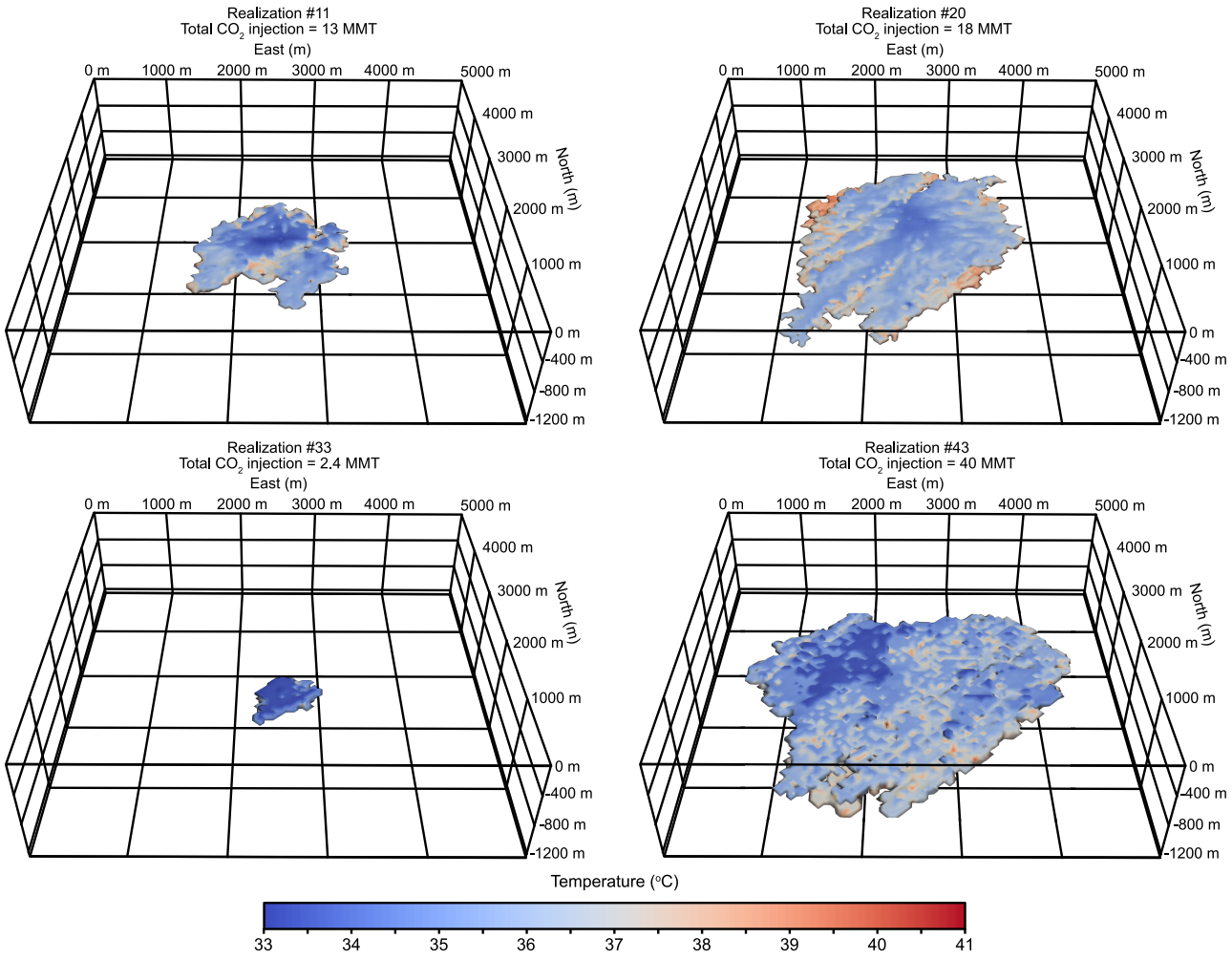

Figure 3.8: 3-D CO_2 plumes. Four different realizations that illustrate the variability in CO_2 plume shape and size after a 20-year CO_2 injection. Isosurface represents the edge of the CO_2 plume, each plume is contoured by temperature. Each realization is an equally-probable outcome for the given permeability dataset, note the different size, shape, and orientation of the CO_2 plumes.

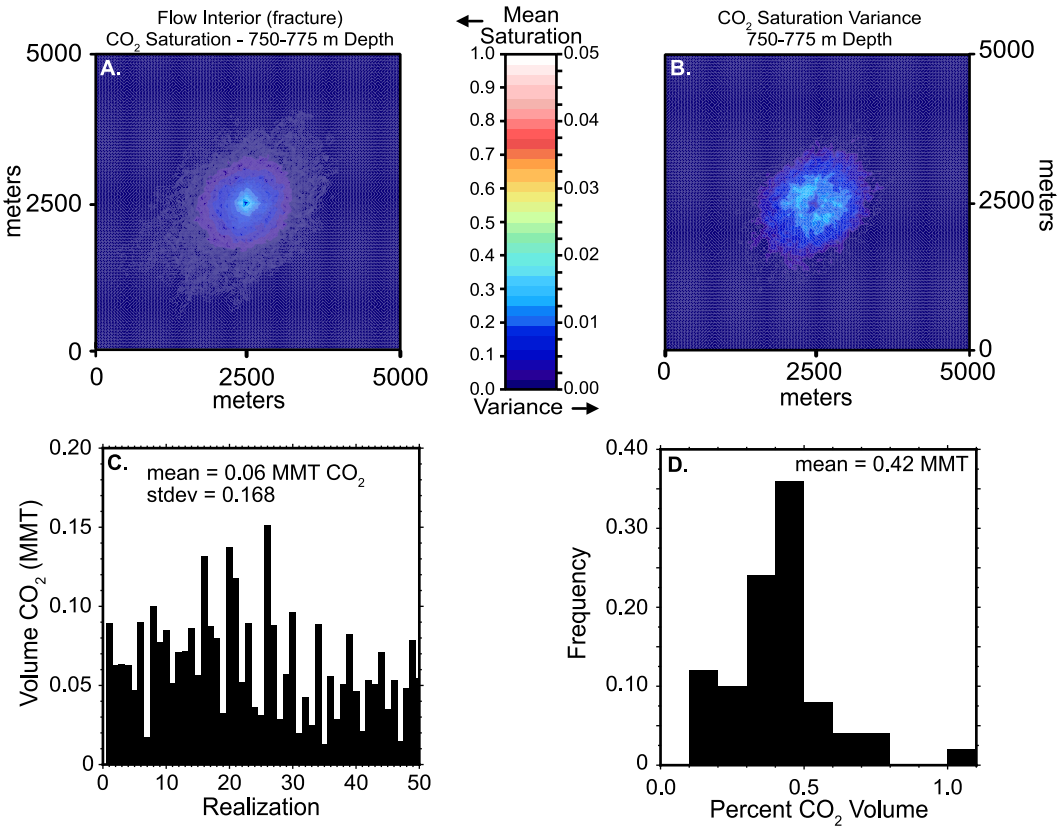

Figure 3.9: Injected CO_2 leakage from target reservoir. A. E-type estimates for mean CO_2 saturation (A) and variance (B) for the flow interior layer bounding the injection zone. C. Total volume of CO_2 in million metric tons (MMT) within the flow interior. D. histogram showing the percentage of the total volume injected that has migrated to into the flow interior.

wellbore due to the pressure gradient imposed by the injection, the CO_2 begins to expand and cool, but at the edges of the plume the CO_2 is dissolving into the reservoir water and giving off enough heat to overcome Joule-Thomson cooling resulting in a net increase in temperature. Conversely, near the wellbore after some time the water becomes saturated and no more CO_2 will dissolve. At this point, Joule-Thomson cooling dominates resulting in a net decrease in temperature near the well (Figure 3.10A - C and E). This result suggests that the competing effects of dissolution heating and Joule-Thomson cooling may be an effective strategy to monitor breakthrough. Namely, the heat of dissolution effect may be used to predict CO_2 breakthrough at monitoring wells within the reservoir. As the CO_2 dissolves into the reservoir water and releases heat, both the CO_2 and reservoir water experience an increase in temperature. This results in a thermal anomaly that migrates throughout the reservoir slightly ahead of the free phase CO_2 plume. As a result, we would expect an increase in temperature would reach a monitoring well before the CO_2 plume. This effect is illustrated in Figure 3.11, which shows how temperature and CO_2 saturation change over the course of the CO_2 injection at two monitoring locations 50 m away from the wellbore. In Figure 3.11 the first change in temperature occurs after 6 days of simulation. Over the next 15 days the black line (red line shows a similar trend) steadily increases in temperature from 34.5°C to 35.5°C, then continues to increase in temperature up to 36.8°C by day 26. At day 26, the maximum temperature at this monitoring location is reached, which occurs contemporaneously with the first appearance of CO_2. For the given simulation, two grid blocks located within the layer bounding the composite injection zone exhibit a steady increase in temperature until the arrival of CO_2 which suggests that temperature may be a proxy for CO_2 breakthrough because water drainage follows the same high permeability pathways as CO_2 imbibition. These results suggest that thermal monitoring may be an effective predictor of CO_2 breakthrough, however more research is needed in this area of study.

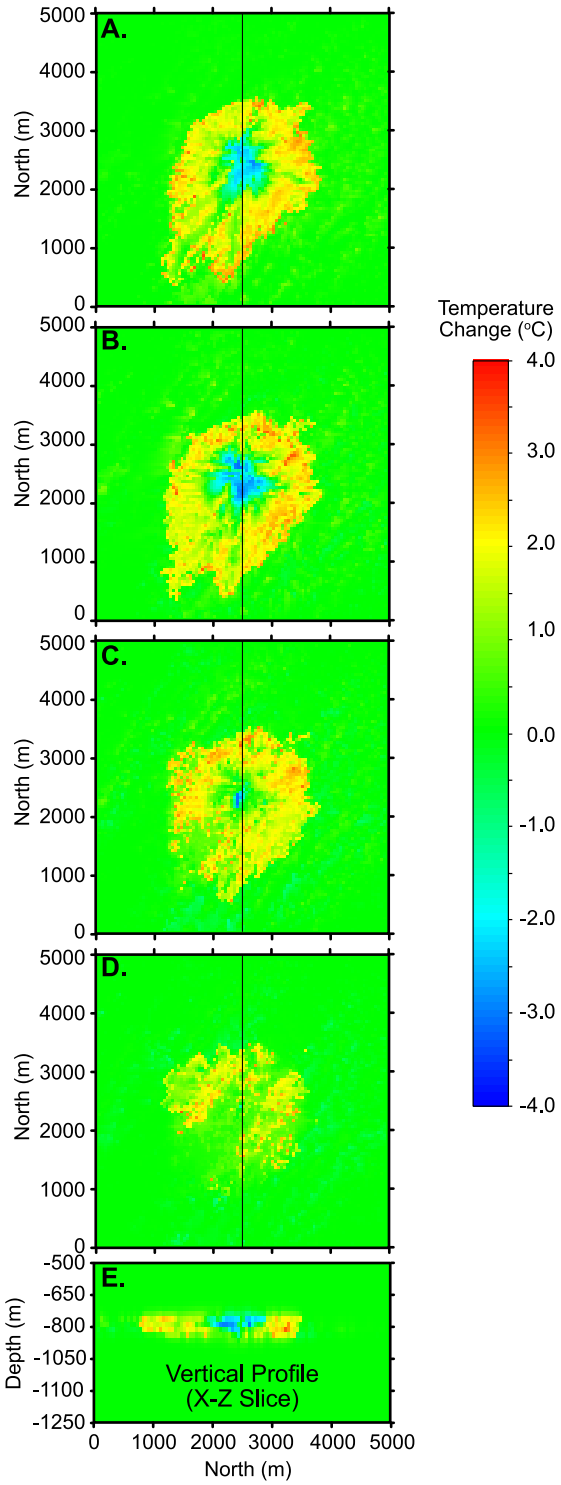

Figure 3.10: Reservoir temperature post-injection. Change in temperature between pre-CO_2 injection temperatures to post-CO_2 injection temperatures for a single realization (20). Panels A-D. represent the 4 injection layers within the model domain. E. A vertical north-south profile through the center (indicated by the black lines in A-D) of the model domain.

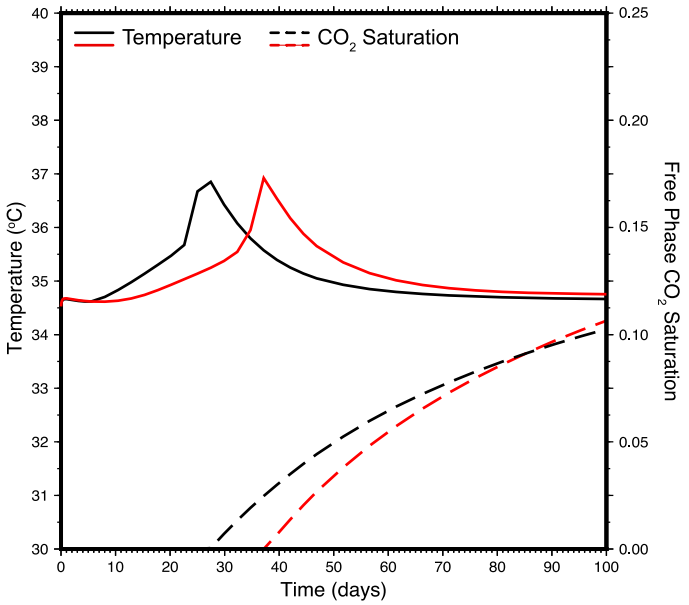

Figure 3.11: Temperature and CO_2 saturation versus time for two monitoring locations within the confining layer (750 - 775 m depth) each 50 m away from the injection. The time lag between the black and red lines illustrates the effects of permeability heterogeneity.

3.4 Conclusion

Flood basalts have been gaining recognition as potential reservoirs for carbon capture and sequestration. The success of recent field experiments in Washington State, USA, and Iceland have validated that injected CO_2 will interact with the basalt to form carbonate minerals at the field-scale and very short timescales. Upscaling these field-scale experiments is required if CCS is to be an effective strategy for mitigating the adverse effect of industrial CO_2 emissions. However, there are a number of uncertainties associated with upscaling to an industrial-scale CO_2 injection. For example, incomplete knowledge of multiphase flow in highly heterogeneous basalt reservoirs and detailed reservoir characterizations are required for proper numerical modeling and to effectively design a monitoring, measuring, and verification plan. This study investigates the uncertainty of a large-scale CO_2 injection into a highly heterogeneous basalt reservoir by focusing on the effects of spatially distributed

permeability on CO_2 plume migration. For a sole CO_2 injection well operating within the CRBG at 95% of borehole breakout pressure, we find:

1. The aggregate behavior of the 50 simulations results in a concentric CO_2 plume shape around the injection well, which suggests that ensemble behavior is not governed by the spatial correlation structures.

2. Ensemble variance shows an ellipse of uncertainty around the CO_2 plume that extends up to 1,800m away from the injection, this ellipse trends parallel to the direction of maximum spatial permeabilitycorrelation, suggesting that the uncertainty associated with a large-scale CO_2 injection is strongly controlled by the permeability correlation structures. This means that spatial variability must be accounted for to fully understand how variability propagates into operational and MMV decisions.

3. Injected CO_2 migrates from the injection zone into the entablature layer bounding the injection zone, but the CO_2 does not migrate any further suggesting that this region has the potential for CO_2-water-basalt interactions to effectively isolate large-scale CO_2 injection volumes.

4. The volume of CO_2 injected at 95% of the borehole breakout pressure for 20 years ranges from 2.4 MMT (0.12 MMT year^{-1}) to 40.0 MMT (2.0 MMT year^{-1}). While the minimum volume injected only accommodates 15% of the volume required for the proposed scenario of offsetting the carbon emissions from a 37 MW generator. The maximum volume injected could support at 1,000 MW gas-fired power plant with a single injection.

5. Non-isothermal effects, namely the heat of dissolution associated with a large-scale CO_2 injection may be an effective MMV strategy for monitoring CO_2 breakthrough.

In conclusion, these results suggest that the implementation of a regional-data set and spatial correlation structures into a numerical model can provide insights into the behavior of CO_2 flow in highly heterogeneous reservoirs. Additionally, these results illustrate the uncertainty associated with highly-heterogeneous flood basalt reservoirs and a CCS project would require extensive reservoir characterization and a unique monitoring, measuring, and verification plan. Significantly more research is required to develop a better understanding of the reactive transport, geomechanical, and thermal processes associated with an industrial-scale CO_2 injection into a flood basalt reservoir.

Chapter 4

Using Heat as a Predictor of CO_2 Breakthrough

Injecting super-critical CO_2 into the subsurface changes the temperature, pressure, and geochemistry of the storage reservoir. Understanding these perturbations within the reservoir may be used to monitor the CO_2 plume during a carbon capture and sequestration (CCS) project. Here we analyze results from 1-, 2-, and 3-D numerical modeling studies to investigate how the thermal signature of the CO_2-water system evolves during CCS. These models show that the thermodynamic processes of the CO_2-water system results in a characteristic thermal profile within a homogeneous storage reservoir during a CO_2 injection. This thermal signature is characterized by warming front of up to 4°C, which is caused by CO_2 dissolution and migrates contemporaneously with free-phase CO_2 migration. When reservoir properties are highly heterogeneous, this thermal front travels well ahead of free-phase CO_2, thus implying that thermal monitoring may be an effective predictor of CO_2 breakthrough.

4.1 Introduction

Heat has been used as a groundwater tracer since Slichter [1905] utilized temperature to show that a pond in Long Island, New York was infiltrating the local groundwater. Thereafter, studies have utilized heat to study groundwater inflow to lakes [Lee, 1985], identify gaining or losing streams [Conant Jr, 2004], quantify seasonal variations in the shallow subsurface [Storey et al., 2003], characterize flow through fractures [Bodvarsson, 1969], quantify fracture attributes in hydrothermal systems [Anderson and Fairley, 2008, Heffner and Fairley, 2006], and identify flow patterns in groundwater basins [Bachu, 1988]. More recently, thermal tracers have been utilized to characterize fractures and heat transfer within enhanced geothermal systems. For example, Pruess and Doughty [2010] simulate a single-well injection-withdrawal test to illustrate the effectiveness of using heat as a tracer within enhanced geothermal systems. This study also highlights the advantages of using heat over chemical tracers because thermal parameters have much less variability than chemical parameters, and thermal diffusivity is $4-5$ orders of magnitude larger than the diffusivity of solutes in lower permeability reservoirs. Shook and Suzuki [2017] present an analytical solution to show that temperature is a robust tool to characterize EGS environments. Additionally, Manga [2001] points out the advantages of using heat as a tracer, namely the ability to collect high resolution spatial and temporal data.

Numerical models are frequently utilized to study the thermal processes associated with CO_2 storage in geologic reservoirs [André et al., 2010, Hurter et al., 2007, Han et al., 2010, Jayne et al., 2019b, Oldenburg, 2007, Pruess, 2005a, Zhao and Cheng, 2017]. These studies focus largely on Joule-Thomson cooling that occurs during a CO_2 injection; this refers to the cooling that occurs when a gas, e.g., CO_2, expands. For example, Zhang et al. [2011] combines this thermodynamic process with other observations to estimate residual CO_2 saturation based on the difference between water and CO_2 diffusivity. Similarly, Pruess [2005a] models

CO_2 flow and phase change within a hypothetical leakage system using idealized faults to investigate the risks associated with geologic storage of CO_2, and Oldenburg [2007] examines adiabatic cooling (Joule-Thomson effect) caused by the decompression of injected CO_2 into a natural gas reservoir. André et al. [2010] investigates the thermal impact a supercritical CO_2 injection has on the reactive nature of a carbonate saline reservoir and shows relatively small cooling effects (1 – 2°C), which is similar to the results of Oldenburg [2007].

While the thermodyamics of CO_2 expansion are well known to the CCS community, there have been few studies investigating the the thermal effects caused by CO_2 dissolution, i.e., heat-of-dissolution. Thermal monitoring has also been proposed as a method for monitoring CO_2 leakage from a storage reservoir [Zeidouni et al., 2014, Zhang et al., 2018b]. Han et al. [2010] and Han et al. [2012] present numerical modeling studies that evaluate the non-isothermal processes associated with a supercritical CO_2 injection into saline formations. These studies suggest that temperature changes during a CO_2 injection may be an essential monitoring tool when temperature changes are greater than 1°C. However, the temperature changes within the reservoir may not only be caused by CO_2. For example, a recent study of an enhanced geothermal system (EGS) that found the thermodynamic effects associated with H_2O increase temperature at the production well prior to the arrival of the injected fluid [Zhang et al., 2018a]. This thermal anomaly is the result of thermodynamic processes (Joule-Thomson effects) that cause water to release heat when subject to sharp pressure gradients [Stauffer et al., 2014], as is the case during fluid circulation in EGS systems [Zhang et al., 2018a].

The thermal effects associated with interactions between CO_2 and water have been well studied individually; however, the relationship between reservoir properties (permeability and porosity) and the thermodynamic processes governing fluid temperature remains an open question. Moreover, the influence of spatially heterogeneous reservoir properties on

thermal fluid processes has yet to be considered. To fill this gap in knowledge, this study is designed to learn how the fluid temperature signal responds to (i) systematic variations of bulk permeability and porosity and (ii) spatially heterogeneous permeability fields, e.g., in a basalt reservoir.

4.2 Thermal Processes in the CO_2-Water System

Injecting free-phase CO_2 into the subsurface changes the thermal regime by altering the natural conduction and advection of heat, and imposing four thermodynamic processes related to the CO_2-water system: (i) Joule-Thomson cooling from CO_2 expansion, (ii) heat released by CO_2 dissolution, (iii) cooling caused by water vaporization [Han et al., 2012], and (iv) Joule-Thomson heating from water expansion. Each of these thermal processes occurs at different locations within and/or around the CO_2 plume and they are affected by pressure gradients caused by the injection of CO_2 into the storage reservoir. The combination of these effects results in a dynamically changing thermal profile within the storage reservoir over the course of a CCS project.

4.2.1 Joule-Thomson Effect

The Joule-Thomson effect is the temperature change associated with the expansion or compression of a fluid (i.e., change in pressure), such as CO_2 or H_2O [Roebuck et al., 1942]. In the context of this study, Joule-Thomson cooling refers to the cooling associated with the decompression of CO_2 and Joule-Thomson heating refers to the heating caused by the decompression of H_2O. The resulting temperature change (ΔT) due to a pressure change

(ΔP) has been derived experimentally under isenthalpic (constant enthalpy) conditions,

$$\mu_{JT} = \lim_{x \to 0} \left[\frac{\Delta T}{\Delta P}\right]_H = \left[\frac{\delta T}{\delta P}\right]_H \tag{4.1}$$

where μ_{JT} is the Joule-Thomson coefficient, and can be determined by the limiting ratio of ΔT to ΔP under a constant enthalpy (H) [Engel and Reid, 2010]. When μ_{JT} is positive, a fluid will heat upon compression and cool upon expansion and vice versa when μ_{JT} is negative. For conditions of interest in CCS (T $\approx$ 30 – 80°C and P $\approx$ 10 – 40 MPa), Han et al. [2010] points out that μ_{JT} for CO_2 is positive, generally increases as T and P decrease, and ranges from 0.125 – 5°C MPa^{-1}. Conversely, at these same conditions μ_{JT} of H_2O can range from ~0.17 – 0.22°C MPa^{-1} [NIST, 2018], which results in H_2O heating upon expansion and cooling upon compression [Stauffer et al., 2014, Zhang et al., 2018a].

4.2.2 Heat of Dissolution and Vaporization

When supercritical CO_2 is injected into a reservoir, the interface between the CO_2 and reservoir water allows for CO_2 to dissolve in the water and for the water to dissolve into the CO_2. At temperature conditions relevant for CCS, the dissolution of CO_2 into water is an exothermic reaction referred to as *heat of dissolution*. Koschel et al. [2006] provides experimental data on the enthalpy and solubility of CO_2 in water, the enthalpy of solution at 50°C and pressures from 5-20 MPa is -15.2 kJ/mol and at 100°C with pressures from 5 - 20 MPa is -7.9 kJ/mol. As thermal energy is released from this reaction, the surrounding water, CO_2, and reservoir rock experience an increase in temperature. Conversely, water vaporization into the supercritical-phase CO_2 requires the input of energy (positive enthalpy) resulting in cooling of the surrounding water, CO_2, and reservoir rock [Han et al., 2010]. While the heat of dissolution and water vaporization are competing processes at the water-

CO_2 interface, the solubility of CO_2 in water is $\sim 8.4 \times 10^{-3}$ mole fraction [King Jr and Coan, 1971] and the solubility of water in CO_2 is $\sim 4.0 \times 10^{-4}$ mole fraction [Carroll et al., 1991]. Since the solubility of CO_2 in water is 20× greater than that of water in CO_2, the effects of water vaporization are negligible.

When free-phase CO_2 is pumped into a disposal reservoir, the competing effects of Joule-Thomson cooling (CO_2), Joule-Thomson heating (H_2O), and heat of dissolution results in a dynamically changing thermal profile within the CO_2-water-rock system. This study is designed to (i) quantify the thermal contributions of the Joule-Thomson and heat of dissolution effects during a CO_2 injection scenario, (ii) show how these processes vary with changes in permeability and porosity, and (iii) evaluate the efficacy of thermal monitoring to predict CO_2 breakthrough in reservoirs characterized by homogeneous and highly heterogeneous hydraulic properties.

4.3 Methods

We implement a numerical modeling study to quantify the thermal structure that develops during a typical CCS scenario. For this scenario, CO_2 is injected at 40°C for 20 years at a constant rate of 1 kg s^{-1} into a reservoir with an initial temperature of 40°C. The purpose of injecting the CO_2 at the same temperature as the initial reservoir temperature is to isolate the thermophysical effects of a CO_2 injection. We initially characterize the thermal structure of the CO_2-water system using a 1-D simulation ensemble comprising 459 homogeneous reservoirs with unique combinations of permeability and porosity. To analyze how vertical flow affects the thermal profile during a CO_2 injection, we repeat the model scenario by adding vertical discretization to the 1-D model, which results in a 2-D radially symmetric grid. We then consider the effects of reservoir heterogeneity by interrogating the thermal

structure of a 3-D CCS simulation that was originally developed by Jayne et al. [2019b] to understand the implications of spatially uncertain permeability distributions during CO_2 injections into flood basalt reservoirs.

The 1-D homogeneous model is conceptualized as a single, radially symmetric layer with 16 m thickness (829 m – 845 m depth) and 100 km lateral extent, the latter of which approximates a semi-infinite radial dimension (Figure 4.1). The injection well comprises a single grid cell with a radius of 0.1 m and represents the inner boundary for the model domain. Beyond the injection well, 949 grid cells are discretized with logarithmically increasing increments (Δr) from 0.1 m to 10,000 m. In order to simulate a semi-infinite far-field dimension, an additional 50 grid cells with logarithmically increasing Δr are specified from 10,000 m to 100,000 m. The high resolution of the grid near the injection well is chosen to minimize discretization effects that create a non-physical pressure spike in early time [Mathias et al., 2013]. Owing to the success of recent CCS pilot projects in highly heterogeneous basalt reservoirs [Matter et al., 2016, McGrail et al., 2017], the initial conditions and hydraulic properties specified for this project are representative of basalt [Pollyea, 2016] (Figure 4.1). Initial conditions are specified as 8.3 MPa fluid pressure, reservoir temperature is 40°C, and salt concentration is 10,000 ppm, which reproduce conditions encountered within the pilot borehole at the Wallula Basalt Sequestration Pilot Project in southeast Washington State, USA [McGrail et al., 2017].

To account for the interfering effects of CO_2 and water occupying the same pore space, we implement the Van Genuchten [1980] constitutive relationships for relative permeability and capillary pressure. While the multi-phase properties of basalt are uncertain, Gran et al. [2017] found that relative permeability is highly interfering. In addition, Pollyea [2016] interrogated the relative permeability parameter space and found that a phase-interference parameter (λ) of 0.55 and residual CO_2 saturation (S_{gr}) of 0.25 result the in highly interfering behavior

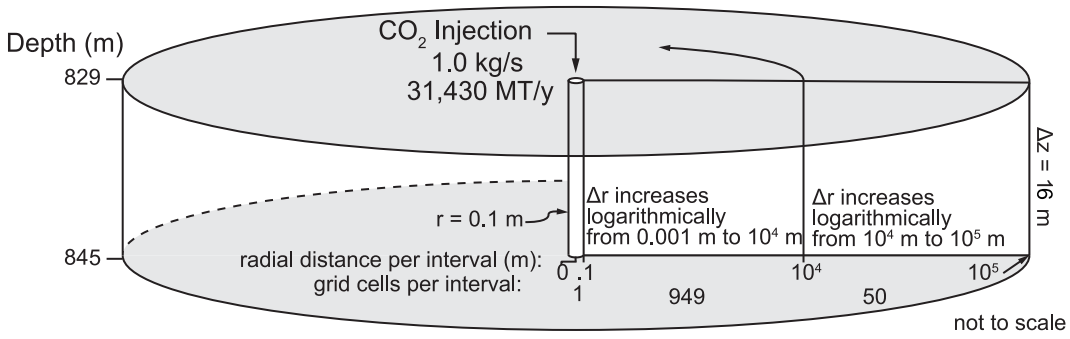

Reservoir Parameters

	Relative Permeability	Capillary Pressure
P_f = 8.30 MPa	λ = 0.550	λ = 0.500
T = 40.0 °C	S_{lr} = 0.30	S_{lr} = 0.0
NaCl = 10,000 ppm	S_{ls} = 1.0	α (Pa^{-1}) = 1.39 x 10^{-5}
k = 1.0 × 10^{-13} - 10^{-15} m^2	S_{gr} = 0.25	S_{ls} = 0.999
φ = 0.05 - 0.45		

Figure 4.1: Schematic for 1-D radially symmetric model domain. Schematic illustration and model properties for the 1-D radially symmetric model domain used for this study. The injection well is idealized as a single grid cell with a radius of 0.1 m. The next 949 grid cells increase logarithmically from 0.001 m to 10,000 m, another 50 grid cells that increase logarithmically are added to represent semi-infinite lateral dimensions of 100,000 m.

reported by Gran et al. [2017] while maintaining plausible reservoir injectivity. Figure 4.1 presents the complete parameter set for the relative permeability and capillary pressure models used for this study.

The code selection for this study is TOUGH3 [Jung et al., 2017] compiled with the ECO2N fluid property module [Pruess, 2005b], which updates the well-known TOUGH2 simulation code [Pruess et al., 1999] to implement PetSc [Balay et al., 2018] parallel solvers and includes gravitational potential in the energy balance. TOUGH3 solves energy and mass conservation equations for nonisothermal, multiphase flows in a porous geologic media. The ECO2N module simulates mixtures of H_2O, NaCl, and CO_2 for pressures up to 60 MPa, temperature between 10°C and 110°C, and salinity up to full halite saturation. The ECO2N module accounts for phase partitioning between water, CO_2, and NaCl on the basis of equilibrium solubility constraints [Pruess, 2005b].

4.4 Results and Discussion

4.4.1 Thermal Profile

The ensemble of 1-D homogeneous simulations reveal that the thermal fluid signature in a CCS reservoir is characterized by three distinct features: (1) a warming front at the leading edge of the CO_2 plume, (2) a zone of thermal equilibrium in the central portion of the CO_2 plume, and (3) a cooling zone near the injection well. Figure 4.2A presents a schematic illustration of these characteristic thermal features for a single 1-D realization after 20 years of injection. Figure 4.2B shows that permeability and porosity combinations vary the spatial dimensions of each thermal zone, as well as the magnitude of temperature change, but the overall pattern is independent of reservoir properties.

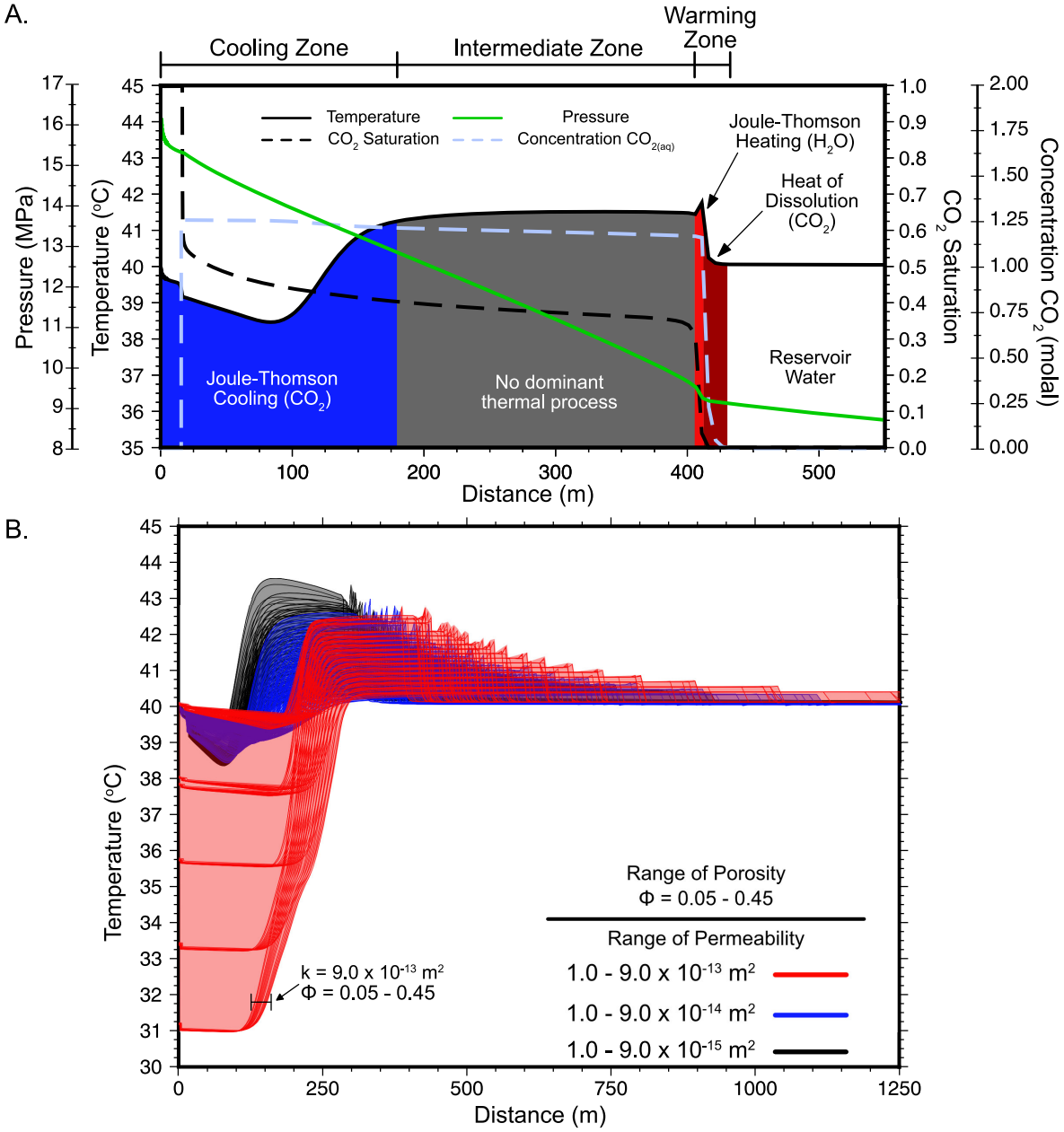

Figure 4.2: Characteristic 1-D thermal profile. A. Schematic illustration of the characteristic 1-D thermal profile after 20 years of injection for a single realization within the complete ensemble ($k = 8.0{\times}10^{-15}\text{m}^2$, $\phi = 0.25$). Shading below the temperature curve (solid black line) denotes each thermal zone; dashed black line is CO_2 saturation, dashed blue line is dissolved CO_2 concentration, and solid green line is fluid pressure. B. Temperature profiles for the complete 1-D simulation ensemble (N = 459) after 20 years of a constant mass CO_2 injection. Results are colored by permeability magnitude.

At the leading edge of the CO_2 plume, two different thermal fluid processes cause a distinct warming front to develop (Fig. 4.2A, red shading). First, CO_2 dissolution into the reservoir water increases fluid temperature (heat of dissolution) as illustrated in Figure 4.2A by the contemporaneous arrival of increasing temperature and aqueous phase CO_2. Second, Joule-Thomson heating due to the expansion of water causes a a small, but sharp temperature spike, which is illustrated in Figure 4.2A at ∼415 m. This sharp thermal spike is caused by the reservoir water experiencing a rapid pressure drop between 405 - 415 m (Figure 4.2A, green line), which produces ∼0.1°C increase over a drop in pressure of 0.5 MPa and results in μ_{JT} of ∼0.2 °C MPa^{-1}. While this increase in temperature is minimal, larger pressure drops caused during a CO_2 injection can result in a more significant temperature increase. The presence of Joule-Thomson heating is in agreement with the laboratory and numerical experiments of Zhang et al. [2018a] that show a pressure drop of 5 MPa causes a +1.1°C temperature change during fluid circulation in an EGS system. This thermal anomaly corresponds with a μ_{JT} of ∼0.2 °C MPa^{-1}, and closely matches the results presented here.

Closer to the injection well, a zone of cooling develops where the expansion of CO_2 consumes thermal energy and the water is fully saturated with respect to CO_2, thus precluding the competing effect of dissolution heating (Fig. 4.2A, blue shading). As a result, the thermal fluid signature near the injection well is characterized by a pronounced temperature depression. The central portion of the CO_2 plume is characterized by a zone of thermal equilibrium where (i) CO_2 is no longer expanding, so Joule Thomson cooling does not occur, (ii) dissolution heating is no longer occurring because the reservoir water is saturated with respect to CO_2, and (iii) the pressure gradient is too low for water expansion, which precludes Joule Thomson warming (Fig. 4.2A, gray shading). Nevertheless, the effects of the warming front are persistent and the fluid temperature remains above background conditions until the near-well zone of cooling.

The complete simulation ensemble shows that the zonal temperature pattern discussed above occurs regardless of permeability and porosity; however, its lateral dimension and magnitude appear to scale with variations in hydraulic properties (Fig. 4.2B). For the CCS scenario considered here, the maximum temperature increase at the warming front is 3.8°C, while the maximum temperature depression in the cooling zone is 8.9°C. To the first order, permeability governs the maximum lateral extent of CO_2 migration, and thus controls the radial extent of the thermal fluid signature. However, the magnitude of temperature change at the warming front appears to increase with higher porosity because additional pore space increases the fluid mass available for dissolution heating. In contrast, the thermal fluid signature of low porosity cases is governed by the thermal contribution of the rock matrix, which keeps the fluid temperature closer to equilibrium with the surrounding reservoir [Oldenburg, 2007, Han et al., 2010]. Within the warming front, these results also show that the temperature spike caused by water expansion increases as bulk permeability decreases (Fig. 4.2B) because lower permeability increases the pressure gradient at the leading edge of the CO_2 plume. Moreover, CO_2 solubility in water also increases with increasing pressure [Carroll et al., 1991], so the maximum temperature increase occurs in the low permeability scenarios (Fig. 4.2B, black), while low temperatures tend to occur in the high permeability scenarios (Fig. 4.2B, red). Interestingly, phase interference between CO_2 and water can also drive pressure gradients at the leading edge of the CO_2 plume [Pollyea, 2016]. Recent numerical studies show that relative permeability effects may cause variability in CO_2 injection pressure[Pollyea, 2016, Yoshida et al., 2016]. For example, Pollyea [2016] utilizes numerical simulations to study how the uncertainty associated with relative permeability can affect a CO_2 injection. This study shows that for a constant mass CO_2 injection, maximum injection pressure can vary from 5 – 60 MPa over a range of van Genuchten parameters. This wide range of injection pressures caused by varying relative permeability parameters suggests that relative permeability effects may be an important contributor to the thermal fluid signature

of CCS operations.

Near the injection well, the ensemble results also show that Joule-Thomson cooling is most pronounced for the cases with high reservoir permeability (Fig. 4.2B, red). This is the result of salt precipitation near the injection well (salting-out), which fills pore space, decreases permeability, and causes steep pressure gradients to develop in the near-well region [Zhao and Cheng, 2017]. These sharp pressure gradients cause the CO_2 to expand rapidly as it migrates beyond the near-well region, which for this study results in a maximum temperature drop of ∼9°C due to Joule-Thomson cooling effects. In fact, Oldenburg [2007] found that Joule-Thomson cooling can account for 20°C temperature drop when CO_2 is injected into natural gas reservoirs.

4.4.2 2D Model - Characteristic Thermal Structure

The 1-D simulation ensemble reveals a characteristic pattern in the radial dimension of fluid temperature during CCS operations. To investigate the vertical dimension, we discretized a single simulation grid into 2 m vertical segments, resulting in a 2-D, radially symmetric, and homogeneous reservoir model. Results from this 2-D simulation are presented as a time series in Figure 4.3 and show that the CO_2 plume and warming front migrate contemporaneously throughout the thickness the reservoir. The vertical temperature distribution is governed by shape the of the CO_2 plume, which is controlled by a combination of capillary and buoyancy forces [Wu et al., 2018b]; however, the characteristic thermal structure illustrated by the 1-D models is still prevalent in Figure 4.3 irrespective of depth. As the CO_2 migrates further into the reservoir the heat produced by CO_2 dissolution and Joule-Thomson warming migrates with the CO_2 plume and reservoir water, while the zone of cooling expands radially from the injection well. These results are similar to those of Han et al. [2012], where they show

that the dissolution of CO_2 into the reservoir water results in a $1 - 5°C$ temperature increase and this maximum temperature increase corresponds to the interface between the CO_2 and reservoir water.

4.4.3 Highly Heterogeneous Reservoir

The 1- and 2-D model results discussed above reveal that an advancing CO_2 plume is accompanied in space and time by a positive thermal anomaly at its leading edge. This result is discordant with a recent study by Jayne et al. [2019b], which found that the positive thermal anomaly advances ahead of the CO_2 plume in a highly heterogeneous basalt reservoir. While Jayne et al. [2019b] suggested that thermal monitoring may be an effective strategy for heterogeneous reservoirs, they did not provide a mechanistic explanation. As a result, we further analyzed a simulation from Jayne et al. [2019b] to make the mechanistic connection between the temperature distribution in a heterogeneous reservoir and the thermodynamic processes responsible for the thermal signature discussed above. Figure 4.4A shows the isosurface contour for 1% CO_2 saturation in a synthetic Columbia River Basalt reservoir with a spatially correlated [Jayne and Pollyea, 2018], but randomly generated, permeability field. The CO_2 plume is shaded by change in temperature from pre- to post-injection, and shows a positive thermal signature of up to 3.5°C at the edges of the CO_2. This is clearly the same phenomenon revealed by the 1-D simulations that show a warming front governed by heat of dissolution and water expansion. Moreover, by interrogating stream tubes showing the direction of heat flow, we find that heat is migrating laterally ahead of the CO_2 plume and vertically into the confining layer (Figure 4.4B, detail section).

To test temperature monitoring as predictor of CO_2 breakthrough, we reproduced the 3-D basalt CCS simulation developed by Jayne et al. [2019b] and recorded time series tempera-

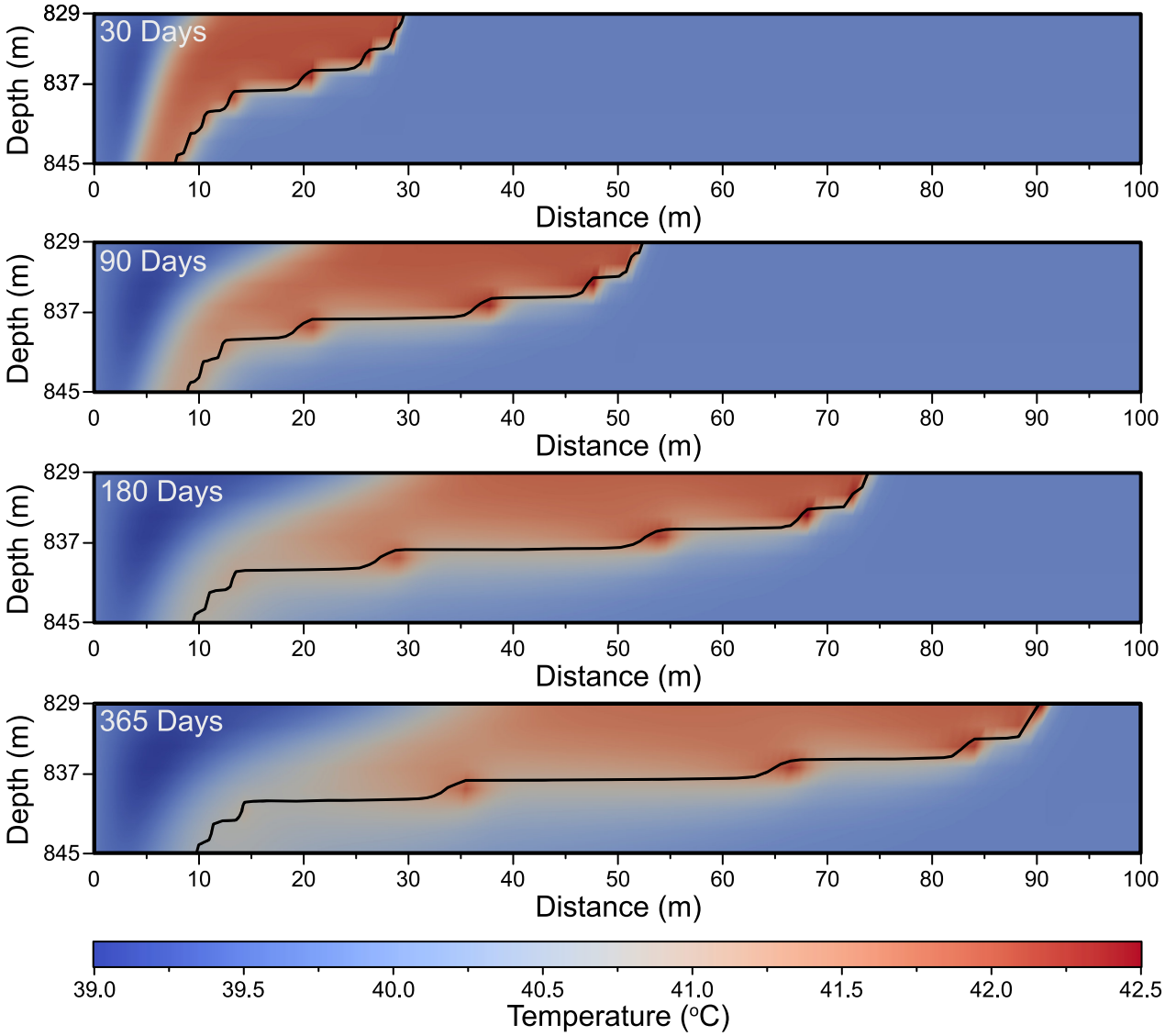

Figure 4.3: 2-D temporal evolution of CO_2 saturation and temperature for 2-D simulation with the same hydraulic reservoir properties as Figure 4.2A. Each panel is colored by reservoir temperature and 1% CO_2 is contoured as a solid black line. Note that 1% CO_2 saturation and the maximum temperature within the reservoir move contemporaneously through time.

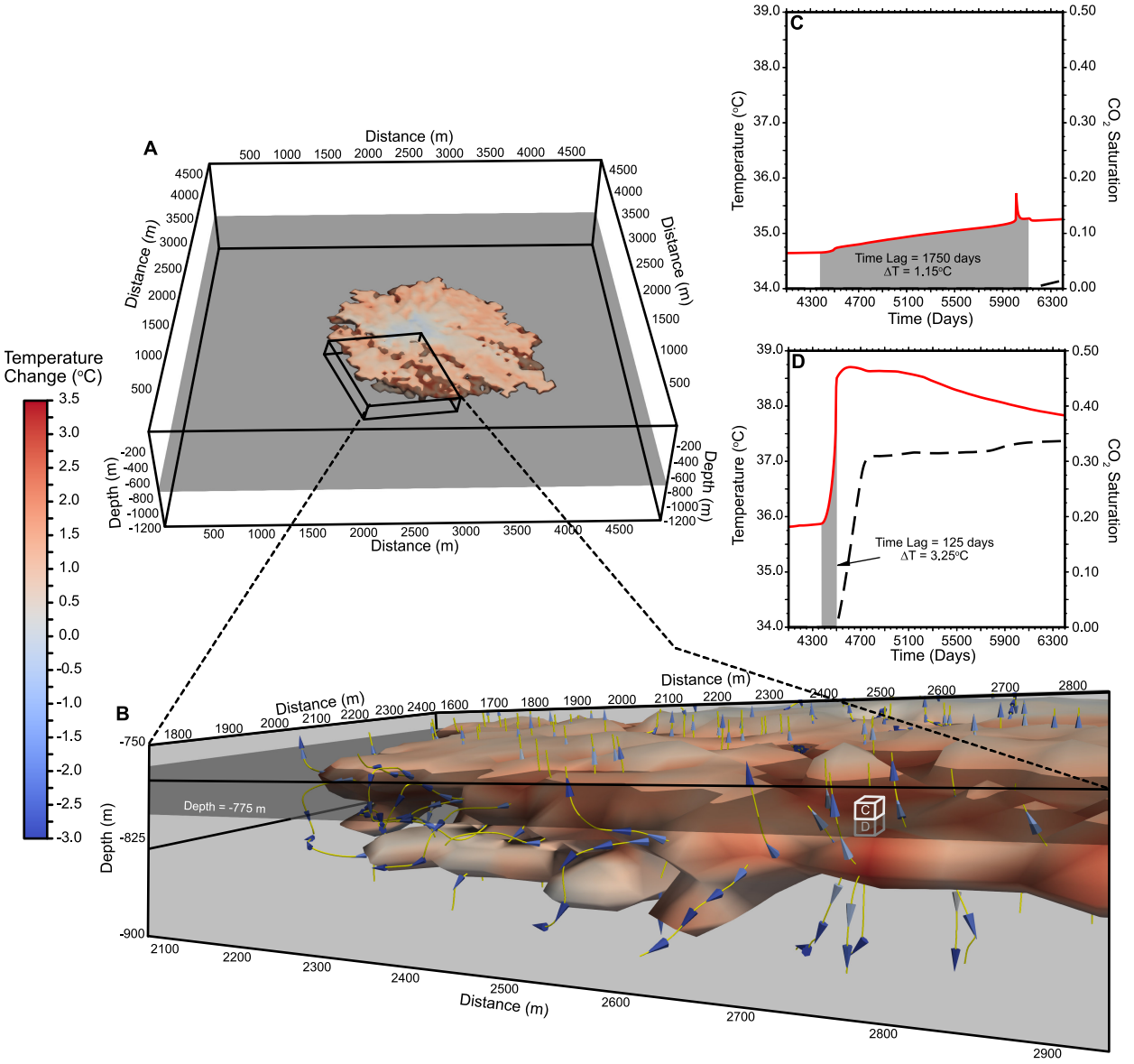

Figure 4.4: Single realization of a 3-D highly heterogeneous. A single realization from Jayne et al. [2019b], A. shows the isosurface for 1% CO_2 saturation after 15 years of a CO_2 injection and is contoured by temperature. B. A subsection of the CO_2 plume is shown along with stream tubes indicating the direction of heat flow. The layer of gray shading corresponds to the boundary between the storage reservoir and overlying caprock. C. and D. Two plots of temperature (red line) and CO_2 saturation (black line) versus time are shown for two grid blocks 400 m away from the injection well; C. Represents a grid block in the entablature zone, D. is a grid block within the injection zone.

ture data for two adjacent grid cells located 400 m from the injection well: Cell C is within the caprock overlying the reservoir and cell D is within the reservoir (Fig. 4.4, detail section). These results show that within the injection zone temperature begins increasing 125 days before the arrival of the CO_2 plume (Fig. 4.4D). However, there is a 1,750 day time lag between temperature change and free-phase CO_2 arrival within the caprock overlying the reservoir (Fig. 4.4C). Within each grid cell temperature increases steadily until the maximum temperature is reached with the arrival of free phase CO_2. The difference in time lag between the reservoir and caprock is explained by the permeability differences between them. However, the presence of the time lag itself is markedly different than what is observed for homogeneous reservoirs. The time lag can be reasonably explained by relative permeability effects in the presence of heterogeneous permeability fields [Pollyea and Fairley, 2012]. Specifically, the positive thermal anomaly associated with heat of dissolution begins when CO_2 dissolves into the aqueous phase. At the leading edge of the CO_2 plume this process occurs at relatively low free-phase CO_2 saturation. As a result, aqueous (wetting) phase mobility is much higher than the non-wetting phase, so the aqueous phase can migrate further into the reservoir under the same pressure gradient. This results in advective transport of the thermal mass ahead of the trailing CO_2 plume (Fig. 4.4, detail section), and the effects become more pronounced as heterogeneous permeability fields facilitate the development of preferential flow paths.

4.5 Conclusions

This study illustrates that thermal effects associated with CCS operations can result in significant temperature changes within and beyond the reservoir. We find that these temperature changes may be a cost-effective and readily implemented monitoring tool during

CCS operations in highly heterogeneous reservoirs. This study implements a numerical modeling experiment to compare the thermal fluid signature that develops during CO_2 injection within homogeneous and heterogeneous geologic reservoirs. The findings from this study are:

1. The thermodynamic processes of Joule-Thomson heating and cooling combined with heat of dissolution result in a characteristic thermal profile in homogeneous reservoirs.

2. At the leading edge of a CO_2 plume, the combination of heat of dissolution and Joule-Thomson heating (H_2O expansion) causes reservoir temperatures to increase up to 4°C.

3. Joule-Thomson cooling (CO_2 expansion) causes reservoir temperatures to decrease as much as 9°C near a CO_2 injection well.

4. In homogeneous reservoirs increased reservoir temperatures due to heat of dissolution and Joule-Thomson heating migrate concurrently through the reservoir, suggesting temperature could be a proxy for CO_2 breakthrough.

5. In highly heterogeneous reservoirs CO_2 injections result in a much more complex thermal structure where increased reservoir temperatures can arrive within a monitoring well weeks before the arrival a free phase CO_2.

In conclusion, results from this study yield important insights into the thermal processes taking place within a CO_2 plume during a CO_2 injection scenario. The heat of dissolution and Joule-Thomson effects of both CO_2 and water cause a temporally and spatially evolving thermal profile within the storage reservoir. The combination of simplified 1-D homogeneous simulations with complex heterogeneous 3-D simulations yield important guidance

in the application of temperature monitoring as a predictor of CO_2 breakthrough in CCS operations.

Chapter 5

Geomechanical Reservoir Integrity During CCS in Flood Basalt Formations

Recent field experiments in Iceland and Washington State, USA, show that basalt formations may be favorable targets for carbon capture and sequestration (CCS) because CO_2 mineralization reactions proceed rapidly. These results imply that there is tremendous opportunity for implementing CCS in large igneous provinces. However, the magnitude of this opportunity comprises commensurate levels of uncertainty because basalt reservoirs are characterized by highly heterogeneous, fracture-controlled hydraulic properties. This geologic uncertainty is propagated as parametric uncertainty in quantitative risk models, thus limiting the efficacy of models to predict CCS performance attributes, such as reservoir integrity and storage potential. To overcome these limitations, this study presents a stochastic approach for quantifying the geomechanical performance attributes of CCS operations in a highly heterogeneous basalt reservoir. We utilize geostatistical reservoir characterization to develop an ensemble of equally probable permeability distributions in a flood basalt reservoir with characteristics of the Wallula Basalt Pilot Project. We then simulate industrial-scale CO_2 injections within the ensemble and calculate the mean and variance of fluid pressure over a 1-year injection period. These calculations are combined with the state of stress in

southeast Washington State, to constrain the spatial extent at which shear failure, fracture initiation, and borehole breakdown may occur. Results from this study show that (i) permeability uncertainty alone causes injection pressure to vary over 25 MPa, (ii) shear failure is likely to occur at 7 times greater distances from the injection than the CO_2 migrates, and (iii) joint initiation pressures are localized within the volume comprising the CO_2 plume.

5.1 Introduction

A growing body of evidence suggests that deep basalt reservoirs (>800 m) may be attractive targets for carbon capture and sequestration (CCS) on the basis of favorable CO_2-water-rock reaction kinetics, which result in permanent CO_2 isolation through mineral trapping [McGrail et al., 2006, Matter and Kelemen, 2009]. Recent pilot-scale experiments have provided evidence of *in situ* mineralization of the injected CO_2 within basalt reservoirs. The CarbFix CCS pilot in Iceland injected 230 tons of CO_2 dissolved in water into a basalt reservoir, and post-injection analysis showed 95% of the CO_2 was permanently converted to mineral phases just two years after injection [Matter et al., 2016]. The Wallula Basalt Sequestration Pilot Project in eastern Washington injected 1,000 metric tons (MT) of supercritical CO_2 into the Columbia River Basalt Group (CRBG) and post-injection analysis showed that carbonate nodules in sidewall cores were (i) widespread and (ii) comprised of the same isotope signature as the injected CO_2 [McGrail et al., 2017]. To complement these results, CCS in deep basalt reservoirs is motivated to a large extent by the relatively high storage potential within both onshore and offshore basalt formations. In particular, CO_2 storage estimates for the Columbia River Basalt Group in the northwestern United States are estimated to be on the order of 100 Gt CO_2 [McGrail et al., 2006], and offshore basalt formations within the Juan de Fuca plate and Central Atlantic Magmatic Province hold potential for CO_2 disposal on comparable scales [Goldberg et al., 2008, 2010]. However, the injection of CO_2 into the subsurface causes a disturbance in the pressure, temperature, and chemical systems within the target reservoir, and this response affects the injectivity, storativity, and confinement potential of the site. While the Wallula Pilot Borehole and CarbFix projects show promising results, transitioning basalt CCS technology from pilot-scale to industrial applications is complicated by the highly heterogeneous nature of fracture-controlled basalt reservoirs [Price and Oldenburg, 2009].

Among the principal challenges for industrial-scale CCS in any geologic environment is to ensure >99% CO_2 isolation per thousand years [USDOE, 2013], which, if not met, will likely postpone rather than mitigate global warming trends [Shaffer, 2010]. In order to achieve >99% CO_2 isolation, the integrity of physical traps (i.e., cap-rock seals) under long-term injection pressure is a paramount concern because excessive reservoir pressure may result in a number of adverse consequences, including fracture propagation/reactivation [Lucier et al., 2006, Goodarzi et al., 2011], shear or joint dilation [Min et al., 2004], induced seismicity [Cappa and Rutqvist, 2011], and cm-scale displacements on small, difficult to characterize faults and fractures [Zoback and Gorelick, 2012]. As a result, geomechanical reservoir integrity has become an important criterion for numerical model-based risk assessment in CCS reservoir siting [NETL, 2011]. In order to address this problem, stochastic methods have been increasingly deployed to understand how spatial, parametric, and geologic uncertainty affects CCS reservoir performance [Srivastava, 1994a, Li et al., 2005, Pollyea and Fairley, 2012, Pollyea et al., 2014, Popova et al., 2014, Gierzynski and Pollyea, 2017, Jayne et al., 2018]. For example, Pollyea et al. [2014] develop and implement ensemble simulation methods to quantify spatially variable sealing behavior within the low-volume Snake River Plains basalts. Jayne et al. [2019a] extends these methods into flood basalt formations to show how permeability uncertainty affects the injectivity and leakage during CCS in flood basalt formations. And in sedimentary basins, Bosshart et al. [2018] shows that heterogeneous properties in a sandstone reservoir impose significant controls on both CO_2 injection rate and storage capacity.

Stochastic simulation methods have been gaining traction as a way to bound the uncertainties associated with heterogeneous reservoirs because spatially variable properties, such as permeability, cannot be upscaled according to simple averaging rules [Tidwell and Wilson, 1997]. It is the uncertainty of permeability distribution at these larger scales that can

have a substantial impact on the results of hydrogeologic models [Pollyea and Fairley, 2012, Pollyea et al., 2014]. For example, constraining permeability at regional scales has implications for studying geological formations that contain multiple resources (e.g. groundwater, geothermal, carbon storage, etc) [Saar and Manga, 2004]. Complete characterization of the geomechanical response to deep CO_2 injections requires *a priori* knowledge of regional tectonic stresses, mechanical reservoir properties, and orientations of pre-existing discontinuities (faults and fractures) within the reservoir. Within CRBG reservoirs, pressure build up is a particular concern because both reservoir and seal rock are ubiquitously fractured. Furthermore, pressure builds rapidly in early time during a CO_2 injection. Mathias et al. [2011] and Pollyea [2016] illustrate that the majority of fluid pressure accumulation occurs within the first few days of a CO_2 injection. This rapid pressure build up in early time is critically important to account for when studying the geomechanical response of the storage reservoir. In order to assess how reservoir integrity is affected by rapid pressure accumulation and heterogeneous reservoir properties this study utilizes a Monte Carlo modeling approach to simulate a CCS injection scenario into the Columbia River Basalt Group. Specifically, we use ensemble simulation methods in combination with known geologic information from the Wallula borehole to quantify how permeability variability affects reservoir integrity during an industrial-scale CO_2 injection. Ensemble analytics are utilized to develop a probabilistic assessment of geomechanical reservoir integrity during CCS operations in a flood basalt reservoir with characteristics of the Wallula Basalt Sequestration Pilot Project.

5.1.1 Geologic Setting

Columbia River Basalt Group

The Columbia River Basalt Group (CRBG) is a continental large igneous province in the northwest United States (Figure 5.1), and comprises a layered assemblage of ∼300 Miocene-age flood basalts with an areal extent of 200,000 km^2, aggregate thickness of 1–5 km, and total estimated volume of 224,000 km^3 [Reidel et al., 2002, McGrail et al., 2009]. The CRBG has been extensively studied due to its wide range of resource potential, including (1) groundwater production [Burns et al., 2011, Kahle et al., 2011], (2) nuclear waste storage (e.g., Gephart et al. [1983]), (3) natural gas storage [Reidel et al., 2002], (4) geologic CO_2 sequestration [McGrail et al., 2017], and (5) geothermal resources [Burns et al., 2016]. Among the principal challenges in assessing the feasibility of engineered CRBG reservoirs is to understand how fracture-controlled reservoir properties (i.e., permeability and porosity) affect both local- and regional-scale fluid flow. These fracture-controlled reservoir properties are governed by individual basalt flow morphology, which is characterized by: (1) densely fractured, vesicular flow-tops, (2) a central entablature comprising narrow, fanning columnar joints, and (3) lower colonnades with vertical, column bounding joints (Figure 5.2) [Mangan et al., 1986]. Within CRBG flows, *in situ* pumping tests reveal that permeability ranges over thirteen orders of magnitude with the entablature zone generally inhibiting groundwater flow (Figure 5.3A), while densely fractured flow tops and flow bottoms are highly productive [Kahle et al., 2011, Jayne and Pollyea, 2018]. To further complicate CRBG reservoir characterization, individual basalt flows exhibit km-scale lateral dimensions and vertical dimensions from cm-scale to greater than 70m [Mangan et al., 1986].

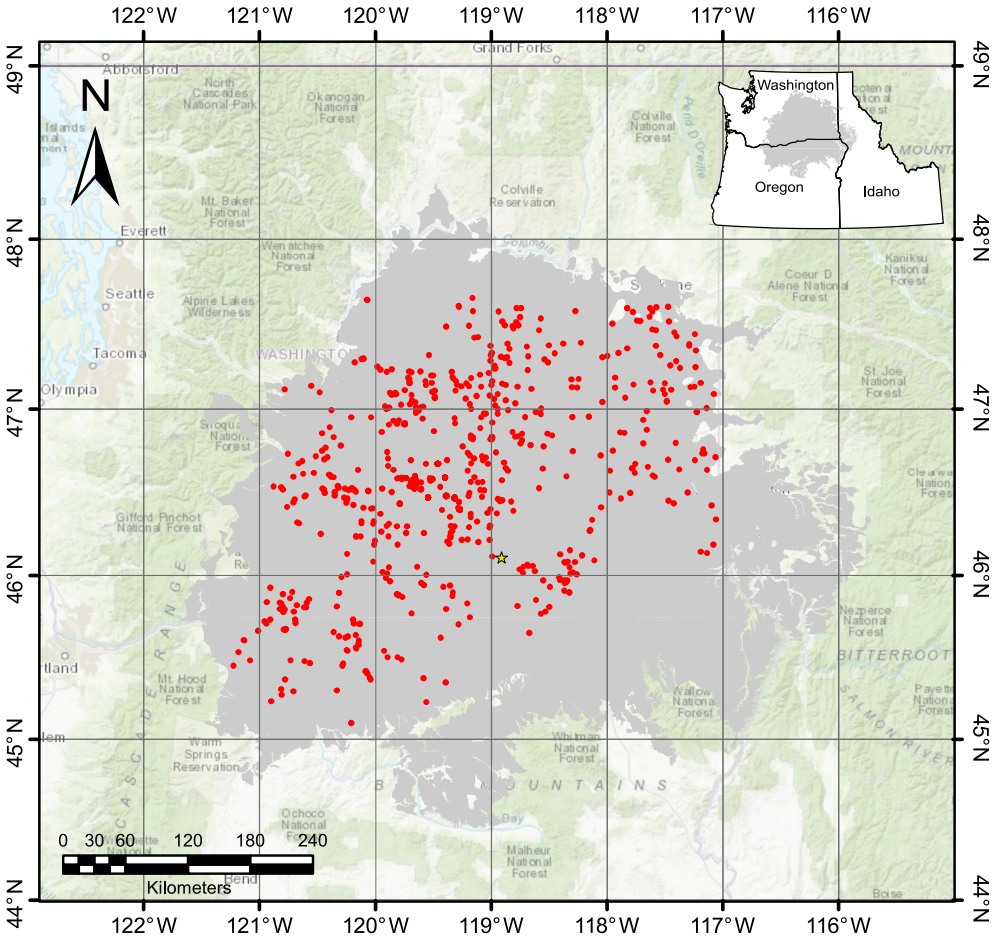

Figure 5.1: Map of Columbia River Basalt Group. Map showing the areal extent of the Columbia River Basalts shaded in grey. Wells with permeability data compiled by Jayne and Pollyea [2018] within the CRBG are shown in red and the Wallula Pilot Borehole is denoted by the yellow star. (Modified from Jayne and Pollyea [2018])

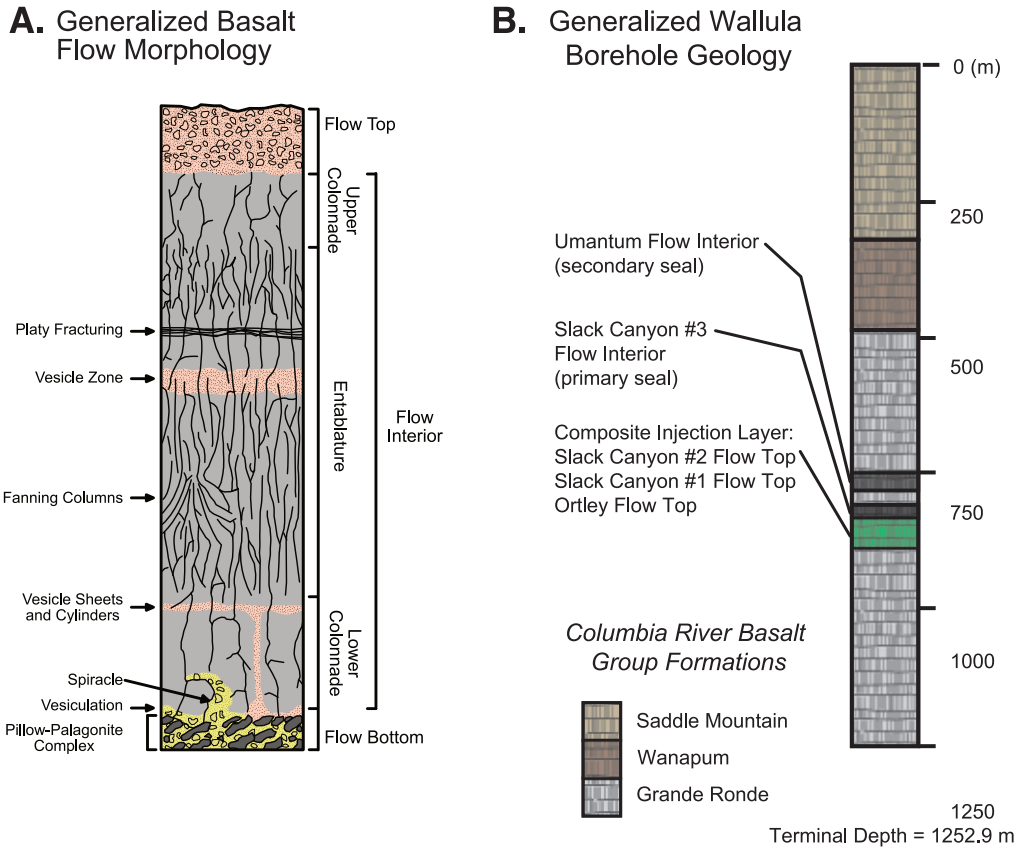

Figure 5.2: Basalt flow morphology. A.Individual CRBG flow morphology (modified from Reidel et al. [2002]). B. Generalized geology within the Wallula Pilot Borehole.

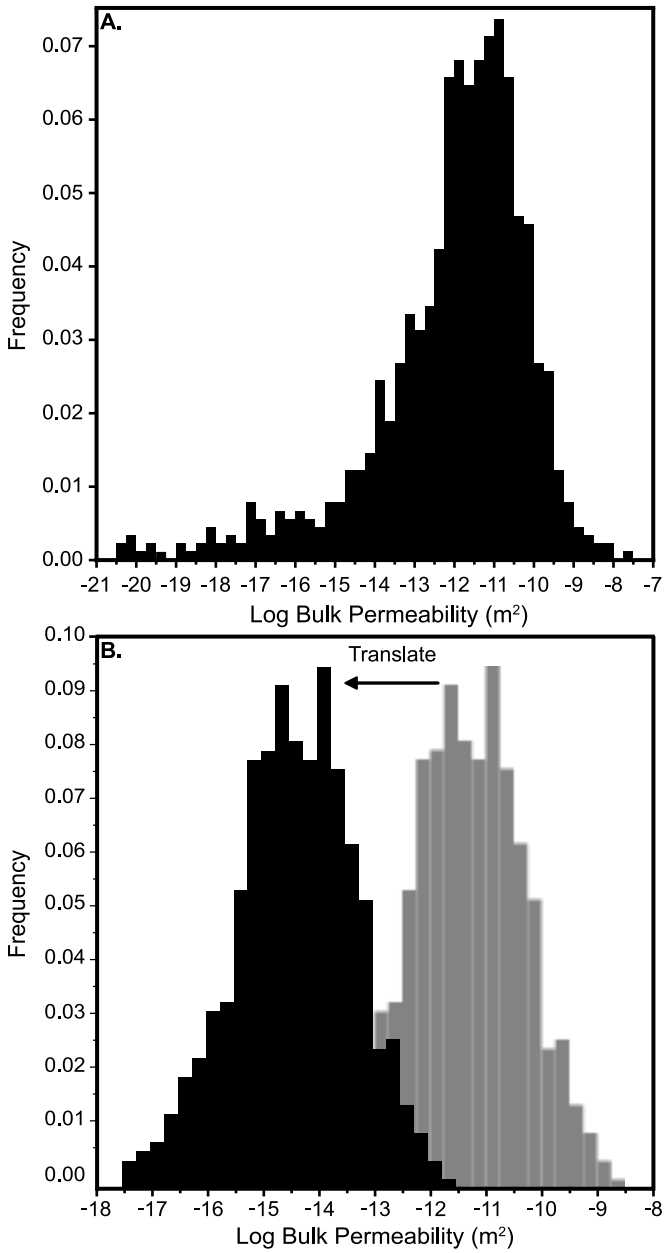

Figure 5.3: Histogram of permeability from compiled well data. A. Histogram of log permeability from well data compiled by Jayne and Pollyea [2018]. B. Histogram of the filtered permeability data to represent the high permeability flow tops. The mean of log permeability is -11.5 m^2 (grey), in order to make this range of permeabilities more representative at the depth of the injection zone the permeability distribution is translated downward so that the mean log permeability is -14.5 m^2, which is congruent with field test from the Wallula borehole.

Wallula Pilot Borehole

As part of the Big Sky Carbon Sequestration Partnership (BSCSP), the U.S. Department of Energy identified the Columbia River Basalt Group (CRBG) as a primary target formation for CCS development in the Pacific Northwest. The CRBG was chosen on the basis of its relatively high CO_2 storage estimates (10 - 50 Gt CO_2), potential for CO_2 isolation, and generally favorable reservoir characteristics [Litynski et al., 2006, McGrail et al., 2006, Rodosta et al., 2011, McGrail et al., 2017]. In order to locate a suitable site for a pilot injection, seismic surveys were conducted in Walla Walla County, WA, which identified areas where major geologic structures would not preclude a CO_2 injection [McGrail et al., 2011]. Drilling for the Wallula Pilot Borehole began in January 2009 and completed in April 2009. The Wallula Pilot Borehole reaches a total depth of 1,253 m and intersects three CRBG formations: Saddle Mountain, Wanapum, and Grande Ronde [McGrail et al., 2009]. The target formation for injection is the Grande Ronde Basalt, of which the Wallula Pilot Borehole intersects 26 flows and 7 members. A candidate (composite) injection zone was identified at 828 - 887 m depth, spanning three brecciated interflow zones within the Grande Ronde Formation [McGrail et al., 2009]. Hydrologic characterization of these three zones show that they represent a single hydraulic unit with relatively high permeability and are bounded by thick low permeability flow interiors, which act as a natural caprock [McGrail et al., 2009]. In 2013, 1,000 MT of supercritical CO_2 were injected at the Wallula Pilot Borehole over the course of three weeks. Since the injection, McGrail et al. [2017] has published results from this field study validating the reactivity of supercritical CO_2 with basalts at the Wallula Pilot Borehole.

5.2 Methods

This study uses numerical modeling and simulation to test the feasibility of industrial-scale CO_2 injections at the Wallula Basalt Sequestration Pilot Site in southeast Washington State, USA. The model scenario reproduces known hydraulic properties within the Wallula borehole, but far-field permeability distributions are subject to substantial uncertainty. To bound this uncertainty, an ensemble of equally probable synthetic reservoirs is developed on the basis of geostatistical reservoir simulation [Deutsch, 2002]. The model scenario simulates CO_2 injections for 1 year within each synthetic reservoir, and the complete set is analyzed using ensemble simulation methods. This results in a probabilistic model of CO_2 transport and injection-induced pressure transients. This probabilistic model is the basis for calculating geomechanical reservoir integrity using static threshold criteria calculated along with utilizing the variance associated with the ensemble simulation methods to account for 3σ variability.

5.2.1 Reservoir Characterization & Model Domain

The conceptual model is based on geologic characteristics of the Wallula Basalt Sequestration Pilot Site, which is a layered assemblage of individual basalt flows with alternating high permeability flow tops/bottoms and low permeability flow interiors (Figure 5.4). The Wallula injection zone occurs between 775 and 865 m depth, within which permeability is well constrained on the basis of highly detailed site characterization [McGrail et al., 2009]. Nevertheless, permeability beyond the borehole is both highly heterogeneous and highly uncertain due to the fracture-controlled nature of basalt formations [Jayne and Pollyea, 2018]. To account for this uncertainty in numerical simulation, this study implements stochastic reservoir characterization to develop an ensemble of 35 equally probable reservoir domains

that each reproduce known borehole geology, but model far-field permeability on the basis of (i) the semivariogram correlation structure of CRBG permeability and (ii) its corresponding probability distribution.

The spatial correlation of CRBG permeability was shown by Jayne and Pollyea [2018] to exhibit spatial anisotropy with directions of maximum and minimum spatial correlation oriented at N40°E and N130°E, respectively. This spatial correlation model is based on a regional CRBG permeability database (Figure 5.1) for which permeability values were filtered on two standard deviations of the mean to ensure that the low permeability entablature (caprock) was not incorporated in the calculations and only the highly productive flow tops and bottoms were included (Figure 5.3B). The present study adopts this convention to constrain permeability distribution within the highly conductive composite injection zone. This results in a range of log permeability (log k) from -8.5 m^2 to -14.5 m^2 with a median log k of -11.5 m^2. However, the present study is focused on permeability at depths greater than 750 m, where the log k in the Wallula Pilot Borehole is known to be ∼-14.5 m^2 [McGrail et al., 2009]. This discrepancy arises because the vast majority of permeability measurements in the Jayne and Pollyea [2018] database are taken at depths less than ∼200 m; however, CRBG permeability decreases with depth until ∼1,000 m. To account for this difference, we adopt the method proposed by Gierzynski and Pollyea [2017] that translates the distribution such that the variability of permeability is maintained but the mean permeability is representative of the composite injection in the Wallula Pilot Borehole. This results in a new range of log k from -11 m^2 to -17 m^2. This probability distribution is combined with the anisotropic semivariogram model to develop 35 equally probable realizations of the composite injection zone by sequential indicator simulation [Deutsch and Journel, 1998]. In this approach, each grid cell is simulated in random order by solving the ordinary kriging equations on the basis of (1) the cumulative distribution function for CRBG permeability, (2) known data points,

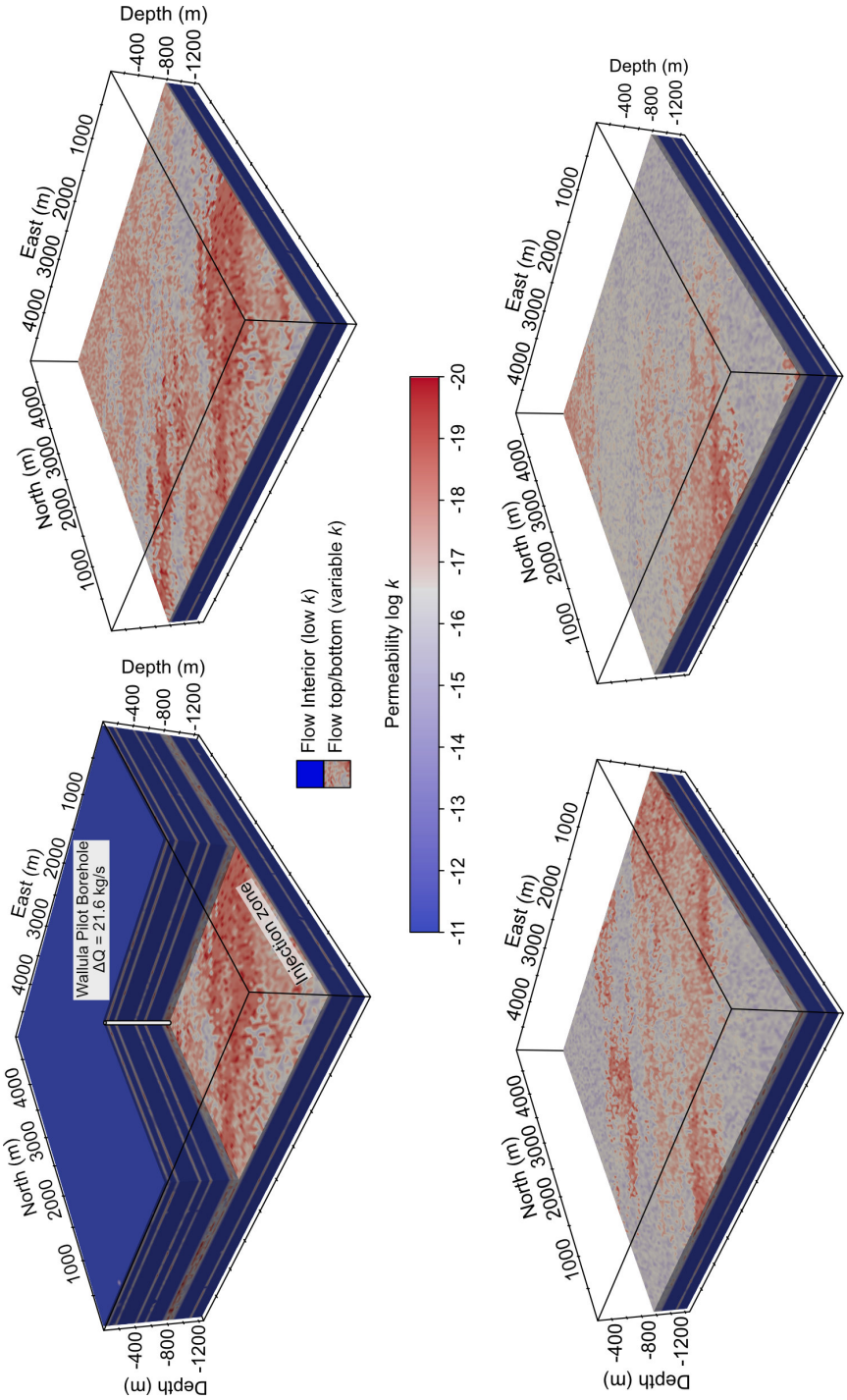

Figure 5.4: Model domain for constant rate injection study. Model domain for CO_2 injection modeling study. The composite injection zone is between 775 – 865 m depth and is populated with spatially-correlated, randomly generated permeability distributions. The cut-away shows the alternating layers of flow interior and flow tops along with the location of the Wallula Pilot Borehole. Three spatially-correlated and equally-probable permeability distributions are shown in the other panels.

which are the borehole permeability tests from the Wallula borehole, (3) previously simulated grid cells, and (4) the chosen spatial correlation model, which for this study is the anisotropic semivariogram model developed Jayne and Pollyea [2018]. For this study, the permeability distribution is simulated for 35 equally probable composite injection zones, each of which reproduces known borehole permeability, as well as the depth-scaled CRBG permeability distribution and spatial correlation characteristics with minor ergotic fluctuation.

Each composite injection zone permeability distribution is inserted into the overall model domain, which comprises an areal extent of 5,000 m × 5,000 m × 1,250 m representing the ground surface to 1,250 m depth with the Wallula Pilot Borehole centrally located. Individual grid blocks have a maximum dimension of 50 m × 50 m × 25 m in the far-field with higher resolution grid refinement of 5 m × 5 m × 5 m near the injection well (Figure 5.4). The complete domain is discretized into 1,467,568 grid blocks by Voronoi tesselation [Haukwa, 1998]. A total of 35 individual model domains are produced with spatially variable and equally probable permeability distributions in the composite injection zone.

5.2.2 Numerical Simulation

In this study, CO_2 injection is simulated within each equally probable synthetic reservoir for 1 year at 21.6 kg/s, which corresponds with the typical CO_2 output from a 500 MW gas-fired power plant. The code selection for this study is TOUGH3 [Jung et al., 2017] compiled with the ECO2M fluid property module [Pruess, 2011]. TOUGH3 solves energy and mass conservation equations for nonisothermal, multiphase flows in a porous geologic media. The ECO2M module simulates mixtures of H_2O - NaCl - CO_2, within the temperature range of 10 - 110°C, pressure ≤60 MPa, and salinity from nil to full halite saturation. The ECO2M module simulates all possible phase conditions for CO_2 - brine mixtures, including transitions

between super- and sub-critical CO_2, as well as the transition between liquid and vapor CO_2 [Pruess, 2011].

Initial conditions are specified with a hydrostatic pressure gradient ranging from 0.101 MPa (1 atm) at ground surface to 12.3 MPa at the bottom of the Wallula Pilot Borehole. Initial temperature is calculated by imposing the regional heat flux of $\sim$65 mW/m^2 [Pollack et al., 1993] as a thermal boundary at the base of the model and a constant temperature of 10°C at ground surface. This results in a linear temperature gradient from 10°C at the surface to 50°C at 1,250 m depth. The reservoir water within the CRBG is defined by a NaCl concentration of 10,000 ppm. These initial conditions are consistent with the field measurements taken at the Wallula Pilot Borehole [McGrail et al., 2009]. Within the composite injection zone (775 – 865 m), initial temperature and pressure conditions range from 35 - 38°C and 7.7 - 8.4 MPa, which are within the supercritical field for CO_2. Dirichlet boundary conditions are specified at (i) the upper boundary of the model domain to hold pressure and temperature constant at ground surface and (ii) the lateral boundaries of the model domain to maintain temperature and pressure gradients in the far field.

For this modeling study, the relative permeability, capillary pressure models, and geologic properties are listed in Table 5.1. The bulk reservoir properties for the CRBG are based on petrophysical [Zakharova et al., 2012] and modeling [Gierzynski and Pollyea, 2017] studies extant in the literature. The effects of multi-phase flow (CO_2 and brine) are accounted for using the Van Genuchten [1980] models for relative permeability and capillary pressure (Table 5.1). It is important to note here that relative permeability of basalt flows remains a subject of much uncertainty [Pollyea, 2016]; however, it is generally accepted that the relative permeability characteristics of basalt fractures are highly interfering Bertels et al. [2001].

As with all modeling studies, a brief mention of the model limitations is warranted. This

Table 5.1: Model parameters - 1 year injection scenario.

	Matrix	Fracture	Flow Top	Basal Boundary
Density ($kg \cdot m^{-3}$)	2900.0	2300.0	2300.0	2900.0
Porosity	0.05	0.1	0.3	0.05
Permeability(m^2)	10^{-20}	10^{-16}	varies	10^{-20}
Thermal Conductivity ($W \cdot m°C^{-1}$)	2.11	2.11	2.11	2.11
Heat Capacity ($J \cdot kg^{-1}°C^{-1}$)	840	840	840	840
van Genuchten parameters				
Relative Permeability			Capillary Pressure	
λ	0.550		λ	0.457
S_{lr}	0.30		S_{lr}	0.0
S_{ls}	1.0		α (Pa^{-1})	5.e-5
S_{gr}	0.25		P_{max} (Pa)	1e.7
			S_{ls}	0.999

modeling study does not account for basalt dissolution or secondary mineral precipitation, so permeability alteration from secondary mineral precipitation is neglected. Thus, the simulation results presented here are a conservative estimate of both CO_2 storage potential and fluid pressure accumulation. In addition, relative permeability hysteresis is not accounted for in the simulations because only the injection phase of a CCS project is simulated, thus imbibition does not occur. Similarly, mass transport by molecular diffusion is not accounted for because CO_2 is under constant injection pressure, which results in a high Péclet number. And finally, geomechanical reservoir integrity is evaluated on the basis of threshold criteria that depend on changes in fluid pressure, thus geomechanical *processes* are not explicitly simulated.

5.2.3 Data Analysis

The simulations that completed each discrete time step were analyzed using ensemble simulation analytics (e-type estimates) [Deutsch and Journel, 1998]. In this approach, the mean

and variance of fluid pressure and free-phase CO_2 saturation are calculated for each grid cell. The e-type calculation for mean fluid pressure ($\bar{P}_{f,(x,y,z)}$) within each grid cell is

$$\bar{P}_{f(x,y,z)} = \frac{1}{35}\sum_{i=1}^{35} P_{f,i(x,y,z)} \tag{5.1}$$

where, $P_{f,i(x,y,z)}$ is the modeled fluid pressure for simulation i at location (x, y, z). Similarly, the variance ($s^2_{(x,y,z)}$) associated with Equation 5.1 for each grid cell is computed as:

$$s^2_{(x,y,z)} = \frac{1}{35}\sum_{i=1}^{35}(P_{f,i(x,y,z)} - \bar{P}_{f,(x,y,z)})^2 \tag{5.2}$$

Because reservoir integrity during CCS is based to a large extent on injection-induced fluid pressure transients, the ensemble analysis (Equations 5.1 & 5.2) forms the basis for calculating geomechanical threshold criteria with corresponding uncertainty estimates. The geomechanical parameters used to calculate these threshold criteria can be found in Table 5.2. However, these calculations require knowledge about the regional stress state within the CRBG in southeast Washington. Stress data are available from site characterization efforts at the Hanford Nuclear Reservation, which is located ~30 km northeast of the Wallula site. Specifically, *in situ* stress measurements are reported from borehole tests between 924 and 1,195 m depth [Paillet and Kim, 1987], which is ~40 m below the Wallula composite injection zone (Figure 5.7). Extending a linear regression model of S_H and S_V to 800 m depth suggests 38 MPa differential stress within the CO_2 injection zone (Figure 5.7). These are combined with a friction coefficient (μ_s) of 0.85 [Byerlee, 1978] to estimate the upper and lower bounds of stable stress as,

$$\sigma_1 = \sigma_3[(\mu_s^2 + 1)^{1/2} + \mu_s]^2 \tag{5.3}$$

$$\sigma_3 = \sigma_1[(\mu_s^2 + 1)^{1/2} + \mu_s]^{-2} \tag{5.4}$$

where, σ_1 and σ_3 are the maximum and minimum compressive stresses, respectively [Engelder, 2014]. Equations 5.3 and 5.4 assume that internal cohesion is nil because fractures are weaker than intact rock and mounting pore fluid pressure will significantly reduce fault and/or fracture cohesion [Engelder, 2014].

Table 5.2: Geomechanical Parameters.

μ_s	0.85	Byerlee [1978]
T_o (MPa)	1.5	Schultz [1995]
β_i (MPa^{-1})	1.9×10^{-11}	Schultz [1995]
β_b (MPa^{-1})	4.8×10^{-11}	Schultz [1995]
K_{IC} (MPa $m^{\frac{1}{2}}$)	2.203	Engelder [2014]
Y	$\frac{2}{\sqrt{\pi}}$	Engelder [2014]
c (mm)	0.01	Kowallis et al. [1982]
ν	0.3	Schultz [1995]

Since the disposal reservoir is fully saturated, effective stress theory is invoked to account for the influence of pore fluid pressure acting in opposition to the compressive stresses, e.g., $S_{V,eff} = S_V$ - P_f. In the context of Figure 5.7, pore fluid pressure translates S_H, S_h, and S_V to the left, while the failure criteria exhibit a non-linear translation such that the upper bounding failure line is reduced in greater proportion than the minimum bound [Engelder, 2014]. This means that the envelope of stable stress narrows while differential stress remains unchanged, so that $S_{V,eff}$ becomes closer to the minimum bounding failure line. To quantify which CO_2 injection scenarios produce sufficient pore fluid pressure to move $S_{V,eff}$ out of the stable stress envelope, the Mohr-Coulomb failure criteria is evaluated within each grid cell of the simulation ensemble by calculating the mean minimum effective compressive stress ($\bar{S}_{V,eff(x,y,z)}(t)$) within each grid cell of the model domain as,

$$\bar{S}_{V,eff(x,y,z)}(t) = S_V - \bar{P}_{f(x,y,z)}(t). \tag{5.5}$$

Here, S_V is the vertical stress (σ_3) and $\bar{P}_{f(x,y,z)}(t)$ is mean grid block injection pressure for time step (t) computed per Equation 5.1. Once all $\bar{S}_{V,eff(x,y,z)}(t)$ are computed for each CO_2 injection scenario, the likelihood of failure less than 1% for each grid cell is computed as:

$$\text{Failure} > 1\% \text{ if} : \bar{S}_{V,eff(x,y,z)}(t) - 3s_{(x,y,z)} > S_H[(\mu_s^2+1)^{1/2} + \mu_s]^2 \tag{5.6}$$

where, $S_H[(\mu_s^2+1)^{1/2} + \mu_s]^{-2}$ is the lower bound of σ_3 given in Equation 5.4, and $s_{(x,y,z)}$ is the standard deviation of mean grid cell pore fluid pressure (square root of Equation 5.2).

Increasing fluid pressure during CO_2 injections may result in fracture dilation and fracture propagation, both of which can occur at scales ranging from local borehole effects to far-field reservoir effects. Within CRBG reservoirs, fracture dilation is a particular concern because densely fractured entablature zones represent the cap rock seal for CO_2 isolation prior to widespread mineralization. Although pumping tests show that the hydraulic conductivity of CRBG entablatures is approximately seven orders of magnitude lower than the composite injection zone, the permeability of these units is governed primarily by fracture networks. This means that permeability in the flow interiors may be highly sensitive to fracture dilation because permeability is known to scale non-linearly with aperture [Witherspoon et al., 1980]. A typical estimate for the onset of fracture dilation is when fluid pressure exceeds the normal stress acting on a fault plane [Engelder, 2014]; however, the concept of a "deformable fracture" has been shown relevant for quantifying aperture changes in response to changing effective normal stress on a fracture plane [Pyrak-Nolte and Morris, 2000, Rutqvist and Stephansson, 2003, Min et al., 2004, Jiang et al., 2009]. To quantify the deformable nature of a fracture, the specific stiffness (κ) is invoked, such that κ is the ratio of change in effective normal stress ($\Delta\sigma_{n,eff}$) to change in fracture aperture (Δe). In crystalline rocks, experimental results show that κ is $\sim$100 MPa mm^{-1} for effective normal stress conditions expected at the Wallula site [Pyrak-Nolte and Morris, 2000]. Since stress-dependent per-

meability is highly non-linear, particularly below 5 MPa effective stress, we implement a conservative fracture dilation criterion of $\sigma_{n,eff} \leq 5$ MPa, which, in the entablature overlying the proposed injection zone correlates with ΔP_f of ~5 MPa and > 0.1 mm fracture dilation.

At the Wallula Site, the smallest effective normal stress that can act on fault plane is the minimum compressive effective stress $S_{V,eff}$, suggesting that column-normal (horizontal) fractures in the S_H - S_h plane may be the first to dilate in the presence of excessive fluid pressure. To compute the potential for fracture dilation within the sealing formation (entablature) overlying the injection zone (Figure 5.2), the dilation criterion of $S_{V,eff} \leq 5MPa$ is evaluated within each grid cell of the ensemble. To assess the potential for >1% dilation within the Wallula sealing formations this criterion was augmented to account for uncertainty in the fluid pressure component of $S_{V,eff}$:

$$S_V - [\bar{P}_{f(x,y,z)}(t) + 3s_{(x,y,z)}] \leq 5MPa \tag{5.7}$$

where, $s_{(x,y,z)}$ is the standard deviation of $\bar{P}_{f(x,y,z)}(t)$ at time t.

At the borehole scale, tensile failure (hydraulic fracture) is governed by the interactions between radial stress concentrations along the borehole wall, well bore fluid pressure, and the far-field horizontal stresses, S_H and S_h. Horizontal compressive stresses acting normal to the borehole circumference are deflected 90° as tensile stresses; where as, horizontal compressive stresses acting tangential to the borehole will be magnified 3×. These local scale effects become superimposed on the regional stress field, which results in a somewhat complex criterion for hydraulic fracture (or breakdown) pressure (P_b):

$$P_b = \frac{3S_h - S_H + T_o - 2\eta P_f}{1 + \beta - 2\eta} \tag{5.8}$$

$$\eta = \frac{\alpha(1-2\nu}{2(1-\nu)} \tag{5.9}$$

$$\alpha = 1 - \frac{\beta_i}{\beta_b} \tag{5.10}$$

where, T_o is the tensile strength of rock, β is the effective stress coefficient for tensile failure, and η accounts for poroelastic effects in a permeable rock mass [Jaeger et al., 2009]. This poroelastic term includes the bulk and unfractured rock mass compressibility (β_b and β_i, respectively), Poisson's ratio (ν), and the Biot parameter (α), all of which have been constrained for either CRBG basalts [Schultz, 1993, Degraff and Aydin, 1993, Goehring and Morris, 2008] or analogous jointed basalt formations [Adams and Gibson, 1926, Simmons and Brace, 1965]. To assess the potential for fluid pressure in excess of P_b during the CCS scenario presented here at the Wallula Site, Equation 5.8 is solved for each grid cell representing the CO_2 injection zone.

At the reservoir scale, i.e., far-field from the CO_2 injection well, the potential for tensile failure is governed primarily by the regional stress field, microcrack geometry, intact rock properties, and pore fluid pressure [Engelder, 2014]. The tensile failure criterion for a poroelastic rock mass is the fluid pressure above which new joints can be formed, i.e., the joint initiation pressure (P_i):

$$P_i = \frac{K_{IC}}{Y\sqrt{c}} + \frac{\nu}{1-\nu}S_V + \frac{(1-2\nu)}{(1-\nu)}\alpha P_f \tag{5.11}$$

where, K_{IC} is the fracture toughness, Y is the crack-shape factor, and c is the crack half-length [Engelder, 2014]. In this formulation for joint initiation pressure, K_{IC} is used in place of uniaxial tensile strength because K_{IC} accounts for the shape and size of cracks, which, in combination with the crack-shape factor (Y), is more representative of the unfractured rock mass [Engelder, 2014]. Constraints on K_{IC} are provided in Degraff and Aydin [1993]. In applying the crack-shape factor Y, the two choices suggested by Sih [1973] are accounted for: $Y = \frac{2}{\sqrt{\pi}}$ for a penny-shaped initial crack, and $Y = \sqrt{\pi}$ for a blade-shaped initial crack.

Microcrack geometry in basalt rocks generally occurs along individual grain boundaries, so that microcrack length is limited by grain size, e.g., the average observable crack lengths in Icelandic basalt is ∼0.01 mm on the basis of SEM imaging [Kowallis et al., 1982]. To assess the potential for fluid pressure in excess of P_i during the CCS scenario considered here, Equation 5.11 is solved for each grid cell in the domain with a particular interest in the composite injection zone between 775 and 865 m below ground surface. Here, the P_f term in Equation 5.11 is replaced with mean simulated pore fluid pressure for selected time steps ($\bar{P}_{f(inj)}$), and the likelihood of <1% tensile failure is assessed by increasing $\bar{P}_{f(inj)}$ by three standard deviations.

5.3 Results and Discussion

This study implements ensemble simulation methods to test the feasibility of industrial-scale CCS in a flood basalt reservoir with characteristics of the Wallula Basalt Sequestration Pilot Project in southeast Washington State, USA. To account for highly uncertain and *a priori* unknowable permeability distributions beyond the well bore, the model scenario is simulated within 35 synthetic reservoirs comprising equally probable and spatially correlated permeability distributions. Ensemble analytics (e-type estimates) are used to bound the uncertainty of both injection-induced pressure transients and CO_2 saturation. These results are combined with threshold criteria for geomechanical reservoir performance in composite injection zone and overlying flow interiors (sealing units). The following section includes results and discussion for shear failure (Equations 5 - 6), fracture dilation (Equations 7), borehole breakout (Equations 8 - 10), and joint-initiation pressure (Equation 11).

5.3.1 Spatial Variability

The Columbia River Basalt Group exhibits highly heterogeneous and spatially correlated permeability, which imposes considerable influence on both CO_2 plume geometry and injection-induced fluid pressure accumulation. These effects are most pronounced within the uppermost portion of the composite injection zone, where the ensemble mean calculations (Equation 5.1) show that (i) free-phase CO_2 at 1% saturation extends radially ∼425 m from the injection well after 1 year and (ii) maximum injection pressure reaches ∼24.5 MPa (Figure 5.5). The temporal evolution of both fluid overpressure (Figure 5.5, red contour line) and 1% CO_2 saturation (Figure 5.5, black contour line) indicate that fluid pressure propagates much faster than CO_2 transport and in different spatial configurations. Within the first month of injection, the CO_2 has migrated 20 m, while the reservoir experiences increased fluid pressures up to 1,000 m away. Across the complete ensemble, the bulk pressure front radiates in an elliptical pattern (Figure 5.5). The long axis of this ellipse is oriented ∼N40°E, which is the direction of maximum spatial correlation for CRBG permeability [Jayne and Pollyea, 2018]. This indicates that the spatial correlated permeability is a first-order control over the ensemble mean pressure distribution within the model.

The different geometric configurations assumed by the injection-induced pressure front and the CO_2 plume are most likely explained by the different mechanisms governing saturated and unsaturated flow. For example, Pollyea and Fairley [2012] showed that relative permeability feedbacks exacerbate the influence of highly conductive flow paths because free-phase CO_2 will initially enter a high permeability flow path, and in doing so the non-wetting phase (CO_2) permeability increases thus increasing conductivity of the initial flow path and further increasing CO_2 mobility. In addition, Pollyea [2016] showed that fluid pressure propagation is largely controlled by wetting phase drainage, thus far-field pressure transients are governed by fully saturated permeability. As a consequence, CO_2 migration is concentrated in the

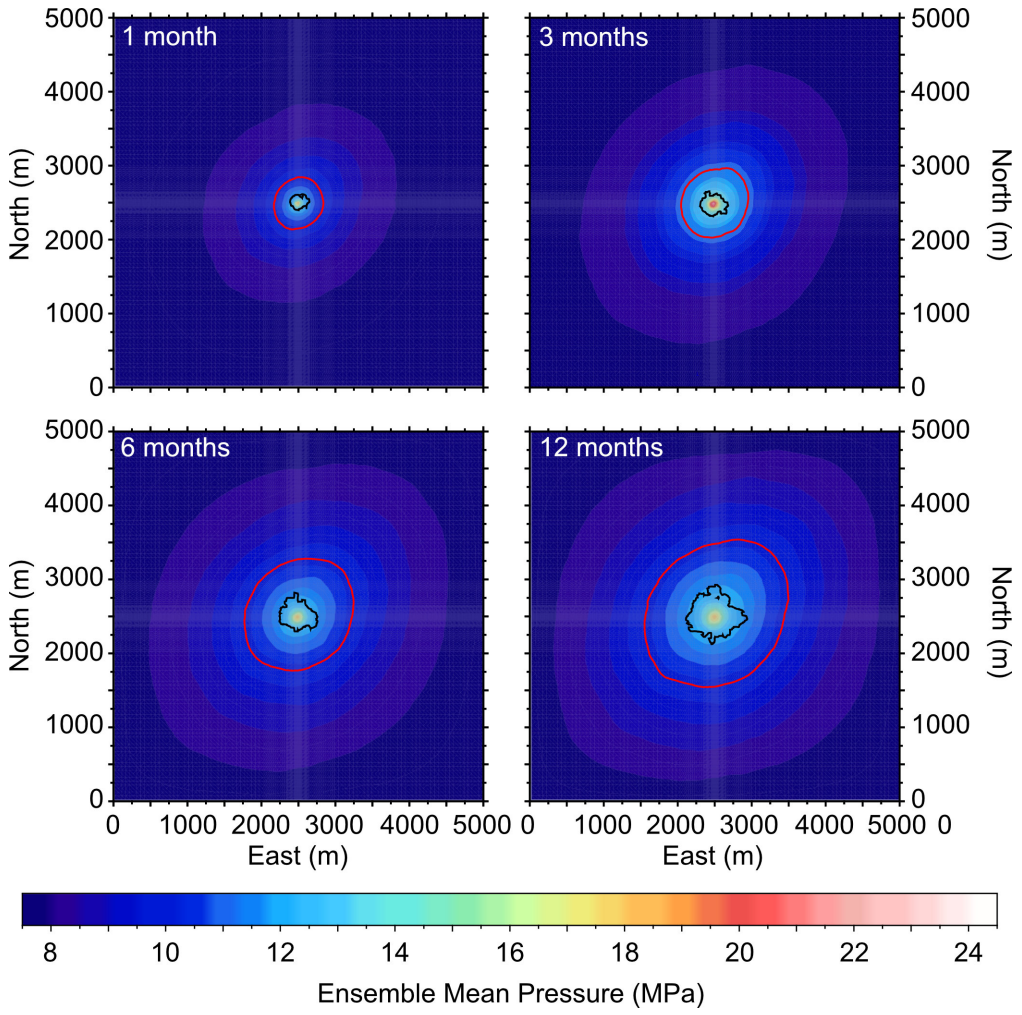

Figure 5.5: Ensemble mean fluid pressure evolution. Ensemble mean fluid pressure (N=35) (Equation 5.1) within the uppermost injection interval (775 - 780 m depth) at time steps ranging from 1 to 12 months. Black contour line denotes 0.01 (1%) CO_2 saturation. Area within red contour line denotes fluid pressure $\geq$2.5 MPa above pre-injection levels.

most conductive, near-field flow paths as non-wetting phase permeability increases, while far-field pressure diffusion is governed by the larger-scale bulk permeability architecture.

The uncertainty implied by the ensemble calculations is further reinforced in the context of individual realizations. For example, Figure 5.6 shows the change in pressure and free-phase CO_2 saturation for an individual simulation run after 1 year of injection. In this simulation run, fluid pressure propagates asymmetrically to the southeast across the full thickness of the disposal reservoir. In contrast, the CO_2 plume trends north-south at the top of the reservoir, while minimal CO_2 has accumulated deeper within the reservoir. This result shows that the combination of buoyancy forces [Wu et al., 2018b], relative permeability feedbacks [Pollyea and Fairley, 2012, Jayne et al., 2018], and reservoir heterogeneity [Pollyea et al., 2014] work in aggregate to control the CO_2 plume geometry. The overall implication of these results suggest that fluid pressure monitoring is unlikely to be an effective predictor of CO_2 plume geometry or breakthrough; however, recent research suggests that the thermal signature from CO_2 dissolution may be an effective tool for breakthrough monitoring [Jayne et al., 2019b].

5.3.2 Potential for Injection-Induced Shear Failure

Fluid pressure transients caused by industrial-scale CCS operations may drive effective stress below the stable stress envelope (Figure 5.7) inducing slip on optimally aligned faults or fractures. This consideration is particularly relevant for CCS in basalt formations because they are characterized by fanning columnar joints (Figure 5.2), of which a subset is likely to optimally align with the regional stress field. This is further complicated because the orientation of basalt fracture networks at depths of interest for CCS are *a priori* unknowable at spatial scales beyond the borehole(s). To arrive at a conservative (worst case) estimate of the potential for injection-induced shear failure, the Mohr-Coulomb failure criterion is

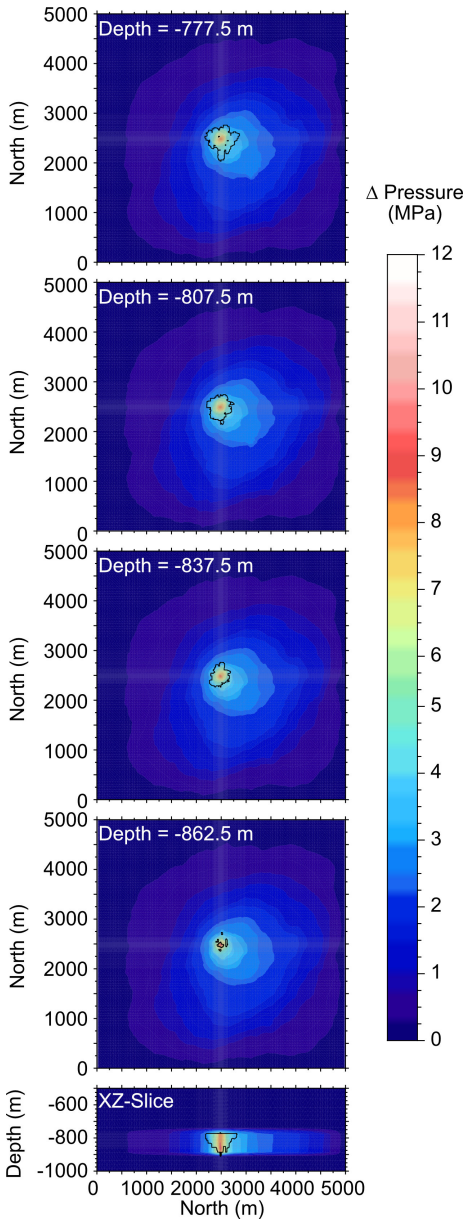

Figure 5.6: Single realization of fluid pressure after 1 year. Injection-induced fluid pressure change (ΔP_f) for a single realization after 10 years of injection. Top four panels are horizontal slices and the bottom panel is an xz-slice through the injection well. Black contour line denotes 1% free-phase CO_2 saturation.

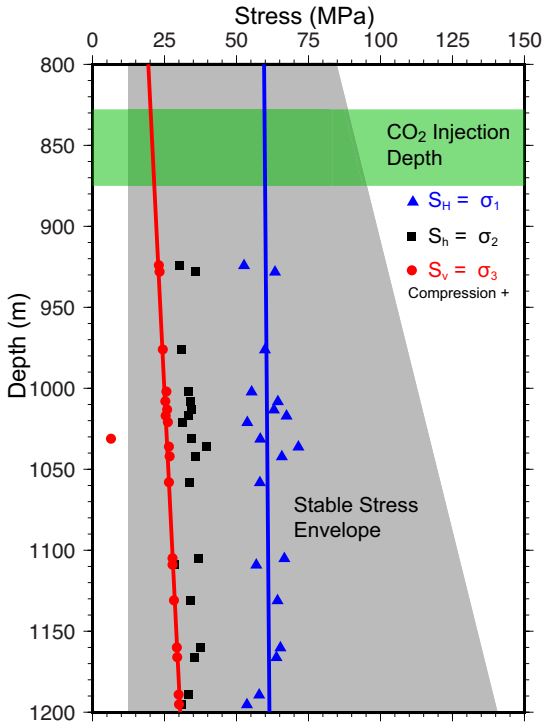

Figure 5.7: Regional stress state near the Wallula Basalt Sequestration Pilot Project. Regional stress state near the Wallula Basalt Sequestration Pilot Project. Maximum compressive horizontal stress (S_H), minimum compressive horizontal stress (S_h), and lithostatic stress (S_V) are *in situ* stress measurements at Hanford Nuclear Reservation, approximately 60 km northwest of the Wallula site. Gray Shading denotes a stable stress field on the basis of Mohr-Coloumb failure criteria. Green shading denotes the depth interval for CO_2 injection at the Wallula site. (Modified from Pollyea [2016])

evaluated at each grid cell in the model domain using Equation 5.4, but modified to account for effective stress. Within the model scenario considered here, shear failure is probable for any optimally oriented fractures within 2,000 m of the injection well after 1 year of injection (Figure 5.8, black contour) and the bounding entablature layer (Figure 5.9, black contour). The uncertainty about this result is calculated for three standard deviations variation about the mean (Figure 5.8 and 5.9, orange contour), which illustrates reservoir volume within which the probability of inducing shear failure in the target reservoir is greater than 1%.

These results suggest that a shear failure may occur on optimally-aligned fractures within a

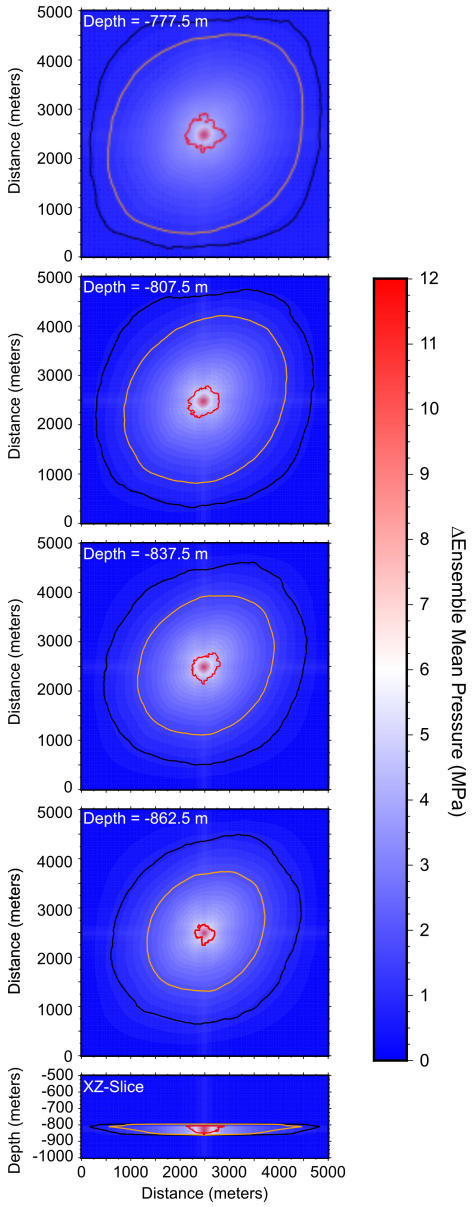

Figure 5.8: Potential for shear failure after 1 year of injection. Potential for shear failure after 1 year of injection in four horizontal slices through the composite injection zone (top four panels) and one vertical slice through the injection well (bottom panel). Each panel is colored by ensemble mean fluid pressure change ($\Delta\bar{P}_f$). Area within black contour exceeds Mohr-Coulomb failure criterion when minimum effective stress is calculated on the basis of ensemble mean fluid pressure. Area within orange contour comprises $\geq$1% probability of shear failure calculated by Eq. 5.6. Area within red contour line is $\geq$ 1% free-phase CO_2 saturation.

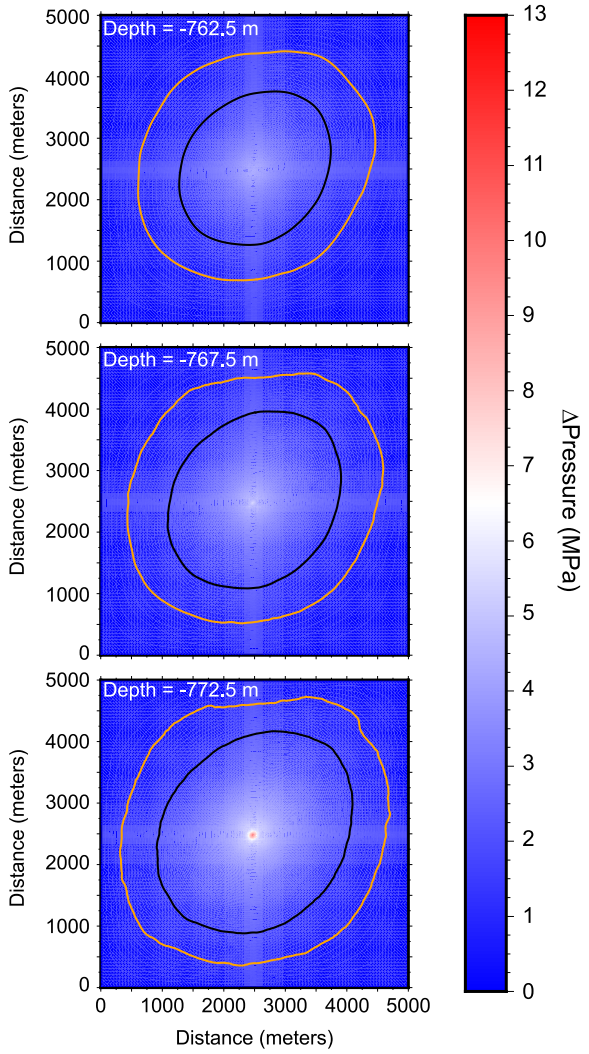

Figure 5.9: Caprock shear failure after 1 year of injection. Potential for shear failure after 1 year of injection in three horizontal slices through the entablature layer bounding the injection zone. Each panel is colored by ensemble mean fluid pressure change ($\Delta\bar{P}_f$). Area within black contour exceeds Mohr-Coulomb failure criterion when minimum effective stress is calculated on the basis of ensemble mean fluid pressure. Area within orange contour comprises $\geq$1% probability of shear failure calculated by Eq. 5.6.

substantial volume of the target reservoir. Because the CRBG is relatively aseismic, these results suggest that numerous cm-scale displacements are more likely to affect storage potential and seal efficacy than large-scale displacements that are known to trigger earthquakes during oilfield wastewater disposal [Pollyea et al., 2018]. The implications of numerous cm-scale displacements are that shear dilation may increase fracture permeability resulting in hydraulic pathways for the CO_2 to escape the disposal reservoir [Zoback and Gorelick, 2012]. The entablature layers shown in Figure 5.9 represents the caprock seal separating the current injection zone from another high permeability zone above it ($\sim$750 m depth - Figure 5.2). This suggests that shear failure may occur optimally aligned fractures within a substantial volume of the caprock, which may facilitate leakage out of the storage reservoir. However, the CO_2 sequestration in basalt reservoirs is predicated on rapid conversion of CO_2 into permanent mineral phases, the result of which decreases permeability as fractures are filled with secondary alteration products [Wu et al., 2018a]. As a result, basalt fracture networks may exhibit self-sealing characteristics, which would offset the adverse effects of permeability enhancement caused by cm-scale displacements on optimally-oriented fractures. However, further research is clearly warranted to gain a more complete understanding of the complex feedbacks between hydraulic, chemical, and mechanical processes.

5.3.3 Fracture Dilation in Overlying Flow Interior

During industrial-scale CO_2 injections, pressure transients may propagate beyond the disposal reservoir into the overlying flow interior that serves as a caprock seal prior to widespread mineralization. Although basalt flow interiors are characterized by substantially lower permeability (up to 7 orders of magnitude) than the injection interval, this pressure propagation may dilate pre-existing fractures leading to reservoir leakage. To quantify the potential for fracture dilation to affect the flow interior overlying the composite injection zone in this

study, the probability of 1% fracture dilation is calculated for three standard deviations above the ensemble mean fluid pressure (Equation 5.7). Figure 5.10 presents the results of this calculation in comparison with the ensemble mean fluid pressure change ($\Delta\bar{P}_f$) after 1, 3, 6, and 12 months of injection. These results show that the probability of fracture dilation exceeds 1% within ∼1,000 m radial distance of the injection well after 1 year.

These results are congruent with a number of studies that show pressure transients induced by CO_2 injection operations affect a much larger reservoir volume than the fluid itself [Van der Meer, 1992, Holloway, 1996, Gunter et al., 1996]. This is apparent in Figure 5.6, which shows that the injected CO_2 migrates a maximum of 400 m, while the target reservoir experiences pressure changes up to 2,200 m away from the injection well. Similarly, Birkholzer et al. [2009] shows that after a 30 year CO_2 injection from a single well a pressure increase of 100 kPa extends almost 85 km laterally, while the CO_2 only migrates ∼2 km. In the context of vertical CO_2 flow, the simulation results presented here show that no free-phase CO_2 enters the overlying flow interior; however, this may be an artifact of the static permeability approach, i.e., permeability in the model does not vary with changes in effective stress. Nevertheless, this result agrees with the outcrop-scale study by Gierzynski and Pollyea [2017], which shows that free-phase CO_2 only migrates upwards ∼3 m over 10 years when entering from below at constant overpressure. These authors show that relative permeability causes free-phase CO_2 to accumulate at fracture intersections, thus slowing the leakage rate. Similarly, Jayne et al. [2019a] simulates CO_2 injections into a flood basalt reservoir at constant pressure and shows that free-phase CO_2 only migrates 25 m into the entablature after 20-years CO_2 injection. Although these former results are generally encouraging, aditional advances in stress-dependent permeability are needed to more fully understand this process.

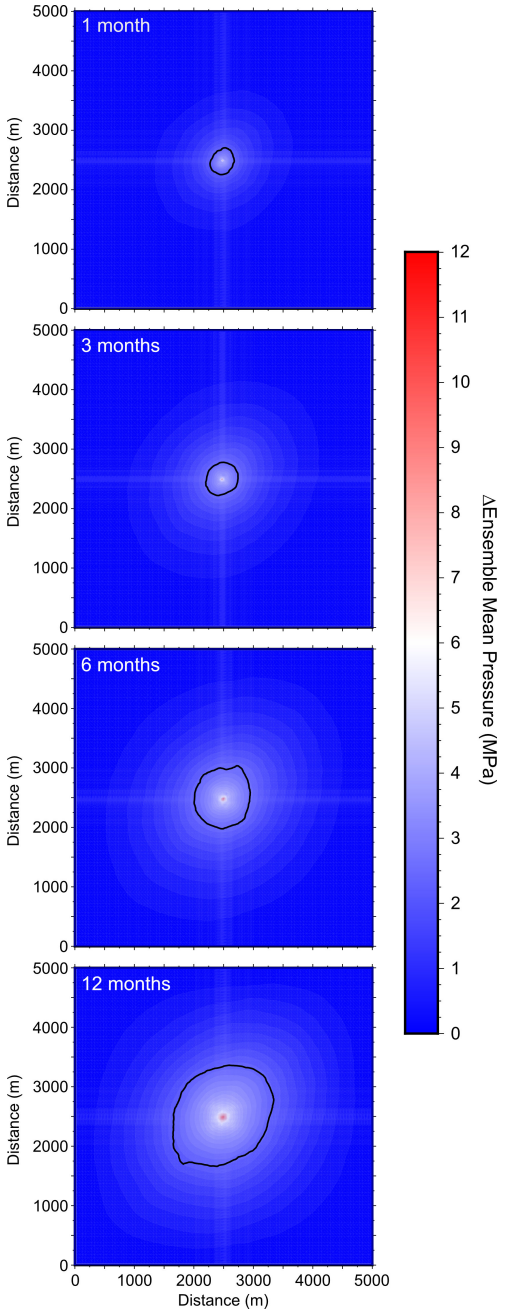

Figure 5.10: Potential for fracture dilation within the basalt flow interior. Potential for fracture dilation the basalt flow interior that overlies the composite injection zone (770 - 775 m depth) after 1, 3, 6, and 12 months. Each panel is colored by ensemble mean fluid pressure change ($\Delta\bar{P}_f$. Area inside black contour lines denotes $\geq$1% probability that preexisting fractures will experience dilation.

5.3.4 Borehole Breakdown

The time series of injection pressure is shown in Figure 5.11 for each of the 35 simulations. Because the model scenario delivers CO_2 at a constant mass flow rate, variations of fluid pressure are due solely to the spatially variable and equally probable permeability distributions. Results show that maximum injection pressure ranges from ∼14.5 – 34 MPa (hydrostatic pressure = 8.5 MPa), which results in 50% of the simulations exceeding the borehole breakdown threshold of 23.7 MPa (Equation 5.8) . For simulations exceeding the breakdown criterion (Figure 5.11, red lines), fluid pressure rapidly increases and the threshold is exceeded within one day of injection. However, injection pressure in several simulations remains below the breakdown threshold for several months before exceeding the breakdown threshold. Research by Pollyea [2016] shows the pressure accumulation during CO_2 injections is controlled primarily by wetting-phase relative permeability. Because the relative permeability characteristics of basalt reservoirs are highly interfering [Bertels et al., 2001], a small increase in CO_2 saturation results in a large drop in wetting-phase permeability. As a result, injection pressure accumulation is strongly influenced by the interconnectedness of high permeability flow paths away from the borehole [Pollyea and Fairley, 2012]. And while it is unlikely that an industrial-scale CCS project will operate at constant mass flow rates for 12 months, the broader implication is of these results is that permeability variability in the near field strong influences overall reservoir injectivity.

5.3.5 Joint Initiation

In basalt reservoirs, the initiation and propagation of new fractures presents an operational paradox that remains unresolved. Specifically, fracture initiation and propagation may facilitate reservoir leakage before widespread mineralization can isolate the CO_2. However,

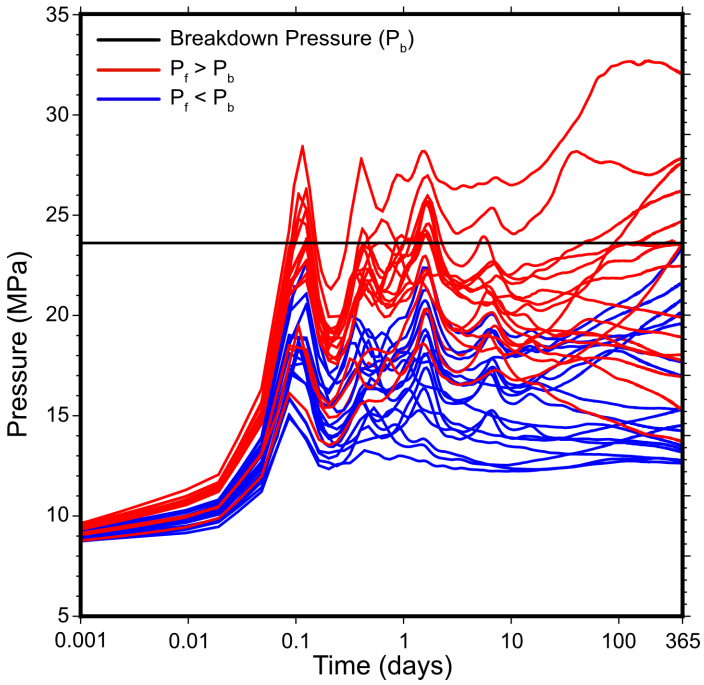

Figure 5.11: Time series of injection pressure for each simulation. Time series of injection pressure for each simulation in the ensemble. The black line indicates the pressure above which borehole break will occur (P_b). Red lines denote simulation results that exceed breakdown pressure within the 1 year injection period. Blue lines denote simulation results that remain below breakdown pressure for the injection period. Half (50%) of the simulations exceed P_b.

new fractures also provide fresh surface area, which increases the mineral storage potential of the reservoir. Although this study does not purport to answer this underlying research question, we begin to understand its scope by constraining the spatial extent for which the probability of new joint initiation is ≥1%. Figure 5.12 presents the volume within which the probability of joint initiation is ≥1% after 1, 3, 6, and 12 months (Equation 5.11). These results show that the probability of joint initiation ≥1% occurs within ∼75 m from the well after 3 months, and increases to 125 m after 1 year. This indicates that joint initiation primarily occurs within areas of the reservoir occupied by free-phase CO_2, and, as a result, joint initiation will increase leakage potential. This result contrasts with the spatial extent of shear failure ≥1% (Figure 5.8), which encompasses a much larger footprint than the CO_2 plume. For example, probability of joint initiation ≥1% is likely to occur within 125 m of the injection well after 1 year; whereas, the corresponding probability of shear failure extends beyond 2,300 m away from the injection well.

Joint initiation is the process of generating tensile fractures, which open in the direction of the least compressive principle stress, and then propagate in the plane of the intermediate and greatest compressive principle stresses. Because the Columbia River Plateau is in a compressive stress regime (σ_3 is vertical), new fractures will open in the vertical direction and propagate horizontally. Although this is a favorable scenario for CO_2 storage, basalt formations are characterized by columnar (vertical) joints, and, as a result, joint initiation is likely to increase the connectivity of fracture networks. This may be a positive outcome in the context of overall reservoir injectivity because this study finds that borehole breakdown is largely controlled by the interconnected fracture networks within close proximity to the borehole, where the probability of joint initiation is highest.

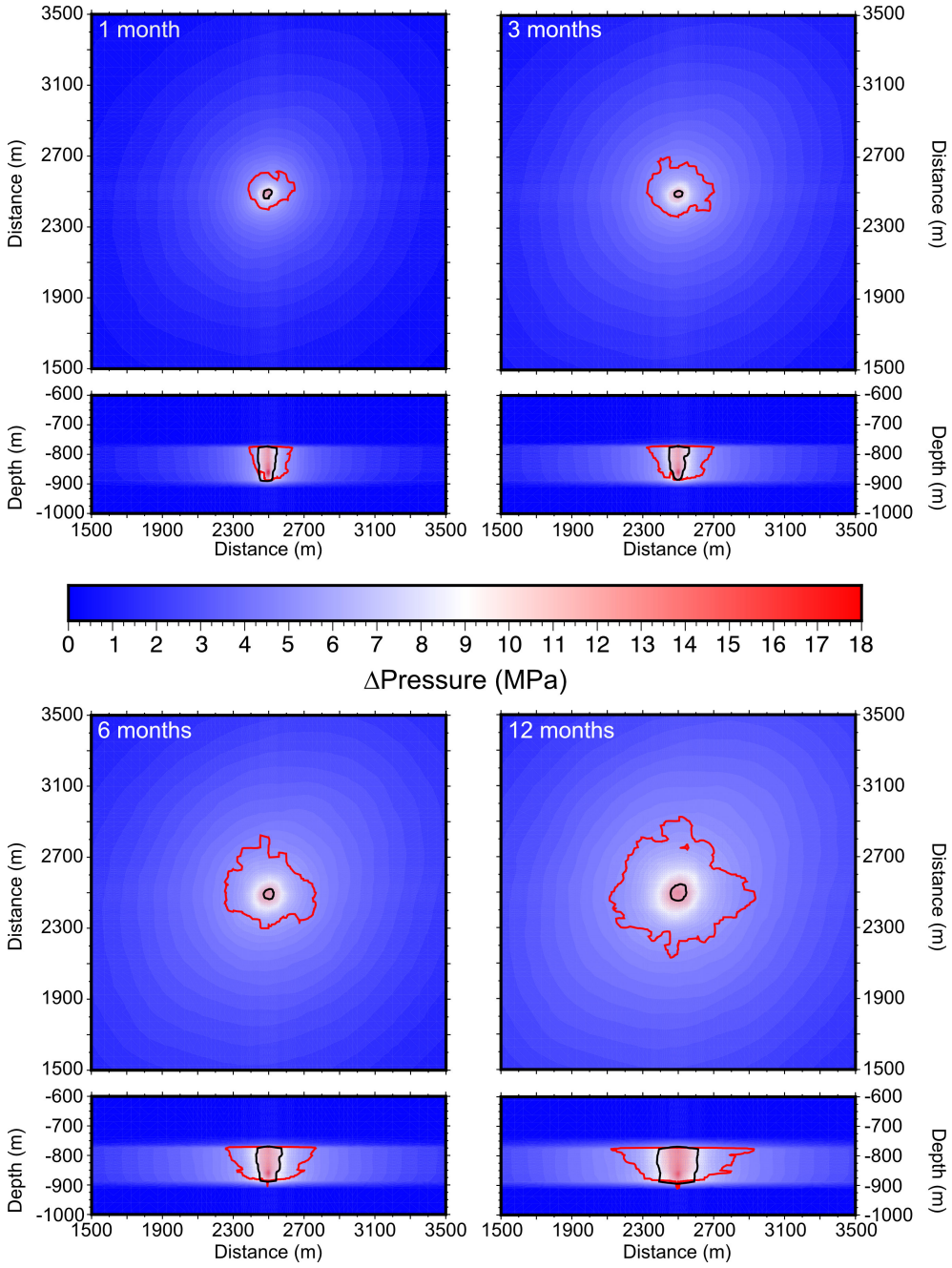

Figure 5.12: Time-series for the potential for joint initiation. Potential for joint initiation within the uppermost layer of the composite injection zone (775 - 780 m depth) after 1, 3, 6, and 12 months of injection. Each panel is a horizontal and vertical slice and note time. Shading denotes ensemble mean fluid pressure ($\Delta\bar{P}_f$). Area within black contours denotes $\geq$1% probability of joint initiation. Red contours represent 1% CO_2 saturation.

5.4 Conclusions

Flood basalts have been gaining recognition as potential reservoirs for carbon capture and sequestration. The success of recent field experiments in Washington State, USA, and Iceland show that injected CO_2 will interact with the basalt to form carbonate minerals at the field-scale and very short timescales. However, upscaling these field-scale experiments to industrial-scale CO_2 injections is required if CCS is going to be an effective strategy to mitigate climate change. Transitioning basalt CCS from the pilot-scale to industrial scales introduces a number of uncertainties, including feedbacks between multi-phase flow processes and fracture-controlled reservoir properties, incomplete knowledge of reservoir characteristics, and coupled dynamics between hydraulic, thermal, mechanical, and geochemical processes. This study is an important first step towards understanding the relationships between multi-phase fluid flow processes, spatial reservoir uncertainty, and reservoir geomechanics. We implement ensemble simulation and analytics to bound the uncertainty associated with industrial-scale CO_2 injection into a flood basalt reservoir. For a single CO_2 injection well operating at a constant mass injection of 21.6 kg/s, we find:

1. The aggregate behavior over the ensemble of simulations shows that fluid pressure forms roughly an ellipse around the injection well trending N40°E, which suggests that the permeability correlation structure exhibits control on the pressure evolution within the target reservoir.

2. Joint initiation mainly occurs around or within the CO_2 plume during the injection phase. Joint initiation within the injection may increase permeability leading to better injectivity and storage, but if these joints coalesce into a larger fracture network it may compromise the integrity of the reservoir.

3. Fluid pressure builds rapidly during a CO_2 injection causing the storage reservoir to

experience increased fluid pressures up to 1,000 m away within the first month and 2,200 m away during the first year.

4. Results from this study suggest that implementing multiple injection wells to accommodate the annual CO_2 emission from a 500 MW power plant may be an effective strategy to mitigate the potential for geomechanical reservoir failure. The effects of multiple wells may effectively offset the uncertainty that is presented by highly heterogeneous permeability fields in the mid- to far-field regions.

5. Combining ensemble simulation with geomechanical threshold criteria is an effective method for risk analysis associated with a CCS project.

In conclusion, these results suggest that the implementation of a regional-data set and spatial correlation structures into a numerical model can provide insights into the behavior of fluid pressure within heterogeneous reservoirs. Additionally, these results illustrate the uncertainty associated with highly-heterogeneous flood basalt reservoirs and a CCS project would require extensive reservoir characterization for a geomechanical risk assessment. Significantly more research is required to develop a better understanding of the reactive transport, thermal processes, fracture behavior and response associated with an industrial-scale CO_2 injection into a flood basalt reservoir.

Bibliography

LH Adams and RE Gibson. The compressibilities of dunite and of basalt glass and their bearing on the composition of the earth. *Proceedings of the National Academy of Sciences*, 12(5):275–283, 1926.

Todd R Anderson and Jerry P Fairley. Relating permeability to the structural setting of a fault-controlled hydrothermal system in southeast Oregon, USA. *Journal of Geophysical Research: Solid Earth*, 113(B5), 2008.

Laurent André, Mohamed Azaroual, and André Menjoz. Numerical simulations of the thermal impact of supercritical CO_2 injection on chemical reactivity in a carbonate saline reservoir. *Transport in porous media*, 82(1):247–274, 2010.

Stefan Bachu. Analysis of heat transfer processes and geothermal pattern in the alberta basin, canada. *Journal of Geophysical Research: Solid Earth*, 93(B7):7767–7781, 1988.

Stefan Bachu. Sequestration of CO_2 in geological media: criteria and approach for site selection in response to climate change. *Energy conversion and Management*, 41(9):953–970, 2000.

Stefan Bachu. Screening and ranking of sedimentary basins for sequestration of CO_2 in geological media in response to climate change. *Environmental Geology*, 44(3):277–289, 2003.

Stefan Bachu. CO_2 storage in geological media: role, means, status and barriers to deployment. *Progress in Energy and Combustion Science*, 34(2):254–273, 2008.

Diana H Bacon, Ramya Ramanathan, H Todd Schaef, and B Peter McGrail. Simulating geologic co-sequestration of carbon dioxide and hydrogen sulfide in a basalt formation. *International Journal of Greenhouse Gas Control*, 21:165–176, 2014.

Satish Balay, Shrirang Abhyankar, Mark F. Adams, Jed Brown, Peter Brune, Kris Buschelman, Lisandro Dalcin, Alp Dener, Victor Eijkhout, William D. Gropp, Dinesh Kaushik, Matthew G. Knepley, Dave A. May, Lois Curfman McInnes, Richard Tran Mills, Todd Munson, Karl Rupp, Patrick Sanan, Barry F. Smith, Stefano Zampini, Hong Zhang, and Hong Zhang. PETSc users manual. Technical Report ANL-95/11 - Revision 3.10, Argonne National Laboratory, 2018. URL http://www.mcs.anl.gov/petsc.

Thibaut Barreyre, Jean-Arthur Olive, Timothy J Crone, and Robert A Sohn. Depth-dependent permeability and heat output at basalt-hosted hydrothermal systems across mid-ocean ridge spreading rates. *Geochemistry, Geophysics, Geosystems*, 19(4):1259–1281, 2018.

Sally M Benson et al. Monitoring carbon dioxide sequestration in deep geological formations for inventory verification and carbon credits. In *SPE Annual Technical Conference and Exhibition*. Society of Petroleum Engineers, 2006.

Stephanie P. Bertels, David A. DiCarlo, and Martin J. Blunt. Measurement of aperture distribution, capillary pressure, relative permeability, and in situ saturation in a rock fracture using computed tmomgraphy scanning. *Water Resources Research*, 37:649–662, March 2001. Paper Number: 2000WRR900316.

Todd Anthony Bianco, Garrett Ito, Janet M Becker, and Michael O Garcia. Secondary hawaiian volcanism formed by flexural arch decompression. *Geochemistry, Geophysics, Geosystems*, 6(8), 2005.

Jens T Birkholzer, Quanlin Zhou, and Chin-Fu Tsang. Large-scale impact of CO_2 storage in deep saline aquifers: A sensitivity study on pressure response in stratified systems. *International Journal of Greenhouse Gas Control*, 3(2):181–194, 2009.

Gunnar Bodvarsson. On the temperature of water flowing through fractures. *Journal of Geophysical Research*, 74(8):1987–1992, 1969.

Nicholas W Bosshart, Nicholas A Azzolina, Scott C Ayash, Wesley D Peck, Charles D Gorecki, Jun Ge, Tao Jiang, and Neil W Dotzenrod. Quantifying the effects of depositional environment on deep saline formation CO_2 storage efficiency and rate. *International Journal of Greenhouse Gas Control*, 69:8–19, 2018.

GS Boulton and P Caban. Groundwater flow beneath ice sheets: Part ii—its impact on glacier tectonic structures and moraine formation. *Quaternary Science Reviews*, 14(6): 563–587, 1995.

Sean T Brennan and Robert Carlton Burruss. *Specific sequestration volumes: A useful tool for CO_2 storage capacity assessment.* US Department of the Interior, US Geological Survey, 2003.

Erick R Burns, David S Morgan, Rachael S Peavler, and Sue C Kahle. Three-dimensional model of the geologic framework for the Columbia Plateau Regional Aquifer System, Idaho, Oregon, and Washington. Technical report, US Geological Survey, 2011.

Erick R Burns, Colin F Williams, Steven E Ingebritsen, Clifford I Voss, Frank A Spane, and Jacob DeAngelo. Understanding heat and groundwater flow through continental flood basalt provinces: insights gained from alternative models of permeability/depth relationships for the Columbia Plateau, USA. *Geofluids*, 15(1-2):120–138, 2015.

Erick R Burns, Colin F Williams, Terry Tolan, and J Ole Kaven. Are the Columbia River

Basalts, Columbia Plateau, Idaho, Oregon, and Washington, USA, a Viable Geothermal Target? A Preliminary Analysis. *PROCEEDINGS, 41st Workshop on Geothermal Reservoir Engineering*, 2016.

McMillan Burton, Navanit Kumar, and Steven L Bryant. CO_2 injectivity into brine aquifers: Why relative permeability matters as much as absolute permeability. *Energy Procedia*, 1 (1):3091–3098, 2009.

James Byerlee. Friction of rocks. In *Rock friction and earthquake prediction*, pages 615–626. Springer, 1978.

Frédéric Cappa and Jonny Rutqvist. Impact of CO_2 geological sequestration on the nucleation of earthquakes. *Geophysical Research Letters*, 38(17), 2011.

John J Carroll, John D Slupsky, and Alan E Mather. The solubility of carbon dioxide in water at low pressure. *Journal of Physical and Chemical Reference Data*, 20(6):1201–1209, 1991.

Andy Chadwick, Rob Arts, Christian Bernstone, Franz May, Sylvain Thibeau, and Peter Zweigel. *Best Practice for the Storage of CO_2 in Saline Aquifers-Observations and Guidelines from the SACS and CO_2STORE projects*, volume 14. British Geological Survey, 2008.

Chun Chang, Quanlin Zhou, Timothy J Kneafsey, Mart Oostrom, Thomas W Wietsma, and Qingchun Yu. Pore-scale supercritical CO_2 dissolution and mass transfer under imbibition conditions. *Advances in water resources*, 92:142–158, 2016.

David A Clague and G Brent Dalrymple. The hawaiian-emperor volcanic chain. part i. geologic evolution. *Volcanism in Hawaii*, 1:5–54, 1987.

Stephen M Clifford and Timothy J Parker. The evolution of the martian hydrosphere: Implications for the fate of a primordial ocean and the current state of the northern plains. *Icarus*, 154(1):40–79, 2001.

Millard F Coffin and Olav Eldholm. Large igneous provinces: crustal structure, dimensions, and external consequences. *Reviews of Geophysics*, 32(1):1–36, 1994.

Brewster Conant Jr. Delineating and quantifying ground water discharge zones using streambed temperatures. *Groundwater*, 42(2):243–257, 2004.

James M Degraff and Atilla Aydin. Effect of thermal regime on growth increment and spacing of contraction joints in basaltic lava. *Journal of Geophysical Research: Solid Earth*, 98 (B4):6411–6430, 1993.

Al J Desbarats and S Bachu. Geostatistical analysis of aquifer heterogeneity from the core scale to the basin scale: A case study. *Water Resources Research*, 30(3):673–684, 1994.

Clayton V. Deutsch. *Geostatistical Reservoir Modeling*. Oxford University Press, New York, 2002.

Clayton V Deutsch and Andre G Journel. *GSLIB: Geostatistical software library and user's guide*. Oxford University Press New York, 1998.

Christine Doughty. Investigation of CO_2 plume behavior for a large-scale pilot test of geologic carbon storage in a saline formation. *Transport in porous media*, 82(1):49–76, 2010.

Christine Doughty and Karsten Pruess. Modeling supercritical carbon dioxide injection in heterogeneous porous media. *Vadose Zone Journal*, 3(3):837–847, 2004.

Thomas Engel and Philip J Reid. *Thermodynamics, statistical thermodynamics, and kinetics*. Prentice Hall Upper Saddle River, NJ, USA, 2010.

Terry Engelder. *Stress regimes in the lithosphere*, volume 151. Princeton University Press, 2014.

Grant Garven. Continental-scale groundwater flow and geologic processes. *Annual Review of Earth and Planetary Sciences*, 23(1):89–117, 1995.

RE Gephart, SM Price, RL Jackson, and CW Myers. Geohydrologic Factors and Current Concepts Relevant to Characterization of a Potential Nuclear Waste Repository Site in Columbia River Basalt, Hanford Stte, Washington. In *MRS Proceedings*, volume 26, page 85. Cambridge Univ Press, 1983.

Alec O Gierzynski and Ryan M Pollyea. Three-Phase CO_2 Flow in a Basalt Fracture Network. *Water Resources Research*, 53(11):8980–8998, 2017.

Tom Gleeson, Leslie Smith, Nils Moosdorf, Jens Hartmann, Hans H Dürr, Andrew H Manning, Ludovicus PH van Beek, and A Mark Jellinek. Mapping permeability over the surface of the earth. *Geophysical Research Letters*, 38(2), 2011.

Lucas Goehring and Stephen W Morris. Scaling of columnar joints in basalt. *Journal of geophysical research: Solid Earth*, 113(B10), 2008.

David S Goldberg, Taro Takahashi, and Angela L Slagle. Carbon dioxide sequestration in deep-sea basalt. *Proceedings of the National Academy of Sciences*, 105(29):9920–9925, 2008.

David S Goldberg, Dennis V Kent, and Paul E Olsen. Potential on-shore and off-shore reservoirs for CO_2 sequestration in Central Atlantic magmatic province basalts. *Proceedings of the National Academy of Sciences*, 107(4):1327–1332, 2010.

Somayeh Goodarzi, Antonin Settari, Mark Zoback, and David Keith. A coupled geomechan-

ical reservoir simulation analysis of carbon dioxide storage in a saline aquifer in the Ohio River Valley. *Environmental Geosciences*, 18(3):189–207, 2011.

M Gran, C Zahasky, C Garing, RM Pollyea, and SM Benson. Core-flooding experiments combined with X-rays and micro-PET imaging as a tool to calculate fluid saturations in a fracture. Fall Meeting of the American Geophysical Union, December 2017. Abstract H21C-1466.

WD Gunter, Stefan Bachu, DH-S Law, Vinod Marwaha, DL Drysdale, DE MacDonald, and TJ McCann. Technical and economic feasibility of CO_2 disposal in aquifers within the Alberta Sedimentary Basin, Canada. *Energy Conversion and Management*, 37(6-8): 1135–1142, 1996.

Tristin C Hales, David L Abt, ED Humphreys, and Joshua J Roering. A lithospheric instability origin for Columbia River flood basalts and Wallowa Mountains uplift in northeast Oregon. *Nature*, 438(7069):842, 2005.

Weon Shik Han, Greg A Stillman, Meng Lu, Chuan Lu, Brian J McPherson, and Eungyu Park. Evaluation of potential nonisothermal processes and heat transport during CO_2 sequestration. *Journal of Geophysical Research: Solid Earth*, 115(B7), 2010.

Weon Shik Han, Kue-Young Kim, Eungyu Park, Brian J McPherson, Si-Yong Lee, and Myong-Ho Park. Modeling of spatiotemporal thermal response to CO_2 injection in saline formations: interpretation for monitoring. *Transport in porous media*, 93(3):381–399, 2012.

Charles Haukwa. AMESH A mesh creating program for the integral finite difference method: A User's Manual. *Lawrence Berkeley National Laboratory*, 1998.

David G Hawkins. No exit: thinking about leakage from geologic carbon storage sites. *Energy*, 29(9):1571–1578, 2004.

James Heffner and Jerry Fairley. Using surface characteristics to infer the permeability structure of an active fault zone. *Sedimentary Geology*, 184(3-4):255–265, 2006.

Gabriele C Hegerl, Francis W Zwiers, Pascale Braconnot, Nathan P Gillett, Yong Luo, JA Marengo Orsini, Neville Nicholls, Joyce E Penner, and Peter A Stott. Understanding and attributing climate change. 2007.

Christoph F Hieronymus and David Bercovici. Discrete alternating hotspot islands formed by interaction of magma transport and lithospheric flexure. *Nature*, 397(6720):604, 1999.

Sam Holloway. An overview of the Joule II project the underground disposal of carbon dioxide. In *Fuel and Energy Abstracts*, volume 4, page 306, 1996.

Peter R Hooper and RM Conrey. A model for the tectonic setting of the Columbia River basalt eruptions. *Geological Society of America Special Papers*, 239:293–306, 1989.

Suzanne Hurter, Andrew Alf Garnett, Andreas Bielinski, Andreas Kopp, et al. Thermal signature of free-phase CO_2 in porous rocks: detectability of CO_2 by temperature logging. In *Offshore Europe*. Society of Petroleum Engineers, 2007.

SE Ingebritsen and Craig E Manning. Geological implications of a permeability-depth curve for the continental crust. *Geology*, 27(12):1107–1110, 1999.

Everett D Jackson and Thomas L Wright. Xenoliths in the honolulu volcanic series, hawaii. *Journal of Petrology*, 11(2):405–433, 1970.

John Conrad Jaeger, Neville GW Cook, and Robert Zimmerman. *Fundamentals of rock mechanics*. John Wiley & Sons, 2009.

Richard S Jayne and Ryan M Pollyea. Permeability correlation structure of the columbia river plateau and implications for fluid system architecture in continental large igneous provinces. *Geology*, 46(8):715–718, 2018.

Richard S Jayne, Hao Wu, and Ryan M Pollyea. Geologic CO_2 sequestration and permeability uncertainty in a highly heterogeneous reservoir. *International Journal of Greenhouse Gas Control*, 83:128–139, 2019a.

Richard S Jayne, Yingqi Zhang, and Ryan M Pollyea. Using heat as a predictor of CO_2 breakthrough in highly heterogeneous reservoirs. *Geophysical Research Letters*, 2019b.

RS Jayne, W Hao, and RM Pollyea. Geologic CO_2 sequestration in a basalt reservoir: Constraining permeability uncertainty within the Columbia River Basalt Group. In *TOUGH Symposium*, 2018.

Xiao-Wei Jiang, Li Wan, Xu-Sheng Wang, Si-Hai Liang, and Bill X Hu. Estimation of fracture normal stiffness using a transmissivity-depth correlation. *International Journal of Rock Mechanics and Mining Sciences*, 46(1):51–58, 2009.

Paul Johnston, Patrick Wu, and Kurt Lambeck. Dependence of horizontal stress magnitude on load dimension in glacial rebound models. *Geophysical Journal International*, 132(1): 41–60, 1998.

Yoojin Jung, George Shu Heng Pau, Stefan Finsterle, and Ryan M Pollyea. TOUGH3: A new efficient version of the TOUGH suite of multiphase flow and transport simulators. *Computers & Geosciences*, 108:2–7, 2017.

SC Kahle, DS Morgan, WB Welch, DM Ely, SR Hinkle, JJ Vaccaro, and LL Orzol. Hydrogeologic framework and hydrologic budget components of the Columbia Plateau Regional Aquifer System, Washington, Oregon, and Idaho. Technical report, US Geological Survey, 2011.

Derrill M Kerrick and Ken Caldeira. Metamorphic CO_2 degassing from orogenic belts. *Chemical Geology*, 145(3-4):213–232, 1998.

Allen Dupree King Jr and CR Coan. Solubility of water in compressed carbon dioxide, nitrous oxide, and ethane. evidence for hydration of carbon dioxide and nitrous oxide in the gas phase. *Journal of the American Chemical Society*, 93(8):1857–1862, 1971.

Diana Koschel, Jean-Yves Coxam, Laurence Rodier, and Vladimir Majer. Enthalpy and solubility data of CO_2 in water and NaCl (aq) at conditions of interest for geological sequestration. *Fluid phase equilibria*, 247(1-2):107–120, 2006.

Bart J Kowallis, Evelyn A Roeloffs, and Herbert F Wang. Microcrack studies of basalts from the Iceland Research Drilling Project. *Journal of Geophysical Research: Solid Earth*, 87 (B8):6650–6656, 1982.

Klaus S Lackner. A guide to CO_2 sequestration. *Science*, 300(5626):1677–1678, 2003.

David Robert Lee. Method for locating sediment anomalies in lakebeds that can be caused by groundwater flow. *Journal of Hydrology*, 79(1-2):187–193, 1985.

Yusong Li, Eugene J LeBoeuf, Prodyot K Basu, and Sankaran Mahadevan. Stochastic modeling of the permeability of randomly generated porous media. *Advances in Water Resources*, 28(8):835–844, 2005.

John T Litynski, Scott M Klara, Howard G McIlvried, and Rameshwar D Srivastava. The United States Department of Energy's regional carbon sequestration partnerships program: a collaborative approach to carbon management. *Environment international*, 32 (1):128–144, 2006.

Philip E Long and Bernard J Wood. Structures, textures, and cooling histories of Columbia River basalt flows. *Geological Society of America Bulletin*, 97(9):1144–1155, 1986.

Amie Lucier, Mark Zoback, Neeraj Gupta, and TS Ramakrishnan. Geomechanical aspects of

CO_2 sequestration in a deep saline reservoir in the Ohio River Valley region. *Environmental Geosciences*, 13(2):85–103, 2006.

Michael Manga. Using springs to study groundwater flow and active geologic processes. *Annual Review of Earth and Planetary Sciences*, 29(1):201–228, 2001.

Margaret T Mangan, Thomas L Wright, Donald A Swanson, and Gary R Byerly. Regional correlation of Grande Ronde Basalt flows, Columbia River Basalt Group, Washington, Oregon, and Idaho. *Geological Society of America Bulletin*, 97(11):1300–1318, 1986.

CE Manning and SE Ingebritsen. Permeability of the continental crust: Implications of geothermal data and metamorphic systems. *Reviews of Geophysics*, 37(1):127–150, 1999.

Simon A Mathias, Jon G Gluyas, Gerardo J González Martínez de Miguel, and Seyyed A Hosseini. Role of partial miscibility on pressure buildup due to constant rate injection of CO_2 into closed and open brine aquifers. *Water Resources Research*, 47(12), 2011.

Simon A Mathias, Jon G Gluyas, Gerardo J González Martínez de Miguel, Steven L Bryant, and David Wilson. On relative permeability data uncertainty and CO_2 injectivity estimation for brine aquifers. *International Journal of Greenhouse Gas Control*, 12:200–212, 2013.

Allan Mathieson, John Midgley, Kevin Dodds, Iain Wright, Philip Ringrose, and Nabil Saoul. CO_2 sequestration monitoring and verification technologies applied at Krechba, Algeria. *The Leading Edge*, 29(2):216–222, 2010.

Juerg M Matter and Peter B Kelemen. Permanent storage of carbon dioxide in geological reservoirs by mineral carbonation. *Nature Geoscience*, 2(12):837–841, 2009.

Juerg M Matter, Taro Takahashi, and David Goldberg. Experimental evaluation of in situ

CO_2-water-rock reactions during CO_2 injection in basaltic rocks: Implications for geological CO_2 sequestration. *Geochemistry, Geophysics, Geosystems*, 8(2), 2007.

Juerg M Matter, Martin Stute, Sandra Ó Snæbjörnsdottir, Eric H Oelkers, Sigurdur R Gislason, Edda S Aradottir, Bergur Sigfusson, Ingvi Gunnarsson, Holmfridur Sigurdardottir, Einar Gunnlaugsson, et al. Rapid carbon mineralization for permanent disposal of anthropogenic carbon dioxide emissions. *Science*, 352(6291):1312–1314, 2016.

B McGrail, E Sullivan, F Spane, D Bacon, G Hund, P Thorne, C Thompson, S Reidel, and F Colwell. Topical Report–Preliminary Hydrogeologic Characterization Results from the Wallula Basalt Pilot Study. Tech. rep. Technical report, Pacific Northwest National Laboratory, 2009. Report PNWD-4129.

B Peter McGrail, H Todd Schaef, Anita M Ho, Yi-Ju Chien, James J Dooley, and Casie L Davidson. Potential for carbon dioxide sequestration in flood basalts. *Journal of Geophysical Research: Solid Earth*, 111(B12), 2006.

B Peter McGrail, Herbert T Schaef, Frank A Spane, John B Cliff, Odeta Qafoku, Jake A Horner, Christopher J Thompson, Antoinette T Owen, and Charlotte E Sullivan. Field validation of supercritical CO_2 reactivity with basalts. *Environmental Science & Technology Letters*, 4(1):6–10, 2017. doi: 10.1021/acs.estlett.6b00387.

BP McGrail, FA Spane, EC Sullivan, DH Bacon, and G Hund. The Wallula basalt sequestration pilot project. *Energy Procedia*, 4:5653–5660, 2011.

BP McGrail, CJ Freeman, CF Brown, EC Sullivan, SK White, S Reddy, RD Garber, D Tobin, JJ Gilmartin, and EJ Steffensen. Overcoming business model uncertainty in a carbon dioxide capture and sequestration project: Case study at the Boise White Paper Mill. *International Journal of Greenhouse Gas Control*, 9:91–102, 2012.

Bert Metz, Ogunlade Davidson, Heleen De Coninck, Manuela Loos, and Leo Meyer. IPCC special report on carbon dioxide capture and storage. Technical report, Intergovernmental Panel on Climate Change, Geneva (Switzerland). Working Group III, 2005.

Ki-Bok Min, Jonny Rutqvist, Chin-Fu Tsang, and Lanru Jing. Stress-dependent permeability of fractured rock masses: a numerical study. *International Journal of Rock Mechanics and Mining Sciences*, 41(7):1191–1210, 2004.

JG Moore. Relationship between subsidence and volcanic load, hawaii. *Bulletin Volcanologique*, 34(2):562–576, 1970.

Alexis K Navarre-Sitchler, Reed M Maxwell, Erica R Siirila, Glenn E Hammond, and Peter C Lichtner. Elucidating geochemical response of shallow heterogeneous aquifers to CO_2 leakage using high-performance computing: Implications for monitoring of CO_2 sequestration. *Advances in Water Resources*, 53:45–55, 2013.

NETL. Best Practices for: Risk Analysis and Simulation of Geologic Storage of CO_2., 2011.

Jerome A Neufeld, Dominic Vella, and Herbert E Huppert. The effect of a fissure on storage in a porous medium. *Journal of Fluid Mechanics*, 639:239–259, 2009.

Shlomo P Neuman. Universal scaling of hydraulic conductivities and dispersivities in geologic media. *Water resources research*, 26(8):1749–1758, 1990.

NIST. Thermophysical properties of fluid systems. *Avaliable Online: http://webbook.nist.gov/chemistry/fluid/(access on 7 May 2019)*, 2018.

CM Oldenburg and JL Lewicki. On leakage and seepage of CO_2 from geologic storage sites into surface water. *Environmental Geology*, 50(5):691–705, 2006.

Curtis M Oldenburg. Joule-Thomson cooling due to CO_2 injection into natural gas reservoirs. *Energy Conversion and Management*, 48(6):1808–1815, 2007.

Franklin M Orr. Onshore geologic storage of CO_2. *Science*, 325(5948):1656–1658, 2009.

Stephen Pacala and Robert Socolow. Stabilization wedges: solving the climate problem for the next 50 years with current technologies. *science*, 305(5686):968–972, 2004.

Frederick L Paillet and Kunsoo Kim. Character and distribution of borehole breakouts and their relationship to in situ stresses in deep Columbia River Basalts. *Journal of Geophysical Research: Solid Earth*, 92(B7):6223–6234, 1987.

Rajesh J Pawar, Theresa L Watson, and Carl W Gable. Numerical simulation of CO_2 leakage through abandoned wells: Model for an abandoned site with observed gas migration in Alberta, Canada. *Energy Procedia*, 1(1):3625–3632, 2009.

Henry N Pollack, Suzanne J Hurter, and Jeffrey R Johnson. Heat flow from the Earth's interior: analysis of the global data set. *Reviews of Geophysics*, 31(3):267–280, 1993.

Ryan M Pollyea. Influence of relative permeability on injection pressure and plume configuration during CO_2 injections in a mafic reservoir. *International Journal of Greenhouse Gas Control*, 46:7–17, 2016.

Ryan M Pollyea and Jerry P Fairley. Implications of spatial reservoir uncertainty for CO_2 sequestration in the east Snake River Plain, Idaho (USA). *Hydrogeology Journal*, 20(4): 689–699, 2012.

Ryan M Pollyea and J Donald Rimstidt. Rate equations for modeling carbon dioxide sequestration in basalt. *Applied Geochemistry*, 81:53–62, 2017.

Ryan M Pollyea, Jerry P Fairley, Robert K Podgorney, and Travis L Mcling. Physical constraints on geologic CO_2 sequestration in low-volume basalt formations. *Geological Society of America Bulletin*, 126(3-4):344–351, 2014.

Ryan M Pollyea, Erik W Van Dusen, and Mark P Fischer. Topographically driven fluid flow within orogenic wedges: Effects of taper angle and depth-dependent permeability. *Geosphere*, 11(5):1427–1437, 2015.

Ryan M Pollyea, Neda Mohammadi, John E Taylor, and Martin C Chapman. Geospatial analysis of Oklahoma (USA) earthquakes (2011–2016): Quantifying the limits of regional-scale earthquake mitigation measures. *Geology*, 46(3):215–218, 2018.

Olga H Popova, Mitchell J Small, Sean T McCoy, AC Thomas, Stephen Rose, Bobak Karimi, Kristin Carter, and Angela Goodman. Spatial stochastic modeling of sedimentary formations to assess CO_2 storage potential. *Environmental science & technology*, 48(11): 6247–6255, 2014.

Phillip N Price and Curtis M Oldenburg. The consequences of failure should be considered in siting geologic carbon sequestration projects. *International Journal of Greenhouse Gas Control*, 3(5):658–663, 2009.

K Pruess, T Xu, J Apps, and J Garcia. Numerical Modeling of Aquifer Disposal of CO_2. SPEJ 8 (1): 49–60. Technical report, SPE-83695-PA. DOI: 10.2118/83695-PA, 2003.

Karsten Pruess. Brief guide to the MINC-method for modeling flow and transport in fractured media. *Earth science division. Lawrence Berkeley Laboratory, University of California, Berkeley*, 10179, 1992.

Karsten Pruess. Numerical simulations show potential for strong nonisothermal effects during fluid leakage from a geologic disposal reservoir for CO_2. *Dynamics of fluids and transport in fractured rock*, pages 81–89, 2005a.

Karsten Pruess. *ECO2N: A TOUGH2 fluid property module for mixtures of water, NaCl, and CO_2*. Lawrence Berkeley National Laboratory Berkeley, CA, 2005b.

Karsten Pruess. Numerical studies of fluid leakage from a geologic disposal reservoir for CO_2 show self-limiting feedback between fluid flow and heat transfer. *Geophysical research letters*, 32(14), 2005a.

Karsten Pruess. ECO_2M: a TOUGH2 fluid property module for mixtures of water, NaCl, and CO_2, including super-and sub-critical conditions, and phase change between liquid and gaseous CO_2. Technical report, Ernest Orlando Lawrence Berkeley National Laboratory, Berkeley, CA (US), 2011.

Karsten Pruess and Christine Doughty. Thermal single-well injection-withdrawal tracer tests for determining fracture-matrix heat transfer area. Technical report, Lawrence Berkeley National Lab.(LBNL), Berkeley, CA (United States), 2010.

Karsten Pruess and Julio Garcia. Multiphase flow dynamics during CO_2 disposal into saline aquifers. *Environmental Geology*, 42(2-3):282–295, 2002.

Karsten Pruess, Curt Oldenburg, and George Moridis. TOUGH2 User's Guide, Version 2. Technical report, Lawrence Berkeley National Laboratory, November 1999. LBNL-43134.

LJ Pyrak-Nolte and JP Morris. Single fractures under normal stress: The relation between fracture specific stiffness and fluid flow. *International Journal of Rock Mechanics and Mining Sciences*, 37(1-2):245–262, 2000.

John G Ramsay. Folding and fracturing of rocks. *Mc Graw Hill Book Company*, 568, 1967.

Stephen P Reidel, Karl R Fecht, Michael C Hagood, and Terry L Tolan. The geologic evolution of the central Columbia Plateau. *Geological Society of America Special Papers*, 239:247–264, 1989.

Steve P Reidel, Frank A Spane, and Vernon G Johnson. Natural gas storage in basalt aquifers

of the Columbia basin, Pacific Northwest USA: A guide to site characterization. Technical report, Pacific Northwest National Laboratory (PNNL), Richland, WA (US), 2002.

CA Rochelle, I Czernichowski-Lauriol, and AE Milodowski. The impact of chemical reactions on CO_2 storage in geological formations: a brief review. *Geological Society, London, Special Publications*, 233(1):87–106, 2004.

Traci Rodosta, John Litynski, Sean Plasynski, Lee Spangler, Robert Finley, Edward Steadman, David Ball, Gerald Hill, Brian McPherson, Elizabeth Burton, et al. US Department of Energy's regional carbon sequestration partnership initiative: Update on validation and development phases. *Energy Procedia*, 4:3457–3464, 2011.

JR Roebuck, TA Murrell, and EE Miller. The Joule-Thomson effect in carbon dioxide. *Journal of the American Chemical Society*, 64(2):400–411, 1942.

Jonny Rutqvist and Ove Stephansson. The role of hydromechanical coupling in fractured rock engineering. *Hydrogeology Journal*, 11(1):7–40, 2003.

Martin O Saar. Geothermal heat as a tracer of large-scale groundwater flow and as a means to determine permeability fields. *Hydrogeology Journal*, 19(1):31–52, 2011.

MO Saar and Michael Manga. Depth dependence of permeability in the Oregon Cascades inferred from hydrogeologic, thermal, seismic, and magmatic modeling constraints. *Journal of Geophysical Research: Solid Earth*, 109(B4), 2004.

RA Schultz. Limits on strength and deformation properties of jointed basaltic rock masses. *Rock Mechanics and Rock Engineering*, 28(1):1–15, 1995.

Richard A Schultz. Brittle strength of basaltic rock masses with applications to venus. *Journal of Geophysical Research: Planets*, 98(E6):10883–10895, 1993.

Gary Shaffer. Long-term effectiveness and consequences of carbon dioxide sequestration. *Nature Geoscience*, 3(7):464, 2010.

G Michael Shook and Anna Suzuki. Use of tracers and temperature to estimate fracture surface area for egs reservoirs. *Geothermics*, 67:40–47, 2017.

George C Sih. Handbook of stress-intensity factors: Stress-intensity factor solutions and formulas for reference. *Bethlehem, Pa., Lehigh University, 1973. 815 p*, 1973.

Gene Simmons and William F Brace. Comparison of static and dynamic measurements of compressibility of rocks. *Journal of geophysical research*, 70(22):5649–5656, 1965.

Charles Sumner Slichter. Field measurements of the rate of movement of underground waters. *United States Geological Survey Water-Supply and Irrigation Paper*, 140, 1905.

Frank A Spane. Preliminary Analysis of Grande Ronde Basalt Formation Flow Top Transmissivity as it Relates to Assessment and Site Selection Applications for Fluid/Energy Storage and Sequestration Projects. Technical report, Pacific Northwest National Laboratory (PNNL), Richland, WA (US), 2013.

R Mohan Srivastava. An overview of stochastic methods for reservoir characterization. *AAPG Computational Applied Geology*, (3):3–16, 1994a.

Philip H Stauffer, KC Lewis, Joshua S Stein, Bryan J Travis, Peter Lichtner, and George Zyvoloski. Joule–thomson effects on the flow of liquid water. *Transport in porous media*, 105(3):471–485, 2014.

Richard G Storey, Kenneth WF Howard, and D Dudley Williams. Factors controlling riffle-scale hyporheic exchange flows and their seasonal changes in a gaining stream: A three-dimensional groundwater flow model. *Water Resources Research*, 39(2), 2003.

Vincent C Tidwell and John L Wilson. Laboratory method for investigating permeability upscaling. *Water Resources Research*, 33(7):1607–1616, 1997.

John Townend and Mark D Zoback. How faulting keeps the crust strong. *Geology*, 28(5): 399–402, 2000.

USDOE. Carbon Technology Program Plan. Technical report, 2013.

LGH Van der Meer. Investigations regarding the storage of carbon dioxide in aquifers in the Netherlands. *Energy Conversion and management*, 33(5-8):611–618, 1992.

LGH Van der Meer. The CO_2 storage efficiency of aquifers. *Energy conversion and management*, 36(6-9):513–518, 1995.

M.Th. Van Genuchten. A closed-form equation for predicting the hydraulic conductivity of unsaturated soils. *Soil Science Society of America*, 44:892–898, 1980.

RI Walcott. Isostatic response to loading of the crust in Canada. *Canadian Journal of Earth Sciences*, 7(2):716–727, 1970a.

RI Walcott. Flexural rigidity, thickness, and viscosity of the lithosphere. *Journal of Geophysical Research*, 75(20):3941–3954, 1970b.

Philipp Weis. The dynamic interplay between saline fluid flow and rock permeability in magmatic-hydrothermal systems. *Geofluids*, 15(1-2):350–371, 2015.

Thomas ML Wigley, Richard Richels, and Jae A Edmonds. Economic and environmental choices in the stabilization of atmospheric CO_2 concentrations. *Nature*, 379(6562):240–243, 1996.

Paul Adams Witherspoon, Joseph SY Wang, K Iwai, and John E Gale. Validity of cubic law for fluid flow in a deformable rock fracture. *Water resources research*, 16(6):1016–1024, December 1980.

H. Wu, R.S. Jayne, and R.M. Pollyea. Quantifying permeability alteration effects to CO_2 storage potential in a basalt fracture network. Fall Meeting of the American Geophysical Union, December 2018a. Abstract S51F-1615.

Hao Wu, Richard S. Jayne, and Ryan M. Pollyea. A parametric analysis of capillary pressure effects during geologic carbon sequestration in a sandstone reservoir. *Greenhouse Gases: Science and Technology*, 8(6):1039–1052, 2018b.

Nozomu Yoshida, Jonathan S Levine, and Philip H Stauffer. Investigation of uncertainty in CO_2 reservoir models: A sensitivity analysis of relative permeability parameter values. *International Journal of Greenhouse Gas Control*, 49:161–178, 2016.

Natalia V Zakharova, David S Goldberg, E Charlotte Sullivan, Michael M Herron, and James A Grau. Petrophysical and geochemical properties of Columbia River flood basalt: Implications for carbon sequestration. *Geochemistry, Geophysics, Geosystems*, 13(11), 2012.

Mehdi Zeidouni, Jean-Philippe Nicot, and Susan D Hovorka. Monitoring above-zone temperature variations associated with CO_2 and brine leakage from a storage aquifer. *Environmental earth sciences*, 72(5):1733–1747, 2014.

Y. Zhang, C. Doughty, L. Pan, T. Kneafsey, et al. What could we see at the proudction well before the thermal breakthrough? In *Proceedings, 43rd Workshop on Geothermal Reservoir Engineering*. Stanford University, 2018a.

Yingqi Zhang, Barry Freifeld, Stefan Finsterle, Martin Leahy, Jonathan Ennis-King, Lincoln

Paterson, and Tess Dance. Estimating CO_2 residual trapping from a single-well test: experimental design calculations. *Energy Procedia*, 4:5044–5049, 2011.

Yingqi Zhang, Yoojin Jung, Barry Freifeld, and Stefan Finsterle. Using distributed temperature sensing to detect CO_2 leakage along the injection well casing. *International Journal of Greenhouse Gas Control*, 74:9–18, 2018b.

Ruirui Zhao and Jianmei Cheng. Effects of temperature on salt precipitation due to formation dry-out during CO_2 injection in saline aquifers. *Greenhouse Gases: Science and Technology*, 7(4):624–636, 2017.

Mark D Zoback and Steven M Gorelick. Earthquake triggering and large-scale geologic storage of carbon dioxide. *Proceedings of the National Academy of Sciences*, 109(26): 10164–10168, 2012.

Appendices

Appendix A

Data Sources

For this study, a database of spatially referenced permeability values are compiled from previously published well data within the Columbia River Basalt Group [Reidel et al., 2002, Spane, 2013, Burns et al., 2015]. The database consists of 598 individual wells with hydrologic data comprising, hydraulic conductivity (K), transmissivity (T), or permeability (k), as well as geographic location, center interval depth, and estimated temperature, viscosity (μ), and water density (ρ). In addition, numerous wells include multiple test intervals, and, as a result, the complete database comprises 874 records. It should be noted that the center interval depth represents the depth utilized by Burns et al. [2015] and represents the middle of the testing interval reported from Reidel et al. [2002] and Spane [2013]. For this study, K is converted to permeability using the relation $k = (K\mu)/(\rho g)$, and T is converted to permeability as $k = (T\mu)/(\rho g b)$, where μ, ρ, g, and b are water viscosity, water density, gravitational acceleration, and open well interval, respectively. InBurns et al. [2015], the authors adopt a convention in which b is either the open well interval or 30 m (which ever is greater). This convention is based on the idea that a typical CRBG basalt flow thickness is ~30 m. The present study adopts this convention in order to maintain consistency with the substantial CRBG permeability database already reported by Burns et al. [2015]. Burns et al. [2015] utilizes hydrologic data from both Kahle et al. [2011] and Spane [2013], to keep consistency and remove any redundant entries two measures were taken. First, only the data compiled by Burns et al. [2015] from Kahle et al. [2011] are used. The data from Spane

[2013] is used as a test to ensure consistencies, by testing the conversion of hydrologic data to bulk permeability in this study to the converted bulk permeabilities in Burns et al. [2015]. To test the consistency between the Burns et al. [2015] and this study, the percent error was calculated using % error = ((experimental – theoretical)/theoretical)*100, where the experimental value is log bulk permeability from this study and theoretical value is log bulk permeability from Burns et al. [2015]. This comparison between 42 bulk permeability values results in an average difference of 0.7% between this study and Burns et al. [2015], which gives confidence to the consistency of the tabulated data. Second, to check for redundancy within the database a shell script was used to filter the entire database on unique combinations of Easting, Northing, and center interval depth, this results in 874 unique spatial locations (x, y, and z) of permeability values. In order to account for thermal effects on water properties, the temperature for each open well interval where temperature is not reported, it is estimated by using the regional heat flux of ∼65 mW/m^2 [Pollack et al., 1993]. In addition, all geospatial locations are converted to Universal Transverse Mercator coordinates using the Geospatial Data Abstraction Library.

The spatial variability of CRBG scalar permeability as a function of distance is calculated using the experimental semivariogram, which is a two-point measure of spatial autocorrelation. The experimental semivariogram is defined mathematically as,

$$\gamma(h) = \frac{1}{2N(h)} \sum_{i=1}^{N(h)} (z_i - z_{i+h})^2 \tag{A.1}$$

where, $N(h)$ is the total number of data pairs separated by a spatial lag distance (h), and z_i and z_{i+h} are the head and tail values of each data pair, respectively [Deutsch and Journel, 1998]. Owing to the large range of permeabilities within the database, a logarithmic (base 10) transform is applied to the permeability data, which results in a lognormal permeability

distribution. In order to search for horizontal anisotropy in the spatial distribution of bulk permeability values, a 2-D semivariogram map is developed using Geostatistical Software Library^{TM} (GSLIB; Deutsch and Journel, 1998). A semivariogram map is way to quantify $\gamma(h)$ in all horizontal directions and lag distances (Fig. 2.2A). This allows for the directions of minimum and maximum spatial continuity to be determined in the horizontal plane. The directions of minimum and maximum spatial continuity are then used to calculate directional semivariograms. In order to calculate directional horizontal semivariograms Equation A.1 is implemented by narrowing the search window for data pairs. In order to narrow the search window the experimental semivariogram values are calculated between pairs of points along an azimuth defined by the directions of maximum and minimum continuity, 40° and 130° respectively. To narrow the search window in these directions additional parameters must be defined. The azimuth tolerance defines the maximum and minimum search azimuth. For example, The direction of maximum continuity is 40° and the azimuth tolerance chosen for this study is 45°, this means the full search window for data pairs is from 355° to 85°. Additionally, an azimuth bandwidth must be defined, which restricts the amount of deviation from the azimuth is allowed while searching for data pairs. For this study an azimuth bandwidth of 25km is chosen. The azimuth tolerance and bandwidth control the swath of data for which the calculations are done, by increasing or decreasing these values effects the number of data points involved in each calculation for a given lag distance. Defining an azimuth, azimuth tolerance, and azimuth bandwidth changes the search pattern from a circular (isotropic) pattern to an angular band. Using an angular band to calculate the two horizontal semivariograms orthogonal to one another is a way to quantify both the spatial correlation of permeability values in those directions and also the spatial anisotropy of permeability values within the CRBG. For horizontal semivariogram calculations, multiple permeability values within a single well present a unique challenge because collocated data are known to increase the uncertainty at short lag distances. To address this challenge, the arithmetic

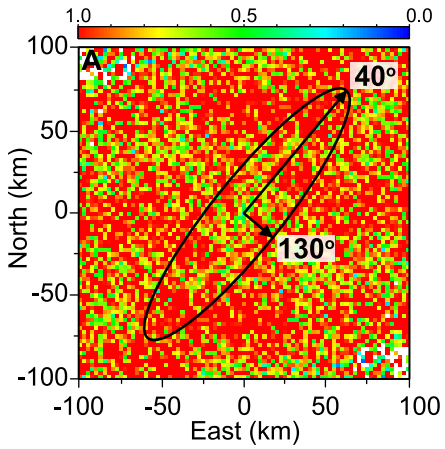

Figure A.1: Semivariogram map of CRBG permeability. Note that the axis refer to North and East directions in kilometers, these are still representative of lag distance $\gamma(h)$, as shown in Equation A.1

mean of permeability is taken within wells that have multiple testing intervals. This method has shown to be a suitable method for aggregating collocated data [Desbarats and Bachu, 1994]. Once the experimental semivariograms are calculated, each semivariogram can be fit with a linear combination of a priori permissible functions, e.g., spherical, exponential, Gaussian, hole effect, or power law [Deutsch and Journel, 1998]. The models that are fit to the semivariogram can be fully characterized by: (1) the nugget effect, which represents spatial variability at a lower resolution than the defined lag distance; (2) the sill, represents the variance of the dataset and once the semivariogram oscillates around the sill, the data is considered to be spatially random; and (3) the range, which is the distance at which spatial correlation can be inferred. In order to compare the semivariogram calculations for different directions, each experimental semivariogram is normalized over its respective variance so that the sill (variance) in each direction is one. By fitting each experimental semivariogram with a linear combination of permissible functions, a 3-D model of spatial autocorrelation for CRBG permeability is constructed as shown by Figure 2.2B-D.

Well ID	Easting	Northing	Center Interval Depth (m)	T(m^2/d)	K (ft/d)	K (m/s)	Est. T (C°)	Viscosity (kg/(m*s))	Density (kg/m^3)	Bulk Perm. (m^2)	log perm	Source
1	169708	5041533	310		1.22E+00	4.30E-06	17.0	1.08E-03	9.99E+02	4.74E-14	-13.32	Burns et al., 2015
2	181029	5044474	177		4.31E+01	1.52E-04	16.6	1.09E-03	9.99E+02	1.69E-12	-11.77	Burns et al., 2015
3	369635	5056461	297		4.59E+02	1.62E-03	21.5	9.66E-04	9.98E+02	1.60E-11	-10.80	Burns et al., 2015
4	377921	5069352	526		6.67E+00	2.35E-05	29.1	8.13E-04	9.96E+02	1.96E-13	-12.71	Burns et al., 2015
5	362311	5074804	107		5.82E-01	2.05E-06	15.1	1.14E-03	9.99E+02	2.38E-14	-13.62	Burns et al., 2015
6	374824	5078645	198		6.52E-01	2.30E-06	18.3	1.05E-03	9.99E+02	2.46E-14	-13.61	Burns et al., 2015
7	383580	5073875	350		2.56E+01	9.03E-05	23.3	9.27E-04	9.98E+02	8.55E-13	-12.07	Burns et al., 2015
8	380733	5070656	500		1.10E+01	3.88E-05	28.3	8.28E-04	9.96E+02	3.29E-13	-12.48	Burns et al., 2015
9	312577	5024339	146		4.20E+00	1.48E-05	12.9	1.20E-03	9.99E+02	1.82E-13	-12.74	Burns et al., 2015
10	299227	5011375	88		5.36E+01	1.89E-04	10.9	1.27E-03	1.00E+03	2.45E-12	-11.61	Burns et al., 2015
11	291190	5071939	95		3.35E+01	1.18E-04	18.3	1.04E-03	9.99E+02	1.26E-12	-11.90	Burns et al., 2015
12	281718	5085397	83		4.49E+01	1.58E-04	18.1	1.05E-03	9.99E+02	1.70E-12	-11.77	Burns et al., 2015
13	285351	5083138	121		1.16E+02	4.07E-04	19.0	1.03E-03	9.98E+02	4.28E-12	-11.37	Burns et al., 2015
14	299927	5090713	117		3.56E-01	1.26E-06	18.9	1.03E-03	9.98E+02	1.32E-14	-13.88	Burns et al., 2015
15	298357	5092155	305		1.97E+02	6.94E-04	23.2	9.29E-04	9.98E+02	6.59E-12	-11.18	Burns et al., 2015
16	313091	5089158	113		8.86E+00	3.12E-05	18.8	1.03E-03	9.98E+02	3.29E-13	-12.48	Burns et al., 2015
17	301856	5097757	293		2.26E+03	7.97E-03	22.9	9.36E-04	9.98E+02	7.62E-11	-10.12	Burns et al., 2015
18	296068	5103074	302		5.45E+02	1.92E-03	23.1	9.31E-04	9.98E+02	1.83E-11	-10.74	Burns et al., 2015
19	208522	5043353	184		2.40E+01	8.46E-05	15.1	1.13E-03	9.99E+02	9.78E-13	-12.01	Burns et al., 2015
20	217694	5042222	82		3.29E+01	1.16E-04	12.2	1.22E-03	1.00E+03	1.45E-12	-11.84	Burns et al., 2015
21	221425	5041004	93		1.22E+00	4.29E-06	12.5	1.21E-03	9.99E+02	5.31E-14	-13.27	Burns et al., 2015
22	204073	5030633	158		5.18E+01	1.83E-04	14.4	1.16E-03	9.99E+02	2.15E-12	-11.67	Burns et al., 2015
23	200961	5023852	90		1.88E+01	6.63E-05	12.5	1.22E-03	9.99E+02	8.22E-13	-12.09	Burns et al., 2015
24	178045	5058365	202		2.91E+01	1.03E-04	17.1	1.08E-03	9.99E+02	1.13E-12	-11.95	Burns et al., 2015
25	177338	5058556	117		4.51E+02	1.59E-03	16.1	1.10E-03	9.99E+02	1.79E-11	-10.75	Burns et al., 2015
26	173647	5050672	325		5.47E-01	1.93E-06	18.4	1.04E-03	9.99E+02	2.05E-14	-13.69	Burns et al., 2015
27	310282	5054956	131		3.48E+01	1.23E-04	20.1	1.00E-03	9.98E+02	1.25E-12	-11.90	Burns et al., 2015
28	384329	5087383	191		5.05E+00	1.78E-05	16.6	1.09E-03	9.99E+02	1.98E-13	-12.70	Burns et al., 2015
29	393911	5084618	320		4.66E+01	1.64E-04	21.2	9.75E-04	9.98E+02	1.64E-12	-11.79	Burns et al., 2015
30	397146	5083452	31		4.41E+01	1.55E-04	12.1	1.23E-03	1.00E+03	1.95E-12	-11.71	Burns et al., 2015
31	397275	5083419	125		5.42E+00	1.91E-05	14.3	1.16E-03	9.99E+02	2.26E-13	-12.65	Burns et al., 2015

Well ID	Easting	Northing	Center Interval Depth (m)	T(m^2/d)	K (ft/d)	K (m/s)	Est. T (C°)	Viscosity (kg/(m*s))	Density (kg/m^3)	Bulk Perm.- (m^2)	log perm	Source
32	379657	5091918	337		1.59E+02	5.62E-04	21.7	9.62E-04	9.98E+02	5.52E-12	-11.26	Burns et al. 2015
33	391194	5091827	303		2.20E+02	7.77E-04	20.6	9.88E-04	9.98E+02	7.84E-12	-11.11	Burns et al. 2015
34	394303	5089890	219		1.60E+02	5.64E-04	17.7	1.06E-03	9.99E+02	6.11E-12	-11.21	Burns et al. 2015
35	271664	5047133	107		1.98E-01	6.98E-07	16.4	1.10E-03	9.99E+02	7.81E-15	-14.11	Burns et al. 2015
36	274021	5042628	58		1.47E+02	5.19E-04	15.5	1.12E-03	9.99E+02	5.95E-12	-11.23	Burns et al. 2015
37	280726	5042360	145		2.01E+01	7.08E-05	17.2	1.07E-03	9.99E+02	7.76E-13	-12.11	Burns et al. 2015
38	283307	5040972	145		3.33E+01	1.18E-04	17.2	1.07E-03	9.99E+02	1.29E-12	-11.89	Burns et al. 2015
39	297462	5027772	389		2.14E+00	7.54E-06	22.0	9.56E-04	9.98E+02	7.36E-14	-13.13	Burns et al. 2015
40	322531	5063491	552		2.35E+02	8.27E-04	24.0	9.12E-04	9.97E+02	7.71E-12	-11.11	Burns et al. 2015
41	330102	5068128	391		1.88E+02	6.62E-04	23.6	9.19E-04	9.97E+02	6.21E-12	-11.21	Burns et al. 2015
42	314337	5073892	44		9.68E+01	3.41E-04	17.5	1.07E-03	9.99E+02	3.72E-12	-11.43	Burns et al. 2015
43	328734	5077339	366		5.90E+00	2.08E-05	23.6	9.20E-04	9.97E+02	1.96E-13	-12.71	Burns et al. 2015
44	317513	5090014	170		6.08E+03	2.14E-02	23.0	9.33E-04	9.98E+02	2.04E-10	-9.69	Burns et al. 2015
45	319354	5085172	76		4.79E+00	1.69E-05	19.8	1.01E-03	9.98E+02	1.74E-13	-12.76	Burns et al. 2015
46	318823	5082501	101		1.18E+00	4.17E-06	21.2	9.74E-04	9.98E+02	4.15E-14	-13.38	Burns et al. 2015
47	200118	5019984	52		2.83E+01	9.99E-05	13.3	1.19E-03	9.99E+02	1.21E-12	-11.92	Burns et al. 2015
48	209239	5022105	130		1.18E+01	4.15E-05	16.7	1.09E-03	9.99E+02	4.61E-13	-12.34	Burns et al. 2015
49	193901	5015994	217		7.31E+01	2.58E-04	20.5	9.90E-04	9.98E+02	2.61E-12	-11.58	Burns et al. 2015
50	254996	5054624	331		3.20E+00	1.13E-05	22.8	9.38E-04	9.98E+02	1.08E-13	-12.97	Burns et al. 2015
51	254787	5053149	190		1.21E+05	4.26E-01	14.6	1.15E-03	9.99E+02	4.99E-09	-8.30	Burns et al. 2015
52	254893	5051781	333		2.05E+00	7.24E-06	22.9	9.35E-04	9.98E+02	6.92E-14	-13.16	Burns et al. 2015
53	252802	5050167	380		1.05E+01	3.69E-05	25.5	8.81E-04	9.97E+02	3.33E-13	-12.48	Burns et al. 2015
54	252962	5049264	312		8.46E-01	2.98E-06	21.7	9.62E-04	9.98E+02	2.93E-14	-13.53	Burns et al. 2015
55	247285	5047946	248		6.87E+00	2.42E-05	18.2	1.05E-03	9.99E+02	2.60E-13	-12.59	Burns et al. 2015
56	246700	5048526	197		7.37E+00	2.60E-05	15.7	1.12E-03	9.99E+02	2.96E-13	-12.53	Burns et al. 2015
57	244014	5039671	114		4.32E+01	1.52E-04	13.9	1.17E-03	9.99E+02	1.82E-12	-11.74	Burns et al. 2015
58	243219	5038312	145		2.51E+01	8.84E-05	14.5	1.15E-03	9.99E+02	1.04E-12	-11.98	Burns et al. 2015
59	243926	5057274	189		1.47E+02	5.17E-04	15.5	1.12E-03	9.99E+02	5.92E-12	-11.23	Burns et al. 2015
60	241821	5058184	305		2.26E+02	7.97E-04	21.3	9.71E-04	9.98E+02	7.90E-12	-11.10	Burns et al. 2015
61	247750	5057849	404		1.45E+01	5.12E-05	26.8	8.55E-04	9.97E+02	4.48E-13	-12.35	Burns et al. 2015
62	258628	5033962	61		8.72E+01	3.08E-04	12.8	1.21E-03	9.99E+02	3.78E-12	-11.42	Burns et al. 2015

Well ID	Easting	Northing	Center Interval Depth (m)	T(m^2/d)	K (ft/d)	K (m/s)	Est. T (C°)	Viscosity (kg/(m*s))	Density (kg/m^3)	Bulk Perm. (m^2)	log perm	Source
63	258822	5033923	68		2.55E+01	8.98E-05	12.9	1.20E-03	9.99E+02	1.10E-12	-11.96	Burns et al., 2015
64	259735	5032188	120		4.37E+01	1.54E-04	14.0	1.17E-03	9.99E+02	1.83E-12	-11.74	Burns et al., 2015
65	261539	5029246	113		1.75E+01	6.18E-05	13.9	1.17E-03	9.99E+02	7.39E-13	-12.13	Burns et al., 2015
66	261957	5028179	213		1.22E+01	4.30E-05	16.2	1.10E-03	9.99E+02	4.84E-13	-12.32	Burns et al., 2015
67	238661	5021251	232		2.65E-01	9.35E-07	17.3	1.07E-03	9.99E+02	1.02E-14	-13.99	Burns et al., 2015
68	247503	4998947	177		2.15E+01	7.58E-05	15.2	1.13E-03	9.99E+02	8.75E-13	-12.06	Burns et al., 2015
69	283411	5118710	189		1.97E+02	6.94E-04	22.3	9.48E-04	9.98E+02	6.72E-12	-11.17	Burns et al., 2015
70	283298	5130642	98		1.06E+03	3.73E-03	18.2	1.05E-03	9.99E+02	3.99E-11	-10.40	Burns et al., 2015
71	289822	5130383	366		3.40E+02	1.20E-03	44.0	6.04E-04	9.91E+02	7.46E-12	-11.13	Burns et al., 2015
72	289059	5126268	163		1.12E+02	3.96E-04	20.7	9.84E-04	9.98E+02	3.98E-12	-11.40	Burns et al., 2015
73	278145	5132681	284		1.36E+03	4.80E-03	33.6	7.39E-04	9.95E+02	3.63E-11	-10.44	Burns et al., 2015
74	394303	5103690	494		6.66E+01	2.35E-04	33.3	7.44E-04	9.95E+02	1.79E-12	-11.75	Burns et al., 2015
75	394873	5103063	471		1.05E+03	3.69E-03	31.9	7.65E-04	9.95E+02	2.89E-11	-10.54	Burns et al., 2015
76	209979	5085252	45		3.63E+01	1.28E-04	13.4	1.19E-03	9.99E+02	1.55E-12	-11.81	Burns et al., 2015
77	222722	5084174	125		8.80E-02	3.10E-07	16.2	1.10E-03	9.99E+02	3.49E-15	-14.46	Burns et al., 2015
78	220937	5081966	107		1.28E+00	4.50E-06	15.5	1.12E-03	9.99E+02	5.15E-14	-13.29	Burns et al., 2015
79	211819	5089496	87		7.22E-01	2.55E-06	14.8	1.14E-03	9.99E+02	2.97E-14	-13.53	Burns et al., 2015
80	337998	5158440	95		8.38E-01	2.96E-06	18.9	1.03E-03	9.98E+02	3.11E-14	-13.51	Burns et al., 2015
81	340918	5158486	139		1.62E+00	5.72E-06	21.1	9.75E-04	9.98E+02	5.70E-14	-13.24	Burns et al., 2015
82	339526	5153396	42		3.92E+00	1.38E-05	15.7	1.12E-03	9.99E+02	1.57E-13	-12.80	Burns et al., 2015
83	342010	5152991	64		4.31E-01	1.52E-06	16.9	1.08E-03	9.99E+02	1.68E-14	-13.77	Burns et al., 2015
84	331464	5166341	138		2.97E+02	1.05E-03	21.1	9.76E-04	9.98E+02	1.04E-11	-10.98	Burns et al., 2015
85	335769	5161867	53		1.07E+02	3.76E-04	16.3	1.10E-03	9.99E+02	4.21E-12	-11.38	Burns et al., 2015
86	333342	5158814	56		7.82E+01	2.76E-04	16.4	1.10E-03	9.99E+02	3.09E-12	-11.51	Burns et al., 2015
87	353764	5159397	400		1.62E+01	5.73E-05	26.0	8.71E-04	9.97E+02	5.10E-13	-12.29	Burns et al., 2015
88	344677	5170434	116		3.86E+02	1.36E-03	20.0	1.00E-03	9.98E+02	1.39E-11	-10.86	Burns et al., 2015
89	332737	5137611	188		8.56E+00	3.02E-05	21.5	9.65E-04	9.98E+02	2.98E-13	-12.53	Burns et al., 2015
90	381097	5166486	207		9.99E+02	3.53E-03	15.2	1.13E-03	9.99E+02	4.06E-11	-10.39	Burns et al., 2015
91	396593	5161106	53		5.23E+02	1.85E-03	11.8	1.24E-03	1.00E+03	2.33E-11	-10.63	Burns et al., 2015
92	381903	5181508	155		5.89E+01	2.08E-04	15.2	1.13E-03	9.99E+02	2.40E-12	-11.62	Burns et al., 2015
93	401086	5178074	116		5.02E+01	1.77E-04	14.9	1.14E-03	9.99E+02	2.06E-12	-11.69	Burns et al., 2015

Well ID	Easting	Northing	Center Interval Depth (m)	T(m^2/d)	K (ft/d)	K (m/s)	Est. T (C°)	Viscosity (kg/(m*s))	Density (kg/m^3)	Bulk Perm. (m^2)	log perm	Source
94	384564	5189670	65		1.48E+02	5.23E-04	12.7	1.21E-03	9.99E+02	6.44E-12	-11.19	Burns et al. 2015
95	387717	5188375	189		5.58E+02	1.97E-03	15.2	1.13E-03	9.99E+02	2.27E-11	-10.64	Burns et al. 2015
96	377155	5204362	311		3.66E+01	1.29E-04	15.3	1.13E-03	9.99E+02	1.49E-12	-11.83	Burns et al. 2015
97	380444	5202936	127		9.72E+02	3.43E-03	15.1	1.14E-03	9.99E+02	3.97E-11	-10.40	Burns et al. 2015
98	400947	5200430	47		3.44E+02	1.21E-03	11.4	1.25E-03	1.00E+03	1.35E-11	-10.81	Burns et al. 2015
99	411859	5200629	230		6.60E+01	2.33E-04	15.3	1.13E-03	9.99E+02	2.68E-12	-11.57	Burns et al. 2015
100	380937	5206447	184		1.04E+03	3.65E-03	15.2	1.13E-03	9.99E+02	4.21E-11	-10.38	Burns et al. 2015
101	420055	5210195	35		2.57E+03	9.06E-03	10.5	1.28E-03	1.00E+03	1.19E-10	-9.93	Burns et al. 2015
102	436109	5212730	35		2.74E+02	9.65E-04	10.5	1.28E-03	1.00E+03	1.26E-11	-10.90	Burns et al. 2015
103	372883	5101718	335		4.16E+01	1.47E-04	32.8	7.51E-04	9.95E+02	1.13E-12	-11.95	Burns et al. 2015
104	364322	5099492	83		5.85E+00	2.07E-05	18.2	1.05E-03	9.99E+02	2.21E-13	-12.66	Burns et al. 2015
105	374419	5097981	312		1.70E+02	5.99E-04	32.2	7.61E-04	9.95E+02	4.67E-12	-11.33	Burns et al. 2015
106	366590	5096973	46		4.92E+02	1.73E-03	15.8	1.11E-03	9.99E+02	1.97E-11	-10.71	Burns et al. 2015
107	369571	5102652	107		1.42E+03	5.01E-03	19.8	1.01E-03	9.98E+02	5.15E-11	-10.29	Burns et al. 2015
108	370047	5101746	52		1.92E+01	6.77E-05	16.2	1.10E-03	9.99E+02	7.62E-13	-12.12	Burns et al. 2015
109	366787	5101106	329		2.00E+01	7.04E-05	32.7	7.53E-04	9.95E+02	5.43E-13	-12.26	Burns et al. 2015
110	369019	5155397	344		2.17E+02	7.64E-04	24.8	8.94E-04	9.97E+02	6.99E-12	-11.16	Burns et al. 2015
111	369087	5154961	276		4.18E+02	1.48E-03	22.6	9.42E-04	9.98E+02	1.42E-11	-10.85	Burns et al. 2015
112	274342	5156495	349		1.86E+03	6.57E-03	25.0	8.91E-04	9.97E+02	5.98E-11	-10.22	Burns et al. 2015
113	258963	5169422	41		8.87E+03	3.13E-02	14.8	1.14E-03	9.99E+02	3.65E-10	-9.44	Burns et al. 2015
114	321740	5129335	96		3.32E+00	1.17E-05	19.1	1.03E-03	9.98E+02	1.23E-13	-12.91	Burns et al. 2015
115	331422	5128721	72		2.84E+02	1.00E-03	18.9	1.03E-03	9.98E+02	1.05E-11	-10.98	Burns et al. 2015
116	330190	5120600	89		6.67E+01	2.35E-04	18.9	1.03E-03	9.98E+02	2.47E-12	-11.61	Burns et al. 2015
117	318700	5135819	118		4.36E+01	1.54E-04	19.1	1.02E-03	9.98E+02	1.61E-12	-11.79	Burns et al. 2015
118	332544	5135269	107		2.25E+01	7.92E-05	19.1	1.02E-03	9.98E+02	8.28E-13	-12.08	Burns et al. 2015
119	336678	5132284	40		3.62E+02	1.28E-03	18.9	1.03E-03	9.98E+02	1.34E-11	-10.87	Burns et al. 2015
120	2170?7	5135922	460		8.68E+01	3.06E-04	31.4	7.74E-04	9.95E+02	2.43E-12	-11.61	Burns et al. 2015
121	218296	5135408	215		6.57E+02	2.32E-03	21.5	9.66E-04	9.98E+02	2.29E-11	-10.64	Burns et al. 2015
122	210035	5146753	160		2.51E+01	8.85E-05	19.1	1.02E-03	9.98E+02	9.24E-13	-12.03	Burns et al. 2015
123	215263	5149770	306		5.22E+02	1.84E-03	25.3	8.84E-04	9.97E+02	1.66E-11	-10.78	Burns et al. 2015
124	223764	5153830	382		8.76E+00	3.09E-05	28.3	8.26E-04	9.96E+02	2.61E-13	-12.58	Burns et al. 2015

Well ID	Easting	Northing	Center Interval Depth (m)	T(m^2/d)	K (ft/d)	K (m/s)	Est. T (C°)	Viscosity (kg/(m*s))	Density (kg/m^3)	Bulk Perm. (m^2)	log perm	Source
125	234800	5157878	152		6.95E+02	2.45E-03	18.8	1.03E-03	9.98E+02	2.58E-11	-10.59	Burns et al., 2015
126	235756	5157439	162		3.62E+02	1.28E-03	19.2	1.02E-03	9.98E+02	1.33E-11	-10.88	Burns et al., 2015
127	236101	5155074	91		7.09E+00	2.50E-05	16.1	1.10E-03	9.99E+02	2.82E-13	-12.55	Burns et al., 2015
128	245094	5159202	296		3.27E+02	1.15E-03	24.9	8.92E-04	9.97E+02	1.05E-11	-10.98	Burns et al., 2015
129	249942	5157269	675		3.99E+01	1.41E-04	39.6	6.56E-04	9.92E+02	9.49E-13	-12.02	Burns et al., 2015
130	245585	5158192	420		1.48E+02	5.23E-04	29.8	8.00E-04	9.96E+02	4.28E-12	-11.37	Burns et al., 2015
131	242844	5155464	140		7.17E+01	2.53E-04	18.3	1.05E-03	9.99E+02	2.70E-12	-11.57	Burns et al., 2015
132	242908	5152957	168		1.81E+02	6.37E-04	19.5	1.01E-03	9.98E+02	6.60E-12	-11.18	Burns et al., 2015
133	316584	5119480	155		5.84E+01	2.06E-04	20.5	9.90E-04	9.98E+02	2.08E-12	-11.68	Burns et al., 2015
134	317782	5117930	133		4.84E+01	1.71E-04	19.6	1.01E-03	9.98E+02	1.76E-12	-11.75	Burns et al., 2015
135	319056	5129785	27		3.78E+02	1.33E-03	14.1	1.16E-03	9.99E+02	1.58E-11	-10.80	Burns et al., 2015
136	320272	5128205	108		9.09E+01	3.21E-04	18.6	1.04E-03	9.99E+02	3.39E-12	-11.47	Burns et al., 2015
137	320333	5126628	337		2.14E+02	7.56E-04	28.2	8.29E-04	9.96E+02	6.42E-12	-11.19	Burns et al., 2015
138	319102	5125583	82		1.19E+00	4.20E-06	17.6	1.06E-03	9.99E+02	4.57E-14	-13.34	Burns et al., 2015
139	318562	5123251	274		9.65E+01	3.40E-04	25.5	8.81E-04	9.97E+02	3.07E-12	-11.51	Burns et al., 2015
140	318560	5122479	244		1.18E+02	4.16E-04	24.1	9.08E-04	9.97E+02	3.86E-12	-11.41	Burns et al., 2015
141	326050	5120501	368		6.15E+01	2.17E-04	29.5	8.05E-04	9.96E+02	1.79E-12	-11.75	Burns et al., 2015
142	207569	5160035	246		2.21E+02	7.78E-04	17.4	1.07E-03	9.99E+02	8.49E-12	-11.07	Burns et al., 2015
143	202685	5161016	88		1.40E+02	4.93E-04	13.1	1.19E-03	9.99E+02	6.00E-12	-11.22	Burns et al., 2015
144	208629	5158561	314		1.33E+02	4.67E-04	19.7	1.01E-03	9.98E+02	4.82E-12	-11.32	Burns et al., 2015
145	215863	5166630	171		1.59E+01	5.61E-05	15.2	1.13E-03	9.99E+02	6.47E-13	-12.19	Burns et al., 2015
146	222704	5168415	320		3.55E+02	1.25E-03	19.9	1.00E-03	9.98E+02	1.29E-11	-10.89	Burns et al., 2015
147	213157	5182317	277		8.23E+00	2.90E-05	18.4	1.04E-03	9.99E+02	3.09E-13	-12.51	Burns et al., 2015
148	219728	5175450	365		1.09E+01	3.84E-05	21.4	9.69E-04	9.98E+02	3.80E-13	-12.42	Burns et al., 2015
149	231599	5179578	88		6.95E+00	2.45E-05	13.2	1.19E-03	9.99E+02	2.99E-13	-12.52	Burns et al., 2015
150	222602	5176832	308		5.37E+01	1.89E-04	19.5	1.02E-03	9.98E+02	1.96E-12	-11.71	Burns et al., 2015
151	238155	5185071	391		7.67E+02	2.70E-03	22.3	9.48E-04	9.98E+02	2.62E-11	-10.58	Burns et al., 2015
152	235695	5183231	65		1.39E+02	4.91E-04	12.7	1.21E-03	9.99E+02	6.06E-12	-11.22	Burns et al., 2015
153	241620	5198372	336		2.91E+01	1.03E-04	20.4	9.92E-04	9.98E+02	1.04E-12	-11.98	Burns et al., 2015
154	236303	5194615	311		1.38E+03	4.87E-03	19.6	1.01E-03	9.98E+02	5.03E-11	-10.30	Burns et al., 2015
155	243858	5191720	177		6.99E+01	2.47E-04	15.3	1.13E-03	9.99E+02	2.84E-12	-11.55	Burns et al., 2015

Well ID	Easting	Northing	Center Interval Depth (m)	T(m²/d)	K (ft/d)	K (m/s)	Est. T (C°)	Viscosity (kg/(m*s))	Density (kg/m³)	Bulk Perm. (m²)	log perm	Source
156	243232	5209712	67		3.76E+01	1.32E-04	12.7	1.21E-03	9.99E+02	1.63E-12	-11.79	Burns et al. 2015
157	255724	5204271	192		2.26E+00	7.96E-06	15.8	1.11E-03	9.99E+02	9.05E-14	-13.04	Burns et al. 2015
158	212981	5224892	152		6.49E+00	2.29E-05	14.7	1.15E-03	9.99E+02	2.68E-13	-12.57	Burns et al. 2015
159	230609	5226229	119		4.09E+00	1.44E-05	13.8	1.17E-03	9.99E+02	1.73E-13	-12.76	Burns et al. 2015
160	236131	5221806	49		1.21E+00	4.26E-06	12.4	1.22E-03	9.99E+02	5.30E-14	-13.28	Burns et al. 2015
161	485174	5109836	175		1.80E+01	6.35E-05	12.5	1.22E-03	9.99E+02	7.88E-13	-12.10	Burns et al. 2015
162	489656	5108871	50		1.29E+01	4.54E-05	6.4	1.44E-03	1.00E+03	6.68E-13	-12.18	Burns et al. 2015
163	493653	5114606	61		2.03E+01	7.15E-05	7.6	1.39E-03	1.00E+03	1.01E-12	-11.99	Burns et al. 2015
164	413351	5131916	147		4.36E+02	1.54E-03	14.8	1.14E-03	9.99E+02	1.79E-11	-10.75	Burns et al. 2015
165	419021	5140204	36		5.56E+02	1.96E-03	13.7	1.18E-03	9.99E+02	2.35E-11	-10.63	Burns et al. 2015
166	432515	5145966	49		1.51E+01	5.32E-05	13.8	1.17E-03	9.99E+02	6.36E-13	-12.20	Burns et al. 2015
167	425144	5150158	27		3.19E+02	1.12E-03	13.6	1.18E-03	9.99E+02	1.35E-11	-10.87	Burns et al. 2015
168	438482	5149638	78		7.57E+00	2.67E-05	14.1	1.16E-03	9.99E+02	3.17E-13	-12.50	Burns et al. 2015
169	425425	5164334	192		2.31E-01	8.15E-07	15.2	1.13E-03	9.99E+02	9.40E-15	-14.03	Burns et al. 2015
170	439817	5165361	85		8.84E+02	3.12E-03	14.2	1.16E-03	9.99E+02	3.69E-11	-10.43	Burns et al. 2015
171	440114	5165827	68		3.37E+03	1.19E-02	14.0	1.17E-03	9.99E+02	1.41E-10	-9.85	Burns et al. 2015
172	441850	5162878	76		8.94E+02	3.15E-03	14.1	1.16E-03	9.99E+02	3.75E-11	-10.43	Burns et al. 2015
173	453811	5161046	54		3.48E+03	1.23E-02	13.9	1.17E-03	9.99E+02	1.47E-10	-9.83	Burns et al. 2015
174	454698	5160113	59		2.39E+03	8.43E-03	13.9	1.17E-03	9.99E+02	1.00E-10	-10.00	Burns et al. 2015
175	419185	5174777	105		2.71E+00	9.57E-06	14.3	1.16E-03	9.99E+02	1.13E-13	-12.95	Burns et al. 2015
176	442119	5168740	221		3.34E+02	1.18E-03	15.5	1.12E-03	9.99E+02	1.35E-11	-10.87	Burns et al. 2015
177	450603	5166844	32		2.97E+02	1.05E-03	13.7	1.18E-03	9.99E+02	1.26E-11	-10.90	Burns et al. 2015
178	463832	5171658	24		7.75E+02	2.74E-03	13.6	1.18E-03	9.99E+02	3.29E-11	-10.48	Burns et al. 2015
179	427461	5177913	49		2.63E+01	9.29E-05	13.8	1.17E-03	9.99E+02	1.11E-12	-11.95	Burns et al. 2015
180	447551	5182427	49		7.47E+01	2.63E-04	13.8	1.17E-03	9.99E+02	3.15E-12	-11.50	Burns et al. 2015
181	468922	5182742	63		2.86E+02	1.01E-03	14.0	1.17E-03	9.99E+02	1.20E-11	-10.92	Burns et al. 2015
182	432270	5189896	122		1.18E+00	4.16E-06	14.5	1.15E-03	9.99E+02	4.89E-14	-13.31	Burns et al. 2015
183	435267	5189462	155		1.89E+01	6.66E-05	14.8	1.14E-03	9.99E+02	7.76E-13	-12.11	Burns et al. 2015
184	449852	5191391	27		5.61E+01	1.98E-04	13.6	1.18E-03	9.99E+02	2.38E-12	-11.62	Burns et al. 2015
185	450083	5203768	29		3.17E+01	1.12E-04	13.6	1.18E-03	9.99E+02	1.34E-12	-11.87	Burns et al. 2015
186	447793	5197953	53		7.11E+03	2.51E-02	13.9	1.17E-03	9.99E+02	2.99E-10	-9.52	Burns et al. 2015

Well ID	Easting	Northing	Center Interval Depth (m)	T(m^2/d)	K (ft/d)	K (m/s)	Est. T (C°)	Viscosity (kg/(m*s))	Density (kg/m^3)	Bulk Perm. (m^2)	log perm	Source
187	462068	5214823	31		1.58E+01	5.58E-05	13.7	1.18E-03	9.99E+02	6.70E-13	-12.17	Burns et al., 2015
188	463601	5210338	69		1.03E+01	3.64E-05	14.0	1.17E-03	9.99E+02	4.33E-13	-12.36	Burns et al., 2015
189	463241	5210124	58		1.21E+01	4.25E-05	13.9	1.17E-03	9.99E+02	5.07E-13	-12.29	Burns et al., 2015
190	460844	5217826	49		2.49E+01	8.79E-05	13.8	1.17E-03	9.99E+02	1.05E-12	-11.98	Burns et al., 2015
191	466048	5217732	15		1.53E+02	5.40E-04	13.5	1.18E-03	9.99E+02	6.51E-12	-11.19	Burns et al., 2015
192	478909	5219247	99		5.93E+00	2.09E-05	14.3	1.16E-03	9.99E+02	2.47E-13	-12.61	Burns et al., 2015
193	363897	5259810	241		5.19E+03	1.83E-02	22.5	9.44E-04	9.98E+02	1.77E-10	-9.75	Burns et al., 2015
194	334974	5262037	285		3.15E+01	1.11E-04	24.4	9.04E-04	9.97E+02	1.03E-12	-11.99	Burns et al., 2015
195	356511	5264311	141		1.41E+03	4.98E-03	18.2	1.05E-03	9.99E+02	5.33E-11	-10.27	Burns et al., 2015
196	358127	5261924	171		6.63E+01	2.34E-04	19.5	1.01E-03	9.98E+02	2.42E-12	-11.62	Burns et al., 2015
197	365577	5263663	212		5.62E+02	1.98E-03	21.3	9.72E-04	9.98E+02	1.97E-11	-10.71	Burns et al., 2015
198	366870	5261626	133		6.96E+01	2.46E-04	17.8	1.06E-03	9.99E+02	2.65E-12	-11.58	Burns et al., 2015
199	363340	5261059	209		7.44E+02	2.62E-03	21.1	9.75E-04	9.98E+02	2.61E-11	-10.58	Burns et al., 2015
200	354458	5270941	229		5.75E+02	2.03E-03	22.0	9.55E-04	9.98E+02	1.98E-11	-10.70	Burns et al., 2015
201	366100	5272763	228		4.32E+01	1.52E-04	21.9	9.56E-04	9.98E+02	1.49E-12	-11.83	Burns et al., 2015
202	368900	5272792	177		4.01E+01	1.41E-04	19.8	1.01E-03	9.98E+02	1.45E-12	-11.84	Burns et al., 2015
203	368288	5266968	170		1.42E+02	5.02E-04	19.5	1.01E-03	9.98E+02	5.20E-12	-11.28	Burns et al., 2015
204	380549	5258057	217		1.33E+03	4.70E-03	21.1	9.75E-04	9.98E+02	4.68E-11	-10.33	Burns et al., 2015
205	465595	5234034	46		2.34E+01	8.26E-05	12.0	1.23E-03	1.00E+03	1.04E-12	-11.98	Burns et al., 2015
206	472038	5232055	94		1.34E+02	4.71E-04	14.7	1.15E-03	9.99E+02	5.51E-12	-11.26	Burns et al., 2015
207	482005	5232819	53		9.10E+00	3.21E-05	12.4	1.22E-03	9.99E+02	3.98E-13	-12.40	Burns et al., 2015
208	431792	5242540	116		6.21E+02	2.19E-03	15.8	1.11E-03	9.99E+02	2.48E-11	-10.60	Burns et al., 2015
209	459127	5240805	83		5.39E+00	1.90E-05	14.1	1.16E-03	9.99E+02	2.26E-13	-12.65	Burns et al., 2015
210	469560	5236729	82		3.66E+00	1.29E-05	14.0	1.17E-03	9.99E+02	1.53E-13	-12.81	Burns et al., 2015
211	482520	5243437	56		1.46E+01	5.15E-05	12.6	1.21E-03	9.99E+02	6.36E-13	-12.20	Burns et al., 2015
212	407589	5249200	31		9.20E+01	3.24E-04	11.2	1.26E-03	1.00E+03	4.16E-12	-11.38	Burns et al., 2015
213	437698	5245253	47		4.01E+00	1.41E-05	12.1	1.23E-03	1.00E+03	1.77E-13	-12.75	Burns et al., 2015
214	456231	5246568	35		7.76E+01	2.74E-04	11.5	1.25E-03	1.00E+03	3.48E-12	-11.46	Burns et al., 2015
215	470084	5252872	53		3.03E+00	1.07E-05	12.4	1.22E-03	9.99E+02	1.32E-13	-12.88	Burns et al., 2015
216	478046	5247588	130		5.63E-01	1.99E-06	16.6	1.09E-03	9.99E+02	2.21E-14	-13.65	Burns et al., 2015
217	478042	5246693	161		4.30E+00	1.52E-05	18.1	1.05E-03	9.99E+02	1.63E-13	-12.79	Burns et al., 2015

Well ID	Easting	Northing	Center Interval Depth (m)	T(m^2/d)	K (ft/d)	K (m/s)	Est. T (C°)	Viscosity (kg/(m*s))	Density (kg/m^3)	Bulk Perm. (m^2)	log perm	Source
218	428124	5261757	31		1.35E+01	4.74E-05	11.3	1.26E-03	1.00E+03	6.08E-13	-12.22	Burns et al. 2015
219	446127	5263077	53		1.06E+00	3.75E-06	12.4	1.22E-03	9.99E+02	4.66E-14	-13.33	Burns et al. 2015
220	444352	5263340	194		8.50E+01	3.00E-04	19.9	1.00E-03	9.98E+02	3.07E-12	-11.51	Burns et al. 2015
221	454010	5257576	84		7.59E+00	2.68E-05	14.2	1.16E-03	9.99E+02	3.18E-13	-12.50	Burns et al. 2015
222	456191	5256735	166		8.91E+00	3.14E-05	18.4	1.04E-03	9.99E+02	3.35E-13	-12.48	Burns et al. 2015
223	464805	5262625	203		1.41E+03	4.97E-03	20.4	9.93E-04	9.98E+02	5.04E-11	-10.30	Burns et al. 2015
224	468547	5255319	110		1.27E+03	4.49E-03	15.5	1.12E-03	9.99E+02	5.14E-11	-10.29	Burns et al. 2015
225	481903	5254182	123		3.46E-01	1.22E-06	16.2	1.10E-03	9.99E+02	1.37E-14	-13.86	Burns et al. 2015
226	381796	5265876	236		1.93E+02	6.82E-04	22.2	9.51E-04	9.98E+02	6.63E-12	-11.18	Burns et al. 2015
227	404096	5270192	229		4.30E+01	1.52E-04	21.8	9.60E-04	9.98E+02	1.49E-12	-11.83	Burns et al. 2015
228	437895	5271772	61		3.31E+02	1.17E-03	12.9	1.20E-03	9.99E+02	1.43E-11	-10.84	Burns et al. 2015
229	441440	5269142	69		1.40E+00	4.95E-06	13.3	1.19E-03	9.99E+02	6.00E-14	-13.22	Burns et al. 2015
230	456859	5271972	38		3.38E+00	1.19E-05	11.6	1.24E-03	1.00E+03	1.51E-13	-12.82	Burns et al. 2015
231	452741	5271479	123		1.44E+02	5.07E-04	16.2	1.10E-03	9.99E+02	5.70E-12	-11.24	Burns et al. 2015
232	454333	5269398	236		2.26E+02	7.96E-04	22.2	9.51E-04	9.98E+02	7.73E-12	-11.11	Burns et al. 2015
233	452634	5265953	11		2.80E+01	9.88E-05	10.2	1.29E-03	1.00E+03	1.30E-12	-11.88	Burns et al. 2015
234	464378	5272230	31		1.01E+02	3.55E-04	11.2	1.26E-03	1.00E+03	4.55E-12	-11.34	Burns et al. 2015
235	251582	5069108	51		2.98E+03	1.05E-02	16.4	1.10E-03	9.99E+02	1.18E-10	-9.93	Burns et al. 2015
236	253869	5066524	75		7.15E+01	2.52E-04	14.2	1.16E-03	9.99E+02	2.98E-12	-11.53	Burns et al. 2015
237	240946	5078283	53		7.11E+00	2.51E-05	16.2	1.10E-03	9.99E+02	2.82E-13	-12.55	Burns et al. 2015
238	242978	5087658	108		1.09E+02	3.85E-04	14.7	1.15E-03	9.99E+02	4.30E-12	-11.35	Burns et al. 2015
239	248982	5099931	114		1.38E+00	4.88E-06	15.1	1.13E-03	9.99E+02	5.64E-14	-13.25	Burns et al. 2015
240	245171	5098418	52		5.68E+00	2.00E-05	16.3	1.10E-03	9.99E+02	2.25E-13	-12.65	Burns et al. 2015
241	249385	5113485	124		9.11E+01	3.21E-04	15.5	1.12E-03	9.99E+02	3.68E-12	-11.43	Burns et al. 2015
242	233424	5127745	213		1.40E+01	4.94E-05	24.5	9.01E-04	9.97E+02	4.35E-13	-12.34	Burns et al. 2015
243	249101	5151398	499		1.08E+01	3.80E-05	32.1	7.63E-04	9.95E+02	2.97E-13	-12.53	Burns et al. 2015
244	251271	5150660	405		5.03E+01	1.77E-04	30.6	7.86E-04	9.95E+02	1.43E-12	-11.85	Burns et al. 2015
245	250933	5149715	494		8.38E+01	2.96E-04	32.9	7.50E-04	9.95E+02	2.27E-12	-11.64	Burns et al. 2015
246	250816	5147700	366		2.30E+03	8.10E-03	29.5	8.06E-04	9.96E+02	6.69E-11	-10.17	Burns et al. 2015
247	254363	5157366	424		9.23E+02	3.26E-03	31.2	7.77E-04	9.95E+02	2.89E-11	-10.59	Burns et al. 2015
248	253960	5156387	215		2.20E+00	7.75E-06	24.6	8.99E-04	9.97E+02	7.12E-14	-13.15	Burns et al. 2015

Well ID	Easting	Northing	Center Interval Depth (m)	T(m^2/d)	K (ft/d)	K (m/s)	Est. T (C°)	Viscosity (kg/(m*s))	Density (kg/m^3)	Bulk Perm. (m^2)	log perm	Source
249	252083	5156408	522		1.28E+00	4.52E-06	33.6	7.40E-04	9.95E+02	3.43E-14	-13.47	Burns et al., 2015
250	256206	5155962	202		9.82E+02	3.47E-03	24.1	9.10E-04	9.97E+02	3.22E-11	-10.49	Burns et al., 2015
251	256981	5155065	90		4.19E+02	1.48E-03	18.6	1.04E-03	9.99E+02	1.56E-11	-10.81	Burns et al., 2015
252	216143	5151677	198		5.14E+02	1.81E-03	19.2	1.02E-03	9.98E+02	1.89E-11	-10.72	Burns et al., 2015
253	222809	5153503	479		1.58E+01	5.56E-05	26.6	8.59E-04	9.97E+02	4.88E-13	-12.31	Burns et al., 2015
254	229492	5168663	122		2.27E+02	8.01E-04	17.2	1.07E-03	9.99E+02	8.79E-12	-11.06	Burns et al., 2015
255	239610	5167104	251		2.67E+02	9.40E-04	20.6	9.88E-04	9.98E+02	9.49E-12	-11.02	Burns et al., 2015
256	240511	5166756	230		2.02E+02	7.13E-04	20.0	1.00E-03	9.98E+02	7.29E-12	-11.14	Burns et al., 2015
257	241135	5165400	255		1.89E+03	6.66E-03	20.7	9.86E-04	9.98E+02	6.71E-11	-10.17	Burns et al., 2015
258	242760	5165021	180		3.61E+01	1.27E-04	18.7	1.03E-03	9.98E+02	1.35E-12	-11.87	Burns et al., 2015
259	238924	5178791	190		2.55E+00	8.98E-06	19.0	1.03E-03	9.98E+02	9.43E-14	-13.03	Burns et al., 2015
260	236776	5177339	116		2.77E+02	9.77E-04	17.0	1.08E-03	9.99E+02	1.08E-11	-10.97	Burns et al., 2015
261	248205	5186094	130		4.29E+02	1.51E-03	17.4	1.07E-03	9.99E+02	1.65E-11	-10.78	Burns et al., 2015
262	209029	5076145	131		1.74E+00	6.14E-06	17.0	1.08E-03	9.99E+02	6.77E-14	-13.17	Burns et al., 2015
263	194170	5083291	181		1.34E+01	4.71E-05	18.1	1.05E-03	9.99E+02	5.05E-13	-12.30	Burns et al., 2015
264	203784	5082236	104		4.20E+00	1.48E-05	16.0	1.11E-03	9.99E+02	1.68E-13	-12.78	Burns et al., 2015
265	203113	5082670	93		9.51E+00	3.35E-05	15.4	1.12E-03	9.99E+02	3.85E-13	-12.41	Burns et al., 2015
266	204627	5079969	218		1.24E+00	4.36E-06	18.8	1.03E-03	9.98E+02	4.59E-14	-13.34	Burns et al., 2015
267	202818	5078323	31		3.97E+01	1.40E-04	12.8	1.21E-03	9.99E+02	1.72E-12	-11.76	Burns et al., 2015
268	205907	5077734	152		1.06E+03	3.73E-03	17.6	1.06E-03	9.99E+02	4.05E-11	-10.39	Burns et al., 2015
269	205166	5088542	116		2.81E-01	9.91E-07	16.5	1.09E-03	9.99E+02	1.11E-14	-13.96	Burns et al., 2015
270	187538	5064503	136		1.16E+01	4.07E-05	14.5	1.15E-03	9.99E+02	4.79E-13	-12.32	Burns et al., 2015
271	206142	5064866	85		4.31E+00	1.52E-05	13.1	1.20E-03	9.99E+02	1.85E-13	-12.73	Burns et al., 2015
272	204718	5064562	149		1.36E-01	4.80E-07	14.8	1.14E-03	9.99E+02	5.59E-15	-14.25	Burns et al., 2015
273	205528	5064276	116		1.19E+01	4.21E-05	13.9	1.17E-03	9.99E+02	5.03E-13	-12.30	Burns et al., 2015
274	195895	5071730	188		2.72E+01	9.59E-05	15.9	1.11E-03	9.99E+02	1.09E-12	-11.96	Burns et al., 2015
275	193370	5069286	95		2.25E+01	7.95E-05	13.3	1.19E-03	9.99E+02	9.64E-13	-12.02	Burns et al., 2015
276	192048	5070589	274		2.40E+01	8.47E-05	18.4	1.04E-03	9.99E+02	9.02E-13	-12.04	Burns et al., 2015
277	463966	5144185	47		1.07E+01	3.76E-05	10.3	1.29E-03	1.00E+03	4.95E-13	-12.31	Burns et al., 2015
278	378267	5153697	99		6.64E+01	2.34E-04	18.2	1.05E-03	9.99E+02	2.51E-12	-11.60	Burns et al., 2015
279	492421	5141027	162		1.56E+04	5.50E-02	12.7	1.21E-03	9.99E+02	6.79E-10	-9.17	Burns et al., 2015

Well ID	Easting	Northing	Center Interval Depth (m)	T(m²/d)	K (ft/d)	K (m/s)	Est. T (C°)	Viscosity (kg/(m*s))	Density (kg/m³)	Bulk Perm. (m²)	log perm	Source
280	439580	5164551	37		4.89E+00	1.73E-05	12.6	1.21E-03	9.99E+02	2.13E-13	-12.67	Burns et al. 2015
281	481499	5171022	183		2.42E+02	8.52E-04	12.7	1.21E-03	9.99E+02	1.05E-11	-10.98	Burns et al. 2015
282	437923	5175605	214		8.38E+02	2.95E-03	12.7	1.21E-03	9.99E+02	3.64E-11	-10.44	Burns et al. 2015
283	495115	5173063	70		5.97E+00	2.11E-05	12.6	1.21E-03	9.99E+02	2.61E-13	-12.58	Burns et al. 2015
284	437122	5178415	122		2.14E+01	7.56E-05	12.6	1.21E-03	9.99E+02	9.34E-13	-12.03	Burns et al. 2015
285	486480	5175834	291		3.15E+01	1.11E-04	12.8	1.20E-03	9.99E+02	1.36E-12	-11.87	Burns et al. 2015
286	482844	5203028	21		2.89E+01	1.02E-04	12.6	1.21E-03	9.99E+02	1.26E-12	-11.90	Burns et al. 2015
287	482844	5203028	27		9.15E+01	3.23E-04	12.6	1.21E-03	9.99E+02	3.99E-12	-11.40	Burns et al. 2015
288	489292	5205698	116		1.12E+04	3.95E-02	12.6	1.21E-03	9.99E+02	4.88E-10	-9.31	Burns et al. 2015
289	494032	5214674	128		2.78E+02	9.81E-04	12.6	1.21E-03	9.99E+02	1.21E-11	-10.92	Burns et al. 2015
290	481396	5219516	147		8.28E-01	2.92E-06	12.6	1.21E-03	9.99E+02	3.60E-14	-13.44	Burns et al. 2015
291	485595	5222097	70		1.47E+02	5.19E-04	12.6	1.21E-03	9.99E+02	6.42E-12	-11.19	Burns et al. 2015
292	230642	5153760	390		2.08E+01	7.33E-05	27.3	8.45E-04	9.96E+02	6.34E-13	-12.20	Burns et al. 2015
293	259017	5146087	184		4.69E+02	1.65E-03	23.1	9.31E-04	9.98E+02	1.57E-11	-10.80	Burns et al. 2015
294	261539	5143972	515		4.45E+02	1.57E-03	32.2	7.60E-04	9.95E+02	1.22E-11	-10.91	Burns et al. 2015
295	267886	5143325	337		1.76E+03	6.22E-03	27.4	8.44E-04	9.96E+02	5.37E-11	-10.27	Burns et al. 2015
296	266528	5143037	305		1.76E+02	6.20E-04	26.6	8.59E-04	9.97E+02	5.45E-12	-11.26	Burns et al. 2015
297	467328	5142530	175		1.81E+01	6.38E-05	17.0	1.08E-03	9.99E+02	7.03E-13	-12.15	Burns et al. 2015
298	476595	5149556	48		8.89E+01	3.14E-04	12.9	1.20E-03	9.99E+02	3.84E-12	-11.42	Burns et al. 2015
299	471169	5164951	76		3.51E+00	1.24E-05	13.7	1.18E-03	9.99E+02	1.48E-13	-12.83	Burns et al. 2015
300	196968	5093176	110		6.86E+01	2.42E-04	14.9	1.14E-03	9.99E+02	2.82E-12	-11.55	Burns et al. 2015
301	359144	5206027	296		4.71E+03	1.66E-02	31.3	7.76E-04	9.95E+02	1.32E-10	-9.88	Burns et al. 2015
302	363954	5210300	274		8.74E+03	3.08E-02	29.8	8.01E-04	9.96E+02	2.53E-10	-9.60	Burns et al. 2015
303	361741	5191327	448		5.58E+03	1.97E-02	41.9	6.28E-04	9.92E+02	1.27E-10	-9.90	Burns et al. 2015
304	348248	5198048	263		2.78E+01	9.81E-05	29.0	8.14E-04	9.96E+02	8.18E-13	-12.09	Burns et al. 2015
305	352180	5203848	47		1.15E+01	4.04E-05	15.5	1.12E-03	9.99E+02	4.62E-13	-12.34	Burns et al. 2015
306	370195	5201174	87		4.90E+02	1.73E-03	17.2	1.07E-03	9.99E+02	1.90E-11	-10.72	Burns et al. 2015
307	357607	5212456	299		1.24E+03	4.39E-03	31.5	7.72E-04	9.95E+02	3.47E-11	-10.46	Burns et al. 2015
308	350583	5209293	194		2.67E+01	9.40E-05	24.2	9.08E-04	9.97E+02	8.72E-13	-12.06	Burns et al. 2015
309	352427	5207023	384		1.82E+02	6.43E-04	37.4	6.84E-04	9.93E+02	4.52E-12	-11.34	Burns et al. 2015
310	398173	5096061	352		4.13E+02	1.46E-03	27.3	8.46E-04	9.96E+02	1.26E-11	-10.90	Burns et al. 2015

Well ID	Easting	Northing	Center Interval Depth (m)	T(m^2/d)	K (ft/d)	K (m/s)	Est. T (C°)	Viscosity (kg/(m*s))	Density (kg/m^3)	Bulk Perm. (m^2)	log perm	Source
311	399606	5096871	187		1.81E+03	6.38E-03	24.5	9.01E-04	9.97E+02	5.88E-11	-10.23	Burns et al., 2015
312	402185	5095410	284		2.93E+02	1.03E-03	26.7	8.57E-04	9.97E+02	9.06E-12	-11.04	Burns et al., 2015
313	395989	5091529	323		4.58E+02	1.61E-03	26.9	8.53E-04	9.97E+02	1.41E-11	-10.85	Burns et al., 2015
314	394464	5091709	178		9.26E+03	3.27E-02	23.9	9.13E-04	9.97E+02	3.05E-10	-9.52	Burns et al., 2015
315	395344	5090305	289		4.21E+03	1.49E-02	26.7	8.57E-04	9.97E+02	1.30E-10	-9.89	Burns et al., 2015
316	401285	5103667	407		4.26E+02	1.50E-03	28.4	8.26E-04	9.96E+02	1.27E-11	-10.90	Burns et al., 2015
317	397746	5100143	430		5.81E+01	2.05E-04	28.9	8.17E-04	9.96E+02	1.71E-12	-11.77	Burns et al., 2015
318	414187	5104522	64		2.00E+01	7.06E-05	16.1	1.11E-03	9.99E+02	7.97E-13	-12.10	Burns et al., 2015
319	396630	5104083	832		3.35E+00	1.18E-05	42.1	6.26E-04	9.91E+02	7.61E-14	-13.12	Burns et al., 2015
320	406104	5108283	242		1.36E+02	4.79E-04	21.4	9.69E-04	9.98E+02	4.74E-12	-11.32	Burns et al., 2015
321	406248	5107880	136		2.40E+00	8.46E-06	17.6	1.06E-03	9.99E+02	9.18E-14	-13.04	Burns et al., 2015
322	391475	5108988	165		3.32E+02	1.17E-03	18.7	1.03E-03	9.99E+02	1.24E-11	-10.91	Burns et al., 2015
323	398046	5111715	214		7.05E+01	2.49E-04	20.4	9.92E-04	9.98E+02	2.52E-12	-11.60	Burns et al., 2015
324	411605	5125057	109		4.95E+02	1.75E-03	16.7	1.09E-03	9.99E+02	1.94E-11	-10.71	Burns et al., 2015
325	411426	5124504	104		1.39E+03	4.91E-03	16.5	1.09E-03	9.99E+02	5.48E-11	-10.26	Burns et al., 2015
326	495295	5131456	69		6.42E+01	2.27E-04	14.6	1.15E-03	9.99E+02	2.66E-12	-11.58	Burns et al., 2015
327	332166	5151742	213		1.11E+01	3.92E-05	23.3	9.26E-04	9.98E+02	3.71E-13	-12.43	Burns et al., 2015
328	331445	5149600	284		2.64E+01	9.32E-05	25.6	8.77E-04	9.97E+02	8.37E-13	-12.08	Burns et al., 2015
329	318005	5173776	427		1.04E+03	3.67E-03	34.3	7.28E-04	9.94E+02	2.74E-11	-10.56	Burns et al., 2015
330	285679	5162788	306		1.83E+03	6.46E-03	27.2	8.48E-04	9.96E+02	5.60E-11	-10.25	Burns et al., 2015
331	284672	5162639	296		1.98E+03	6.97E-03	26.8	8.56E-04	9.97E+02	6.10E-11	-10.21	Burns et al., 2015
332	282200	5168538	38		1.01E+02	3.56E-04	15.9	1.11E-03	9.99E+02	4.04E-12	-11.39	Burns et al., 2015
333	279039	5176379	410		9.80E+01	3.46E-04	25.2	8.86E-04	9.97E+02	3.13E-12	-11.50	Burns et al., 2015
334	279015	5171095	72		4.70E+02	1.66E-03	16.7	1.09E-03	9.99E+02	1.84E-11	-10.73	Burns et al., 2015
335	293987	5174612	159		2.63E+02	9.29E-04	18.9	1.03E-03	9.98E+02	9.76E-12	-11.01	Burns et al., 2015
336	278725	5180532	129		4.35E+01	1.54E-04	18.2	1.05E-03	9.99E+02	1.64E-12	-11.78	Burns et al., 2015
337	356592	5167266	404		2.42E+02	8.53E-04	26.0	8.70E-04	9.97E+02	7.59E-12	-11.12	Burns et al., 2015
338	358003	5165751	199		1.25E+03	4.40E-03	20.1	1.00E-03	9.98E+02	4.49E-11	-10.35	Burns et al., 2015
339	355453	5171185	443		2.85E+01	1.00E-04	27.2	8.48E-04	9.97E+02	8.71E-13	-12.06	Burns et al., 2015
340	350502	5178131	366		2.44E+02	8.61E-04	24.9	8.92E-04	9.97E+02	7.85E-12	-11.10	Burns et al., 2015
341	367992	5185658	202		2.50E+02	8.81E-04	20.2	9.98E-04	9.98E+02	8.98E-12	-11.05	Burns et al., 2015

Well ID	Easting	Northing	Center Interval Depth (m)	T(m^2/d)	K (ft/d)	K (m/s)	Est. T (C°)	Viscosity (kg/(m*s))	Density (kg/m^3)	Bulk Perm. (m^2)	log perm	Source
342	366762	5183709	184		2.36E+03	8.34E-03	19.6	1.01E-03	9.98E+02	8.61E-11	-10.06	Burns et al. 2015
343	373267	5182456	233		2.29E+00	8.07E-06	21.1	9.77E-04	9.98E+02	8.05E-14	-13.09	Burns et al. 2015
344	367918	5189952	248		5.47E+04	1.93E-01	21.5	9.67E-04	9.98E+02	1.90E-09	-8.72	Burns et al. 2015
345	363383	5188078	387		4.81E+02	1.70E-03	25.5	8.80E-04	9.97E+02	1.53E-11	-10.82	Burns et al. 2015
346	365109	5188502	275		2.59E+02	9.14E-04	22.3	9.49E-04	9.98E+02	8.86E-12	-11.05	Burns et al. 2015
347	347875	5186722	236		6.37E+01	2.25E-04	28.6	8.22E-04	9.96E+02	1.89E-12	-11.72	Burns et al. 2015
348	348058	5188076	244		2.20E+02	7.75E-04	29.6	8.05E-04	9.96E+02	6.39E-12	-11.19	Burns et al. 2015
349	347896	5188358	213		1.78E+01	6.26E-05	28.0	8.33E-04	9.96E+02	5.34E-13	-12.27	Burns et al. 2015
350	342965	5203991	97		8.60E+01	3.03E-04	21.8	9.58E-04	9.98E+02	2.97E-12	-11.53	Burns et al. 2015
351	344568	5203856	253		2.42E+02	8.53E-04	30.1	7.96E-04	9.96E+02	6.95E-12	-11.16	Burns et al. 2015
352	335611	5187200	276		1.59E+02	5.61E-04	32.1	7.62E-04	9.95E+02	4.37E-12	-11.36	Burns et al. 2015
353	334829	5187314	308		7.48E+01	2.64E-04	35.0	7.18E-04	9.94E+02	1.94E-12	-11.71	Burns et al. 2015
354	334020	5187934	369		2.19E+02	7.71E-04	40.6	6.44E-04	9.92E+02	5.10E-12	-11.29	Burns et al. 2015
355	346966	5186807	317		7.84E+01	2.77E-04	35.9	7.06E-04	9.94E+02	2.00E-12	-11.70	Burns et al. 2015
356	323990	5198603	55		2.40E+00	8.47E-06	15.7	1.12E-03	9.99E+02	9.65E-14	-13.02	Burns et al. 2015
357	334195	5189679	318		1.74E+02	6.12E-04	36.0	7.05E-04	9.94E+02	4.42E-12	-11.35	Burns et al. 2015
358	335392	5188503	274		1.97E+02	6.95E-04	32.0	7.64E-04	9.95E+02	5.44E-12	-11.26	Burns et al. 2015
359	340612	5194262	120		1.36E+01	4.78E-05	18.4	1.04E-03	9.99E+02	5.09E-13	-12.29	Burns et al. 2015
360	341377	5201531	229		5.90E+01	2.08E-04	27.8	8.35E-04	9.96E+02	1.78E-12	-11.75	Burns et al. 2015
361	334263	5210405	98		2.25E+04	7.93E-02	17.2	1.07E-03	9.99E+02	8.69E-10	-9.06	Burns et al. 2015
362	334920	5207452	139		6.16E+01	2.17E-04	19.9	1.01E-03	9.98E+02	2.23E-12	-11.65	Burns et al. 2015
363	374558	5219517	79		6.08E+00	2.14E-05	11.1	1.26E-03	1.00E+03	2.76E-13	-12.56	Burns et al. 2015
364	405888	5225359	123		8.92E+00	3.15E-05	13.6	1.18E-03	9.99E+02	3.78E-13	-12.42	Burns et al. 2015
365	400004	5225377	47		1.41E+01	4.99E-05	9.0	1.34E-03	1.00E+03	6.80E-13	-12.17	Burns et al. 2015
366	400001	5220128	172		8.76E+01	3.09E-04	16.8	1.09E-03	9.99E+02	3.42E-12	-11.47	Burns et al. 2015
367	404537	5219916	199		3.30E+02	1.17E-03	19.0	1.03E-03	9.98E+02	1.22E-11	-10.91	Burns et al. 2015
368	429375	5219414	41		1.32E+01	4.65E-05	8.5	1.36E-03	1.00E+03	6.43E-13	-12.19	Burns et al. 2015
369	441700	5221379	46		1.27E+01	4.46E-05	8.9	1.34E-03	1.00E+03	6.11E-13	-12.21	Burns et al. 2015
370	452832	5222731	107		3.70E+00	1.30E-05	13.3	1.19E-03	9.99E+02	1.58E-13	-12.80	Burns et al. 2015
371	454453	5217223	61		7.18E+00	2.53E-05	10.1	1.30E-03	1.00E+03	3.35E-13	-12.47	Burns et al. 2015
372	461987	5221986	56		8.59E+00	3.03E-05	9.7	1.31E-03	1.00E+03	4.05E-13	-12.39	Burns et al. 2015

Well ID	Easting	Northing	Center Interval Depth (m)	T(m^2/d)	K (ft/d)	K (m/s)	Est. T (C°)	Viscosity (kg/(m*s))	Density (kg/m^3)	Bulk Perm. (m^2)	log perm	Source
373	372468	5232069	229		9.43E+01	3.33E-04	21.5	9.67E-04	9.98E+02	3.29E-12	-11.48	Burns et al., 2015
374	429474	5225957	35		1.01E+01	3.55E-05	8.1	1.37E-03	1.00E+03	4.98E-13	-12.30	Burns et al., 2015
375	372959	5241169	207		1.53E+03	5.40E-03	19.7	1.01E-03	9.98E+02	5.57E-11	-10.25	Burns et al., 2015
376	383584	5238942	225		2.34E+01	8.25E-05	21.1	9.75E-04	9.98E+02	8.21E-13	-12.09	Burns et al., 2015
377	385729	5236862	234		1.12E+02	3.94E-04	22.0	9.56E-04	9.98E+02	3.85E-12	-11.41	Burns et al., 2015
378	390462	5242763	185		3.55E+02	1.25E-03	17.8	1.06E-03	9.99E+02	1.35E-11	-10.87	Burns et al., 2015
379	424880	5240432	108		1.09E+01	3.84E-05	13.3	1.19E-03	9.99E+02	4.65E-13	-12.33	Burns et al., 2015
380	421406	5239737	61		3.82E+00	1.35E-05	10.1	1.30E-03	1.00E+03	1.79E-13	-12.75	Burns et al., 2015
381	372296	5247391	227		3.36E+02	1.19E-03	21.3	9.70E-04	9.98E+02	1.18E-11	-10.93	Burns et al., 2015
382	386445	5247811	160		1.39E+03	4.90E-03	15.8	1.11E-03	9.99E+02	5.57E-11	-10.25	Burns et al., 2015
383	395946	5248932	107		1.35E+02	4.75E-04	13.3	1.19E-03	9.99E+02	5.76E-12	-11.24	Burns et al., 2015
384	301000	5125744	209		3.70E+03	1.30E-02	21.1	9.76E-04	9.98E+02	1.30E-10	-9.89	Burns et al., 2015
385	331904	5178252	93		1.92E+01	6.76E-05	17.3	1.07E-03	9.99E+02	7.38E-13	-12.13	Burns et al., 2015
386	333235	5176485	221		1.12E+03	3.95E-03	22.8	9.37E-04	9.98E+02	3.78E-11	-10.42	Burns et al., 2015
387	335684	5174379	107		7.73E+00	2.73E-05	17.9	1.05E-03	9.99E+02	2.93E-13	-12.53	Burns et al., 2015
388	333896	5171185	152		1.06E+02	3.75E-04	19.9	1.01E-03	9.98E+02	3.85E-12	-11.41	Burns et al., 2015
389	341164	5175900	113		3.10E+01	1.09E-04	18.2	1.05E-03	9.99E+02	1.17E-12	-11.93	Burns et al., 2015
390	343921	5174901	132		4.17E+01	1.47E-04	19.0	1.03E-03	9.98E+02	1.54E-12	-11.81	Burns et al., 2015
391	341730	5173198	219		9.43E+00	3.33E-05	22.7	9.39E-04	9.98E+02	3.19E-13	-12.50	Burns et al., 2015
392	328590	5182701	72		8.47E+02	2.99E-03	16.5	1.09E-03	9.99E+02	3.34E-11	-10.48	Burns et al., 2015
393	280560	5198700	325		4.89E+01	1.72E-04	25.5	8.80E-04	9.97E+02	1.55E-12	-11.81	Burns et al., 2015
394	275634	5193875	53		3.59E+02	1.27E-03	12.3	1.22E-03	9.99E+02	1.58E-11	-10.80	Burns et al., 2015
395	290168	5198478	244		3.38E+01	1.19E-04	21.7	9.63E-04	9.98E+02	1.17E-12	-11.93	Burns et al., 2015
396	285839	5198848	247		3.63E-01	1.28E-06	21.8	9.59E-04	9.98E+02	1.25E-14	-13.90	Burns et al., 2015
397	290839	5198269	259		1.53E+01	5.38E-05	22.4	9.46E-04	9.98E+02	5.20E-13	-12.28	Burns et al., 2015
398	309847	5193339	78		2.57E+00	9.08E-06	13.9	1.17E-03	9.99E+02	1.08E-13	-12.96	Burns et al., 2015
399	269003	5203865	95		1.63E+01	5.74E-05	14.7	1.15E-03	9.99E+02	6.70E-13	-12.17	Burns et al., 2015
400	279168	5209136	98		2.22E+00	7.84E-06	14.9	1.14E-03	9.99E+02	9.12E-14	-13.04	Burns et al., 2015
401	287338	5201081	135		1.38E+01	4.88E-05	16.7	1.09E-03	9.99E+02	5.42E-13	-12.27	Burns et al., 2015
402	283566	5201000	52		3.34E+01	1.18E-04	12.2	1.22E-03	1.00E+03	1.47E-12	-11.83	Burns et al., 2015
403	300336	5207399	240		2.91E+02	1.02E-03	21.5	9.67E-04	9.98E+02	1.01E-11	-10.99	Burns et al., 2015

Well ID	Easting	Northing	Center Interval Depth (m)	T(m^2/d)	K (ft/d)	K (m/s)	Est. T (C°)	Viscosity (kg/(m*s))	Density (kg/m^3)	Bulk Perm. (m^2)	log perm	Source
404	298638	5208476	137		7.68E+01	2.71E-04	16.8	1.08E-03	9.99E+02	3.00E-12	-11.52	Burns et al. 2015
405	298467	5205917	292		1.29E+01	4.54E-05	23.9	9.12E-04	9.97E+02	4.23E-13	-12.37	Burns et al. 2015
406	296031	5199384	34		2.49E+03	8.79E-03	11.0	1.27E-03	1.00E+03	1.13E-10	-9.95	Burns et al. 2015
407	302628	5201915	48		1.46E+01	5.14E-05	12.0	1.23E-03	1.00E+03	6.46E-13	-12.19	Burns et al. 2015
408	323776	5201531	153		6.52E-01	2.30E-06	17.4	1.07E-03	9.99E+02	2.51E-14	-13.60	Burns et al. 2015
409	278494	5210923	38		5.39E+02	1.90E-03	11.3	1.25E-03	1.00E+03	2.43E-11	-10.61	Burns et al. 2015
410	281253	5210079	204		5.89E+02	2.08E-03	19.8	1.01E-03	9.98E+02	2.14E-11	-10.67	Burns et al. 2015
411	285957	5218561	97		2.14E+02	7.54E-04	14.8	1.14E-03	9.99E+02	8.79E-12	-11.06	Burns et al. 2015
412	285235	5218464	85		2.02E+02	7.13E-04	14.2	1.16E-03	9.99E+02	8.44E-12	-11.07	Burns et al. 2015
413	283118	5218294	108		6.36E+00	2.24E-05	15.0	1.14E-03	9.99E+02	2.60E-13	-12.59	Burns et al. 2015
414	289052	5211806	223		2.54E+01	8.97E-05	20.7	9.86E-04	9.98E+02	9.03E-13	-12.04	Burns et al. 2015
415	296020	5217805	226		1.06E+02	3.73E-04	20.8	9.83E-04	9.98E+02	3.75E-12	-11.43	Burns et al. 2015
416	296158	5214432	491		6.44E+02	2.27E-03	33.4	7.42E-04	9.95E+02	1.73E-11	-10.76	Burns et al. 2015
417	298549	5212713	218		2.85E+03	1.01E-02	20.4	9.92E-04	9.98E+02	1.02E-10	-9.99	Burns et al. 2015
418	294754	5211699	157		7.41E+01	2.61E-04	17.6	1.06E-03	9.99E+02	2.84E-12	-11.55	Burns et al. 2015
419	298545	5209468	293		2.69E+02	9.49E-04	24.0	9.12E-04	9.97E+02	8.84E-12	-11.05	Burns et al. 2015
420	301603	5209242	218		5.65E+02	1.99E-03	20.4	9.92E-04	9.98E+02	2.02E-11	-10.69	Burns et al. 2015
421	303125	5209902	137		1.31E+02	4.62E-04	16.8	1.08E-03	9.99E+02	5.11E-12	-11.29	Burns et al. 2015
422	311033	5216010	149		1.68E+03	5.92E-03	17.3	1.07E-03	9.99E+02	6.49E-11	-10.19	Burns et al. 2015
423	311030	5215238	153		5.34E+03	1.88E-02	17.4	1.07E-03	9.99E+02	2.05E-10	-9.69	Burns et al. 2015
424	281756	5219734	84		3.44E+02	1.21E-03	14.2	1.16E-03	9.99E+02	1.44E-11	-10.84	Burns et al. 2015
425	285249	5219421	86		6.97E+02	2.46E-03	14.3	1.16E-03	9.99E+02	2.90E-11	-10.54	Burns et al. 2015
426	294684	5227957	111		4.46E+02	1.57E-03	15.6	1.12E-03	9.99E+02	1.80E-11	-10.74	Burns et al. 2015
427	295005	5226277	220		1.15E+02	4.04E-04	20.5	9.89E-04	9.98E+02	4.08E-12	-11.39	Burns et al. 2015
428	294849	5225448	44		1.64E+03	5.80E-03	11.7	1.24E-03	1.00E+03	7.34E-11	-10.13	Burns et al. 2015
429	291530	5220990	91		1.40E+02	4.93E-04	14.5	1.15E-03	9.99E+02	5.79E-12	-11.24	Burns et al. 2015
430	305570	5226446	133		1.58E+02	5.56E-04	16.6	1.09E-03	9.99E+02	6.19E-12	-11.21	Burns et al. 2015
431	309449	5225176	215		1.43E+01	5.04E-05	20.3	9.95E-04	9.98E+02	5.12E-13	-12.29	Burns et al. 2015
432	305826	5223965	237		3.88E+01	1.37E-04	21.3	9.70E-04	9.98E+02	1.36E-12	-11.87	Burns et al. 2015
433	309661	5219299	157		1.54E+02	5.44E-04	17.6	1.06E-03	9.99E+02	5.92E-12	-11.23	Burns et al. 2015
434	311264	5219958	140		1.26E+02	4.45E-04	17.0	1.08E-03	9.99E+02	4.91E-12	-11.31	Burns et al. 2015

Well ID	Easting	Northing	Center Interval Depth (m)	T(m^2/d)	K (ft/d)	K (m/s)	Est. T (C°)	Viscosity (kg/(m*s))	Density (kg/m^3)	Bulk Perm. (m^2)	log perm	Source
435	310988	5219905	140		1.84E+03	6.48E-03	17.0	1.08E-03	9.99E+02	7.15E-11	-10.15	Burns et al., 2015
436	274388	5237382	27		6.28E+03	2.21E-02	10.6	1.28E-03	1.00E+03	2.89E-10	-9.54	Burns et al., 2015
437	276243	5235240	73		2.18E+00	7.69E-06	13.5	1.18E-03	9.99E+02	9.26E-14	-13.03	Burns et al., 2015
438	280453	5233506	19		8.15E+02	2.88E-03	10.0	1.30E-03	1.00E+03	3.81E-11	-10.42	Burns et al., 2015
439	283507	5235248	120		1.23E+03	4.35E-03	16.0	1.11E-03	9.99E+02	4.91E-11	-10.31	Burns et al., 2015
440	294831	5233422	48		1.38E+02	4.88E-04	12.0	1.23E-03	1.00E+03	6.13E-12	-11.21	Burns et al., 2015
441	296573	5232651	199		6.89E+01	2.43E-04	19.5	1.01E-03	9.98E+02	2.52E-12	-11.60	Burns et al., 2015
442	294284	5229207	108		4.65E+02	1.64E-03	15.4	1.12E-03	9.99E+02	1.88E-11	-10.73	Burns et al., 2015
443	302405	5233256	87		7.64E+01	2.69E-04	14.3	1.16E-03	9.99E+02	3.18E-12	-11.50	Burns et al., 2015
444	310529	5229931	146		2.62E+02	9.22E-04	17.2	1.07E-03	9.99E+02	1.01E-11	-10.99	Burns et al., 2015
445	309437	5230028	161		5.75E+02	2.03E-03	17.7	1.06E-03	9.99E+02	2.20E-11	-10.66	Burns et al., 2015
446	308281	5243692	564		6.89E+01	2.43E-04	36.9	6.91E-04	9.93E+02	1.72E-12	-11.76	Burns et al., 2015
447	352580	5216563	200		4.55E+03	1.60E-02	27.6	8.39E-04	9.96E+02	1.38E-10	-9.86	Burns et al., 2015
448	349028	5225363	183		3.33E+03	1.18E-02	27.6	8.41E-04	9.96E+02	1.01E-10	-10.00	Burns et al., 2015
449	348583	5222811	508		3.10E+03	1.09E-02	50.4	5.40E-04	9.88E+02	6.09E-11	-10.22	Burns et al., 2015
450	338677	5215844	188		9.17E+01	3.24E-04	27.6	8.40E-04	9.96E+02	2.78E-12	-11.56	Burns et al., 2015
451	331481	5214345	159		5.64E+02	1.99E-03	27.3	8.45E-04	9.96E+02	1.72E-11	-10.76	Burns et al., 2015
452	347013	5215870	38		8.54E+02	3.01E-03	25.7	8.76E-04	9.97E+02	2.70E-11	-10.57	Burns et al., 2015
453	349990	5213416	240		1.64E+02	5.77E-04	28.2	8.29E-04	9.96E+02	4.89E-12	-11.31	Burns et al., 2015
454	325547	5225761	223		2.06E+03	7.25E-03	27.8	8.37E-04	9.96E+02	6.20E-11	-10.21	Burns et al., 2015
455	328820	5222360	246		3.30E+02	1.16E-03	28.4	8.25E-04	9.96E+02	9.82E-12	-11.01	Burns et al., 2015
456	326029	5223523	335		7.48E+02	2.64E-03	35.2	7.15E-04	9.94E+02	1.93E-11	-10.71	Burns et al., 2015
457	329068	5219535	305		5.95E+02	2.10E-03	32.6	7.55E-04	9.95E+02	1.62E-11	-10.79	Burns et al., 2015
458	332159	5224118	83		3.33E+01	1.18E-04	26.3	8.64E-04	9.97E+02	1.04E-12	-11.98	Burns et al., 2015
459	334021	5222120	204		6.77E+01	2.39E-04	27.7	8.39E-04	9.96E+02	2.05E-12	-11.69	Burns et al., 2015
460	341767	5221691	308		3.01E+02	1.06E-03	32.8	7.51E-04	9.95E+02	8.16E-12	-11.09	Burns et al., 2015
461	355548	5223224	202		7.05E+01	2.49E-04	27.6	8.39E-04	9.96E+02	2.13E-12	-11.67	Burns et al., 2015
462	357764	5222521	192		3.61E+01	1.27E-04	27.6	8.40E-04	9.96E+02	1.09E-12	-11.96	Burns et al., 2015
463	365468	5221199	221		9.59E+02	3.38E-03	27.8	8.37E-04	9.96E+02	2.90E-11	-10.54	Burns et al., 2015
464	322896	5232235	245		1.17E+02	4.12E-04	28.4	8.25E-04	9.96E+02	3.48E-12	-11.46	Burns et al., 2015
465	323365	5228885	221		2.76E+02	9.73E-04	27.8	8.37E-04	9.96E+02	8.33E-12	-11.08	Burns et al., 2015

Well ID	Easting	Northing	Center Interval Depth (m)	T(m²/d)	K (ft/d)	K (m/s)	Est. T (C°)	Viscosity (kg/(m*s))	Density (kg/m³)	Bulk Perm. (m²)	log perm	Source
466	323710	5227762	217		1.88E+02	6.64E-04	27.7	8.38E-04	9.96E+02	5.69E-12	-11.24	Burns et al. 2015
467	335476	5227454	201		3.63E+01	1.28E-04	27.6	8.39E-04	9.96E+02	1.10E-12	-11.96	Burns et al. 2015
468	346866	5230577	366		4.73E+02	1.67E-03	38.0	6.77E-04	9.93E+02	1.16E-11	-10.94	Burns et al. 2015
469	341203	5229738	164		8.59E-01	3.03E-06	27.4	8.44E-04	9.96E+02	2.62E-14	-13.58	Burns et al. 2015
470	351552	5213608	160		4.23E+01	1.49E-04	27.4	8.44E-04	9.96E+02	1.29E-12	-11.89	Burns et al. 2015
471	350437	5213605	183		5.99E+02	2.11E-03	27.6	8.41E-04	9.96E+02	1.82E-11	-10.74	Burns et al. 2015
472	273604	5100435	512		8.84E+02	3.12E-03	34.9	7.20E-04	9.94E+02	2.30E-11	-10.64	Burns et al. 2015
473	274683	5096651	398		1.12E+02	3.94E-04	30.7	7.85E-04	9.95E+02	3.16E-12	-11.50	Burns et al. 2015
474	253025	5058534	81		1.37E+01	4.84E-05	23.5	9.23E-04	9.97E+02	4.56E-13	-12.34	Burns et al. 2015
475	256266	5066010	235		7.76E+03	2.74E-02	25.3	8.85E-04	9.97E+02	2.48E-10	-9.61	Burns et al. 2015
476	255747	5066030	240		5.35E+03	1.89E-02	25.4	8.83E-04	9.97E+02	1.70E-10	-9.77	Burns et al. 2015
477	275819	5099452	63		2.24E+02	7.89E-04	23.1	9.30E-04	9.98E+02	7.50E-12	-11.13	Burns et al. 2015
478	277432	5094017	448		4.58E+01	1.62E-04	32.6	7.55E-04	9.95E+02	1.25E-12	-11.90	Burns et al. 2015
479	266630	5107551	305		7.60E-02	2.68E-07	27.4	8.44E-04	9.96E+02	2.31E-15	-14.64	Burns et al. 2015
480	277107	5103485	261		5.71E+02	2.01E-03	25.9	8.73E-04	9.97E+02	1.80E-11	-10.75	Burns et al. 2015
481	268562	5121664	306		2.18E+01	7.68E-05	26.5	8.61E-04	9.97E+02	6.77E-13	-12.17	Burns et al. 2015
482	267865	5119125	152		1.10E+01	3.87E-05	17.9	1.06E-03	9.99E+02	4.17E-13	-12.38	Burns et al. 2015
483	258860	5124882	95		9.73E+00	3.43E-05	14.7	1.14E-03	9.99E+02	4.01E-13	-12.40	Burns et al. 2015
484	256104	5125146	293		3.04E+01	1.07E-04	25.7	8.76E-04	9.97E+02	9.39E-13	-12.02	Burns et al. 2015
485	255720	5125193	55		2.90E+01	1.02E-04	13.4	1.19E-03	9.99E+02	1.24E-12	-11.91	Burns et al. 2015
486	276575	5131317	64		7.53E+01	2.66E-04	13.7	1.18E-03	9.99E+02	3.19E-12	-11.50	Burns et al. 2015
487	272687	5127567	32		1.89E+02	6.68E-04	12.6	1.21E-03	9.99E+02	8.26E-12	-11.08	Burns et al. 2015
488	276551	5124386	36		1.01E+02	3.56E-04	12.7	1.21E-03	9.99E+02	4.38E-12	-11.36	Burns et al. 2015
489	268197	5134659	479		3.31E+01	1.17E-04	36.1	7.03E-04	9.94E+02	8.41E-13	-12.07	Burns et al. 2015
490	259845	5135168	270		1.12E+03	3.96E-03	24.5	9.02E-04	9.97E+02	3.65E-11	-10.44	Burns et al. 2015
491	259907	5133496	128		4.57E+01	1.61E-04	16.6	1.09E-03	9.99E+02	1.80E-12	-11.75	Burns et al. 2015
492	267645	5133072	323		1.72E+02	6.07E-04	27.4	8.43E-04	9.96E+02	5.23E-12	-11.28	Burns et al. 2015
493	272470	5139566	37		1.50E+01	5.30E-05	12.8	1.21E-03	9.99E+02	6.52E-13	-12.19	Burns et al. 2015
494	390688	5093658	478		1.31E+01	4.63E-05	24.9	8.92E-04	9.97E+02	4.22E-13	-12.37	Burns et al. 2015
495	355169	5241271	660		2.77E+02	9.76E-04	41.2	6.37E-04	9.92E+02	6.39E-12	-11.19	Burns et al. 2015
496	338147	5254102	112		2.13E+02	7.50E-04	29.9	8.00E-04	9.96E+02	6.14E-12	-11.21	Burns et al. 2015

Well ID	Easting	Northing	Center Interval Depth (m)	T(m^2/d)	K (ft/d)	K (m/s)	Est. T (C°)	Viscosity (kg/(m*s))	Density (kg/m^3)	Bulk Perm. (m^2)	log perm	Source
497	351005	5235259	187		5.41E+01	1.91E-04	31.4	7.74E-04	9.95E+02	1.51E-12	-11.82	Burns et al., 2015
498	349294	5244013	244		3.08E+02	1.09E-03	32.6	7.55E-04	9.95E+02	8.41E-12	-11.08	Burns et al., 2015
499	348733	5242606	50		2.13E+02	7.51E-04	24.6	8.99E-04	9.97E+02	6.90E-12	-11.16	Burns et al., 2015
500	348217	5238913	175		7.56E+01	2.67E-04	31.1	7.78E-04	9.95E+02	2.13E-12	-11.67	Burns et al., 2015
501	357605	5240347	229		2.16E+02	7.62E-04	32.2	7.60E-04	9.95E+02	5.93E-12	-11.23	Burns et al., 2015
502	359127	5240742	198		1.75E+02	6.16E-04	31.6	7.70E-04	9.95E+02	4.86E-12	-11.31	Burns et al., 2015
503	360747	5237275	227		9.54E+01	3.37E-04	32.2	7.61E-04	9.95E+02	2.62E-12	-11.58	Burns et al., 2015
504	340459	5254316	109		6.18E+01	2.18E-04	29.8	8.01E-04	9.96E+02	1.79E-12	-11.75	Burns et al., 2015
505	348591	5248541	472		4.62E+02	1.63E-03	37.3	6.86E-04	9.93E+02	1.15E-11	-10.94	Burns et al., 2015
506	359696	5249624	213		3.53E+03	1.25E-02	31.9	7.65E-04	9.95E+02	9.77E-11	-10.01	Burns et al., 2015
507	360855	5246292	26		1.42E+04	5.01E-02	20.2	9.97E-04	9.98E+02	5.09E-10	-9.29	Burns et al., 2015
508	259531	5240597	46		8.31E+00	2.93E-05	8.4	1.36E-03	1.00E+03	4.07E-13	-12.39	Burns et al., 2015
509	264187	5242851	30		2.61E+02	9.20E-04	7.9	1.38E-03	1.00E+03	1.29E-11	-10.89	Burns et al., 2015
510	265460	5243110	40		1.04E+02	3.67E-04	8.2	1.37E-03	1.00E+03	5.12E-12	-11.29	Burns et al., 2015
511	265384	5242803	63		2.64E+01	9.32E-05	8.8	1.35E-03	1.00E+03	1.28E-12	-11.89	Burns et al., 2015
512	269097	5281332	223		8.19E-01	2.89E-06	14.9	1.14E-03	9.99E+02	3.36E-14	-13.47	Burns et al., 2015
513	269486	5281131	176		4.79E+00	1.69E-05	13.0	1.20E-03	9.99E+02	2.06E-13	-12.69	Burns et al., 2015
514	319980	5262016	122		8.87E+01	3.13E-04	11.8	1.24E-03	1.00E+03	3.95E-12	-11.40	Burns et al., 2015
515	328921	5274847	38		3.19E+03	1.12E-02	8.9	1.34E-03	1.00E+03	1.54E-10	-9.81	Burns et al., 2015
516	328477	5275355	168		8.38E+03	2.96E-02	13.3	1.19E-03	9.99E+02	3.58E-10	-9.45	Burns et al., 2015
517	337841	5271750	316		3.36E+02	1.19E-03	18.8	1.03E-03	9.98E+02	1.25E-11	-10.90	Burns et al., 2015
518	337805	5280216	311		1.34E+03	4.72E-03	18.6	1.04E-03	9.99E+02	4.99E-11	-10.30	Burns et al., 2015
519	238434	5061200	177		4.04E+01	1.42E-04	20.1	9.99E-04	9.98E+02	1.45E-12	-11.84	Burns et al., 2015
520	212024	5076250	40		5.06E+03	1.78E-02	16.1	1.10E-03	9.99E+02	2.01E-10	-9.70	Burns et al., 2015
521	212532	5070845	305		2.45E+01	8.63E-05	20.8	9.83E-04	9.98E+02	8.66E-13	-12.06	Burns et al., 2015
522	212837	5068543	140		1.44E+01	5.06E-05	19.7	1.01E-03	9.98E+02	5.22E-13	-12.28	Burns et al., 2015
523	214363	5080502	155		7.55E+00	2.66E-05	19.9	1.00E-03	9.98E+02	2.73E-13	-12.56	Burns et al., 2015
524	219257	5078763	48		9.31E+00	3.28E-05	16.5	1.09E-03	9.99E+02	3.66E-13	-12.44	Burns et al., 2015
525	220546	5078582	57		1.23E+01	4.33E-05	16.9	1.08E-03	9.99E+02	4.78E-13	-12.32	Burns et al., 2015
526	344974	5127836	64		1.61E+02	5.68E-04	15.6	1.12E-03	9.99E+02	6.49E-12	-11.19	Burns et al., 2015
527	343563	5137940	70		2.87E-01	1.01E-06	15.8	1.11E-03	9.99E+02	1.15E-14	-13.94	Burns et al., 2015

Well ID	Easting	Northing	Center Interval Depth (m)	T(m²/d)	K (ft/d)	K (m/s)	Est. T (C°)	Viscosity (kg/(m*s))	Density (kg/m³)	Bulk Perm. (m²)	log perm	Source
528	345124	5129531	45		1.50E+03	5.31E-03	14.3	1.16E-03	9.99E+02	6.27E-11	-10.20	Burns et al. 2015
529	349939	5137317	23		1.02E+04	3.60E-02	12.9	1.20E-03	9.99E+02	4.41E-10	-9.36	Burns et al. 2015
530	340452	5148893	33		1.90E+01	6.70E-05	13.6	1.18E-03	9.99E+02	8.06E-13	-12.09	Burns et al. 2015
531	345679	5140450	91		2.39E+00	8.42E-06	16.4	1.10E-03	9.99E+02	9.43E-14	-13.03	Burns et al. 2015
532	350925	5146990	399		6.91E+02	2.44E-03	23.1	9.30E-04	9.98E+02	2.32E-11	-10.64	Burns et al. 2015
533	352171	5146465	340		1.65E+02	5.82E-04	21.8	9.59E-04	9.98E+02	5.71E-12	-11.24	Burns et al. 2015
534	352172	5145631	348		1.93E+03	6.82E-03	22.0	9.55E-04	9.98E+02	6.65E-11	-10.18	Burns et al. 2015
535	353854	5146332	354		6.57E+02	2.32E-03	22.1	9.52E-04	9.98E+02	2.25E-11	-10.65	Burns et al. 2015
536	359696	5145144	206		1.38E+01	4.86E-05	18.9	1.03E-03	9.98E+02	5.11E-13	-12.29	Burns et al. 2015
537	361112	5138904	205		1.15E+00	4.06E-06	18.8	1.03E-03	9.98E+02	4.28E-14	-13.37	Burns et al. 2015
538	346249	5108688	50		1.38E+01	4.88E-05	21.2	9.74E-04	9.98E+02	4.86E-13	-12.31	Burns et al. 2015
539	337149	5118651	169		2.65E+02	9.36E-04	26.0	8.71E-04	9.97E+02	8.33E-12	-11.08	Burns et al. 2015
540	344727	5119813	20		5.84E+04	2.06E-01	19.2	1.02E-03	9.98E+02	2.15E-09	-8.67	Burns et al. 2015
DC-6	316331	5162131	776	2.79E+00	3.52E-07	4.57E+01	44.8	9.89E+02	5.93E-04	2.16E-14	-13.67	Spane, FA (2013)
DC-6	316331	5162131	852	9.29E-01	1.80E-07	4.79E+01	47.7	9.88E+02	5.66E-04	1.05E-14	-13.98	Spane, FA (2013)
DC-6	316331	5162131	925	4.65E-03	2.05E-09	5.01E+01	50.5	9.87E+02	5.39E-04	1.14E-16	-15.94	Spane, FA (2013)
DC-6	316331	5162131	1032	9.29E-01	1.23E-07	5.53E+01	54.6	9.86E+02	5.04E-04	6.41E-15	-14.19	Spane, FA (2013)
DC-6	316331	5162131	1121	8.36E+00	1.08E-06	5.38E+01	58.0	9.84E+02	4.77E-04	5.34E-14	-13.27	Spane, FA (2013)
DC-6	316331	5162131	1296	9.29E-02	2.15E-08	6.47E+01	64.8	9.82E+02	4.31E-04	9.62E-16	-15.02	Spane, FA (2013)
DC-12	304818	5149189	797	4.18E-02	1.65E-08	4.52E+01	45.6	9.89E+02	5.87E-04	9.96E-16	-15.00	Spane, FA (2013)
DC-12	304818	5149189	863	1.86E+02	2.82E-04	4.74E+01	48.1	9.88E+02	5.62E-04	1.64E-11	-10.79	Spane, FA (2013)
DC-12	304818	5149189	934	1.39E-02	3.02E-09	5.10E+01	50.9	9.87E+02	5.36E-04	1.67E-16	-15.78	Spane, FA (2013)
DC-12	304818	5149189	988	4.65E-05	2.13E-11	5.25E+01	52.9	9.87E+02	5.18E-04	1.14E-18	-17.94	Spane, FA (2013)
DC-12	304818	5149189	1233	5.57E+01	4.32E-05	6.16E+01	62.3	9.83E+02	4.47E-04	2.00E-12	-11.70	Spane, FA (2013)
DC-14	322270	5148586	725	1.86E-02	3.21E-08	4.21E+01	42.8	9.90E+02	6.17E-04	2.04E-15	-14.69	Spane, FA (2013)
DC-14	322270	5148586	751	3.90E-01	3.93E-07	4.31E+01	43.8	9.90E+02	6.06E-04	3.70E-14	-13.43	Spane, FA (2013)
DC-14	322270	5148586	835	9.29E-03	2.11E-09	4.71E+01	47.1	9.88E+02	5.72E-04	1.25E-16	-15.90	Spane, FA (2013)
DC-14	322270	5148586	890	5.57E-03	3.71E-09	4.71E+01	47.6	9.88E+02	5.66E-04	2.17E-16	-15.66	Spane, FA (2013)
DC-14	322270	5148586	892	2.79E-02	1.11E-08	4.89E+01	49.3	9.88E+02	5.51E-04	6.33E-16	-15.20	Spane, FA (2013)
DC-14	322270	5148586	945	5.11E-01	2.31E-07	5.09E+01	51.3	9.87E+02	5.32E-04	1.27E-14	-13.90	Spane, FA (2013)
DC-14	322270	5148586	976	3.72E-01	3.14E-07	5.18E+01	52.5	9.87E+02	5.22E-04	1.69E-14	-13.77	Spane, FA (2013)

Well ID	Easting	Northing	Center Interval Depth (m)	T(m^2/d)	K (ft/d)	K (m/s)	Est. T (C°)	Viscosity (kg/(m*s))	Density (kg/m^3)	Bulk Perm. (m^2)	log perm	Source
DC-15	325233	5140505	696	2.04E+02	6.67E-05	4.15E+01	41.7	9.90E+02	6.29E-04	4.32E-12	-11.36	Sponte, FA (2013)
DC-15	325233	5140505	740	1.86E-01	6.36E-08	4.32E+01	43.4	9.90E+02	6.10E-04	4.00E-15	-14.40	Sponte, FA (2013)
DC-15	325233	5140505	768	1.65E+01	1.12E-05	4.39E+01	44.5	9.89E+02	5.99E-04	6.90E-13	-12.16	Sponte, FA (2013)
DC-15	325233	5140505	831	7.53E-01	4.02E-07	4.64E+01	46.9	9.89E+02	5.74E-04	2.38E-14	-13.62	Sponte, FA (2013)
DC-15	325233	5140505	866	2.97E-01	2.05E-07	4.76E+01	48.2	9.88E+02	5.61E-04	1.19E-14	-13.93	Sponte, FA (2013)
DC-15	325233	5140505	926	2.30E+00	5.76E-07	5.05E+01	50.5	9.87E+02	5.39E-04	3.20E-14	-13.49	Sponte, FA (2013)
DC-15	325233	5140505	997	6.41E-01	4.77E-07	5.26E+01	53.3	9.87E+02	5.15E-04	2.54E-14	-13.60	Sponte, FA (2013)
DC-15	325233	5140505	1023	9.29E-02	3.18E-08	5.40E+01	54.3	9.86E+02	5.07E-04	1.67E-15	-14.78	Sponte, FA (2013)
DC-15	325233	5140505	1104	4.83E-04	7.34E-10	5.66E+01	57.4	9.85E+02	4.82E-04	3.66E-17	-16.44	Sponte, FA (2013)
DC-15	325233	5140505	1156	4.83E-03	1.76E-09	5.90E+01	59.4	9.84E+02	4.67E-04	8.54E-17	-16.07	Sponte, FA (2013)
DC-15	325233	5140505	1277	4.74E-01	1.71E-07	6.36E+01	64.0	9.83E+02	4.36E-04	7.74E-15	-14.11	Sponte, FA (2013)
DC-1	306969	5160653	820	1.24E+00	2.63E-07	4.66E+01	46.5	9.89E+02	5.78E-04	1.57E-14	-13.81	Sponte, FA (2013)
DC-1	306969	5160653	860	1.86E-02	3.92E-09	4.81E+01	48.0	9.88E+02	5.63E-04	2.28E-16	-15.64	Sponte, FA (2013)
DC-1	306969	5160653	980	6.78E+00	6.44E-06	5.19E+01	52.6	9.87E+02	5.21E-04	3.46E-13	-12.46	Sponte, FA (2013)
DC-1	306969	5160653	970	3.81E-02	4.82E-08	5.15E+01	52.2	9.87E+02	5.24E-04	2.61E-15	-14.58	Sponte, FA (2013)
DC-1	306969	5160653	1032	5.39E-02	1.56E-08	5.44E+01	54.6	9.86E+02	5.04E-04	8.14E-16	-15.09	Sponte, FA (2013)
DC-1	306969	5160653	1175	4.09E-02	9.70E-09	6.00E+01	60.1	9.84E+02	4.62E-04	4.65E-16	-15.33	Sponte, FA (2013)
DC-5	295741	5161567	906	7.25E-02	1.83E-07	4.90E+01	49.8	9.88E+02	5.46E-04	1.03E-14	-13.99	Sponte, FA (2013)
DC-7	316710	5150155	1050	7.25E-02	3.92E-08	5.48E+01	55.3	9.86E+02	4.98E-04	2.02E-15	-14.69	Sponte, FA (2013)
DC-8	316703	5150169	1050	7.25E-02	3.92E-08	5.48E+01	55.3	9.86E+02	4.98E-04	2.02E-15	-14.69	Sponte, FA (2013)
RRL-2A	295942	5158434	858	6.04E-01	6.74E-07	4.72E+01	48.0	9.88E+02	5.63E-04	3.92E-14	-13.41	Sponte, FA (2013)
RRL-2B/2A	295929	5158586	858	6.04E-01	6.74E-07	4.72E+01	48.0	9.88E+02	5.63E-04	3.92E-14	-13.41	Sponte, FA (2013)
RRL-2B/2C	296006	5158591	858	1.39E-01	1.56E-07	4.72E+01	48.0	9.88E+02	5.63E-04	9.04E-15	-14.04	Sponte, FA (2013)
RRL-14	293782	5159212	1193	7.99E-04	3.89E-10	6.03E+01	60.8	9.84E+02	4.57E-04	1.84E-17	-16.73	Sponte, FA (2013)
RSH-1	285770	5145968	808	6.78E-04	3.39E-10	4.56E+01	46.0	9.89E+02	5.83E-04	2.03E-17	-16.69	Sponte, FA (2013)
RSH-1	285770	5145968	991	3.62E-02	1.81E-08	5.25E+01	53.1	9.87E+02	5.17E-04	9.67E-16	-15.01	Sponte, FA (2013)
RSH-1	285770	5145968	1267	2.23E-03	1.11E-09	6.31E+01	63.7	9.83E+02	4.38E-04	5.06E-17	-16.30	Sponte, FA (2013)
RSH-1	285770	5145968	1484	3.44E-03	1.72E-09	7.14E+01	72.0	9.80E+02	3.88E-04	6.93E-17	-16.16	Sponte, FA (2013)
RSH-1	285770	5145968	1816	3.34E-01	1.67E-07	8.40E+01	84.7	9.76E+02	3.27E-04	5.70E-15	-14.24	Sponte, FA (2013)
RSH-1	285770	5145968	807	6.78E-05	4.77E-11	4.54E+01	46.0	9.89E+02	5.83E-04	2.87E-18	-17.54	Sponte, FA (2013)
RSH-1	285770	5145968	866	2.97E-04	3.23E-10	4.76E+01	48.3	9.88E+02	5.60E-04	1.86E-17	-16.73	Sponte, FA (2013)

Well ID	Easting	Northing	Center Interval Depth (m)	T(m²/d)	K (ft/d)	K (m/s)	Est. T (C°)	Viscosity (kg/(m*s))	Density (kg/m³)	Bulk Perm. (m²)	log perm	Source
DC-6	316331	5162131	1138	4.32E+00	1.25E-05	5.70E+01	57.9	9.85E+02	4.78E-04	6.19E-13	-12.21	Reidel et al. 2002
DC-6	316331	5162131	1141	4.32E+00	1.39E-06	5.85E+01	58.8	9.85E+02	4.72E-04	6.78E-14	-13.17	Reidel et al. 2002
DC-6	316331	5162131	1219	4.32E-07	4.76E-14	6.28E+01	61.8	9.83E+02	4.51E-04	2.22E-21	-20.65	Reidel et al. 2002
DC-6	316331	5162131	1281	4.32E-01	4.55E-07	6.34E+01	64.2	9.83E+02	4.35E-04	2.05E-14	-13.69	Reidel et al. 2002
DC-7	316710	5150155	1190	4.32E-01	1.84E-08	7.25E+01	68.4	9.80E+02	4.09E-04	7.82E-16	-15.11	Reidel et al. 2002
DC-7	316710	5150155	1262	4.32E-04	2.50E-09	6.25E+01	63.5	9.83E+02	4.39E-04	1.14E-16	-15.94	Reidel et al. 2002
DC-7	316710	5150155	1281	4.32E-04	1.25E-09	6.32E+01	64.2	9.83E+02	4.35E-04	5.63E-17	-16.25	Reidel et al. 2002
DC-7	316710	5150155	1290	4.32E-04	8.33E-10	6.36E+01	64.5	9.83E+02	4.32E-04	3.74E-17	-16.43	Reidel et al. 2002
DC-7	316710	5150155	1314	4.32E-04	8.33E-10	6.45E+01	65.5	9.82E+02	4.27E-04	3.69E-17	-16.43	Reidel et al. 2002
DC-7	316710	5150155	1332	4.32E-04	2.00E-10	6.56E+01	66.1	9.82E+02	4.22E-04	8.77E-18	-17.06	Reidel et al. 2002
DC-7	316710	5150155	1369	5.18E-02	2.00E-07	6.66E+01	67.6	9.82E+02	4.14E-04	8.59E-15	-14.07	Reidel et al. 2002
DC-7	316710	5150155	1379	5.18E-02	6.00E-08	6.71E+01	68.0	9.82E+02	4.11E-04	2.56E-15	-14.59	Reidel et al. 2002
DC-7	316710	5150155	1388	5.18E-02	2.00E-07	6.73E+01	68.3	9.82E+02	4.09E-04	8.50E-15	-14.07	Reidel et al. 2002
DC-7	316710	5150155	1394	5.18E-02	1.50E-07	6.76E+01	68.5	9.81E+02	4.08E-04	6.35E-15	-14.20	Reidel et al. 2002
DC-7	316710	5150155	1432	4.32E-01	1.67E-06	6.90E+01	70.0	9.81E+02	4.00E-04	6.92E-14	-13.16	Reidel et al. 2002
DC-7	316710	5150155	1451	4.32E-01	1.61E-07	7.02E+01	70.7	9.81E+02	3.95E-04	6.63E-15	-14.18	Reidel et al. 2002
DC-7B	316703	5150169	1056	4.32E-02	8.33E-08	5.47E+01	55.6	9.86E+02	4.97E-04	4.28E-15	-14.37	Reidel et al. 2002
DC-12	304818	5149189	378	4.32E+01	5.56E-05	2.89E+01	29.5	9.95E+02	8.03E-04	4.57E-12	-11.34	Reidel et al. 2002
DC-12	304818	5149189	411	4.32E+01	4.55E-05	3.02E+01	30.8	9.94E+02	7.81E-04	3.64E-12	-11.44	Reidel et al. 2002
DC-12	304818	5149189	452	4.32E+00	1.61E-06	3.21E+01	32.3	9.94E+02	7.56E-04	1.25E-13	-12.90	Reidel et al. 2002
DC-12	304818	5149189	517	4.32E+00	1.25E-05	3.41E+01	34.9	9.93E+02	7.18E-04	9.22E-13	-12.04	Reidel et al. 2002
DC-12	304818	5149189	594	4.32E-02	2.17E-08	3.74E+01	37.8	9.92E+02	6.73E-04	1.52E-15	-14.82	Reidel et al. 2002
DC-12	304818	5149189	630	4.32E+01	5.56E-05	3.85E+01	39.2	9.91E+02	6.60E-04	3.77E-12	-11.42	Reidel et al. 2002
DC-12	304818	5149189	681	4.32E-02	7.14E-08	4.04E+01	41.1	9.91E+02	6.37E-04	4.68E-15	-14.33	Reidel et al. 2002
DC-12	304818	5149189	698	4.32E-01	7.14E-07	4.10E+01	41.8	9.90E+02	6.29E-04	4.62E-14	-13.34	Reidel et al. 2002
DC-12	304818	5149189	740	4.32E+00	7.14E-06	4.26E+01	43.4	9.90E+02	6.11E-04	4.49E-13	-12.35	Reidel et al. 2002
DC-12	304818	5149189	796	4.32E-02	2.17E-08	4.51E+01	45.5	9.89E+02	5.88E-04	1.32E-15	-14.88	Reidel et al. 2002
DC-12	304818	5149189	864	4.32E+02	1.67E-03	4.73E+01	48.2	9.88E+02	5.61E-04	9.65E-11	-10.02	Reidel et al. 2002
DC-12	304818	5149189	869	4.32E+01	1.25E-04	4.75E+01	48.4	9.88E+02	5.59E-04	7.21E-12	-11.14	Reidel et al. 2002
DC-12	304818	5149189	920	4.32E-02	3.57E-08	4.97E+01	50.3	9.88E+02	5.41E-04	1.99E-15	-14.70	Reidel et al. 2002
DC-12	304818	5149189	952	4.32E-02	8.33E-08	5.07E+01	51.6	9.87E+02	5.30E-04	4.56E-15	-14.34	Reidel et al. 2002

Well ID	Easting	Northing	Center Interval Depth (m)	T(m^2/d)	K (ft/d)	K (m/s)	Est. T (C°)	Viscosity (kg/(m*s))	Density (kg/m^3)	Bulk Perm. (m^2)	log perm	Source
DC-6	316331	5162131	1118	4.32E+00	1.25E-05	5.70E+01	57.9	9.85E+02	4.78E-04	6.19E-13	-12.21	Reidel et al., 2002
DC-6	316331	5162131	1141	4.32E+00	1.39E-06	5.85E+01	58.8	9.85E+02	4.72E-04	6.78E-14	-13.17	Reidel et al., 2002
DC-6	316331	5162131	1219	4.32E-07	4.76E-14	6.28E+01	61.8	9.83E+02	4.51E-04	2.22E-21	-20.65	Reidel et al., 2002
DC-6	316331	5162131	1281	4.32E-01	4.55E-07	6.34E+01	64.2	9.83E+02	4.35E-04	2.05E-14	-13.69	Reidel et al., 2002
DC-7	316710	5150155	1390	4.32E-01	1.84E-08	7.25E+01	68.4	9.80E+02	4.09E-04	7.82E-16	-15.11	Reidel et al., 2002
DC-7	316710	5150155	1262	4.32E-04	2.50E-09	6.25E+01	63.5	9.83E+02	4.39E-04	1.14E-16	-15.94	Reidel et al., 2002
DC-7	316710	5150155	1281	4.32E-04	1.25E-09	6.32E+01	64.2	9.83E+02	4.35E-04	5.63E-17	-16.25	Reidel et al., 2002
DC-7	316710	5150155	1290	4.32E-04	8.33E-10	6.36E+01	64.5	9.83E+02	4.32E-04	3.74E-17	-16.43	Reidel et al., 2002
DC-7	316710	5150155	1314	4.32E-04	8.33E-10	6.45E+01	65.5	9.82E+02	4.27E-04	3.69E-17	-16.43	Reidel et al., 2002
DC-7	316710	5150155	1332	4.32E-04	2.00E-10	6.56E+01	66.1	9.82E+02	4.22E-04	8.77E-18	-17.06	Reidel et al., 2002
DC-7	316710	5150155	1369	5.18E-02	2.00E-07	6.66E+01	67.6	9.82E+02	4.14E-04	8.59E-15	-14.07	Reidel et al., 2002
DC-7	316710	5150155	1379	5.18E-02	6.00E-08	6.71E+01	68.0	9.82E+02	4.11E-04	2.56E-15	-14.59	Reidel et al., 2002
DC-7	316710	5150155	1388	5.18E-02	2.00E-07	6.73E+01	68.3	9.82E+02	4.09E-04	8.50E-15	-14.07	Reidel et al., 2002
DC-7	316710	5150155	1394	5.18E-02	1.50E-07	6.76E+01	68.5	9.81E+02	4.08E-04	6.35E-15	-14.20	Reidel et al., 2002
DC-7	316710	5150155	1432	4.32E-01	1.67E-06	6.90E+01	70.0	9.81E+02	4.00E-04	6.92E-14	-13.16	Reidel et al., 2002
DC-7	316710	5150155	1451	4.32E-01	1.61E-07	7.02E+01	70.7	9.81E+02	3.95E-04	6.63E-15	-14.18	Reidel et al., 2002
DC-7B	316703	5150169	1056	4.32E-02	8.33E-08	5.47E+01	55.6	9.86E+02	4.97E-04	4.28E-15	-14.37	Reidel et al., 2002
DC-12	304818	5149189	378	4.32E+01	5.56E-05	2.89E+01	29.5	9.95E+02	8.03E-04	4.57E-12	-11.34	Reidel et al., 2002
DC-12	304818	5149189	411	4.32E+01	4.55E-05	3.02E+01	30.8	9.94E+02	7.81E-04	3.64E-12	-11.44	Reidel et al., 2002
DC-12	304818	5149189	452	4.32E+00	1.61E-06	3.21E+01	32.3	9.94E+02	7.56E-04	1.25E-13	-12.90	Reidel et al., 2002
DC-12	304818	5149189	517	4.32E+00	1.25E-05	3.41E+01	34.9	9.93E+02	7.18E-04	9.22E-13	-12.04	Reidel et al., 2002
DC-12	304818	5149189	594	4.32E-02	2.17E-08	3.74E+01	37.8	9.92E+02	6.78E-04	1.52E-15	-14.82	Reidel et al., 2002
DC-12	304818	5149189	630	4.32E+01	5.56E-05	3.85E+01	39.2	9.91E+02	6.60E-04	3.77E-12	-11.42	Reidel et al., 2002
DC-12	304818	5149189	681	4.32E-02	7.14E-08	4.04E+01	41.1	9.91E+02	6.37E-04	4.68E-15	-14.33	Reidel et al., 2002
DC-12	304818	5149189	698	4.32E-01	7.14E-07	4.10E+01	41.8	9.90E+02	6.29E-04	4.62E-14	-13.34	Reidel et al., 2002
DC-12	304818	5149189	740	4.32E+00	7.14E-06	4.26E+01	43.4	9.90E+02	6.11E-04	4.49E-13	-12.35	Reidel et al., 2002
DC-12	304818	5149189	796	4.32E-02	2.17E-08	4.51E+01	45.5	9.89E+02	5.88E-04	1.32E-15	-14.88	Reidel et al., 2002
DC-12	304818	5149189	864	4.32E+02	1.67E-03	4.73E+01	48.2	9.88E+02	5.61E-04	9.65E-11	-10.02	Reidel et al., 2002
DC-12	304818	5149189	869	4.32E+01	1.25E-04	4.75E+01	48.4	9.88E+02	5.59E-04	7.21E-12	-11.14	Reidel et al., 2002
DC-12	304818	5149189	920	4.32E-02	3.57E-08	4.97E+01	50.3	9.88E+02	5.41E-04	1.99E-15	-14.70	Reidel et al., 2002
DC-12	304818	5149189	952	4.32E-02	8.33E-08	5.07E+01	51.6	9.87E+02	5.30E-04	4.56E-15	-14.34	Reidel et al., 2002

Well ID	Easting	Northing	Center Interval Depth (m)	T(m^2/d)	K (ft/d)	K (m/s)	Est. T (C°)	Viscosity (kg/(m*s))	Density (kg/m^3)	Bulk Perm. (m^2)	log perm	Source
DC-12	304818	5149189	945	4.32E-03	1.00E-08	5.04E+01	51.3	9.87E+02	5.33E-04	5.50E-16	-15.26	Riedel et al. 2002
DC-12	304818	5149189	984	8.64E-05	1.11E-10	5.20E+01	52.8	9.87E+02	5.20E-04	5.96E-18	-17.22	Riedel et al. 2002
DC-12	304818	5149189	993	8.64E-05	2.00E-10	5.23E+01	53.1	9.87E+02	5.17E-04	1.07E-17	-16.97	Riedel et al. 2002
DC-12	304818	5149189	1232	4.32E+01	5.00E-05	6.15E+01	62.3	9.83E+02	4.47E-04	2.32E-12	-11.64	Riedel et al. 2002
DC-12	304818	5149189	1302	4.32E+01	4.42E-06	6.61E+01	65.0	9.82E+02	4.30E-04	1.97E-13	-12.70	Riedel et al. 2002
DC-12	304818	5149189	1341	4.32E+01	1.47E-05	6.61E+01	66.5	9.82E+02	4.20E-04	6.41E-13	-12.19	Riedel et al. 2002
DC-14	311850	5171580	123	4.32E-01	8.33E-07	1.91E+01	19.7	9.98E+02	1.01E-03	8.55E-14	-13.07	Riedel et al. 2002
DC-14	311850	5171580	156	4.32E+00	4.17E-06	2.05E+01	21.0	9.98E+02	9.75E-04	4.15E-13	-12.38	Riedel et al. 2002
DC-14	311850	5171580	223	4.32E+01	2.94E-05	2.31E+01	23.5	9.97E+02	9.17E-04	2.76E-12	-11.56	Riedel et al. 2002
DC-14	311850	5171580	273	4.32E+02	8.33E-04	2.48E+01	25.5	9.96E+02	8.77E-04	7.48E-11	-10.13	Riedel et al. 2002
DC-14	311850	5171580	280	4.32E+02	2.50E-03	2.50E+01	25.8	9.96E+02	8.72E-04	2.23E-10	-9.65	Riedel et al. 2002
DC-14	311850	5171580	291	4.32E+01	8.33E-05	2.55E+01	26.2	9.96E+02	8.64E-04	7.37E-12	-11.13	Riedel et al. 2002
DC-14	311850	5171580	313	4.32E+00	1.43E-06	2.69E+01	27.0	9.95E+02	8.48E-04	1.34E-13	-12.91	Riedel et al. 2002
DC-14	311850	5171580	363	4.32E+01	5.00E-04	2.81E+01	28.9	9.95E+02	8.13E-04	4.16E-11	-10.38	Riedel et al. 2002
DC-14	311850	5171580	318	4.32E+02	4.81E-05	2.84E+01	27.2	9.95E+02	8.44E-04	4.16E-12	-11.38	Riedel et al. 2002
DC-14	311850	5171580	323	4.32E+02	4.90E-05	2.86E+01	27.4	9.95E+02	8.40E-04	4.32E-12	-11.37	Riedel et al. 2002
DC-14	311850	5171580	352	4.32E+02	4.42E-05	2.99E+01	28.5	9.94E+02	8.20E-04	3.72E-12	-11.43	Riedel et al. 2002
DC-14	311850	5171580	457	4.32E+00	1.25E-05	3.18E+01	32.5	9.94E+02	7.53E-04	9.65E-13	-12.02	Riedel et al. 2002
DC-14	311850	5171580	482	4.32E+01	6.25E-05	3.32E+01	33.9	9.93E+02	7.33E-04	4.70E-12	-11.33	Riedel et al. 2002
DC-14	311850	5171580	515	4.32E+01	1.00E-04	3.40E+01	34.8	9.93E+02	7.20E-04	7.39E-12	-11.13	Riedel et al. 2002
DC-14	311850	5171580	531	4.32E+01	1.67E-04	3.46E+01	35.4	9.93E+02	7.11E-04	1.22E-11	-10.91	Riedel et al. 2002
DC-14	311850	5171580	538	4.32E+01	1.67E-04	3.49E+01	35.6	9.93E+02	7.07E-04	1.21E-11	-10.92	Riedel et al. 2002
DC-14	311850	5171580	563	4.32E+01	1.00E-04	3.59E+01	36.6	9.92E+02	6.94E-04	7.13E-12	-11.15	Riedel et al. 2002
DC-14	311850	5171580	578	4.32E+02	8.33E-04	3.65E+01	37.2	9.92E+02	6.86E-04	5.87E-11	-10.23	Riedel et al. 2002
DC-14	311850	5171580	592	4.32E+02	5.00E-04	3.71E+01	37.7	9.92E+02	6.79E-04	3.49E-11	-10.46	Riedel et al. 2002
DC-14	311850	5171580	657	4.32E+01	6.25E-05	3.95E+01	40.2	9.91E+02	6.47E-04	4.16E-12	-11.38	Riedel et al. 2002
DC-14	311850	5171580	670	4.32E+01	1.67E-04	3.99E+01	40.7	9.91E+02	6.42E-04	1.10E-11	-10.96	Riedel et al. 2002
DC-14	311850	5171580	674	4.32E+01	1.67E-04	4.01E+01	40.9	9.91E+02	6.40E-04	1.10E-11	-10.96	Riedel et al. 2002
DC-14	311850	5171580	726	4.32E-02	7.14E-08	4.21E+01	42.9	9.90E+02	6.17E-04	4.53E-15	-14.34	Riedel et al. 2002
DC-14	311850	5171580	751	4.32E-02	6.25E-08	4.31E+01	43.8	9.90E+02	6.06E-04	3.90E-15	-14.41	Riedel et al. 2002
DC-14	311850	5171580	822	4.32E-02	1.00E-07	4.57E+01	46.5	9.89E+02	5.77E-04	5.95E-15	-14.23	Riedel et al. 2002

Well ID	Easting	Northing	Center Interval Depth (m)	T(m^2/d)	K (ft/d)	K (m/s)	Est. T (C°)	Viscosity (kg/(m*s))	Density (kg/m^3)	Bulk Perm. (m^2)	log perm	Source
DC-14	311850	5171580	837	4.32E-02	7.14E-08	4.63E+01	47.1	9.89E+02	5.72E-04	4.21E-15	-14.38	Reidel et al., 2002
DC-14	311850	5171580	866	4.32E-02	5.00E-08	4.75E+01	48.3	9.88E+02	5.60E-04	2.89E-15	-14.54	Reidel et al., 2002
DC-14	311850	5171580	881	4.32E-02	1.28E-08	4.86E+01	48.8	9.88E+02	5.55E-04	7.34E-16	-15.13	Reidel et al., 2002
DC-14	311850	5171580	946	4.32E+00	2.50E-06	5.08E+01	51.3	9.87E+02	5.32E-04	1.37E-13	-12.86	Reidel et al., 2002
DC-14	311850	5171580	978	4.32E-01	1.00E-06	5.17E+01	52.5	9.87E+02	5.22E-04	5.39E-14	-13.27	Reidel et al., 2002
DC-14	311850	5171580	1007	4.32E+00	3.13E-06	5.30E+01	53.7	9.86E+02	5.12E-04	1.65E-13	-12.78	Reidel et al., 2002
DC-15	325233	5140505	91	4.32E+01	6.25E-05	1.79E+01	18.5	9.99E+02	1.04E-03	6.61E-12	-11.18	Reidel et al., 2002
DC-15	325233	5140505	142	4.32E+01	2.94E-05	2.00E+01	20.4	9.98E+02	9.88E-04	2.97E-12	-11.53	Reidel et al., 2002
DC-15	325233	5140505	186	4.32E+00	1.00E-05	2.15E+01	22.1	9.97E+02	9.48E-04	9.69E-13	-12.01	Reidel et al., 2002
DC-15	325233	5140505	196	4.32E+00	1.00E-05	2.19E+01	22.5	9.97E+02	9.40E-04	9.61E-13	-12.02	Reidel et al., 2002
DC-15	325233	5140505	230	2.68E+00	1.63E-06	2.34E+01	23.8	9.97E+02	9.11E-04	1.52E-13	-12.82	Reidel et al., 2002
DC-15	325233	5140505	317	4.32E+00	3.57E-06	2.67E+01	27.2	9.95E+02	8.45E-04	3.09E-13	-12.51	Reidel et al., 2002
DC-15	325233	5140505	355	4.32E-02	7.14E-08	2.80E+01	28.6	9.95E+02	8.18E-04	5.99E-15	-14.22	Reidel et al., 2002
DC-15	325233	5140505	385	4.32E+02	3.57E-04	2.93E+01	29.8	9.95E+02	7.98E-04	2.92E-11	-10.53	Reidel et al., 2002
DC-15	325233	5140505	418	4.32E+01	1.67E-04	3.03E+01	31.0	9.94E+02	7.77E-04	1.33E-11	-10.88	Reidel et al., 2002
DC-15	325233	5140505	430	4.32E-01	2.50E-06	3.07E+01	31.5	9.94E+02	7.69E-04	1.97E-13	-12.71	Reidel et al., 2002
DC-15	325233	5140505	456	4.32E+02	1.00E-03	3.18E+01	32.5	9.94E+02	7.54E-04	7.73E-11	-10.11	Reidel et al., 2002
DC-15	325233	5140505	466	4.32E+01	1.00E-04	3.22E+01	32.9	9.94E+02	7.48E-04	7.67E-12	-11.12	Reidel et al., 2002
DC-15	325233	5140505	478	4.32E+02	8.33E-04	3.27E+01	33.4	9.93E+02	7.41E-04	6.33E-11	-10.20	Reidel et al., 2002
DC-15	325233	5140505	531	4.32E-01	5.00E-06	3.46E+01	35.4	9.93E+02	7.11E-04	3.65E-13	-12.44	Reidel et al., 2002
DC-15	325233	5140505	552	4.32E-01	2.78E-07	3.57E+01	36.2	9.92E+02	7.00E-04	2.00E-14	-13.70	Reidel et al., 2002
DC-15	325233	5140505	567	4.32E+02	4.17E-04	3.62E+01	36.8	9.92E+02	6.92E-04	2.96E-11	-10.53	Reidel et al., 2002
DC-15	325233	5140505	653	4.32E-01	3.13E-07	3.95E+01	40.1	9.91E+02	6.49E-04	2.09E-14	-13.68	Reidel et al., 2002
DC-15	325233	5140505	686	4.32E+02	5.00E-03	4.05E+01	41.3	9.91E+02	6.34E-04	3.26E-10	-9.49	Reidel et al., 2002
DC-15	325233	5140505	695	4.32E+02	5.56E-04	4.10E+01	41.7	9.91E+02	6.30E-04	3.60E-11	-10.44	Reidel et al., 2002
DC-15	325233	5140505	746	4.32E-01	1.67E-06	4.28E+01	43.6	9.90E+02	6.08E-04	1.04E-13	-12.98	Reidel et al., 2002
DC-15	325233	5140505	772	4.32E+01	7.14E-05	4.39E+01	44.6	9.90E+02	5.97E-04	4.40E-12	-11.36	Reidel et al., 2002
DC-15	325233	5140505	833	4.32E-01	2.50E-06	4.61E+01	47.0	9.89E+02	5.73E-04	1.48E-13	-12.83	Reidel et al., 2002
DC-15	325233	5140505	868	4.32E-01	4.55E-07	4.76E+01	48.3	9.88E+02	5.60E-04	2.63E-14	-13.58	Reidel et al., 2002
DC-15	325233	5140505	1024	4.32E-01	3.33E-07	5.36E+01	54.3	9.86E+02	5.07E-04	1.75E-14	-13.76	Reidel et al., 2002
DC-15	325233	5140505	1155	4.32E-03	1.85E-09	5.89E+01	59.3	9.84E+02	4.68E-04	8.97E-17	-16.05	Reidel et al., 2002

Well ID	Easting	Northing	Center Interval Depth (m)	T(m^2/d)	K (ft/d)	K (m/s)	Est. T (C°)	Viscosity (kg/(m*s))	Density (kg/m^3)	Bulk Perm.- (m^2)	log perm	Source
DC-15	325233	5140505	1272	4.32E-01	5.00E-07	6.30E+01	63.8	9.83E+02	4.37E-04	2.27E-14	-13.64	Reidel et al. 2002
DC-15	325233	5140505	1284	4.32E-01	1.00E-06	6.34E+01	64.3	9.83E+02	4.34E-04	4.50E-14	-13.35	Reidel et al. 2002
DC-16A	299938	5156024	227	4.32E+02	1.32E-04	2.37E+01	23.7	9.96E+02	9.13E-04	1.23E-11	-10.91	Reidel et al. 2002
DC-16A	299938	5156024	297	4.32E+00	2.63E-06	2.60E+01	26.4	9.96E+02	8.60E-04	2.32E-13	-12.64	Reidel et al. 2002
DC-16A	299938	5156024	348	4.32E-01	2.27E-07	2.30E+01	28.4	9.95E+02	8.23E-04	1.92E-14	-13.72	Reidel et al. 2002
DC-16A	299938	5156024	448	4.32E+01	1.72E-05	3.19E+01	32.2	9.94E+02	7.59E-04	1.34E-12	-11.87	Reidel et al. 2002
DC-16A	299938	5156024	521	4.32E-01	5.00E-06	3.42E+01	35.0	9.93E+02	7.17E-04	3.68E-13	-12.43	Reidel et al. 2002
DC-16A	299938	5156024	542	4.32E+03	1.25E-02	3.51E+01	35.8	9.93E+02	7.05E-04	9.05E-10	-9.04	Reidel et al. 2002
DC-16A	299938	5156024	595	4.32E+02	1.67E-03	3.70E+01	37.8	9.92E+02	6.78E-04	1.16E-10	-9.94	Reidel et al. 2002
DC-16A	299938	5156024	650	4.32E+00	1.67E-05	3.91E+01	39.9	9.91E+02	6.51E-04	1.12E-12	-11.95	Reidel et al. 2002
DC-16A	299938	5156024	683	4.32E+02	2.50E-03	4.04E+01	41.2	9.91E+02	6.35E-04	1.63E-10	-9.79	Reidel et al. 2002
DC-16A	299938	5156024	696	4.32E+00	1.25E-05	4.09E+01	41.7	9.91E+02	6.30E-04	8.10E-13	-12.09	Reidel et al. 2002
DC-16A	299938	5156024	706	4.32E+00	1.25E-05	4.13E+01	42.1	9.90E+02	6.25E-04	8.04E-13	-12.09	Reidel et al. 2002
DC-16A	299938	5156024	712	4.32E+00	1.00E-05	4.15E+01	42.3	9.90E+02	6.23E-04	6.41E-13	-12.19	Reidel et al. 2002
DC-16A	299938	5156024	719	4.32E+00	6.25E-06	4.19E+01	42.6	9.90E+02	6.19E-04	3.99E-13	-12.40	Reidel et al. 2002
DC-16A	299938	5156024	771	4.32E+02	2.78E-04	4.41E+01	44.6	9.89E+02	5.98E-04	1.71E-11	-10.77	Reidel et al. 2002
DC-16A	299938	5156024	797	4.32E+01	5.00E-05	4.49E+01	45.6	9.89E+02	5.87E-04	3.02E-12	-11.52	Reidel et al. 2002
DC-16A	299938	5156024	827	4.32E+01	1.25E-04	4.59E+01	46.8	9.89E+02	5.75E-04	7.41E-12	-11.13	Reidel et al. 2002
DC-16A	299938	5156024	877	4.32E+00	3.13E-06	4.81E+01	48.7	9.88E+02	5.56E-04	1.79E-13	-12.75	Reidel et al. 2002
DC-16A	299938	5156024	914	4.32E-01	5.00E-07	4.94E+01	50.1	9.88E+02	5.43E-04	2.80E-14	-13.55	Reidel et al. 2002
DC-16A	299938	5156024	926	4.32E-01	7.14E-07	4.97E+01	50.5	9.88E+02	5.39E-04	3.98E-14	-13.40	Reidel et al. 2002
DC-16A	299938	5156024	1010	4.32E-04	2.63E-10	5.32E+01	53.8	9.86E+02	5.11E-04	1.39E-17	-16.86	Reidel et al. 2002
DC-16A	299938	5156024	1048	4.32E-05	1.47E-11	5.49E+01	55.2	9.86E+02	4.99E-04	7.59E-19	-18.12	Reidel et al. 2002
DC-16A	299938	5156024	1118	4.32E-01	1.92E-07	5.74E+01	57.9	9.85E+02	4.78E-04	9.52E-15	-14.02	Reidel et al. 2002
DC-16A	299938	5156024	1158	4.32E-04	1.22E-10	5.92E+01	59.4	9.84E+02	4.67E-04	5.90E-18	-17.23	Reidel et al. 2002
DC-16A	299938	5156024	1206	8.64E-02	1.43E-07	6.04E+01	61.3	9.84E+02	4.54E-04	6.72E-15	-14.17	Reidel et al. 2002
DC-19C	300012	5155090	512	4.32E+01	5.56E-05	3.40E+01	34.6	9.93E+02	7.22E-04	4.12E-12	-11.39	Reidel et al. 2002
DC-19C	300012	5155090	583	4.32E+00	3.13E-06	3.68E+01	37.4	9.92E+02	6.83E-04	2.19E-13	-12.66	Reidel et al. 2002
DC-19C	300012	5155090	899	4.32E-02	4.55E-08	4.73E+01	48.0	9.88E+02	5.63E-04	2.64E-15	-14.58	Reidel et al. 2002
DC-19C	300012	5155090	966	4.32E-06	3.57E-12	5.14E+01	52.1	9.87E+02	5.25E-04	1.94E-19	-18.71	Reidel et al. 2002
DC-19C	300012	5155090	1106	4.32E+00	2.38E-06	5.69E+01	57.5	9.85E+02	4.82E-04	1.19E-13	-12.93	Reidel et al. 2002

Well ID	Easting	Northing	Center Interval Depth (m)	T(m^2/d)	K (ft/d)	K (m/s)	Est. T (C°)	Viscosity (kg/(m*s))	Density (kg/m^3)	Bulk Perm. (m^2)	log perm	Source
DC-20C	297294	5160688	571	4.32E+02	7.14E-04	3.62E+01	36.9	9.92E+02	6.90E-04	5.06E-11	-10.30	Reidel et al., 2002
DC-20C	297294	5160688	738	4.32E+00	5.00E-06	4.26E+01	43.3	9.90E+02	6.11E-04	3.15E-13	-12.50	Reidel et al., 2002
DC-20C	297294	5160688	896	4.32E-02	1.67E-07	4.85E+01	49.4	9.88E+02	5.50E-04	9.45E-15	-14.02	Reidel et al., 2002
DC-20C	297294	5160688	1100	4.32E-02	1.47E-08	5.69E+01	57.2	9.85E+02	4.83E-04	7.36E-16	-15.13	Reidel et al., 2002
DC-22C	293868	5159838	882	4.32E-03	6.25E-09	4.81E+01	48.9	9.88E+02	5.55E-04	3.58E-16	-15.45	Reidel et al., 2002
DC-22C	293868	5159838	1146	4.32E+01	1.35E-05	5.87E+01	59.0	9.84E+02	4.70E-04	6.58E-13	-12.18	Reidel et al., 2002
DC-23GR	296428	5163774	422	4.32E+02	2.08E-04	3.09E+01	31.2	9.94E+02	7.74E-04	1.65E-11	-10.78	Reidel et al., 2002
DC-23GR	296428	5163774	490	4.32E+03	2.94E-03	3.33E+01	33.8	9.93E+02	7.34E-04	2.22E-10	-9.65	Reidel et al., 2002
DC-23GR	296428	5163774	666	8.64E-01	5.56E-07	4.01E+01	40.6	9.91E+02	6.43E-04	3.68E-14	-13.43	Reidel et al., 2002
DC-23GR	296428	5163774	750	4.32E-03	3.33E-09	4.32E+01	43.8	9.90E+02	6.06E-04	2.08E-16	-15.68	Reidel et al., 2002
DC-23GR	296428	5163774	809	4.32E-03	2.08E-09	4.56E+01	46.1	9.89E+02	5.82E-04	1.25E-16	-15.90	Reidel et al., 2002
DC-23GR	296428	5163774	899	8.64E-03	6.25E-09	4.89E+01	49.5	9.88E+02	5.48E-04	3.54E-16	-15.45	Reidel et al., 2002
DC-23GR	296428	5163774	1017	4.32E-02	2.38E-08	5.35E+01	54.0	9.86E+02	5.09E-04	1.25E-15	-14.90	Reidel et al., 2002
DB-1	325193	5145745	300	4.32E+02	1.00E-03	2.58E+01	26.5	9.96E+02	8.57E-04	8.78E-11	-10.06	Reidel et al., 2002
DB-1	325193	5145745	338	4.32E+01	2.78E-05	2.75E+01	28.0	9.95E+02	8.30E-04	2.36E-12	-11.63	Reidel et al., 2002
DB-2	322355	5148704	278	4.32E+02	6.25E-04	2.51E+01	25.7	9.96E+02	8.73E-04	5.59E-11	-10.25	Reidel et al., 2002
DB-2	322355	5148704	360	4.32E-01	7.14E-07	2.81E+01	28.8	9.95E+02	8.15E-04	5.96E-14	-13.22	Reidel et al., 2002
DB-2	322355	5148704	376	3.02E-05	1.40E-11	2.91E+01	29.4	9.95E+02	8.04E-04	1.15E-18	-17.94	Reidel et al., 2002
DB-2	322355	5148704	318	4.32E+01	5.00E-05	2.66E+01	27.2	9.95E+02	8.44E-04	4.32E-12	-11.36	Reidel et al., 2002
DB-2	322355	5148704	337	4.32E+01	1.67E-04	2.72E+01	27.9	9.95E+02	8.31E-04	1.42E-11	-10.85	Reidel et al., 2002
DB-4	313124	5156329	422	4.32E+02	3.85E-04	3.06E+01	31.2	9.94E+02	7.75E-04	3.05E-11	-10.51	Reidel et al., 2002
DB-5	322510	5148601	266	4.32E+01	2.17E-05	2.49E+01	25.2	9.96E+02	8.83E-04	1.96E-12	-11.71	Reidel et al., 2002
DB-7	313664	5140762	242	4.32E+02	5.00E-04	2.37E+01	24.3	9.96E+02	9.01E-04	4.61E-11	-10.34	Reidel et al., 2002
DB-9	322317	5148488	165	4.32E+01	1.61E-05	2.12E+01	21.3	9.97E+02	9.67E-04	1.59E-12	-11.80	Reidel et al., 2002
DB-10	322304	5148551	265	4.32E-02	3.33E-08	2.47E+01	25.2	9.96E+02	8.84E-04	3.01E-15	-14.52	Reidel et al., 2002
DB-11	322224	5148532	286	4.32E-02	1.16E-08	2.60E+01	26.0	9.96E+02	8.68E-04	1.03E-15	-14.99	Reidel et al., 2002
DB-12	322215	5148594	367	4.32E+02	1.25E-03	2.84E+01	29.1	9.95E+02	8.10E-04	1.04E-10	-9.98	Reidel et al., 2002
DB-12	322215	5148594	136	4.32E+03	1.22E-03	2.03E+01	20.2	9.98E+02	9.93E-04	1.24E-10	-9.91	Reidel et al., 2002
DB-12	322215	5148594	180	4.32E+03	5.00E-02	2.12E+01	21.9	9.97E+02	9.54E-04	4.87E-09	-8.31	Reidel et al., 2002
DB-12	322215	5148594	209	4.32E+02	1.67E-03	2.23E+01	23.0	9.97E+02	9.29E-04	1.58E-10	-9.80	Reidel et al., 2002
DB-13	322231	5148600	116	4.32E+01	5.00E-04	1.87E+01	19.4	9.98E+02	1.01E-03	5.17E-11	-10.29	Reidel et al., 2002

Well ID	Easting	Northing	Center Interval Depth (m)	T(m^2/d)	K (ft/d)	K (m/s)	Est. T (C°)	Viscosity (kg/(m*s))	Density (kg/m^3)	Bulk Perm.- (m^2)	log perm	Source
DB-13	322231	5148600	152	4.32E+01	2.27E-05	2.05E+01	20.8	9.98E+02	9.73E-04	2.27E-12	-11.64	Riedel et al. 2002
DB-13	322231	5148600	222	4.32E+01	8.33E-05	2.29E+01	23.5	9.97E+02	9.18E-04	7.82E-12	-11.11	Riedel et al. 2002
DB-13	322231	5148600	276	4.32E+01	2.17E-05	2.52E+01	25.6	9.96E+02	8.73E-04	1.95E-12	-11.71	Riedel et al. 2002
DB-13	322231	5148600	379	4.32E+02	1.67E-04	2.93E+01	29.6	9.95E+02	8.02E-04	1.37E-11	-10.86	Riedel et al. 2002
DB-14	322270	5148586	76	8.64E-01	4.17E-07	1.77E+01	17.9	9.99E+02	1.05E-03	4.47E-14	-13.35	Riedel et al. 2002
DB-14	322270	5148586	149	4.32E+00	2.50E-05	2.00E+01	20.7	9.98E+02	9.81E-04	2.51E-12	-11.60	Riedel et al. 2002
DB-14	322270	5148586	195	4.32E+02	3.57E-04	2.20E+01	22.5	9.97E+02	9.40E-04	3.43E-11	-10.46	Riedel et al. 2002
DB-14	322270	5148586	295	4.32E+01	1.67E-05	2.61E+01	26.3	9.96E+02	8.61E-04	1.47E-12	-11.83	Riedel et al. 2002
DB-15	322222	5148645	60	4.41E+01	3.00E-05	1.69E+01	17.3	9.99E+02	1.07E-03	3.27E-12	-11.49	Riedel et al. 2002
DB-15	322222	5148645	126	7.08E-01	1.17E-06	1.92E+01	19.8	9.98E+02	1.00E-03	1.20E-13	-12.92	Riedel et al. 2002
DB-15	322222	5148645	173	1.56E+02	6.21E-05	2.14E+01	21.6	9.97E+02	9.60E-04	6.09E-12	-11.22	Riedel et al. 2002
DB-15	322222	5148645	206	4.32E+01	1.00E-04	2.22E+01	22.9	9.97E+02	9.31E-04	9.52E-12	-11.02	Riedel et al. 2002
DB-15	322222	5148645	220	4.32E+02	2.50E-04	2.31E+01	23.4	9.97E+02	9.19E-04	2.35E-11	-10.63	Riedel et al. 2002
DB-15	322222	5148645	244	4.32E+02	1.85E-04	2.41E+01	24.4	9.96E+02	9.00E-04	1.71E-11	-10.77	Riedel et al. 2002
DB-15	322222	5148645	286	4.32E+02	4.55E-04	2.54E+01	26.0	9.96E+02	8.68E-04	4.04E-11	-10.39	Riedel et al. 2002
DB-15	322222	5148645	330	4.32E+02	3.57E-04	2.72E+01	27.7	9.95E+02	8.35E-04	3.06E-11	-10.51	Riedel et al. 2002
DB-15	322222	5148645	344	4.32E-06	4.17E-12	2.77E+01	28.2	9.95E+02	8.26E-04	3.52E-19	-18.45	Riedel et al. 2002
DB-15	322222	5148645	354	4.32E+01	4.55E-06	2.99E+01	28.6	9.94E+02	8.19E-04	3.81E-13	-12.42	Riedel et al. 2002
DB-15	322222	5148645	416	4.32E+01	1.25E-04	3.02E+01	31.0	9.94E+02	7.78E-04	9.97E-12	-11.00	Riedel et al. 2002
DB-15	322222	5148645	436	4.32E+01	5.56E-05	3.11E+01	31.7	9.94E+02	7.66E-04	4.36E-12	-11.36	Riedel et al. 2002
DB-15	322222	5148645	456	4.32E+00	2.38E-06	3.21E+01	32.5	9.94E+02	7.54E-04	1.84E-13	-12.73	Riedel et al. 2002
DB-15	322222	5148645	483	4.32E+01	1.67E-04	3.28E+01	33.5	9.93E+02	7.38E-04	1.26E-11	-10.90	Riedel et al. 2002
DB-15	322222	5148645	534	4.32E-03	1.67E-08	3.47E+01	35.5	9.93E+02	7.09E-04	1.21E-15	-14.92	Riedel et al. 2002
DB-15	322222	5148645	571	4.32E-04	8.33E-10	3.62E+01	36.9	9.92E+02	6.90E-04	5.90E-17	-16.23	Riedel et al. 2002
DB-15	322222	5148645	599	8.64E-07	2.50E-12	3.72E+01	38.0	9.92E+02	6.75E-04	1.74E-19	-18.76	Riedel et al. 2002
RRL-2.A	295942	5158434	434	4.32E-03	3.13E-09	3.12E+01	31.7	9.94E+02	7.67E-04	2.46E-16	-15.61	Riedel et al. 2002
RRL-2.A	295942	5158434	519	4.32E+01	7.14E-05	3.42E+01	34.9	9.93E+02	7.18E-04	5.26E-12	-11.28	Riedel et al. 2002
RRL-2.A	295942	5158434	535	4.32E+02	1.67E-03	3.47E+01	35.5	9.93E+02	7.09E-04	1.21E-10	-9.92	Riedel et al. 2002
RRL-2.A	295942	5158434	590	4.32E+02	7.14E-04	3.69E+01	37.6	9.92E+02	6.80E-04	4.99E-11	-10.30	Riedel et al. 2002
RRL-2.A	295942	5158434	643	4.32E+02	1.67E-03	3.89E+01	39.7	9.91E+02	6.54E-04	1.12E-10	-9.95	Riedel et al. 2002
RRL-2.A	295942	5158434	677	4.32E+02	3.00E-03	4.01E+01	41.0	9.91E+02	6.38E-04	3.28E-10	-9.48	Riedel et al. 2002

Well ID	Easting	Northing	Center Interval Depth (m)	T(m^2/d)	K (ft/d)	K (m/s)	Est. T (C°)	Viscosity (kg/(m*s))	Density (kg/m^3)	Bulk Perm. (m^2)	log perm	Source
RRL-2A	299942	5158434	696	4.32E+02	7.14E-04	4.10E+01	41.7	9.91E+02	6.30E-04	4.63E-11	-10.33	Reidel et al., 2002
RRL-2A	299942	5158434	730	4.32E+02	5.00E-04	4.23E+01	43.0	9.90E+02	6.15E-04	3.16E-11	-10.50	Reidel et al., 2002
RRL-2A	299942	5158434	761	4.32E+02	1.25E-03	4.34E+01	44.2	9.90E+02	6.02E-04	7.75E-11	-10.11	Reidel et al., 2002
RRL-2A	299942	5158434	798	4.32E+02	1.25E-03	4.48E+01	45.6	9.89E+02	5.87E-04	7.56E-11	-10.12	Reidel et al., 2002
RRL-2A	299942	5158434	817	4.32E-01	8.33E-07	4.56E+01	46.4	9.89E+02	5.79E-04	4.97E-14	-13.30	Reidel et al., 2002
RRL-2A	299942	5158434	835	4.32E-01	4.17E-07	4.64E+01	47.1	9.89E+02	5.72E-04	2.46E-14	-13.61	Reidel et al., 2002
RRL-2A	299942	5158434	863	4.32E-01	8.33E-07	4.73E+01	48.1	9.88E+02	5.62E-04	4.83E-14	-13.32	Reidel et al., 2002
RRL-2A	299942	5158434	902	4.32E-06	3.33E-12	4.90E+01	49.6	9.88E+02	5.48E-04	1.88E-19	-18.72	Reidel et al., 2002
RRL-2A	299942	5158434	915	3.89E-03	7.50E-09	4.93E+01	50.1	9.88E+02	5.43E-04	4.20E-16	-15.38	Reidel et al., 2002
RRL-2A	299942	5158434	943	2.42E-05	5.60E-11	5.04E+01	51.2	9.87E+02	5.33E-04	3.08E-18	-17.51	Reidel et al., 2002
RRL-2A	299942	5158434	979	4.06E-07	2.24E-13	5.20E+01	52.6	9.87E+02	5.21E-04	1.21E-20	-19.92	Reidel et al., 2002
RRL-2A	299942	5158434	1004	7.08E+01	3.42E-05	5.31E+01	53.6	9.86E+02	5.13E-04	1.81E-12	-11.74	Reidel et al., 2002
RRL-2A	299942	5158434	1033	4.32E-05	1.25E-10	5.38E+01	54.7	9.86E+02	5.04E-04	6.51E-18	-17.19	Reidel et al., 2002
RRL-2A	299942	5158434	1044	4.32E-05	7.14E-11	5.42E+01	55.1	9.86E+02	5.00E-04	3.70E-18	-17.43	Reidel et al., 2002
RRL-2A	299942	5158434	1062	4.32E-05	8.33E-11	5.49E+01	55.8	9.86E+02	4.95E-04	4.26E-18	-17.37	Reidel et al., 2002
RRL-2A	299942	5158434	1092	4.32E-06	7.14E-12	5.61E+01	56.9	9.85E+02	4.86E-04	3.59E-19	-18.44	Reidel et al., 2002
RRL-2A	299942	5158434	1120	4.41E+01	1.06E-05	5.79E+01	58.0	9.85E+02	4.78E-04	5.25E-13	-12.28	Reidel et al., 2002
RRL-2A	299942	5158434	1142	4.32E-01	1.67E-06	5.79E+01	58.8	9.85E+02	4.72E-04	8.13E-14	-13.09	Reidel et al., 2002
RRL-2A	299942	5158434	1154	1.47E-06	1.31E-12	5.86E+01	59.3	9.84E+02	4.68E-04	6.34E-20	-19.20	Reidel et al., 2002
RRL-2A	299942	5158434	1165	8.12E+01	4.70E-04	5.88E+01	59.7	9.84E+02	4.65E-04	2.26E-11	-10.65	Reidel et al., 2002
RRL-2A	299942	5158434	1174	4.32E+01	6.25E-05	5.92E+01	60.1	9.84E+02	4.62E-04	2.99E-12	-11.52	Reidel et al., 2002
RRL-2B/A	299929	5158586	863	6.05E-01	1.17E-06	4.73E+01	48.1	9.88E+02	5.62E-04	6.76E-14	-13.17	Reidel et al., 2002
RRL-2B/C	299929	5158586	861	1.38E-01	2.67E-07	4.73E+01	48.1	9.88E+02	5.62E-04	1.55E-14	-13.81	Reidel et al., 2002
RRL-2C	296006	5158591	886	4.32E-05	7.14E-11	4.82E+01	49.0	9.88E+02	5.53E-04	4.08E-18	-17.39	Reidel et al., 2002
RRL-2C	296006	5158591	912	4.32E-05	1.00E-10	4.92E+01	50.0	9.88E+02	5.44E-04	5.61E-18	-17.25	Reidel et al., 2002
RRL-2C	296006	5158591	963	4.32E-05	7.14E-11	5.12E+01	52.0	9.87E+02	5.27E-04	3.88E-18	-17.41	Reidel et al., 2002
RRL-2C	296006	5158591	991	4.32E+01	4.17E-05	5.23E+01	53.1	9.87E+02	5.17E-04	2.23E-12	-11.65	Reidel et al., 2002
RRL-2C	296006	5158591	1014	4.32E-05	7.14E-11	5.31E+01	53.9	9.86E+02	5.10E-04	3.76E-18	-17.42	Reidel et al., 2002
RRL-6	294429	5156771	649	4.32E-06	1.25E-11	3.91E+01	39.9	9.91E+02	6.51E-04	8.37E-19	-18.08	Reidel et al., 2002
RRL-7	295789	5160426	655	4.32E-06	5.00E-11	3.93E+01	40.1	9.91E+02	6.49E-04	3.34E-18	-17.48	Reidel et al., 2002
RRL-8	293735	5161027	946	4.32E-06	1.00E-11	5.05E+01	51.3	9.87E+02	5.32E-04	5.30E-19	-18.26	Reidel et al., 2002

Well ID	Easting	Northing	Center Interval Depth (m)	T(m^2/d)	K (ft/d)	K (m/s)	Est. T (C°)	Viscosity (kg/(m*s))	Density (kg/m^3)	Bulk Perm. (m^2)	log perm	Source
RRL-9	297185	5158520	985	4.32E-07	8.06E-14	5.31E+01	52.8	9.86E+02	5.19E-04	4.33E-21	-20.36	Riedel et al. 2002
RRL-10	294514	5157828	1029	4.32E-04	2.50E-10	5.39E+01	54.5	9.86E+02	5.03E-04	1.31E-17	-16.88	Riedel et al. 2002
RRL-11	292675	5157359	1115	8.64E-08	4.55E-14	5.73E+01	57.8	9.85E+02	4.79E-04	2.25E-21	-20.65	Riedel et al. 2002
RRL-12	296041	5156079	1147	4.32E-01	1.72E-07	5.86E+01	59.0	9.84E+02	4.70E-04	8.39E-15	-14.08	Riedel et al. 2002
RRL-13	299980	5155006	1183	4.32E-07	1.47E-13	6.01E+01	60.4	9.84E+02	4.60E-04	7.01E-21	-20.15	Riedel et al. 2002
RRL-14	293782	5159212	1205	4.32E-04	1.67E-09	6.03E+01	61.3	9.84E+02	4.54E-04	7.84E-17	-16.11	Riedel et al. 2002
RRL-16	296342	5157752	984	4.32E-07	9.43E-14	5.28E+01	52.8	9.86E+02	5.20E-04	5.06E-21	-20.30	Riedel et al. 2002
RRL-17	296811	5159633	1024	4.32E+00	2.08E-06	5.38E+01	54.3	9.86E+02	5.07E-04	1.09E-13	-12.96	Riedel et al. 2002
McGee	290212	5162800	249	4.32E+03	1.25E-02	2.39E+01	24.6	9.96E+02	8.96E-04	1.15E-09	-8.94	Riedel et al. 2002
McGee	290212	5162800	284	4.32E+03	1.67E-02	2.52E+01	25.9	9.96E+02	8.69E-04	1.48E-09	-8.83	Riedel et al. 2002
McGee	290212	5162800	538	4.32E-01	1.00E-06	3.57E+01	36.4	9.92E+02	6.97E-04	7.16E-14	-13.15	Riedel et al. 2002
McGee	290212	5162800	569	4.32E-03	1.67E-08	3.60E+01	36.8	9.92E+02	6.91E-04	1.18E-15	-14.93	Riedel et al. 2002
McGee	290212	5162800	583	4.32E-02	1.25E-07	3.66E+01	37.4	9.92E+02	6.83E-04	8.78E-15	-14.06	Riedel et al. 2002
McGee	290212	5162800	595	4.32E-02	1.25E-07	3.71E+01	37.8	9.92E+02	6.77E-04	8.70E-15	-14.06	Riedel et al. 2002
McGee	290212	5162800	611	4.32E+01	6.25E-05	3.78E+01	38.5	9.92E+02	6.69E-04	4.30E-12	-11.37	Riedel et al. 2002
McGee	290212	5162800	660	4.32E+01	1.25E-04	3.96E+01	40.3	9.91E+02	6.46E-04	8.31E-12	-11.08	Riedel et al. 2002
McGee	290212	5162800	673	4.32E-02	8.33E-08	4.01E+01	40.8	9.91E+02	6.40E-04	5.49E-15	-14.26	Riedel et al. 2002
McGee	290212	5162800	680	4.32E+01	2.50E-04	4.03E+01	41.1	9.91E+02	6.37E-04	1.64E-11	-10.79	Riedel et al. 2002
McGee	290212	5162800	743	4.32E-01	6.25E-07	4.28E+01	43.5	9.90E+02	6.09E-04	3.92E-14	-13.41	Riedel et al. 2002
McGee	290212	5162800	801	4.32E-01	1.67E-06	4.49E+01	45.7	9.89E+02	5.86E-04	1.01E-13	-13.00	Riedel et al. 2002
McGee	290212	5162800	809	4.32E-01	6.25E-07	4.53E+01	46.1	9.89E+02	5.82E-04	3.75E-14	-13.43	Riedel et al. 2002
McGee	290212	5162800	817	4.32E-01	1.25E-06	4.55E+01	46.4	9.89E+02	5.79E-04	7.46E-14	-13.13	Riedel et al. 2002
McGee	290212	5162800	925	4.32E-02	1.00E-07	4.97E+01	50.5	9.88E+02	5.39E-04	5.57E-15	-14.25	Riedel et al. 2002
McGee	290212	5162800	933	4.32E-02	7.14E-08	5.00E+01	50.8	9.87E+02	5.37E-04	3.96E-15	-14.40	Riedel et al. 2002
McGee	290212	5162800	942	4.32E-02	2.50E-07	5.03E+01	51.2	9.87E+02	5.33E-04	1.38E-14	-13.86	Riedel et al. 2002
OBRIAN	286971	5162908	211	4.32E+04	1.67E-01	2.34E+01	23.1	9.97E+02	9.27E-04	1.58E-08	-7.80	Riedel et al. 2002
FORD	287782	5162980	228	4.32E+03	1.67E-02	2.30E+01	23.7	9.97E+02	9.13E-04	1.56E-09	-8.81	Riedel et al. 2002
ENYEART	287753	5161879	329	4.32E+03	8.33E-03	2.70E+01	27.6	9.95E+02	8.36E-04	7.13E-10	-9.15	Riedel et al. 2002
699-52-48	307052	5161734	52	8.64E-01	6.67E-07	1.66E+01	17.0	9.99E+02	1.04E-03	7.33E-14	-13.14	Riedel et al. 2002
699-53-50	306428	5162267	52	8.64E+00	7.14E-06	1.66E+01	17.0	9.99E+02	1.04E-03	7.85E-13	-12.11	Riedel et al. 2002
699-51-46	307350	5161518	44	8.64E-01	7.69E-07	1.62E+01	16.7	9.99E+02	1.09E-03	8.52E-14	-13.07	Riedel et al. 2002

Well ID	Easting	Northing	Center Interval Depth (m)	T(m^2/d)	K (ft/d)	K (m/s)	Est. T (C°)	Viscosity (kg/(m*s))	Density (kg/m^3)	Bulk Perm. (m^2)	log perm	Source
699-52-46	307731	5161866	60	8.64E+00	5.26E-06	1.69E+01	17.3	9.99E+02	1.07E-03	5.74E-13	-12.24	Reidel et al., 2002
699-50-45	307974	5161280	48	8.64E+00	7.69E-06	1.64E+01	16.8	9.99E+02	1.08E-03	8.49E-13	-12.07	Reidel et al., 2002
699-50-48	306953	5161227	71	8.64E+00	9.09E-06	1.72E+01	17.7	9.99E+02	1.06E-03	9.81E-13	-12.01	Reidel et al., 2002
699-47-50	306562	5160446	85	8.64E+00	9.09E-06	1.77E+01	18.2	9.99E+02	1.04E-03	9.68E-13	-12.01	Reidel et al., 2002
699-SII-EI2A	324538	5141915	77	8.64E-01	1.25E-06	1.74E+01	18.0	9.99E+02	1.05E-03	1.34E-13	-12.87	Reidel et al., 2002
BH-16	304025	5171864	273	4.32E+00	3.33E-06	2.50E+01	25.5	9.96E+02	8.78E-04	2.99E-13	-12.52	Reidel et al., 2002